A Search for Second-generation Leptoquarks in pp Collisions at $\sqrt{s} = 7$ TeV with the ATLAS Detector

A Dissertation Presented

by

Burton DeWilde

to

The Graduate School

in Partial Fulfillment of the Requirements

for the Degree of

Doctor of Philosophy

in

Physics

Stony Brook University

August 2012

Stony Brook University

The Graduate School

Burton DeWilde

We, the dissertation committee for the above candidate
for the Doctor of Philosophy degree,
hereby recommend acceptance of this dissertation.

Dmitri Tsybychev – Dissertation Advisor
Assistant Professor, Department of Physics and Astronomy

John Hobbs – Chairperson of Defense
Professor, Department of Physics and Astronomy

Abhay Deshpande
Associate Professor, Department of Physics and Astronomy

George Sterman
Distinguished Professor, Department of Physics and Astronomy

George Redlinger
Staff Physicist
Brookhaven National Laboratory

This dissertation is accepted by the Graduate School.

Charles Taber
Interim Dean of the Graduate School

Abstract of the Dissertation

A Search for Second-generation Leptoquarks in *pp* Collisions at $\sqrt{s} = 7$ TeV with the ATLAS Detector

by

Burton DeWilde

Doctor of Philosophy

in

Physics

Stony Brook University

2012

The apparent symmetry between the quark and lepton families of the Standard Model (SM) are, at the very least, suggestive of a more fundamental relationship between them. In some Beyond the Standard Model theories, such interactions are mediated by leptoquarks (LQs): hypothetical color-triplet bosons with both lepton and baryon number and fractional electric charge. The results of a search for pair-production of second-generation scalar LQs are presented for a final state consisting of one muon, missing transverse energy, and at least two jets. The search is performed on 1.03 fb^{-1} of integrated luminosity of proton-proton collision data produced by the Large Hadron Collider at a center-of mass energy of 7 TeV, as recorded by the ATLAS detector. Observed event yields in selected signal regions are found to be consistent with SM background expectations. Therefore, limits

are set: LQs with mass $m_{\mathrm{LQ}} < 545$ GeV are excluded at 95% confidence level (CL), assuming the branching ratio of a LQ to a muon and a quark $\beta \equiv \mathrm{BR}(LQ \to \mu q) = 0.5$. When these results are combined with those of a complementary search in the $\mu\mu jj$ final state, LQs with mass $m_{\mathrm{LQ}} < 594$ (685) GeV are excluded at 95% CL for $\beta = 0.5$ (1.0). These are currently the world's most stringent limits on second-generation scalar LQ production.

To my family.

*

To The Family.

Contents

List of Figures

List of Tables

List of Abbreviations

ATLAS A Toroidal Lhc ApparatuS

BR Branching Ratio, as in how often a particle decays in a certain way

BRW Buchmüller, Rückl, and Wyler, an effective leptoquark model

BSM Beyond the Standard Model

CERN European Organization for Nuclear Research

CL Confidence Level, as in a Frequentist limit

CR Control Region

CSC Cathode-Strip Chamber, a technology used in the Muon Spectrometer

DDTC Double-sided, Double Type Column, a 3D pixel sensor design

DUT Device Under Test

DQ Data Quality

EM ElectroMagnetic

EWSB ElectroWeak Symmetry Breaking

EWK ElectroWeak, shorthand for backgrounds arising from electroweak processes

EWT ElectroWeak Theory

FCNC Flavor-Changing Neutral Currents

FSR Final State Radiation, additional QCD radiation from final state particles involved in a hard scattering interaction

GRL Good Runs List

GEANT GEometry ANd Tracking, for the simulation of particle interactions with matter

GUT Grand Unified Theory

HEC Hadronic End-cap Calorimeter

HEP High-Energy Physics

ID Inner Detector, a component of the ATLAS detector

IP Interaction Point, where proton-proton collisions occur

ISR Initial State Radiation, additional QCD radiation from initial state particles involved in a hard scattering interaction

JES Jet Energy Scale

LAr Liquid Argon, as in a type of calorimeter technology (shorthand)

LHC Large Hadron Collider

LLR Log-Likelihood Ratio

LO Leading Order, as in a cross section or perturbative expansion

LQ LeptoQuark

MC Monte Carlo, as in a simulation based on random sampling

MCP Muon Combined Performance, a working group in ATLAS

MDT Muon Drift Tube, a technology used in the Muon Spectrometer

MET Missing Transverse Energy

MJ Multi-Jet, shorthand for backgrounds arising from QCD processes

MPI Multiple Parton Interactions

MS Muon Spectrometer, a component of the ATLAS detector

(N)NLO (Next to) Next to Leading Order, as in a cross section or perturbative expansion

PDF Parton Distribution Function *or* Probability Distribution Function

QCD Quantum ChromoDynamics

QED Quantum ElectroDynamics

QFT Quantum Field Theory

RPC Resistive Plate Chamber, a technology used in the Muon Spectrometer

SCT SemiConductor Tracker, a component of the Inner Detector

SF Scale Factor

SM Standard Model of particle physics

SPS Super Proton Synchrotron

STACO STAtistical COmbination, a muon reconstruction algorithm

SUSY SUperSYmmetry, a Beyond the Standard Model principle

TDAQ Trigger and Data AcQuisition, a system that selects and records collision data

TGC Thin Gap Chamber, a technology used in the Muon Spectrometer

TRT Transition Radiation Tracker, a component of the Inner Detector

Acknowledgements

Many people have contributed to this work both directly and indirectly, for which they have my sincerest thanks.

Thanks to my advisor, Dmitri Tsybychev, for constantly pushing me to succeed, in spite of all my complaining. Thanks to my unofficial co-advisor, John Hobbs, for making every moment a teachable one and leading by example. Thanks to the rest of the Stony Brook HEP group for showing me how physics research actually works — and facilitating my own.

Thanks to Carolina, Regina, and John for working with me on the leptoquark search through an endless series of bugs, cuts, plots, and approvals. Thanks to Jet for frequent tech support and inappropriate conversation topics. Thanks to Flip for delightful discussions of theory and whimsy. Thanks to Stephanie, Michael, Julia, Josh, the family Strauss, Jake, Daisy, Tim, Brian, Dan, and the rest of my CERNois crew for all the coffee, all the laughs, and all the lessons learned. Thanks to Poppy, Marlin, Paul, Sara, Jason, Katy, John, and the rest of my SBU crew for more coffee, more laughs, more lessons learned.

Thanks to Clif, Justin, and Aaron for a much-needed weekly distraction. Thanks to Max and Arcadio for a much-draggier weekly distraction. Thanks to Luke and the LHCz Collaboration for the non-physics to-do list and getting me into all sorts of unexpected adventures.

Thanks to Tom for unconditional support, generosity, and a place to call home.

Thanks to my family and The Family, for everything.

CHAPTER 1

Introduction

> I am now convinced that theoretical physics is actually philosophy.
>
> Max Born

Particle physics is the study of Nature at its most basic level: the elementary particles of matter and their interactions. Born in 1897 with Thomson's discovery of the electron, particle physics progressed rapidly thereafter through the work of Einstein, Rutherford, Bohr, Dirac, and many others. Scattering experiments revealed the nucleus and subsequently the protons and neutrons that comprise it, while studies of radiation revealed the inherently quantized nature of light in the form of *photons*. These and other results were in conflict with existing theory. In the case of small objects, then, classical mechanics was replaced by quantum mechanics; in the case of fast objects, it was superseded by special relativity; and in the case of small *and* fast objects (e.g. elementary particles), the union of these two theories led to quantum field theory (QFT).

Four fundamental forces of Nature are known: electromagnetism, the strong and weak nuclear forces, and gravity. By the mid-twentieth century, physicists had a working QFT called quantum electrodynamics (QED) that accurately described electromagnetic interactions between electrically charged particles by way of photon exchange. Around this time, physicists were discovering a multitude of seem-

ingly fundamental[1] particles, colloquially known as the "particle zoo." In 1961, Gell-Mann succeeded in classifying the particles into groups and went on to suggest the existence of particles called *quarks* that, in various combinations, make up most of the particles in the zoo.[2] Experimental verification of the quark model and related theoretical advances contributed to the development of quantum chromodynamics (QCD), a QFT describing the interactions of quarks via *gluon* exchange that are responsible for the strong force. Understanding of the weak force came through Glashow, Weinberg, and Salam, who expressed the electromagnetic and weak interactions as different expressions of a single *electroweak* interaction[3] mediated by three massive particles (W^+, W^-, Z^0) in addition to the photon. [1]

The Standard Model (SM) of particle physics represents the culmination of these theoretical and experimental developments: it is a self-consistent QFT framework in which elementary particles undergo electromagnetic, strong, and weak interactions through fields, of which they are the sources, with associated particles mediating the interactions. A number of shortcomings (such as the lack of a quantum description for gravity) suggest that it is only an effective, low-energy theory. Nevertheless, the SM has been spectacularly successful.

1.1 The Standard Model of Particle Physics

The Standard Model [1][2] is a theory of interacting fields that determine the dynamics of elementary particles pursuant to fundamental symmetries of Nature, i.e. global space-time and local gauge symmetries, as described mathematically by group theory. This relation runs deep: According to Noether's theorem, for every symmetry of a system there exists a corresponding conservation law.[4] In fact, the construction of the SM was guided by principles of symmetry (as well as symmetry *breaking*), and it can be defined by the symmetry group it represents: $\mathrm{SU}(3)_C \times \mathrm{SU}(2)_L \times \mathrm{U}(1)_Y$, where c is for *color*, L is for "left-handed," and Y is for *hypercharge*. Strong and electroweak interactions derive from the requirement of *local gauge invariance*.

[1] Fundamental, or *elementary*, particles are those with no substructure — that is, they can't be subdivided. Atoms were once considered fundamental until the discovery of the electron and proton; similarly, protons were thought to be elementary until the discovery of quarks.

[2] Independently, Zweig also postulated the existence of quarks, but called them "aces." The name did not stick.

[3] In analogy with QED and QCD, the theory of weak interactions may be called quantum flavordynamics (QFD), but this term is rarely used because the weak force is better understood in the context of the electroweak model, also called the GWS model after its architects.

[4] For example, the invariance of the SM Lagrangian under translations in space and time are associated with the conservation of momentum and energy. Analogously, invariance under a gauge transformation is associated with the conservation of a charge.

Generation	Flavor	Charge [e]	Mass [MeV]
1st	electron (e)	-1	0.511
	electron neutrino (ν_e)	0	$< 2 \times 10^{-6}$
2nd	muon (μ)	-1	105.658
	muon neutrino (ν_μ)	0	< 0.19
3rd	tau (τ)	-1	1776.82
	tau neutrino (ν_τ)	0	< 18.2

Table 1.1: SM leptons. All have spin-1/2. Neutrino masses are small but not yet measured, so current experimental limits are given. Uncertainties are omitted. [4]

First, a brief note on units [3]: In particle physics, it is both convenient and customary to use a system of "natural" units in which the speed of light in a vacuum $c = 2.998 \times 10^8$ m/sec and Planck's constant $\hbar = h/2\pi = 1.055 \times 10^{-34}$ J $\cdot$ sec are set equal to 1. As a result, mass (m), momentum (mc), and energy (mc^2) are all given in terms of electron volts eV or some power thereof, such as MeV $\equiv 10^6$ eV, while length ($\hbar/mc$) and time ($\hbar/mc^2$) have units of eV^{-1} (or MeV^{-1}). Electric charge is typically given in units of elementary charge $e = 1.602 \times 10^{-19}$ C and is related to the fine structure constant by $e = \sqrt{4\pi\alpha}$.

1.1.1 Elementary Particles

According to the SM, matter is composed of two types of elementary particles: *quarks* and *leptons*, each of which comes in six distinct *flavors*. Quarks and leptons are endowed with intrinsic properties that determine which interactions they participate in and also distinguish the types and flavors from each other.[5] All have half-integer intrinsic angular momentum, or *spin*, and therefore belong to a class of particles called *fermions* that behave according to Fermi-Dirac statistics and obey the Pauli exclusion principle, which states that no two identical fermions may simultaneously occupy the same quantum state. They are also characterized by electric charge: leptons have either negative ($Q = -1$) or zero ($Q = 0$) charge, while quarks have either positive ($Q = +2/3$) or negative ($Q = -1/3$) fractional charge. Quark and lepton masses range over many orders of magnitude, with values that seem to follow no obvious pattern; the origin and nature of mass is an unresolved question in the SM. Leptons and quarks are listed in Tables 1.1 and 1.2, respectively, along with some of their properties.

[5] Note, however, that particles of the same type and flavor are *fundamentally* identical and therefore indistinguishable.

Generation	Flavor	Charge [e]	Mass [MeV]
1st	up (u)	$+2/3$	$1.7-3.1$
	down (d)	$-1/3$	$4.1-5.7$
2nd	charm (c)	$+2/3$	1.29×10^3
	strange (s)	$-1/3$	$80-130$
3rd	top (t)	$+2/3$	172.9×10^3
	bottom (b)	$-1/3$	4.19×10^3

Table 1.2: SM quarks. All have spin-1/2. Since isolated quarks do not exist in Nature, their masses are determined indirectly from hadron properties and only make sense in the context of a particular theory; approximate ranges are given for the light quarks. Uncertainties are omitted. [4]

For each particle there exists a corresponding *antiparticle* with the same mass but opposite-sign quantum numbers, such as electric charge. Standard notation for antiparticles is an overbar (e.g. q for a quark and $\bar{q}$ for an antiquark), but in some cases charge is used to distinguish the two (e.g. e^- for an electron and e^+ for a positron). SM interactions are slightly asymmetric with respect to particles and antiparticles [5]; however, it may be insufficient to explain the preponderance of matter over antimatter in the Universe — another unresolved issue [6].

The twelve SM fermions fall naturally into three like generations — of two quarks and two leptons apiece — that differ only in the masses of the particles comprising them. The first generation consists of the up quark (u), down quark (d), electron (e^-), and electron neutrino (ν_e). Together, these particles make up almost all of the everyday matter we're familiar with: bound states of up and down quarks form the protons (uud) and neutrons (udd) of atomic nuclei, which are themselves surrounded by clouds of electrons, while electron neutrinos are produced copiously in nuclear decays and the fusion reactions that power stars. The second and third generations consist of analogous particles at successively larger masses.[6] The SM provides no explanation for the existence of exactly three generations, though certain aspects of the theory *require* at least this many generations. In general, more massive particles are unstable and will decay into lighter, stable particles unless prevented from doing so by kinematics or a conservation law.

All leptons participate in weak interactions, and charged leptons also participate in electromagnetic interactions. They do not participate in strong interactions. Plus, leptons are assigned a *lepton number* L split by generation: L_e, L_μ, and L_τ.

[6] With the possible exception of neutrinos, whose mass hierarchy has not yet been determined. In the original formulation of the SM, neutrinos are *massless*, but experimental proof of non-zero neutrino masses [7] can be incorporated into the theory with only modest changes [8].

Force	Strength	Mediator	Spin	Charge [e]	Mass [GeV]
Strong	10^{+1}	gluon (g_i, i = 1 ... 8)	1	0	0
Electromagnetic	10^{-2}	photon (γ)	1	0	0
Weak	10^{-13}	$W^{\pm}$	1	± 1	80.399
		Z^0	1	0	91.188
Gravitational	10^{-42}	graviton (G)	2	0	$< 7 \times 10^{-41}$

Table 1.3: SM forces and associated bosons. Relative strengths are approximate. Gravity is provided for comparison only: It is not part of the SM, and the graviton is purely hypothetical. Uncertainties are omitted. [4]

Electrons and electron neutrinos have $L_e = 1$ and $L_\mu = L_\tau = 0$; muons, taus, and their associated neutrinos follow the same pattern. Lepton number is accidentally conserved[7] in all SM processes — with the notable exception of *neutrino oscillations*, in which a massive neutrino of one flavor converts into that of another flavor. While this phenomenon means that lepton numbers are not separately conserved, it may leave the overall lepton number $L \equiv L_e + L_\mu + L_\tau$ as a conserved quantity.[8]

All quarks participate in weak and electromagnetic interactions as well as strong interactions. Thus, they require an additional quantum number: the strong charge, called color, with values of red (r), green (g), and blue (b).[9] Unlike leptons, "bare" quarks do not exist in Nature. Instead, quarks are confined to bound states called *baryons*, which consist of three differently-colored quarks (qqq) or antiquarks ($\bar{q}\bar{q}\bar{q}$), or *mesons*, which consist of an oppositely-colored quark and antiquark ($q\bar{q}$). Collectively, they are known as *hadrons*, and all are color-neutral. Analogous to lepton number, a *baryon number* B of $+1/3$ is assigned to quarks and $-1/3$ to antiquarks, such that baryons have $B = \pm 1$ and mesons have $B = 0$. SM interactions appear to accidentally conserve baryon number, which guarantees the stability of the proton and the continued existence of the Universe as we know it.[10]

Forces in the SM are mediated by fundamental particles known alternatively as force mediators, force carriers, or (technically) *gauge bosons*. In contrast with fermions, they have integer spin and thus behave according to Bose-Einstein statistics. Electromagnetic interactions are carried by the photon (γ), weak interactions by the charged and neutral *intermediate vector bosons* ($W^{\pm}$ and Z^0, respectively),

[7] Nature observes this rule, but it isn't *required* by gauge symmetry.

[8] This isn't technically true. While L and B (described in the next paragraph) are conserved "classically," both are broken by quantum effects. The fully conserved quantity is actually $B - L$.

[9] The terminology here is pure whimsy and has no connection with the usual sense of the word. To wit: antiquarks come in antired ($\bar{r}$), antigreen ($\bar{g}$), and antiblue ($\bar{b}$).

[10] Protons are the only stable baryon; no mesons are stable.

and strong interactions by (eight) gluons (g). Table 1.3 lists these particles along with some of their properties. Further details are discussed in context below.

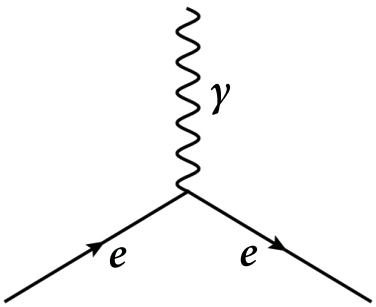

Figure 1.1: The fundamental vertex of electromagnetic interactions.

1.1.2 Quantum Electrodynamics

Quantum electrodynamics is a quantum field theory describing the interactions of electrically charged fermions with an electromagnetic field through the exchange of photons [9]. Historically, QED was the first successful QFT, providing the model on which all subsequent QFTs were self-consciously based, and as such, the qualitative procedure described below generalizes to other interactions.

Free quarks and leptons are represented by fields whose dynamics are specified by a Lagrangian that is invariant under global space-time transformations belonging to the U(1) group[11] [2]. Further imposing that the Lagrangian be invariant under similar but *local* (i.e. at every point in space and time) gauge transformations requires the introduction of a gauge field that transforms in such a way as to leave the Lagrangian invariant. When quantized, this gauge field represents a quantum analogue to the classical electromagnetic field, with photons as excitations or *quanta* of the field; its gauge invariance implies that photons are massless.[12] Interactions between charged fermions and the gauge field via photons also derive directly from local gauge invariance, and since photons are electrically neutral, they do not self-interact.[13] The strength of electromagnetic interactions is determined by a dimensionless coupling "constant":

$$\alpha_e = \frac{g_e^2}{4\pi} \approx \frac{1}{137} \,, \tag{1.1}$$

[11] U(N) stands for the unitary group of degree N. It consists of the group of $N \times N$ unitary matrices, i.e. $U^\dagger U = UU^\dagger = I_1$. U(N) groups have N generators.

[12] If gauge symmetry were broken, the photon would acquire a mass on the order of the symmetry-breaking scale; experimental limits, however, are very tight: $m_\gamma < 2 \times 10^{-16}$ eV [10].

[13] QED is an *Abelian* gauge theory, characterized by generators that commute ($g_i g_j = g_j g_i$).

where $g_e = e$ is the elementary charge.

Interactions can be represented symbolically by Feynman diagrams. The basic QED process is shown in Figure 1.1; more complicated processes are simply combinations of multiple such vertices. In these diagrams, time flows left to right, external lines represent "real" (observable) particles, and internal lines represent "virtual" (unobservable) particles. When combined with so-called Feynman rules, these diagrams can be used to calculate the probability amplitude for given a process to occur. It's worth noting that each vertex adds a factor of α_e to the calculation, so more complicated (many-vertex) processes contribute less to the final result. [1]

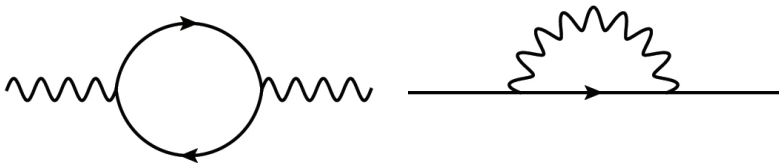

(a) (b)

Figure 1.2: Loop diagrams for (a) vacuum polarization and (b) electron self-energy.

Given the smallness of the electromagnetic coupling, calculations in QED readily lend themselves to perturbation theory, in which measurable quantities are written as expansions order by order in α_e. However, divergent integrals arise (corresponding to Feynman diagrams with closed loops of virtual particles, as shown in Figure 1.2) that predict infinite values for, say, the mass and charge of the electron. Techniques were developed to deal with these divergences, holding up the development of QED for nearly two decades [1]. Essentially, the divergences are absorbed into finite, *renormalized* parameters, necessarily introducing — by hand — an energy scale Λ equivalent to the scale at which a measurement of the parameter is performed. As a result, the parameter must depend on E/Λ and is therefore *not* constant; it is said to be "running." This procedure is called *renormalization*. In a renormalizable theory, all such infinities can be absorbed into a finite number of parameters. In the case of QED, the physical particle masses and charges are finite (as measured at some renormalization energy scale) while their bare (but un-observable) values are infinite.[14] For further details, see also [2], [3], and [11]

Despite such thorny conceptual issues, QED has proven extremely successful. Its effects have been experimentally verified over distance scales ranging 40 orders of magnitude, and theoretical predictions for the values of certain particle properties have been confirmed to better than one part in 10^{-11} [12]. It is the most precisely tested theory in all of physics.

[14] For many years, renormalizability was considered a requirement for any physically-relevant QFT, but a more modern interpretation focuses on the validity of a non-renormalizable QFT as an *effective field theory* [10].

Lastly, in addition to global space-time and local gauge symmetries, QED interactions also conserve flavor and a number of *discrete* symmetries: charge conjugation (C), in which all particles involved in an interaction are exchanged for their antiparticles; parity (P), in which spatial coordinates are inverted (i.e. the interaction is mirrored); time reversal (T), in which an interaction may equally well proceed forward or backward in time; and their combination (CPT), which is considered a fundamental symmetry of *any* self-consistent quantum field theory. [1]

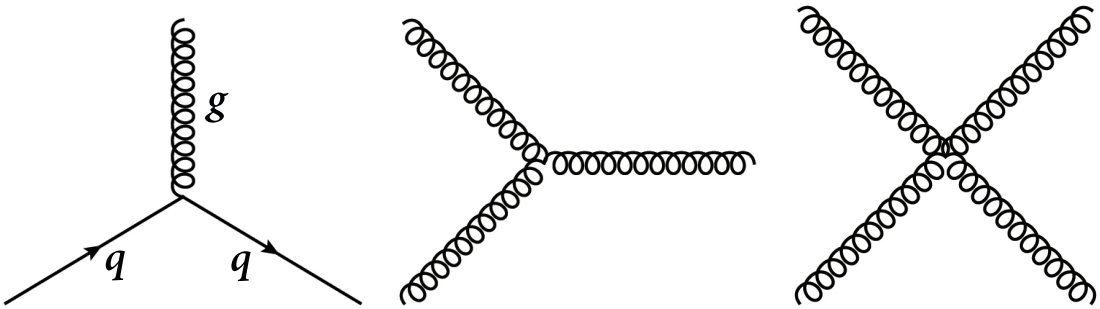

Figure 1.3: The fundamental vertices of strong interactions. Gluon self-interaction permits $3g$ and $4g$ vertices.

1.1.3 Quantum Chromodynamics

Quantum chromodynamics is a renormalizable QFT describing the strong interactions of color-charged particles. Since each flavor of quark comes in three colors, they are arranged in color-triplets, and their Lagrangian is invariant under global SU(3) gauge transformations.[15] In this case, the imposition of local gauge invariance gives rise to *eight* real and independent gauge fields, corresponding to an *octet* of gluons that mediate the interactions. Gluons are massless, spin-1 bosons that also possess color — actually, one unit of color and one of anticolor — and therefore interact with other gluons as well as themselves. This has important consequences! In analogy with QED, the strength of QCD interactions is given by a dimensionless coupling parameter:

$$\alpha_s = \frac{g_s^2}{4\pi} \sim 1, \tag{1.2}$$

where g_s may be thought of as the fundamental unit of color charge. The relative strength of the coupling with respect to the other interactions is what gives

[15] SU(N) stands for the *special* unitary group of degree N. It consists of the group of $N \times N$ unitary matrices with determinant equal to 1, and has (N^2-1) generators. Concretely, SU(3) has $(3^2-1) = 8$ generators.

the strong force its name; it also limits the range of applicability of perturbative methods and complicates analytic calculations of the theory.

Although strong interactions are, in a sense, copies of electromagnetic ones (simply replace α_e by α_s and electric charge by color charge), QCD is distinguished by its *three* charges and two notable features: *asymptotic freedom* and *confinement*. Ultimately, both arise because gluons themselves carry color charge. While virtual $q\bar{q}$ pairs in the vacuum screen color charge as e^+e^- pairs screen electric charge, the addition of gluon-induced vacuum polarization has an opposite (and larger) *anti*-screening effect. So, in contrast with the electromagnetic coupling, α_s gets *smaller* with increasing interaction energy or, equivalently, decreasing distance scale between color-charged particles. As a result, quarks rattle around inside hadrons as if they were free, up to a ~ 1 fm separation; this phenomenon is called asymptotic freedom.[16] The flip side of this is confinement: strong interactions increase in strength with increasing distance, thereby forcing quarks into bound, color-neutral states (hadrons), since separating them would require an infinite amount of energy. In reality, if two bound quarks are separated by a sufficiently large distance, it becomes energetically favorable to simply create a new $q\bar{q}$ pair out of the vacuum, resulting in *two* bound pairs.[17]

Color charge is always conserved in QCD interactions, as is flavor. The discrete C, P, T, and CPT symmetries are also obeyed.

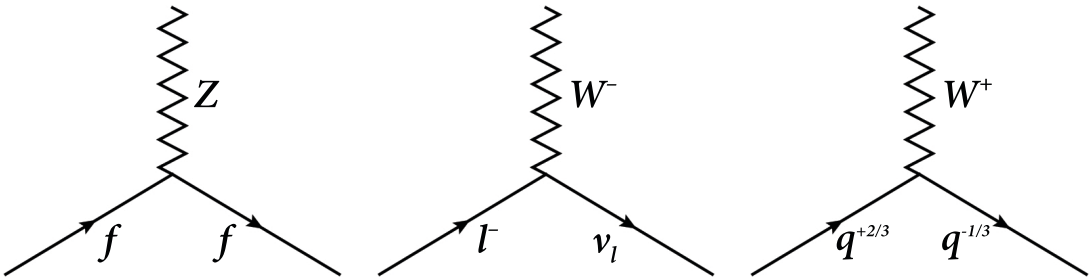

Figure 1.4: The fundamental vertices of weak interactions. W and Z bosons may also directly couple to themselves (not pictured).

[16] In this high-energy/small-distance (small-α_s) regime, perturbative QCD calculations are valid. It is worth noting that the variation in α_s over accessible energy scales is much larger than that of α_e. In other words, the strong coupling "runs" faster than the electromagnetic one.

[17] This phenomenon has significant experimental consequences. See Section 3.1.3.

1.1.4 Electroweak Theory

Weak interactions are unique among the fundamental forces of Nature in a number of ways: they affect *all* quarks and leptons; they are mediated by three *massive* bosons (W^+, W^-, and Z) and therefore have very short range[18]; they come in charged and neutral varieties, where charged weak interactions via $W^\pm$ exchange do not conserve flavor; they also violate parity (maximally), charge conjugation, and CP symmetries. Despite these differences, the electromagnetic and weak interactions are unified at high energies ($\sim$ 100 GeV) and interpreted as different manifestations of a single *electroweak* interaction [13] [14] [15]. A familiar (but mostly heuristic) analogue is the unification of the electric and magnetic forces.

Construction of a renormalizable electroweak theory (EWT) proceeds in a generally familiar manner. Left-handed quarks and leptons are grouped into doublets, while right-handed quarks and charged leptons occupy singlets.[19] The associated fields and Lagrangian are constructed such that they are invariant under local $\mathrm{SU}(2)_L \times \mathrm{U}(1)_Y$ transformations. This requirement gives rise to three SU(2) gauge fields — W^i (i = 1, 2, 3), with corresponding coupling g and $(2^2-1) = 3$ gauge bosons — and one U(1) gauge field — B, with g' and a single gauge boson. Ultimately, the $W^\pm$ bosons are identified as linear combinations of W^1 and W^2, while Z and γ appear as mixtures of W^3 and B:

$$W^\pm = (W^1 \mp iW^2)/\sqrt{2} \tag{1.3}$$

$$\gamma = B\cos\theta_w + W^3 \sin\theta_w \tag{1.4}$$

$$Z = -B\sin\theta_w + W^3\cos\theta_w, \tag{1.5}$$

where θ_w is the weak mixing angle. In electroweak interactions, weak *isospin* T and hypercharge Y are conserved. For consistency with QED, EWT requires that $Q = T^3 + \frac{1}{2}Y$ (only one component of isospin is required, taken to be T^3 by convention) and $g\sin\theta_w = g'\cos\theta_w = g_e$, giving $\theta_w = \tan^{-1}(g'/g)$. Such interrelations in the SM are self-consistent and verified by experiment.[20] Ultimately, the point is this: electromagnetic and weak interactions are not independent of each other.

As in QED and QCD, gauge invariance requires that all four gauge bosons remain massless; however, it is observed experimentally that only the photon is mass-

[18] As in electromagnetic and strong interactions, the weak coupling constant can be written as $\alpha_w = g_w^2/4\pi \approx 1/30$ — *larger* than α_e! The relative weakness of the force (at low energies) actually results from the large masses of its mediators.

[19] The incorporation of massive neutrinos into the SM would involve the addition of singlets for right-handed neutrinos, if neutrinos are Dirac particles (distinct from their antiparticles). However, this is not yet clear: neutrinos may well be Majorana particles (their own antiparticles).

[20] All electroweak parameters can be calculated, given experimental measurements of the Fermi constant G_F, fine structure constant α, and Z boson mass m_Z as input. To first order.

less, while the W and Z bosons are massive. The solution to this fundamental mismatch lies in the phenomenon of *electroweak symmetry breaking* (EWSB), in which the underlying $\mathrm{SU}(2)_L \times \mathrm{U}(1)_Y$ symmetry is spontaneously broken at a particular energy scale. In the SM, EWSB is accomplished by means of the *Higgs mechanism* [16], which gives mass to the W and Z bosons (as well as quarks and leptons) while still preserving the renormalizability of the theory. Basically, the choice of lowest energy (vacuum) state breaks the gauge symmetry.

A complex *scalar* field ϕ is introduced, with a potential of the form

$$V(\phi) = \frac{\mu^2}{2}|\phi|^2 + \frac{\lambda}{4}|\phi|^4, \tag{1.6}$$

where the case $\mu^2 < 0$ and $\lambda > 0$ can be related to the SM. See Figure 1.5. The minimum point ϕ_0 of this potential occurs at a finite value of $|\phi|$, giving it a non-zero *vacuum expectation value* $v = \sqrt{-\mu^2/\lambda}$ determined by experiment to be $v \approx 246$ GeV. The choice of ϕ_0 spontaneously breaks both $\mathrm{SU}(2)_L$ and $\mathrm{U}(1)_Y$ gauge symmetries[21] but leaves the $\mathrm{U}(1)_{em}$ subgroup intact; as a result, the W and Z bosons acquire mass while the γ does not. Fermions also acquire mass from interactions with this scalar field (albeit through a different mechanism), with masses directly dependent on the strengths of their couplings. Associated with the field is an elementary scalar (spin-0) particle called the *Higgs boson*, whose mass is given by $m_h = v\sqrt{\lambda/2}$, where λ is its self-coupling parameter. While the couplings to other particles are predicted, its self-coupling (and, in turn, its mass) are not; currently, the Higgs boson is the last unobserved piece of the SM. After two decades of searches, however, experiments may finally have detected the first signs of its existence [17] [18].

Nevertheless, the as-yet unconfirmed mechanism by which EWSB occurs, and the Higgs boson itself, are closely linked to some known shortcomings of the SM, and may point to physics beyond it.

1.2 Beyond the Standard Model

1.2.1 Shortcomings of the SM

Although the Standard Model is a mathematically consistent theory in agreement with almost all experimental results to date[22] , it is widely considered an incomplete, effective "low-energy" theory, valid only up to energy scales on the order of

[21] The Lagrangian remains invariant, but the vacuum does *not*.

[22] For example, recent experimental measurements of the muon anomalous magnetic moment are in persistent disagreement with the SM theoretical prediction, with a significance of about three standard deviations [20]. This may indicate a source of new physics.

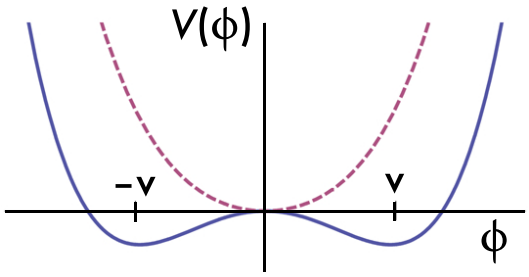

Figure 1.5: The Higgs potential: for $\mu^2 > 0$ (dashed line), $\phi_0 = 0$ and symmetry is unbroken; for $\mu^2 < 0$ (solid line), choosing $\phi_0 = v$ or $-v$ breaks the symmetry. [19]

$\sim$ 1 TeV [21]. There are numerous reasons for this assumption, both experimental and theoretical [19], including the following:

- The SM does not include gravitational interactions, and it appears that QFT can not accommodate a quantum theory of gravity.
- Cosmological measurements indicate that SM particles ("baryonic matter") make up just 4.6% of the Universe, with the remainder split between so-called *dark matter* (23%) and *dark energy* (72%); the SM offers no explanation or viable candidate particles for either [22] [23].[23] Additionally, the observed isotropy and homogeneity of the Universe seems to demand some mechanism, such as *inflation*, that is similarly non-existent in the SM.
- While CP violation is incorporated into the SM, it is orders of magnitude too small to account for the observed matter-antimatter asymmetry of the Universe. On a related theoretical note, CP violation is theoretically permissible in QCD, but no such interactions have been observed.
- Charge is quantized, such that all particles have charges in multiples of $e/3$ and all anti-particles have *exactly* the same but opposite-sign charges.[24] The SM provides no explanation, but does require it to be true.
- The SM contains a large number of free parameters: 12 fermion masses (neutrinos included), 6 mixing angles, 2 CP-violating phases, 3 gauge couplings, and the Higgs boson mass, among others. A more fundamental theory might be expected to *predict* these values rather than accept them as ad hoc inputs.

[23] Once confirmed as massive particles, SM neutrinos were proposed as possible dark matter candidates, if only for their "undisputed virtue of being known to exist." However, experimental evidence indicates that they are at most a tiny fraction of the total dark matter in the Universe.

[24] Current limits have $|Q_{e^-} + Q_{e^+}|/e < 1.0 \times 10^{-21}$, strongly suggesting that $Q_{e^-} = -Q_{e^+}$ [4].

- The mechanism by which EWSB occurs (the Higgs mechanism, in the SM) is added in "by hand," and the scale at which it occurs is unexplained (a free parameter). And why should there be a single scalar field whose only role is to break a symmetry of Nature, anyway?!

- Quantum corrections to the mass of the Higgs boson are quadratically divergent, depending on the scale Λ at which new physics occurs: $m_h^2 = m_0^2 + c\Lambda^2$, where m_0 is the bare Higgs mass and c is a dimensionless constant. If Λ is taken to be large, possibly up to the Planck scale (10^{19} GeV), getting $m_h \sim 100$ GeV instead of $m_h \sim \Lambda$ requires *unnaturally* fine-tuned cancellations between terms. This is called the "naturalness" or "hierarchy" problem.

A number of "Beyond the Standard Model" (BSM) theories have been proposed that resolve or at least address one or more of these shortcomings.

1.2.2 Overview of BSM Physics

In a general sense, BSM physics refers to *any* possible extension of the SM [24]. While the associated "theory-space" of new interactions, charges, symmetries, and other parameters is vast, the region of most immediate interest corresponds to those models predicting new phenomena at the TeV-scale, to which the current generation of particle collider experiments (see Chapter 2) are sensitive. At this scale, the mechanism of EWSB and the hierarchy problem are particularly salient. No formal classification of BSM frameworks exists; however, models may be grouped by the shared, basic assumptions from which they derive [25] [26]:

- The SM is a subgroup of some larger symmetry group, which results in new interactions and unification of seemingly distinct particles and/or forces. New physics is weakly coupled to the SM. For example: supersymmetry, grand unified theories.

- SM particles (including the Higgs boson) are actually composites of new, fundamental particles. The associated new gauge group is strongly coupled but asymptotically free, as in QCD. For example: technicolor, compositeness.

- The scale of new physics is close to the electroweak scale — that is, the *apparent* high-energy scale at which gravity becomes significant (the Planck scale) is the result of "extra" space-time dimensions that serve to reduce the strength of gravitational coupling at large distances. For example: large, flat, or warped extra dimensions.

Brief overviews of some principle BSM scenarios are given here. In the next section, additional details are discussed with regards to a particular class of hypothetical particles.

1.2 Beyond the Standard Model

Supersymmetry

Supersymmetry (SUSY) is perhaps the most well-known and mathematically mature BSM framework. It extends the Poincaré symmetry group[25], relating elementary particles of different spins [27]. The generic prediction is a "super-partner" for each SM particle that differs only by a half-integer unit of spin: quarks and leptons (fermions) have squarks and sleptons (bosons), gauge and Higgs bosons have gauginos and Higgsinos (fermions). Given that such super-partners have never been experimentally observed, SUSY must be a broken symmetry, potentially at the TeV-scale. In order to avoid processes that fail to conserve lepton and baryon number, a discrete *R-parity* symmetry may be imposed: SM fields have $R = 1$, while super-partner fields have $R = -1$. This general model provides a candidate for dark matter (the lightest SUSY particle is stable) and baryon-antibaryon asymmetry (additional CP violation), protects the Higgs mass from quadratic divergences (contributions from super-partners exactly cancel the SM ones out), can provide an explanation for EWSB, and suggests the unification of the strong and electroweak gauge couplings at high energies. [26]

Grand Unified Theories

Grand Unified Theories (GUTs) seek to unify the electroweak and strong interactions at very high energies — a logical continuation of the electromagnetic and weak unification — and possibly unify quarks and leptons as different states of one family. Given that the strong and weak couplings *decrease* with increasing interaction energy while the electromagnetic coupling *increases*, it is tempting to suspect that they become equal at the "GUT scale" ($\sim 10^{16}$ GeV), yielding a single, universal α_G. To this end, GUTs embed the SU(3) $\times$ SU(2) $\times$ U(1) symmetry of the SM into a larger gauge group: the original proposals were Pati-Salam SU(4) [28] and Georgi-Glashow SU(5) [29], as well as SO(10) [30]. In the SU(5) case, SM fermions are conveniently arranged in multiplets (a quintet and a decuplet) that correctly quantizes their hypercharge quantum numbers. SU(5) has $(5^2 - 1) = 24$ gauge bosons, only 12 of which correspond to known SM force mediators (more on this in Section 1.3). As with SUSY, the symmetries proposed by GUTs must be broken at some high-energy scale. It's worth noting that SUSY and GUTs are not exclusive, and in fact are combined quite naturally. [25]

[25] Poincaré symmetry covers all of special relativity: translations in space and time, rotations in space, and boosts — the last two of which make up the Lorentz group.

Technicolor

Technicolor (TC) is the canonical example of a strong, dynamical model of EWSB — no Higgs mechanism required [31] [32] [33]. It posits a new, strongly-interacting gauge field (originally inspired by QCD) that is asymptotically free at high energies but confining at lower energies, close to or at the electroweak scale. Associated with this field is a new charge called technicolor (hence the theory's name) and new massless particles called *technifermions* that form bound states of *technihadrons* and, in Extended Technicolor (ETC) models [34], couple to SM quarks and leptons. At energy scales below Λ_{TC}, the global chiral symmetries of technifermions are spontaneously broken, giving rise to EWSB and mass to the W and Z bosons and, in ETC, the ordinary quarks and leptons as well. This model provides a more "natural" explanation for EWSB than the Higgs mechanism and avoids the pitfalls associated with a fundamental scalar particle, such as the hierarchy problem. [35]

1.3 Leptoquark Phenomenology

The apparent symmetry between quarks and leptons in the Standard Model is, at the very least, *suggestive* of a more fundamental relationship between them. Some BSM scenarios expand the space-time or gauge symmetries of the SM, putting quarks and leptons on equal footing and thereby permitting new interactions between them. Such interactions are mediated by a class of hypothetical particles called *leptoquarks* (LQs) that couple directly to lepton-quark pairs (hence the name).

LQs have a rich phenomenology, but they share some general features. They are bosons, either scalar (spin-0) or vector (spin-1). They are color triplets under $\text{SU}(3)_C$. They carry both lepton and baryon number, and fractional electric charge. Scalar LQs couple to lepton-quark pairs by a single Yukawa coupling λ, while vector LQs have additional magnetic moment and electric quadrupole moment interactions whose strengths are governed by two couplings, κ_G and λ_G. [36] [4]

A general, effective Lagrangian for LQ interactions with lepton-quark pairs was formulated by Buchmüller, Rückl, and Wyler [37]. In the BRW model, LQ interactions are 1) renormalizable, 2) invariant under the $\text{SU}(3)_C \times \text{SU}(2)_L \times \text{U}(1)_Y$ SM gauge group, and 3) only occur with SM particles. The possible quantum numbers of LQ states are reduced by requiring that 4) their interactions separately conserve L and B — a good assumption given experimental constraints discussed in Section 1.3.3. In the *minimal* BRW model, additional requirements are imposed: 5) LQs have pure chiral couplings and 6) couple to a single lepton-quark generation. This implies the existence of three LQ generations: LQ_1, LQ_2, and LQ_3. Such LQs can be classified by their *fermion number* $F = L + 3B$, where those with $F = 0$ (-2) couple to $\ell\bar{q}$ (ℓq) pairs [38]. Quantum numbers for electric charge, weak isospin,

and other properties depend on the LQ model. A full listing is given in Table 1.4.

1.3.1 Examples in BSM

Leptoquark-like particles appear commonly in BSM scenarios. In most cases, only a subset of those LQs listed in Table 1.4 appear in a given model. A few specific examples are given below.

SUSY models allow for leptoquark-like interactions, provided R-parity is not conserved and a superpotential with additional Yukawa couplings is added to the SUSY Lagrangian. As a result, squarks perform the role of LQs, coupling (decaying) directly to lepton-quark pairs.[26] Note that such interactions violate lepton number conservation, which in turn requires that baryon number be conserved for consistency with the observed stability of protons. [36]

In the Pati-Salam $SU(4)_C$ GUT, lepton number is treated as the fourth color, and quarks and leptons are grouped together into fermionic multiplets. A general consequence is the existence of exotic gauge mesons that carry both lepton and baryon number, i.e. leptoquarks. In Georgi-Glashow SU(5), half of the 24 gauge bosons correspond to SM bosons, while the other 12 X and Y bosons[27] mediate new interactions and may directly couple to lepton-quark pairs. Although the minimal SU(5) scenario predicts LQ masses on the order of the GUT scale, far beyond the reach of current experiments, certain models (e.g. [39]), allow for much lighter masses at the electroweak scale. [25]

In order to avoid large flavor-changing neutral current (FCNC) interactions[28] ruled out experimentally, the Extended Technicolor model was updated to Walking Technicolor [40], in which the technicolor gauge coupling runs more slowly ("walks") in the presence of numerous technifermions. This, in turn, implies the existence of many technimesons at a relatively low mass scale, including color-triplet leptoquark technipions (π_{LQ}) consisting of a techniquark and an anti-technilepton bound by the technicolor force. [38]

1.3.2 Production at Hadron Colliders

In hadron-hadron collisions, LQs can be produced either singly or in pairs [41]. Single LQ production occurs in association with a lepton, as shown in Figure 1.6, and therefore depends directly on the (unknown) strength of its Yukawa coupling, $\lambda_{\ell q}$. In contrast, pair-production occurs through QCD processes, dominantly gluon

[26] This also allows for two other interactions: slepton to lepton-lepton and squark to quark-quark.

[27] X bosons have $Q = \pm 4/3$, Y bosons have $Q = \pm 1/3$, and each comes in three colors — for a total of 12 [1].

[28] Interactions that change the flavor of a fermion without changing its charge occur only via charged currents (mediated by W bosons). For example, $\mu^- \to e^- + Z^0$ is not permitted in the SM.

LQ Type	Q [e]	T^3	$\lvert F\rvert$	LQ Decay	BR(LQ$\rightarrow eq$)
S_0^L	$-1/3$	0	2	$e_L u_L$	0.5
				$\nu_e d_L$	0.5
S_0^R	$-1/3$	0	2	$e_R u_R$	1
$\tilde{S}_0^R$	$-4/3$	0	2	$e_R d_R$	1
S_1^L	$-4/3$	-1	2	$e_L d_L$	1
	$-1/3$	0	2	$e_L u_L$	0.5
				$\nu_e d_L$	0.5
	$+2/3$	$+1$	2	$\nu_e u_L$	0
$V_{1/2}^L$	$-4/3$	$-1/2$	2	$e_L d_R$	1
	$-1/3$	$+1/2$	2	$\nu_e d_R$	0
$V_{1/2}^R$	$-4/3$	$-1/2$	2	$e_R d_L$	1
	$-1/3$	$+1/2$	2	$e_L u_L$	1
$\tilde{V}_{1/2}^L$	$-1/3$	$-1/2$	2	$e_L u_R$	1
	$+2/3$	$+1/2$	2	$\nu_e u_R$	0
V_0^L	$-2/3$	0	0	$e_L \bar{d}_R$	0.5
				$\nu_e \bar{u}_R$	0.5
V_0^R	$-2/3$	0	0	$e_R \bar{u}_L$	1
$\tilde{V}_0^R$	$-5/3$	0	0	$e_R \bar{u}_L$	1
V_1^L	$-5/3$	-1	0	$e_L \bar{u}_R$	1
	$-2/3$	0	0	$e_L \bar{d}_R$	0.5
				$\nu_e \bar{u}_R$	0.5
	$+1/3$	$+1$	0	$\nu_e \bar{d}_R$	0
$S_{1/2}^L$	$-5/3$	$-1/2$	0	$e_L \bar{u}_L$	1
	$-2/3$	$+1/2$	0	$\nu_e \bar{u}_L$	0
$S_{1/2}^R$	$-5/3$	$-1/2$	0	$e_R \bar{u}_R$	1
	$-2/3$	$+1/2$	0	$e_R \bar{d}_R$	1
$\tilde{S}_{1/2}^L$	$-2/3$	$-1/2$	0	$e_L \bar{d}_L$	1
	$+1/3$	$+1/2$	0	$\nu_e \bar{d}_L$	0

Table 1.4: Scalar (S) and vector (V) leptoquark states in the BRW model, grouped by weak isospin (subscript index). LQs coupling to left- and right-handed leptons (L, R superscript) are assumed independent. Electric charge Q, third component of weak isospin T^3, fermion number F, as well as the LQ decay modes and their branching ratios are given. Global replacement of first-generation fermions for corresponding second- and third-generation fermions gives LQ_2 and LQ_3.

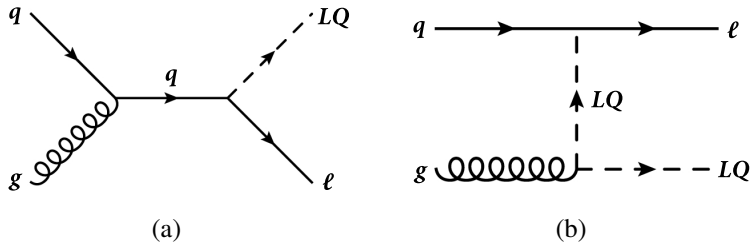

Figure 1.6: Leading order Feynman diagrams for single LQ production, in association with a lepton.

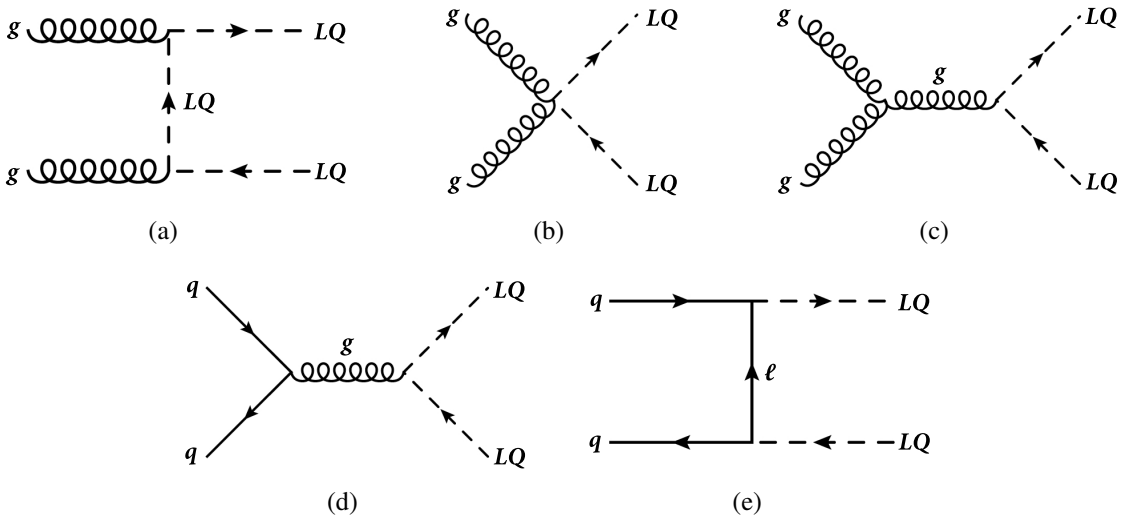

Figure 1.7: Leading order Feynman diagrams for LQ pair-production, from gluon fusion and quark-antiquark annihilation.

fusion and quark-antiquark annihilation as shown in Figure 1.7, and thus depends only on the (known) strong coupling α_s.[29] For its relative model-independence, only pair-production is considered hereon.

Furthermore, the gauge couplings of *scalar* LQs are fixed by a particular set of quantum numbers (as listed in Table 1.4), whereas the magnetic-dipole- and electric-quadrupole-type interactions of *vector* LQs are not. As a result, the total cross section for scalar LQ pair-production depends on the LQ mass alone, while vector LQ pair-production depends additionally on model-specific anomalous κ_G and λ_G couplings, with different values yielding cross section variations one or two orders in magnitude [38]. In all cases, the LQ decay rate depends on the unknown

[29]Note: The contribution to pair-production from t-channel lepton exchange is of order $\lambda^2_{\ell q}$ [36].

Yukawa coupling. Conventionally, $\lambda_{\ell q}$ is given in terms of the electromagnetic coupling — as a fraction thereof, since indirect experimental constraints have placed upper bounds on its value [42]. However, in direct searches for LQ pair-production, the most practical concern is that it not be *too small* ($\lambda_{\ell q} \sim e \times 10^{-6}$), otherwise LQs would not decay promptly inside the detector (see Section 2.2). Owing to its minimal model dependence, scalar LQ pair-production is the focus of the remainder of this section.

Krämer *et al.* [43] have calculated the leading order (LO), parton-level cross sections for scalar LQ pair-production as the following:

$$\hat{\sigma}_{\mathrm{LO}}\left[q\bar{q} \to LQ\overline{LQ}\right] = \frac{2\alpha_s^2\pi}{27\hat{s}}v^3 \tag{1.7}$$

$$\hat{\sigma}_{\mathrm{LO}}\left[gg \to LQ\overline{LQ}\right] = \frac{\alpha_s^2\pi}{96\hat{s}}\left[v\left(41-31v^2\right)+\left(18v^2-v^4-17\right)\log\frac{1+v}{1-v}\right], \tag{1.8}$$

where $\hat{s}$ is the center-of-mass energy squared and $v \equiv (1-4m_{\mathrm{LQ}}^2/\hat{s})^{1/2}$ is the LQ velocity. The renormalization and factorization scale μ is conventionally set equal to m_{LQ}, giving a more conservative limit on σ. Gluon fusion is the dominant production mechanism for small m_{LQ}, but quark-antiquark annihilation becomes increasingly important for larger masses (about 30% of the total cross section for $m_{\mathrm{LQ}} \sim 1.5$ TeV). QCD radiative corrections to the total production cross section

$$\sigma\left[pp \to LQ\overline{LQ}\right] = \sigma_{gg} + \sigma_{q\bar{q}} + \sigma_{gq} \tag{1.9}$$

are significant, particularly near the LQ production threshold. The perturbative expansion of the total partonic cross section (see Equation 3.1) can be expressed as

$$\hat{\sigma}_{ij} = \frac{\alpha_s^2(m_{\mathrm{LQ}}^2)}{m_{\mathrm{LQ}}^2}\left\{f_{ij}^B(v) + 4\pi\alpha_s(m_{\mathrm{LQ}}^2)\left[f_{ij}^{V+S}(v) + f_{ij}^H(v)\right]\right\}, \tag{1.10}$$

where $i, j = g, q$, f^B is the Born cross section term, and $f^{V+S,\,H}$ represent the QCD corrections for virtual + soft and hard gluons, respectively. These scaling functions depend on $\sqrt{\hat{s}}$ through v; near threshold ($v \ll 1$), they are evaluated as

$$\begin{aligned}
f_{gg}^B &= \frac{7\pi v}{384} & f_{q\bar{q}}^B &= \frac{\pi v^3}{54} \\
f_{gg}^{V+S}/f_{gg}^B &= \frac{11}{336v} & f_{q\bar{q}}^{V+S}/f_{q\bar{q}}^B &= -\frac{1}{48v} \\
f_{gg}^H/f_{gg}^B &= \frac{3}{2\pi^2}\log^2(8v^2) - \frac{183}{28\pi^2}\log(8v^2) & f_{q\bar{q}}^H/f_{q\bar{q}}^B &= \frac{2}{3\pi^2}\log^2(8v^2) - \frac{107}{36\pi^2}\log(8v^2).
\end{aligned} \tag{1.11}$$

Inclusion of such next-to-leading order (NLO) terms greatly reduces the depen-

dence of σ on the choice of scale μ and also increases its value over σ_{LO}, thereby extending the reach of direct searches for scalar LQ pair-production! The ratio of $\sigma_{\mathrm{NLO}}/\sigma_{\mathrm{LO}}$ ranges from about 1.5 at $m_{\mathrm{LQ}} = 200$ GeV to about 2.1 at $m_{\mathrm{LQ}} = 2000$ GeV. LO and NLO cross sections are shown in Figure 1.8.

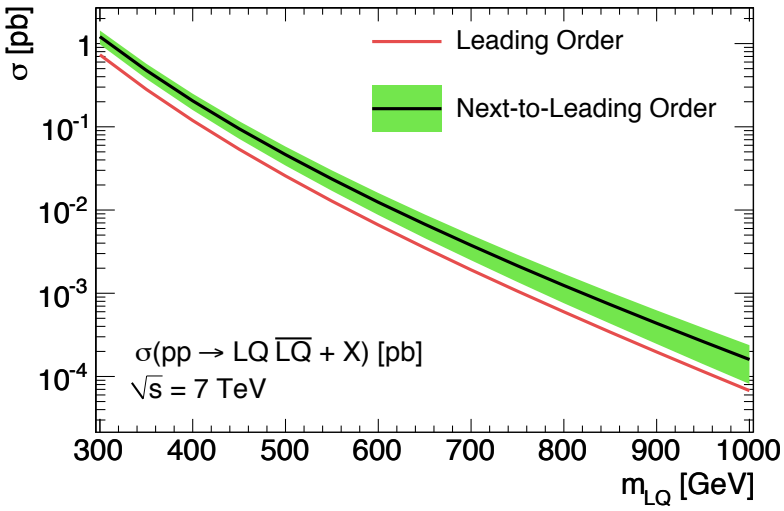

Figure 1.8: LO and NLO cross sections for pair-production of scalar LQs in pp collisions at $\sqrt{s} = 7$ TeV, as a function of LQ mass. The green represents the theoretical uncertainty on the NLO calculation coming from the choice of renormalization and factorization scales as well as the parton distribution function. Values taken from code written by the authors of [43].

In $LQ\overline{LQ}$ production, each leptoquark decays into a lepton and a quark, depending on the branching ratio $\beta \equiv \mathrm{BR}(LQ \to \ell q)$, where ℓ is a charged lepton.[30] This gives three possible final states: $qq\ell^+\ell^-$, $qq\ell^\pm\nu$, and $qq\nu\nu$. In an experimental context, quark confinement results in the production of hadronic "jets" (see Chapter 3), while neutrinos escape the detector unmeasured and are reconstructed from a momentum imbalance in the event denoted $\not{E}_{\mathrm{T}}$ (see Chapter 4). Thus, the experimental signatures of such LQ events are actually $\ell\ell$ + jets, $\ell + \not{E}_{\mathrm{T}}$ + jets, and $\not{E}_{\mathrm{T}}$ + jets. These decay modes define the "channels" in which direct searches are conducted.

1.3.3 Experimental Constraints

Bounds on leptoquark states come from direct searches for their production at high-energy colliders as well as indirect precision measurements at lower energies.

[30] Evidently, the branching ratio for LQ decay into a neutrino and a quark is $1 - \beta$.

1.3 Leptoquark Phenomenology

In very general models, LQs may couple to more than one SM generation and both left- and right-handed quarks as well as mediate interactions that violate lepton and baryon number conservation. Indirect limits provide the strongest bounds on their production. For example, the observed stability of the proton[31], whose decay would proceed by L and B non-conserving interactions, places strict limits on possible LQ masses and couplings. A very conservative bound of $\lambda_{\ell q} \lesssim (m_{\mathrm{LQ}}/25\ \mathrm{TeV})$ is given by [42]. LQs that couple to more than one SM generation can result in flavor-changing neutral currents, whose strong suppression in the SM is in agreement with numerous experimental measurements. Non-chiral LQs — that is, LQs that couple to both left- and right-handed quarks — contribute to the muon anomalous magnetic moment a_μ, whose observed discrepancy with the SM prediction *could* be accommodated by certain types of LQs, but not others, and only over restricted mass ranges [45]. Indirect studies *strongly* constrain the most general LQ models; for this reason, the minimal BRW model (reasonably) assumes chiral, flavor-diagonal, L- and B-conserving LQs. For reviews of indirect bounds on LQ production, see [46] and [47].

Direct searches for LQs at particle colliders have placed limits on their production cross sections and, in turn, masses. In particular, searches at hadron colliders usually deal with pair-produced scalar LQs of all generations, since they are independent of the LQ Yukawa coupling (as discussed in Section 1.3.2). To date, no evidence for LQ production has been found.

- Searches at HERA (an ep collider at $\sqrt{s} = 319$ GeV) using the full H1 experiment's data sample ($\mathscr{L}_{\mathrm{int}} = 446\mathrm{pb}^{-1}$) excluded at 95% confidence level (CL) first-generation LQs with $m_{\mathrm{LQ}} < 800$ GeV, assuming couplings of electromagnetic strength ($\lambda_{\ell q} \approx 0.3$) [48]. (Note that, by its nature, an ep collider is primarily sensitive to first-generation LQ single production.) A search for second-generation LQs via lepton flavor-violating processes excluded $m_{\mathrm{LQ}} < 712$ GeV at 95% CL, also assuming $\lambda_{\ell q} \approx 0.3$ [49].

- At the Tevatron (a $p\bar{p}$ collider at $\sqrt{s} = 1.96$ TeV), the DØ experiment has searched for pair-production of LQ_1 in all three channels using 1 fb^{-1} of data [50]; LQ_2 in the $\mu\mu qq$ and $\mu\nu qq$ channels, also using 1 fb^{-1} of data [51]; and LQ_3 with $Q = -1/3$ using $L = 5.2$ fb^{-1} of data [52]. For example, second-generation scalar LQs were excluded at 95% CL with masses up to 316 (270) GeV for $\beta = 1$ (0.5), as shown in Figure 1.9.

- More recent searches for both LQ_1 and LQ_2 at the LHC (a pp collider at $\sqrt{s} =$ 7 TeV described in Chapter 2) have been performed by both the ATLAS and CMS experiments. The first searches, using approximately 35 pb^{-1} of data,

[31] Current experimental limits on the proton lifetime have it at greater than 10^{33} years! [44]

surpassed the previous best limits set at the Tevatron (ATLAS [53], CMS [54] [55]). The analysis presented in Chapter 5 is an update to the initial second-generation ATLAS search, in which scalar LQ_2 production was excluded at 95% CL for $m_{\mathrm{LQ}} < 422\ (362)$ GeV and $\beta = 1\ (0.5)$; these limits are shown in Figure 1.10. A brand new result from CMS in the $\mu\mu qq$ and $\mu\nu qq$ channels excludes second-generation LQs with masses below 632 (523) GeV for $\beta = 1\ (0.5)$ [4].

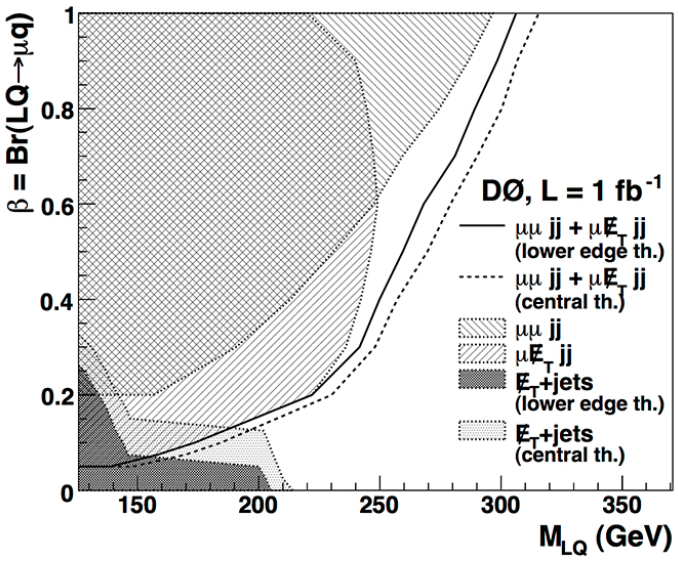

Figure 1.9: 95% CL exclusion region for second-generation scalar LQ production in the $\beta - m_{\mathrm{LQ}}$ plane, for individual search channels and their combination, with the DØ detector [51].

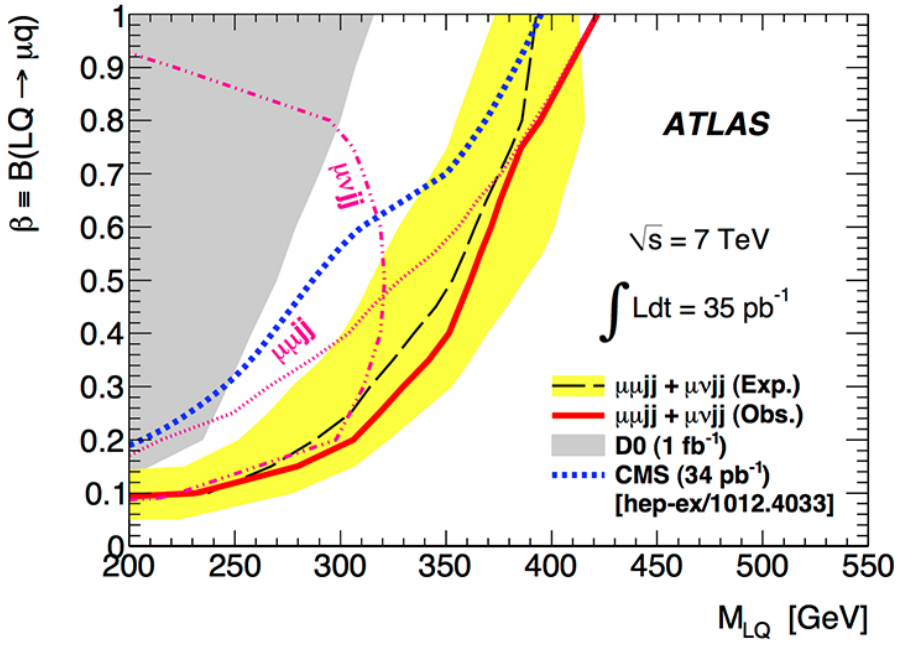

Figure 1.10: 95% CL exclusion region for second-generation scalar LQ production in the $\beta - m_{\mathrm{LQ}}$ plane, for individual search channels and their combination, with the ATLAS detector [53]. Existing limits from DØ (those shown in Figure 1.9) and CMS are overlaid for comparison.

CHAPTER 2

Experimental Apparatus

> I am turned into a sort of machine for observing facts and grinding out conclusions.
>
> Charles Darwin

Experimental particle physics has been driven, in large part, by a need for ever more energetic collisions: the higher energies involved allow for the production of more massive particles and the study of shorter-range interactions. Currently, the most powerful particle accelerator in the world is the Large Hadron Collider (LHC) [56], located on the French-Swiss border near Geneva, Switzerland and operated by the European Organization for Nuclear Research (abbreviated CERN, for historical reasons) [57]. Installed 100 m underground in a roughly circular tunnel 26.7 km long[1], the LHC is a two-ring, superconducting particle accelerator designed to collide protons[2] at a center-of-mass energy ($\sqrt{s}$) of 14 TeV and an instantaneous luminosity ($\mathscr{L}$) of 10^{34} cm^{-2} s^{-1} — when it's ready. A severe technical malfunction during initial commissioning of beams in the LHC (September 2008) resulted in damage to infrastructure and pollution of the vacuum system, which required more

[1] The tunnel already existed, having been bored in the 1980s for the Large Electron Positron (LEP) collider, and was re-used as a cost-saving measure.

[2] The LHC is also designed to collide heavy lead ions in dedicated runs at 5.5 TeV per nucleon pair and $\mathscr{L} = 10^{27}$ cm^{-2} s^{-1}.

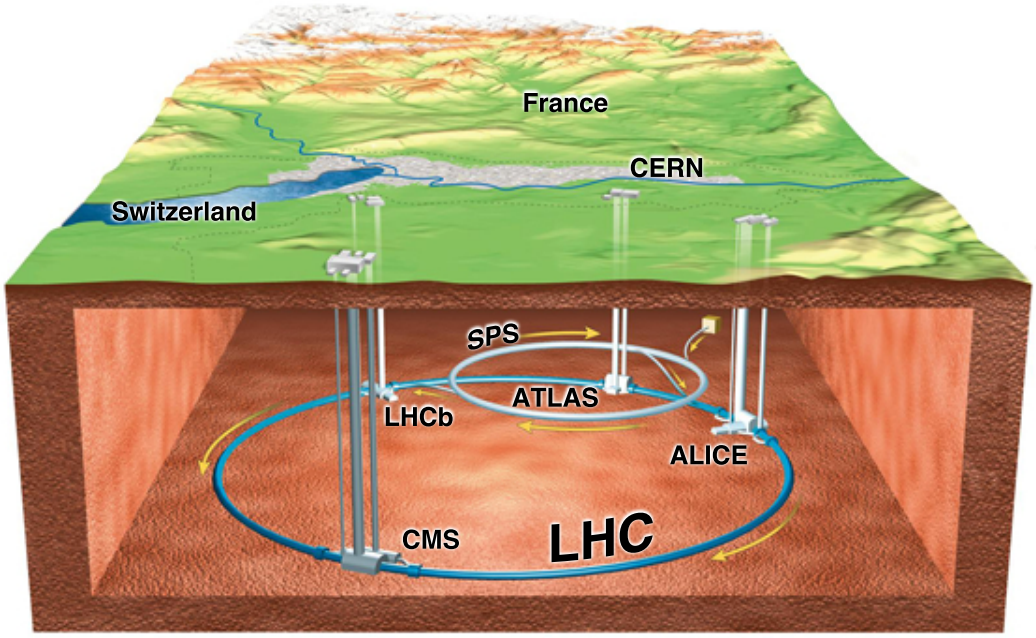

Figure 2.1: Overall view of the LHC and its four primary experiments, located underground on the French-Swiss border. © CERN

than a year of repairs [58]. As a precautionary measure, the LHC began collisions at just $\sqrt{s} = 7$ TeV, and a correspondingly lower instantaneous luminosity, in the spring of 2010.

The CERN accelerator complex is a chain of smaller, less powerful machines that serves to accelerate particles to successively higher energies then inject them into the LHC for final acceleration and collision. To detect and measure the properties of these collisions, six particle detectors — individual experiments, run by international collaborations — are located at different points around the ring: ATLAS [59] and CMS [60], for high-luminosity collisions and sensitivity to a wide range of physics; LHCb [61] and ALICE [62], for lower-luminosity studies of specific phenomena (b-physics in pp collisions and the quark-gluon plasma in lead-lead collisions, respectively); TOTEM [63] and LHCf [64], for studying "forward" particles not accessible to the other detectors. An overall view of the experimental layout is shown in Figure 2.1.

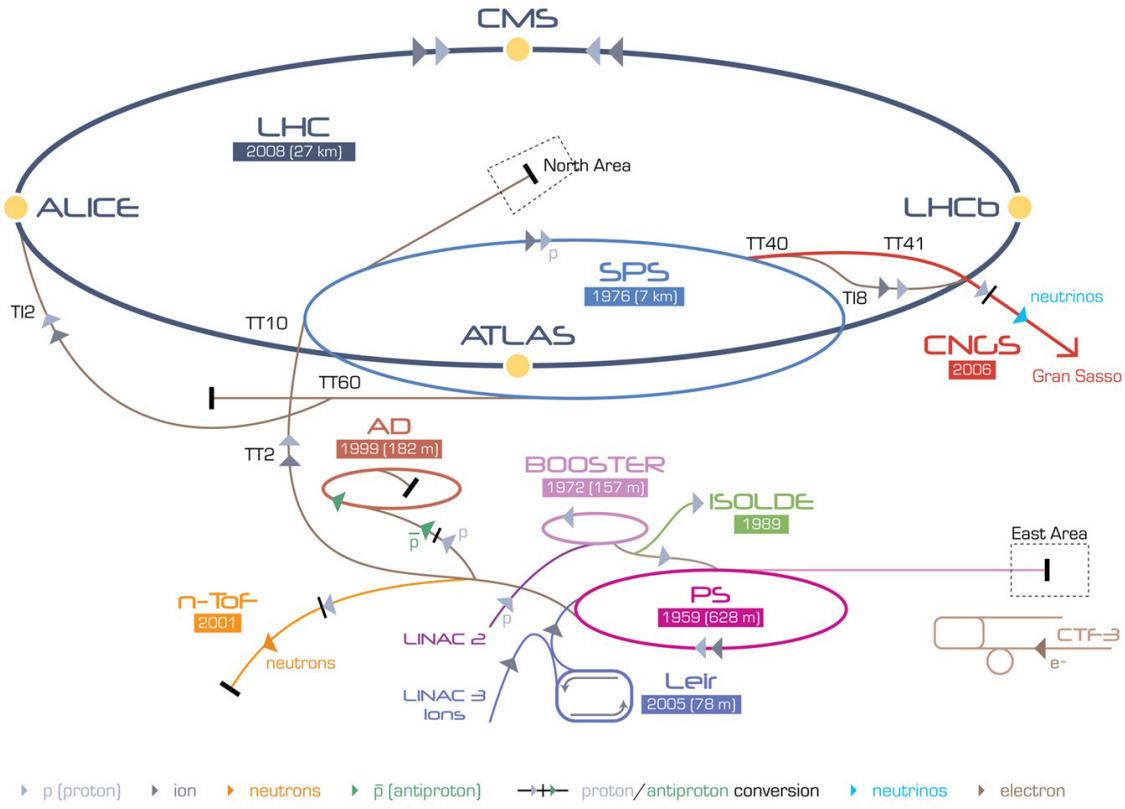

Figure 2.2: Illustration of the full CERN accelerator complex, with the paths taken by different particles indicated by unique arrows. Not to scale. © CERN

2.1 The CERN Accelerator Complex

The series of linked accelerators that successively increase the energy of the hadron beams and store them until needed for collisions — the CERN accelerator complex — is shown in Figure 2.2. The LHC is the final destination for protons to-be-collided in the ATLAS detector; it imposes strict requirements on the accelerators through which the protons must first pass, collectively referred to as the *injection chain*. This chain also provides beams of particles at lower energies to other experiments along the way.

2.1.1 Injection Chain

Protons are produced by a duoplasmatron source [65], in which electrons "boiled" off a metal cathode into a vacuum chamber are used to ionize hydrogen gas introduced into the chamber. The resulting plasma is accelerated through multiple

Figure 2.3: Schematic drawing of the 25 ns filling scheme used for nominal pp collisions in the LHC. Inspired by [68].

charged grids and collimated down into a beam. The protons first pass into the Linac2 (LINear ACcelerator), where they are accelerated to 50 MeV. They are then injected into the first synchrotron in the chain, the Proton Synchrotron Booster (PSB, or "Booster"), and *boosted* to energies of 1.4 GeV. Next in line is the Proton Synchrotron (PS) in which the protons are accelerated to 25 GeV. Finally, protons enter the Super Proton Synchrotron (SPS) and are accelerated to 450 GeV; the SPS acts as the injector for the LHC. For more details on the injection chain, see [66] and [67].

The LHC is filled with protons arranged in different schemes for different modes of operation [68], but in general, protons are grouped into *bunches*, bunches into *batches*, and batches separated by *gaps* comprise a *beam*. Since the synchrotrons in the injection chain grow progressively larger, each is capable of holding multiple injections or "fills" from the previous accelerator. For nominal proton-proton collisions in the LHC, a "25 ns scheme" is used: one LHC beam consists of 39 batches of 72 bunches each, with bunches separated by 25 ns and larger gaps between batches to allow for safely "dumping" the beam when necessary. Out of a possible 3564 bunch positions (in units of 25 ns), 2808 are filled. A schematic drawing of this *bunch pattern* is shown in Figure 2.3.

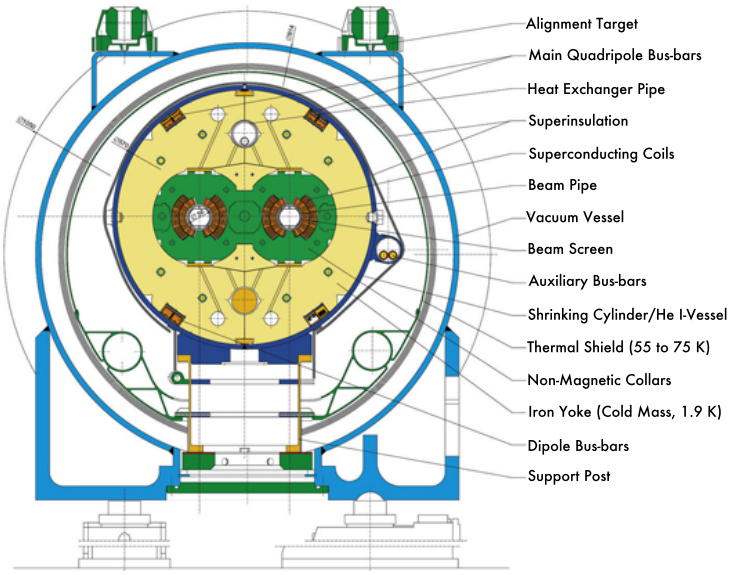

Figure 2.4: Schematic diagram showing the cross section of an LHC dipole magnet. © CERN, 1999.

2.1.2 Large Hadron Collider

The design of the LHC was driven by its physics goals: to further understanding of the Standard Model and to discover physics beyond it. Most interesting and/or new physics processes are exceedingly rare, with probabilities of occurrence (or *cross sections*) that depend on the collision energy; therefore, the LHC design aims to maximize both beam energies and beam intensities. The number of events produced in LHC collisions per second (or *production rate*) is given by

$$\mathscr{R} = \mathscr{L} \times \sigma_{\text{event}}, \tag{2.1}$$

where σ_{event} is the cross section of the event under study and $\mathscr{L}$ is the instantaneous luminosity, which itself is a function of several beam parameters:

$$\mathscr{L} = \frac{N_b^2 \, n_b \, f_{\text{rev}} \, \gamma_r}{4\pi \, \varepsilon_n \, \beta^*} F, \tag{2.2}$$

where N_b is the number of particles per bunch, n_b is the number of bunches per beam, f_{rev} is the beam revolution frequency, γ_r is the relativistic gamma factor, $4\pi \, \varepsilon_n \, \beta^*$ is effectively the geometric cross section of the beam, and F is a geometric luminosity reduction factor to account for the (non-zero) angle at which the beams cross.

As a particle-particle (and not particle-antiparticle) collider, the LHC has two

parallel rings with counter-rotating beams that cross at four *interaction points* (IPs), each occupied by a detector: ATLAS (IP1), ALICE (IP2), CMS (IP5), and LHCb (IP8). The beams are guided through ultra-high vacuum tubes by superconducting NbTi magnets, cooled to temperatures below 2 K using superfluid helium, that produce magnetic fields in excess of 8 T. Most of the magnets employ a "twin-bore" design, in which both beam channels are enclosed in a shared "cold mass" but their magnetic fluxes point in opposing directions; Figure 2.4 shows such a configuration. 1232 dipole magnets bend the beams around the ring; 392 quadrupole magnets focus the beams; and a variety of specialized magnets are used around IPs to squeeze the beams together for optimal collisions, to connect sectors of the ring, to dump the beams, etc. Radio frequency (RF) cavities accelerate the beams to (or maintain them at) collision energy as well as keep the protons tightly bunched together. In fact, the operational frequency of the RF cavities determines the possible bunch structures of the beams. For full details of the LHC design, see [69] (or [56] for an abridged version).

The LHC delivered a total of 5.61 fb^{-1} of integrated luminosity of data during the course of its 2011 pp run, of which ATLAS recorded 5.25 fb^{-1} with stable beams and detector systems.[3] The LHC achieved a peak instantaneous luminosity of $\mathscr{L} = 3.65 \times 10^{33}\ \text{cm}^{-2}\,\text{s}^{-1}$. Instantaneous and integrated luminosities are shown over the full 2011 run in Figure 2.5.

2.2 The ATLAS Detector

ATLAS (A Toroidal LHC ApparatuS) is a general-purpose particle detector designed for precision measurements of SM processes and sensitivity to a wide range of new physics processes. ATLAS is also a *collaboration*, consisting of more than 3,000 physicists, engineers, and technicians from more than 174 institutions and 38 countries, making it one of the largest scientific collaborations ever formed [71].

The ATLAS detector [72] is approximately 25 m tall, 46 m long, and weighs 7,000 tons. It has a cylindrical geometry with forward-backward symmetry relative to the LHC interaction point at its center. It consists of several sub-detectors layered concentrically around the LHC ring — the Inner Detector (ID), Electromagnetic and Hadronic Calorimeters (EMCAL, HCAL), and the Muon Spectrometer (MS) — that each contribute to the identification and reconstruction of the many particles produced in high-energy hadron collisions. These sub-detectors are immersed in a magnetic field produced by an inner solenoid and three outer toroid magnets whose

[3] Integrated luminosity is conventionally given in units of *inverse barns*, where a barn is a unit of area: $\text{b} = 10^{-24}\,\text{cm}^2$, roughly the size of a uranium nucleus (from which, historically, it got its unusual name: "big as a barn"). At the LHC, so much data is collected that the femto- prefix is convenient, giving inverse femtobarns (fb^{-1}) of data. [70]

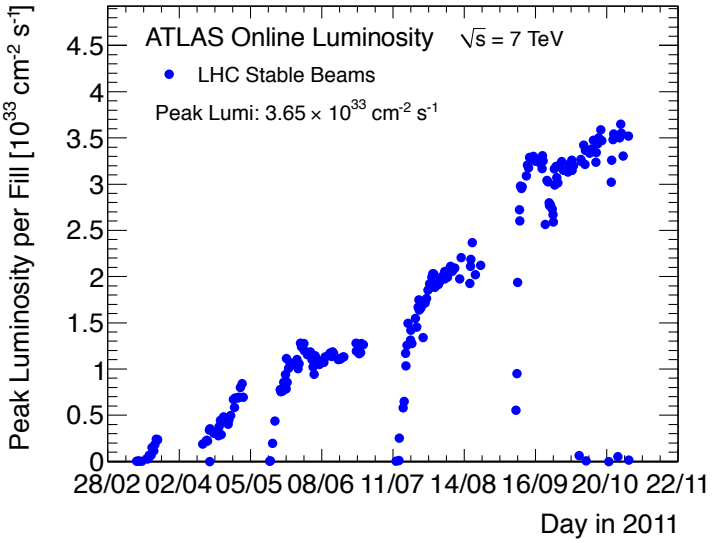

(a)

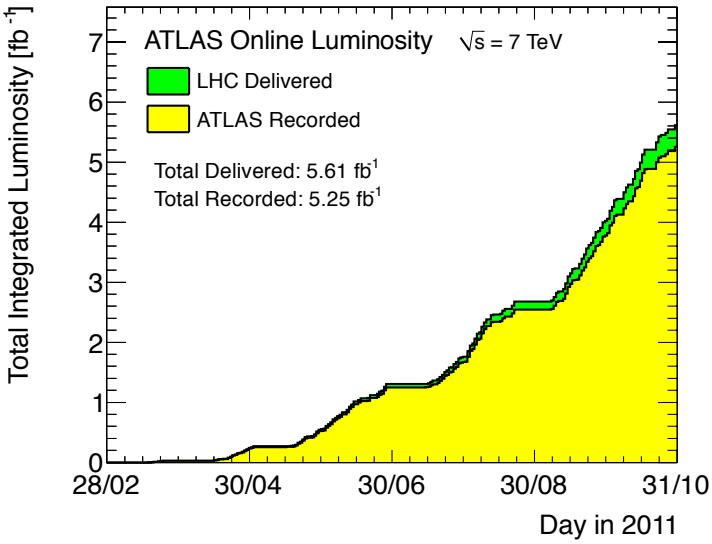

(b)

Figure 2.5: The (a) maximum instantaneous luminosity and (b) total integrated luminosity achieved with the LHC each day of its 2011 pp run, as determined from counting rate measurements by the ATLAS luminosity detectors.

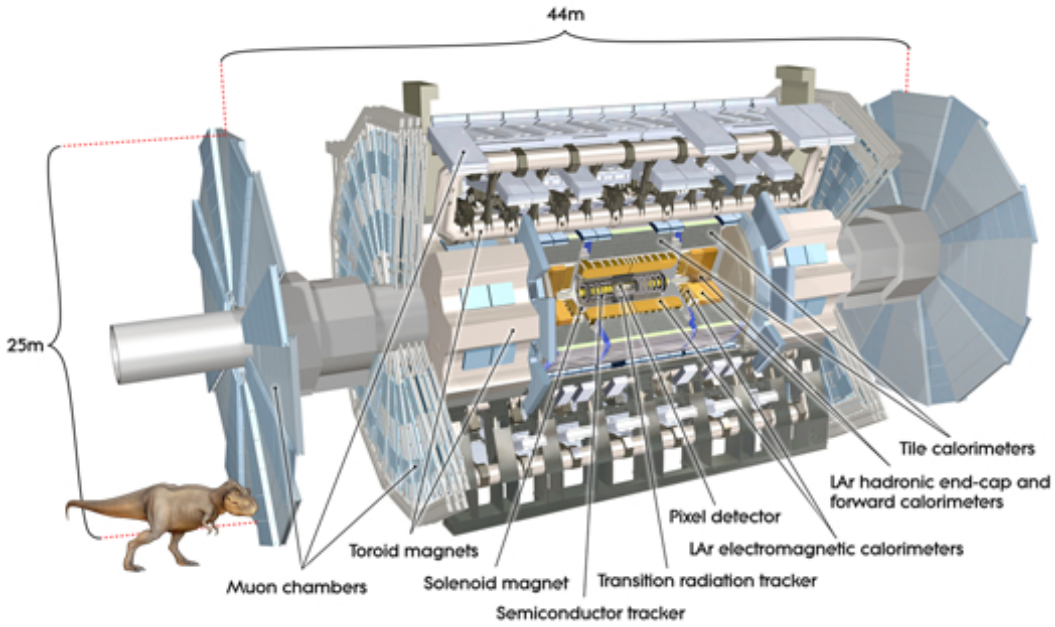

Figure 2.6: Cut-away view of the full ATLAS detector, with dimensions and primary components labeled (© CERN). Tyrannosaurus Rex shown for scale (© David Cano).

configuration played a large role in the sub-detectors' overall designs. Figure 2.6 shows a diagram of the full detector. While the LHC's nominal *interaction* rate is about 1 GHz (one billion interactions per second!), technical limitations allow for a final *event*-recording rate of just $\sim$ 400 Hz; consequently, ATLAS uses a three-tiered trigger system to reject the vast majority of events while maintaining maximal efficiency for "interesting physics" events.

The broad physics goals of the experiment and the unprecedented luminosity achieved by the LHC (and the resulting interaction rate and radiation levels) set demanding requirements on the design and performance of all these detector components, which are described in more detail in the following sections.

2.2.1 Coordinate System

ATLAS uses a particular coordinate system and nomenclature to describe the detector and the particles that pass through it. The origin of the coordinate system is at the nominal IP, with the positive x-axis pointing toward the center of the LHC ring, the positive y-axis pointing upward (away from the center of the earth), and the positive z-axis pointing along the direction of the beam traveling counter-clockwise

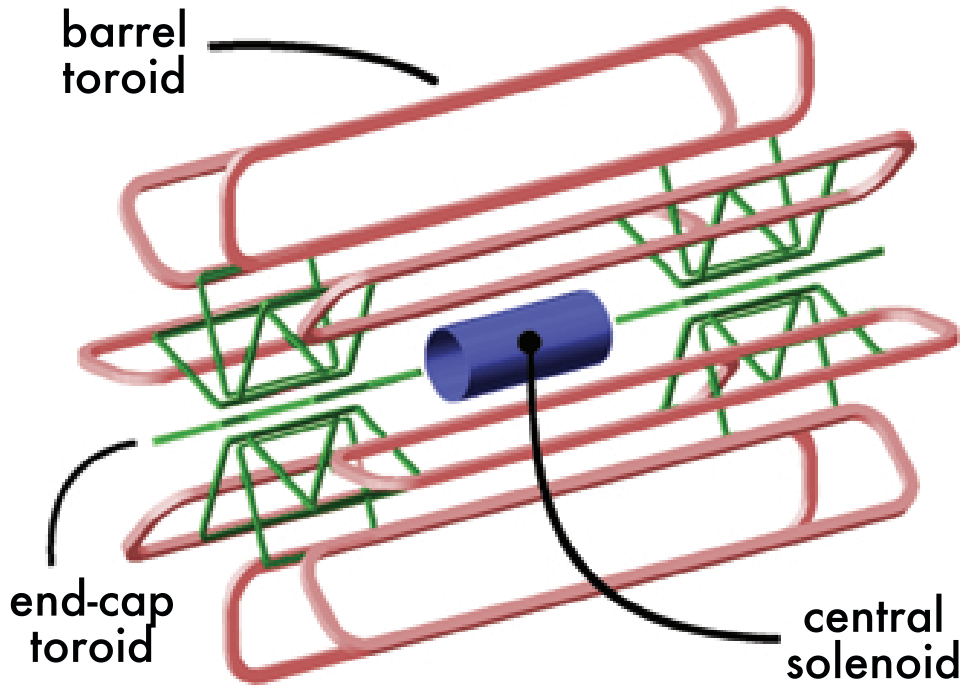

Figure 2.7: Geometry of magnet windings in the magnet system, consisting of a central solenoid, a barrel toroid, and two end-cap toroid magnets.

around the LHC ring when viewed from above. The $x-y$ plane is *transverse* to the z-axis; quantities such as transverse momentum (p_{T}), transverse energy (E_{T}), and missing transverse energy ($\not{E}_{\mathrm{T}}$) are defined in this plane. The azimuthal angle ϕ is measured around the z-axis, with $\phi = 0$ pointing along the positive x-axis. The polar angle θ is measured from the z-axis, though in practice the more common and convenient quantity is *pseudorapidity*, defined as $\eta = -\ln[\tan(\theta/2)]$. Distances in $\eta - \phi$ space are given in terms of ΔR, where $\Delta R \equiv \sqrt{\Delta\eta^2 + \Delta\phi^2}$.

2.2.2 Magnet System

The magnet system used in ATLAS [73] consists of four large, superconducting magnets: a solenoid located just outside the ID, plus a barrel toroid and two end-cap toroids interspersed with the Muon Spectrometer. These are shown in Figure 2.7. They provide the strong magnetic field required for precise momentum measurements of charged particles from the bend in their trajectories, and the larger the bend (technically, the *sagitta*), the more precise the measurement.

The central solenoid is aligned on the z-axis, with an inner (outer) diameter of 2.46 (2.56) m and an axial length of 5.8 m. It provides a 2 T axial magnetic field

for the ID. In order to minimize the amount of material in front of the calorimeters (it contributes just ~ 0.66 radiation lengths to the total — see Section 2.2.4), the solenoid uses a single-layer coil of superconducting NbTi wire supported by an aluminum shell and is embedded within the LAr Calorimeter cryostat.

The barrel toroid ($|\eta| < 1.4$) consists of eight racetrack-shaped coils arranged radially and symmetrically about the z-axis, with an inner (outer) diameter of 9.4 (20.1) m and an installed length of 25.3 m. It produces a $0.2-2.5$ T toroidal magnetic field for the MS using 120-turn coils of superconducting NbTiCu wire; the field has the advantage of being almost perpendicular to the particle trajectories. The weight of the coils and their stainless-steel casings, as well as the Lorentz forces generated by the field, are borne by inner and outer rings of aluminum struts.

The end-cap toroids ($1.6 < |\eta| < 2.7$) consist of eight, similarly ϕ-symmetric coils housed inside a gear-shaped, internally-reinforced aluminum casing, with an inner (outer) diameter of 1.65 (10.7) m and a length of 5 m. The 116-turn superconducting coils generate a toroidal field of $0.2-3.5$ T in the end-caps of the MS; they are offset by 22.5° with respect to the barrel toroid to allow for some radial overlap and to optimize the field's bending power in the "transition region" ($1.4 < |\eta| < 1.6$) at their interface. The magnets are supported on and can slide along rails, so the detector can easily be "opened" for access and maintenance.

2.2.3 Inner Detector

The ATLAS Inner Detector (ID) [74] provides hermetic tracking of charged particles in the high-radiation environment between the LHC beam pipe and the Electromagnetic Calorimeter in the pseudorapidity range $|\eta| < 2.5$. The set of measured "hits" corresponding to such particles are processed with robust pattern recognition algorithms (see Chapter 4) to make precise measurements of particle position and momentum as well as measurements of primary and secondary vertices. The ID is contained in a cylindrical envelope 2.3 m in diameter and 7 m in length, and is immersed in a 2 T solenoidal magnetic field. It consists of three independent, complementary sub-detectors: the Pixel detector, Semiconductor Tracker (SCT), and Transition Radiation Tracker (TRT), each comprising one barrel and two end-cap components. An overview of the ID is shown in Figure 2.8, and detailed 3D slices of the barrel and end-caps are shown in Figure 2.9.

Several (often competing) factors drove the design of the ID. The material budget is tightly constrained to avoid degradation of the calorimeter energy resolution, but structural stability for the sensors and the sensitivity of the sensors themselves must be ensured. Accurate vertexing requires high granularity at inner radii, and efficient track reconstruction (plus fake track rejection) requires good spatial resolution, but these conditions must be balanced against cost — silicon is *expensive*. Most significantly, the high-radiation environment close to the IP imposes strin-

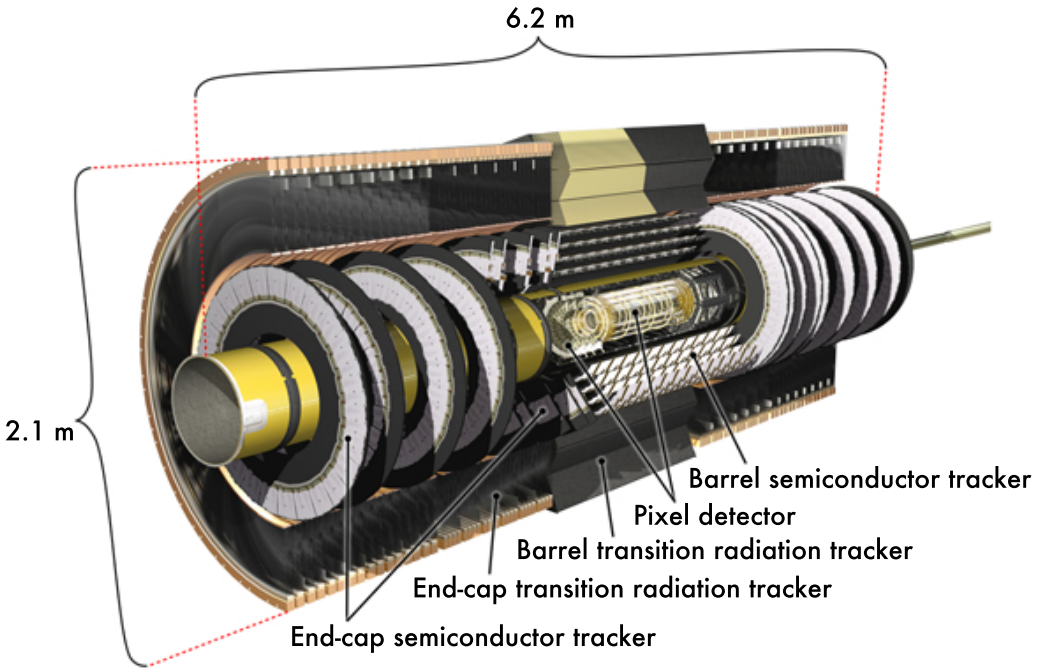

Figure 2.8: Cut-away view of the Inner Detector, with dimensions and primary components labeled. © CERN

gent requirements on the sensors, electronics, and services in the ID. Radiation damage degrades electronics performance, causes *type inversion* in silicon sensors, and forces those sensors to operate at higher depletion voltages and/or lower temperatures, in turn requiring cooling for the Pixel and SCT and thermal insulation between the SCT and TRT. Nevertheless, the sub-detectors must continue functioning throughout the full design lifetime of the ATLAS experiment, with the notable exception of the innermost "B-layer" of the Pixel detector, which will have to be replaced after approximately three years of nominal LHC operation (or a 1 MeV neutron equivalent fluence $F \sim 10^{15}\text{cm}^{-2}$). See Appendix A.

The relative resolution of the ID's momentum measurement is approximately $\sigma_{p_\text{T}}/p_\text{T} = 0.05\% \cdot p_\text{T} \oplus 1\%$. In the particular case of muons, it may be approximately parametrized as

$$\frac{\sigma(p)}{p} = p_1^\text{ID} \oplus p_2^\text{ID} \cdot p_\text{T} \qquad \text{for } |\eta| < 1.9 \tag{2.3}$$

$$\frac{\sigma(p)}{p} = p_1^\text{ID} \oplus p_2^\text{ID} \cdot \frac{p_\text{T}}{\tan^2\theta} \qquad \text{for } |\eta| > 1.9 \tag{2.4}$$

where p_1^{ID} and p_2^{ID} are the multiple scattering and intrinsic resolution terms, respectively, and $\oplus$ represents "addition in quadrature." Resolution varies significantly with pseudorapidity, so *in-situ* measurements are split into four η regions, as shown in Table 2.1 [75] [76].

Region	η Range	p_1^{ID} [%]	p_2^{ID} [TeV^{-1}]
barrel	$0 < \lvert\eta\rvert < 1.05$	1.55 ± 0.01	0.417 ± 0.011
transition	$1.05 < \lvert\eta\rvert < 1.7$	2.55 ± 0.01	0.801 ± 0.567
end-caps	$1.7 < \lvert\eta\rvert < 2.0$	3.32 ± 0.02	0.985 ± 0.019
CSC/no TRT	$2.0 < \lvert\eta\rvert < 2.5$	4.86 ± 0.22	0.069 ± 0.003

Table 2.1: Inner Detector muon momentum resolution parametrization, as defined in Equations 2.3 and 2.4.

Pixel Detector

The Pixel detector [77] provides high-granularity, high-precision spatial measurements as close as possible to the interaction point, critical information for both tracking and secondary vertex reconstruction. The barrel consists of three concentric cylinders at radii of 50.5, 88.5, and 122.5 mm aligned parallel to the beam; each end-cap consists of three successive disks with inner and outer radii of 88.8 and 149.6 mm, respectively, positioned perpendicular to the beam at z = 495, 580, 650 mm, covering the full ID acceptance of $|\eta| < 2.5$.

A total of 1744 identical *modules*, i.e. a silicon sensor plus its active electronics, are mounted on barrel *staves* and end-cap *sectors* and arranged such that a typical outgoing particle passes through three of them. The silicon sensors themselves are 250 μm thick, with oxygenated n^+ implants on n-type substrates and readout pixels on the n^+ side bump-bonded to read-out chips — design choices made for increased radiation hardness. Each sensor contains over 47,000 *pixels*, most with a sensitive area of 50×400 μm^2 dictated by the read-out pitch of the front-end electronics. In total, the Pixel detector constitutes roughly 80.4 million read-out channels! The silicon sensors have uniformly excellent performance: typical signals of $15,000 - 20,000$ electrons and noise at just ~ 170 electrons, and an intrinsic accuracy of R-$\phi \times z \approx 10 \times 115$ μm in the barrel and R-$\phi \times R \approx 10 \times 115$ μm in the end-caps.

The sensors operate at temperatures around -10° (using evaporative cooling) and a nominal depletion voltage of 150 V that, over time, will be increased to upwards of 600 V in order to compensate for radiation damage.

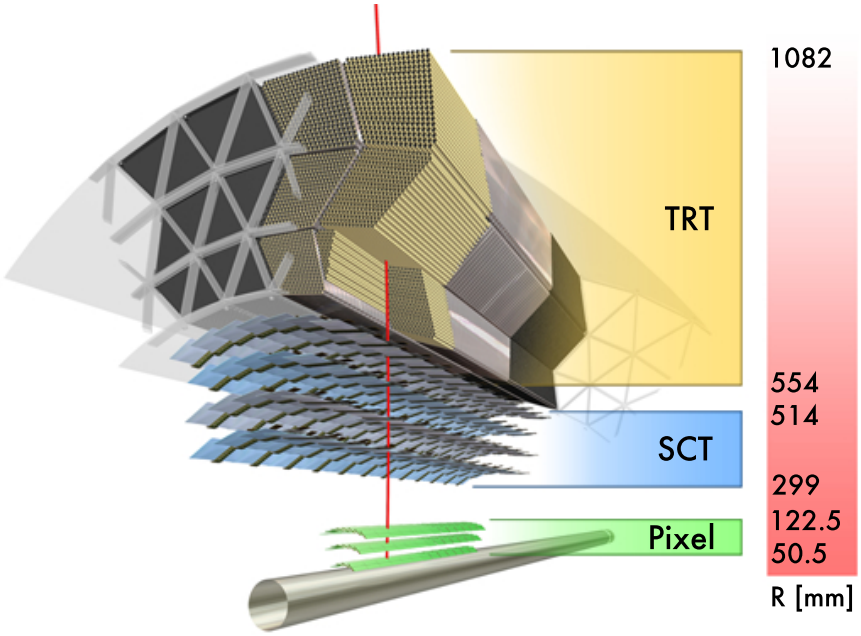

(a)

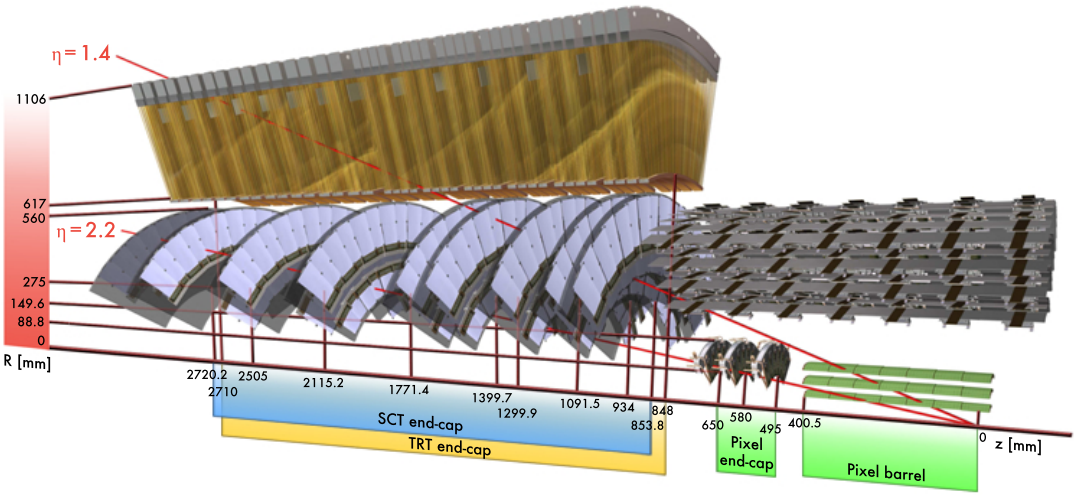

(b)

Figure 2.9: Slices of the Inner Detector: (a) ID barrel traversed by a charged particle ($p_{\mathrm{T}} = 10$ GeV, $\eta = 0.3$), with inner and outer radii of the Pixel, SCT, and TRT sub-detectors labeled; and (b) ID end-cap traversed by two charged tracks ($p_{\mathrm{T}} = 10$ GeV, $\eta = 1.4$, 1.2), with labels for illustrative values of R and z. Modified versions of images © CERN.

Semiconductor Tracker

Immediately outside the Pixel detector, an additional set of high-precision measurements is provided by the Semiconductor Tracker [74] to aid in measurements of particle momentum and impact parameter as well as vertex position. The SCT consists of four concentric layers in the barrel between R = 299 and 514 mm plus nine successive disks in each end-cap with outer radii of 560 mm (the inner radii vary from 275 to 439 mm) and z positions between 853.8 and 2720.2 mm. As with the Pixel detector, the SCT covers all the way out to $|\eta| < 2.5$.

Given the challenges of radiation damage (discussed previously) and scale (the SCT's surface area is ~ 63 m^2, more than an order of magnitude larger than any previous, comparable detector), the 15,912 sensors in the SCT use a relatively conservative design: single-sided, p-in-n silicon microstrip technology, 285 μm thick, with 768 read-out strips of 80 μm pitch.[4] A module is composed of two sensors, daisy-chained together and aligned parallel to the beam, glued back-to-back with two identical sensors rotated by 40 mrad in order to provide a z-measurement. The net result is a total of roughly 6 million read-out channels. The sensors are arrayed such that a typical outgoing particle produces eight hits, where two hits in the same module are combined into a discrete space-point. They have a resolution of R-$\phi \times z \approx 17 \times 580$ μm in the barrel and R-$\phi \times R \approx 17 \times 580$ μm in the end-caps.

As in the Pixel detector, the SCT sensors are run cold at $T \approx -7^\circ$ and an initial bias voltage of ~ 150 V, to be increased to upwards of 400 V as required to mitigate cumulative radiation damage.

Transition Radiation Tracker

The outermost component of the ID is the Transition Radiation Tracker, which complements the discrete, precision measurements of the Pixel and SCT detectors with continuous tracking based on a high number (~ 30) of lower-resolution hits. The TRT is sub-divided into a barrel at radii between 554 and 1082 mm and end-caps that span $827 < |z| < 2744$ mm; unlike the other sub-detectors, the TRT only covers out to $|\eta| < 2.1$.

The basic measurement unit in the TRT is a *straw*: a proportional drift tube 4 mm in diameter and 144 (37) cm in length in the barrel (end-cap), with a central gold-plated tungsten anode 31 μm in diameter separated from the aluminum-coated cathode walls by a gaseous mixture of $Xe/CO_2/O_2$. The cathodes are biased at -1530 V while the anodes are grounded, so charged particles passing through a straw leave a trail of ionized electrons that drift toward the anode and *avalanche* as they approach. The barrel contains roughly 53,000 straws aligned parallel to the

[4] In the SCT end-caps, sensors have a trapezoidal (as opposed to rectangular) shape with strips in a radial pattern, with a *mean* pitch of ~ 80 μm that actually varies between 57 and 94 μm.

beam, grouped into three concentric rings, and read out on both ends; each end-cap contains about 123,000 straws aligned radially and grouped into 12 wheels with 8-mm spacing between straws followed by 8 wheels with 15-mm spacing. The TRT has a total of $\sim 350,000$ read-out channels. This configuration yields a resolution of 130 μm in z (barrel) or R (end-cap). While the TRT is inherently radiation-hard, it faces other challenges associated with its relatively high occupancy.

The TRT also complements the calorimeter's electron identification capabilities by detecting transition radiation (photons) produced when high-γ particles pass between materials with different dielectric constants — polypropylene/polyethylene fibers in the TRT barrel and polypropylene foils in the TRT end-caps, interleaved between straws. Transition radiation typically produces a much larger signal than ionization, so a separate, second threshold is used.

2.2.4 Calorimetry

ATLAS employs several calorimeters for full, ϕ-symmetric coverage around the beam over a wide pseudorapidity range of $|\eta| < 4.9$. The primary purpose of a calorimeter is to stop particles from passing through it (with the exception of muons and neutrinos), and in so doing measure their energies and positions. The calorimeters closest to the beam — the electromagnetic barrel, electromagnetic end-caps, and forward calorimeters — are all liquid argon (LAr) sampling calorimeters with cryogenically liquefied noble gas as the active medium and lead (or other high-Z metal) absorbers; this technology was chosen for its intrinsic radiation-hardness as well as its stable, linear behavior. Farther from the beam, a hadronic barrel calorimeter uses scintillating tiles as the active medium alternating with steel absorbers; this technology provides a significant and cost-effective radial extension of the calorimeter necessary for full containment of electromagnetic (EM) and hadronic showers. This thickness and large η-coverage ensure a good $\not{E}_{\mathrm{T}}$ measurement. The overall layout of ATLAS calorimetry is shown in Figure 2.10, and relative resolutions on energy measurements are given in Table 2.2 (see, e.g. [78]

Component	Resolution (σ_E/E)
Electromagnetic (LAr)	$10\%/\sqrt{E} \oplus 0.7\%$
Hadronic (Tile and LAr)	$50\%/\sqrt{E} \oplus 3\%$
Forward (LAr)	$100\%/\sqrt{E} \oplus 10\%$

Table 2.2: Approximate relative resolutions on energy measurements [GeV] in each component of the calorimetry system.

While traversing matter, electrons lose energy primarily through *bremsstrahlung*

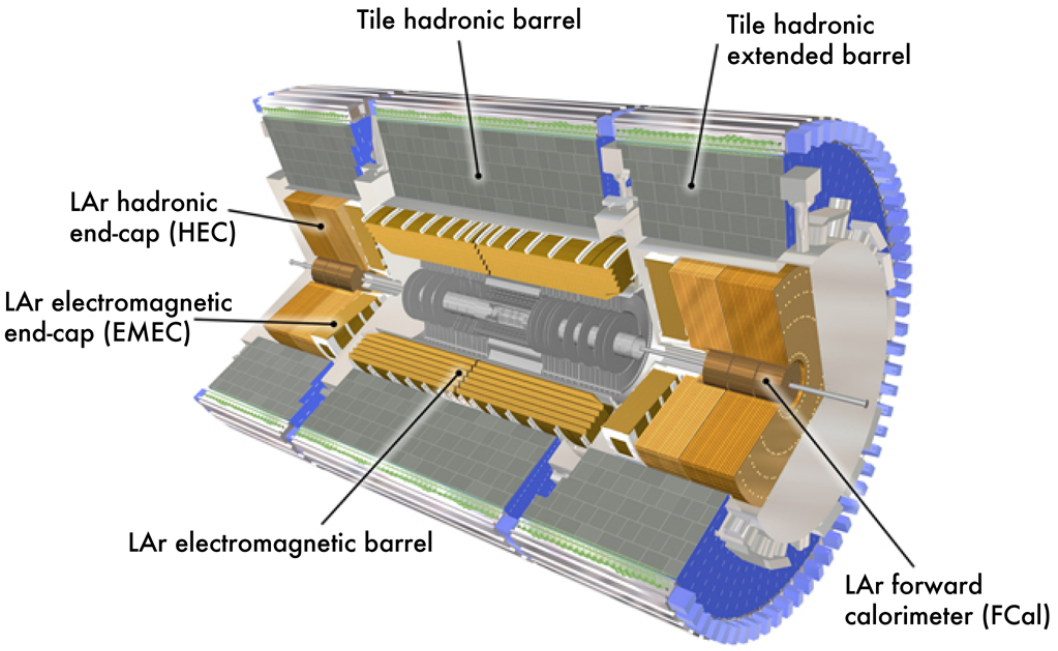

Figure 2.10: Cut-away view of the calorimetry system, with primary components labeled. © CERN

and photons through pair-production, resulting in EM showers; the characteristic length of such interactions is given by the *radiation length* X_0. In contrast, hadrons lose energy in matter through successive inelastic interactions with nuclei, leading to comparitively broad and complex hadronic showers; the mean path between interactions is given by the *interaction length* λ_0.

LAr Calorimeters

In the LAr Calorimeters [79], absorbers induce EM showers that subsequently ionize the liquid argon, producing an electron current pulse measured at electrodes and sent on to a series of electronics boards for shaping, digitization, and so on.

The EM barrel calorimeter has inner and outer radii of 1.4 and 2 m, respectively, and an axial length of 6.4 m split into two identical half-barrels, covering up to $|\eta| < 1.475$. It uses three layers of accordion-shaped electrodes and lead absorber plates that provide full coverage and uniform performance in ϕ, without azimuthal cracks. The first layer is finely-segmented in η to provide an accurate position/direction measurement; the second layer is the deepest, collecting the bulk of the energy deposited by EM showers; the third layer collects only the high-energy tails and helps to distinguish EM from hadronic showers. These three layers have a total

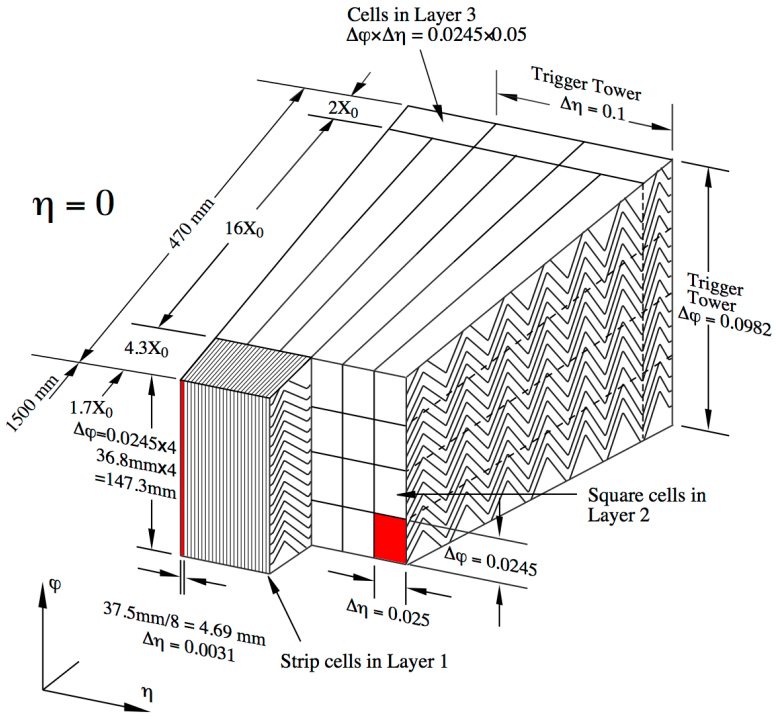

(a)

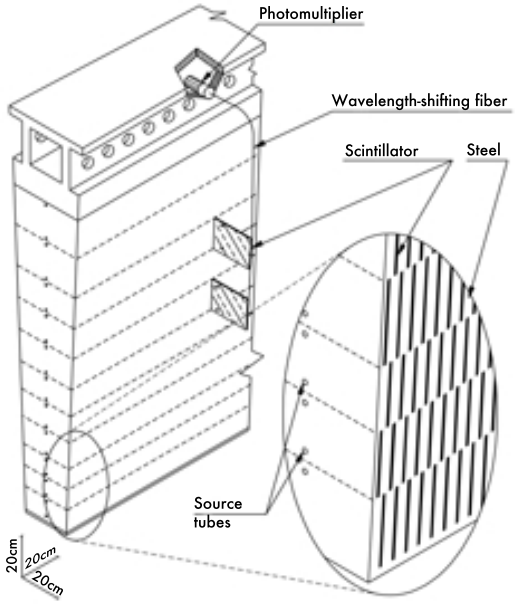

(b)

Figure 2.11: Schematic of (a) a LAr EM barrel module, showing the granularity of cells in η and ϕ, the three radial layers, and the accordion electrode geometry; and (b) a Tile hadronic barrel module, showing the orientation of scintillating tiles and absorbers as well as the fiber and photomultiplier tube used for optical signal read-out. [72]

thickness of at least 22 X_0 and a geometry as shown in Figure 2.11. The EM end-cap calorimeters consist of two co-axial wheels (each) on either side of the EM barrel, with overall inner and outer radii of 0.33 and 2.1 m, respectively, covering the range $1.375 < |\eta| < 3.2$. A similar but radially-oriented accordion geometry is employed. The end-caps have a total thickness of at least 24 X_0.

Installed just in front of the innermost calorimeter layer, *presamplers* consisting of a thin, active layer of liquid argon provide a first sampling of shower energies in order to estimate (and compensate for) energy lost in "upstream" material, e.g. the Inner Detector and central solenoid. These provide coverage over $|\eta| < 1.8$.

The hadronic end-cap calorimeters consist of two concentric wheels (each) located on either side of the EM end-caps, with inner (outer) radii of 0.475 (2.03) m, covering the range $1.5 < |\eta| < 3.2$. Each wheel is divided into two longitudinal layers. Flat copper plate absorbers are interleaved with LAr drift zones and electrodes, giving a total thickness of 10 λ_0.

Lastly, the forward calorimeters (FCAL) are composed of three cylindrical modules 0.455 m in radius and 0.45 m thick; they're located about 4.7 m from the interaction point, covering $3.1 < |\eta| < 4.9$. Owing to its proximity to the LHC beam and resulting high-radiation environment, the FCAL uses a high-density design: a matrix of narrow tubes oriented parallel to the beam and filled with liquid argon surrounding copper electrode rods. The first module uses copper plate absorbers for primarily EM measurements, and the latter two modules use tungsten plates for hadronic measurements. The total thickness is about 10 λ_0.

Tile Calorimeter

Where radiation-hardness is less of a concern than overall thickness and cost, ATLAS employs a different sampling calorimeter technology with steel as the passive absorbers and scintillating plastic tiles as the active medium. Ionizing particles passing through the tiles produce ultraviolet scintillation light, the amount of which is proportional to the amount of hadronic shower energy deposited.

The Tile Calorimeter [80] is sub-divided into a central barrel 5.8 m in length and two extended barrels 2.6 m in length, all located immediately outside the LAr calorimeters at radii of $2.28 - 4.25$ m; pseudorapidity coverage is $|\eta| < 1.0$ for the barrel and $0.8 < |\eta| < 1.7$ for the extensions, and radial depth throughout is about 7.4 λ_0. Each calorimeter consists of 64 modules of azimuthal width $\Delta\phi \sim 0.1$ segmented into three radial layers, with η granularity of 0.1 in the first two layers and 0.2 in the third. The alternating layers of steel and tile are connected on both ends to wavelength-shifting fibers that guide the scintillation light to linear photomultiplier tubes and front-end electronics. Figure 2.11 shows the geometry of a module.

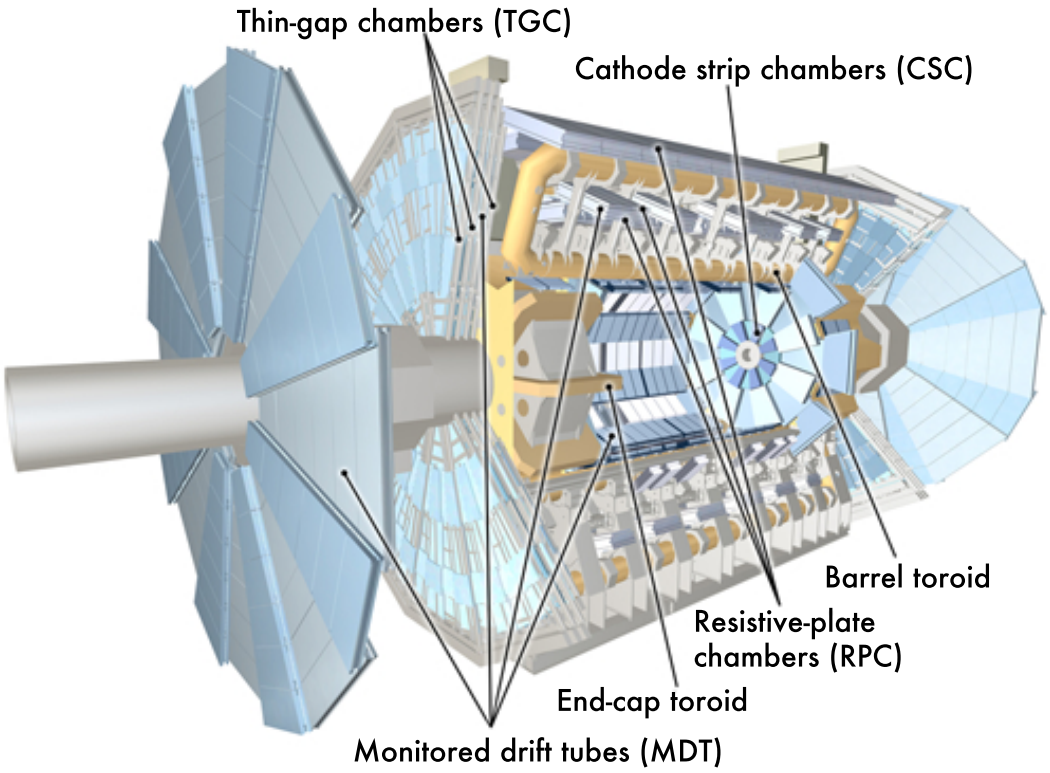

Figure 2.12: Cut-away view of the muon spectrometer, with primary components labeled. © CERN

2.2.5 Muon Spectrometer

The outermost ATLAS sub-detector is the Muon Spectrometer [81], designed to measure the position and momentum of charged particles that pass out of the calorimeters (i.e. muons) within $|\eta| < 2.7$ and trigger accordingly on those particles within $|\eta| < 2.4$. To accomplish this, four types of detectors are used: Muon Drift Tube chambers (MDTs) and Cathode-Strip Chambers (CSCs) provide precise spatial measurements for tracking, while Resistive Plate Chambers (RPCs) and Thin Gap Chambers (TGCs) provide fast measurements for triggering. Chambers are grouped into a barrel and two end-caps, all with an eight-fold azimuthal symmetry to match the magnet system. The MS barrel consists of three concentric layers or *stations* of chambers aligned parallel to the beam axis at approximate radii of 5, 7.5, and 10 m, while the MS end-caps each have four stations of chambers arranged in disks perpendicular to the beam at $|z| \approx 7.4$, 10.8, 14, and 21.5 m. A typical muon passes through three stations. The overall geometry of the MS in relation to ATLAS is shown in Figure 2.12; cross-sectional slices are shown in Figure 2.13.

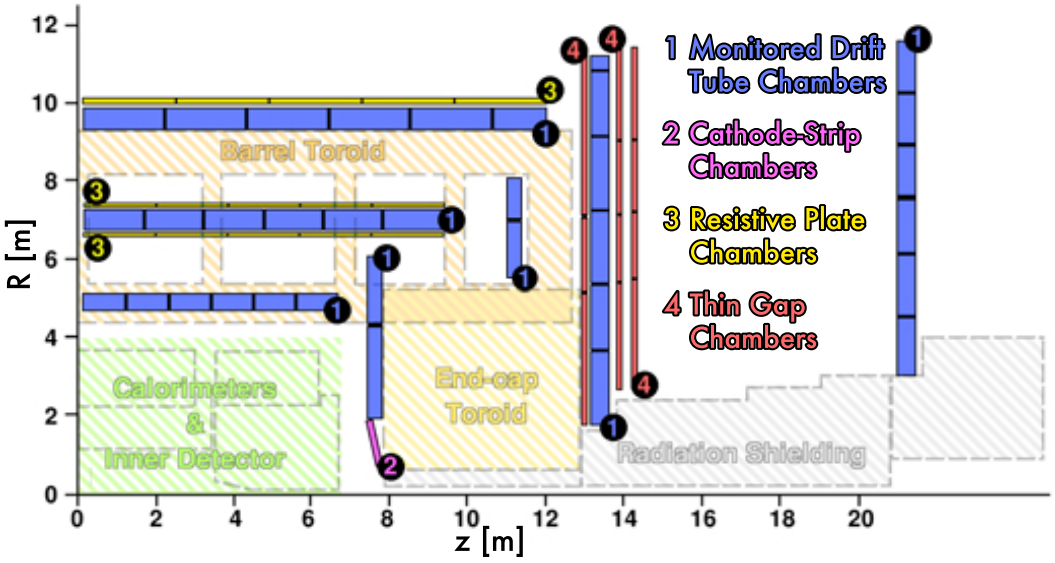

(a)

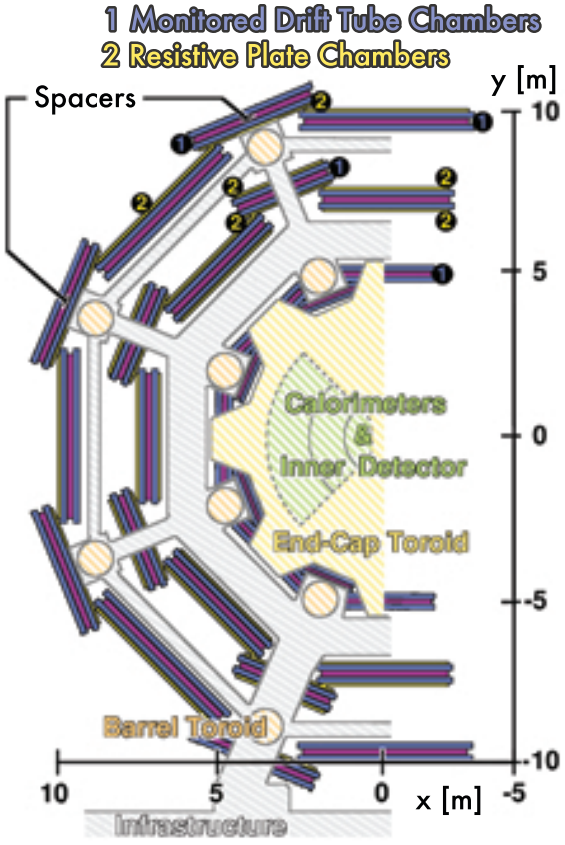

(b)

Figure 2.13: Muon spectrometer cross sections in (a) the $R-z$ plane, and (b) the $x-y$ plane (barrel only). Chamber types are labeled by numbers, as indicated in legends. Modified from [82].

The MS works by measuring the curvature or *bend* of muon trajectories resulting from interaction with the toroidal magnetic field described in Section 2.2.2. Precision, stand-alone measurements are required over a wide momentum range of $3 < p_{\mathrm{T}} < 1000$ GeV. Muons with $p_{\mathrm{T}} \approx 1000$ GeV have a sagitta of ≈ 500 μm, so the performance goal of 10% or better momentum resolution requires a measurement resolution of $\lesssim 50$ μm. This depends heavily on the relative alignment of muon chambers with respect to each other and ATLAS; therefore, a sophisticated optical alignment system monitors the positions and internal deformations of MDTs, supplemented by track-based alignment algorithms [83] [84]. Similar to the ID, the MS muon momentum resolution may be parametrized as

$$\frac{\sigma(p)}{p} = \frac{p_0^{\mathrm{MS}}}{p_{\mathrm{T}}} \oplus p_1^{\mathrm{MS}} \oplus p_2^{\mathrm{MS}} \cdot p_{\mathrm{T}}, \tag{2.5}$$

where p_0^{MS}, p_1^{MS}, and p_2^{MS} are the calorimeter energy loss, multiple scattering, and intrinsic resolution terms, respectively. The *in-situ* measurements of these parameters are given in Table 2.3 [75] [76].

Region	η Range	p_0^{MS} [TeV]	p_1^{MS} [%]	p_2^{MS} [TeV^{-1}]
barrel	$0 < \lvert\eta\rvert < 1.05$	0.25 ± 0.01	3.27 ± 0.05	0.168 ± 0.016
transition	$1.05 < \lvert\eta\rvert < 1.7$	0	6.49 ± 0.26	0.336 ± 0.072
end-caps	$1.7 < \lvert\eta\rvert < 2.0$	0	3.79 ± 0.11	0.196 ± 0.069
CSC/no TRT	$2.0 < \lvert\eta\rvert < 2.5$	0.15 ± 0.01	2.82 ± 0.58	0.469 ± 0.028

Table 2.3: Muon Spectrometer momentum resolution parametrization, as defined in Equation 2.5.

Precision-tracking Chambers

The purpose of MDTs and CSCs is to precisely determine the coordinate of a muon track in the bending plane of the toroidal field, i.e. y-z (or η).

Muon Drift Tube chambers are composed of individual, cylindrical drift tubes: 30 mm in diameter, filled with Ar/CO_2 gas pressurized at 3 bar, with a central, tungsten-rhenium, 50-μm anode wire held at 3080 V and an average resolution of about 80 μm. Through-going muons leave a trail of ionized electrons that drift to the anode within 700 ns. Three[5] layers of drift tubes make up a *multi-layer*, and two multi-layers separated by a support frame make up an MDT chamber. Four

[5] In the innermost barrel station only, multi-layers have *four* layers of drift tubes to improve pattern recognition.

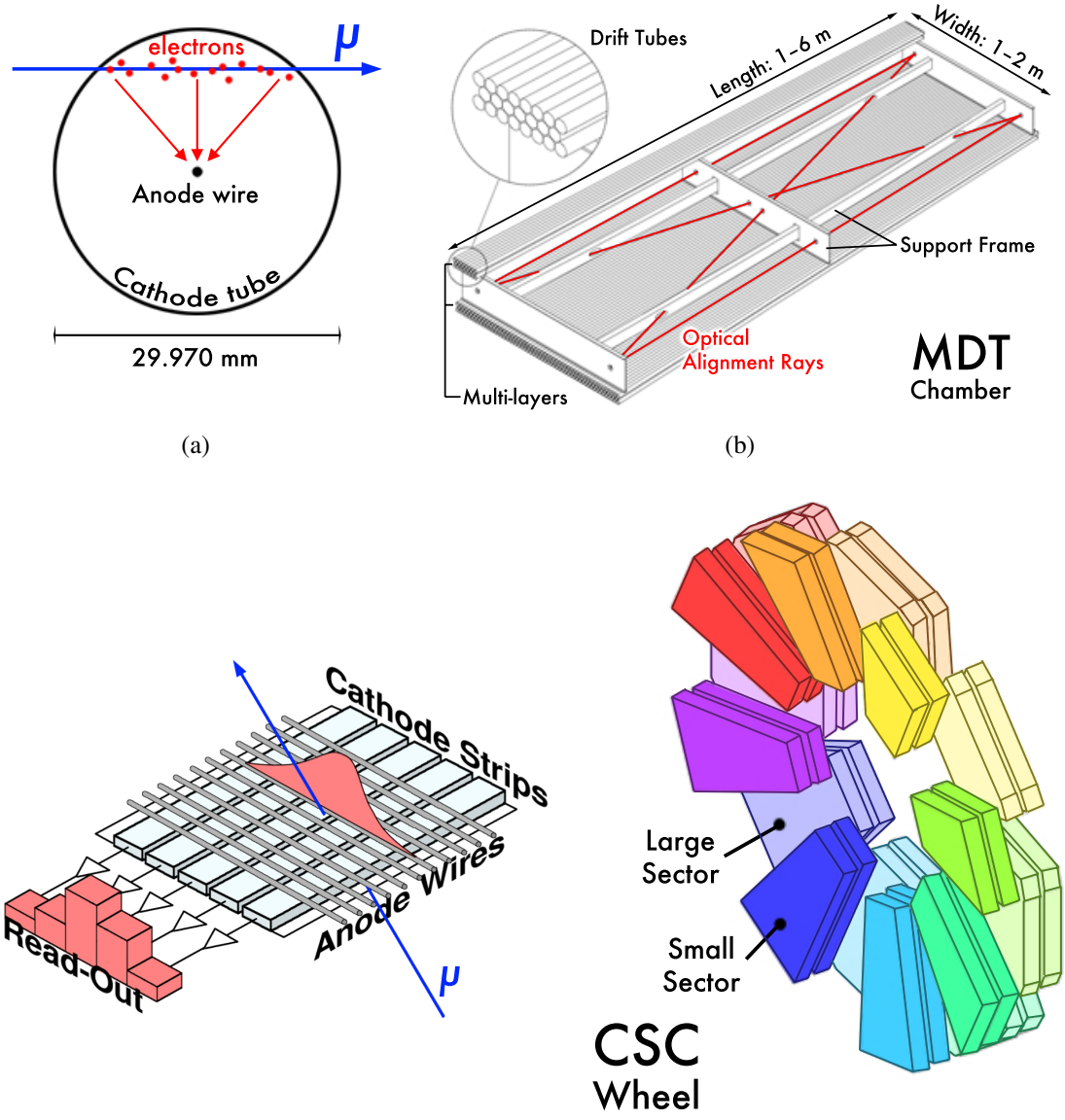

(a) (b)

(c) (d)

Figure 2.14: (a) Cross section of an MDT drift tube. (b) Schematic of a typical MDT chamber, with dimensions and primary components labeled. (c) Segmentation of cathode strips with perpendicular anode wires in the CSC. (d) Geometry of a CSC wheel. [72]

optical alignment rays (a light-emitting diode on one end, a CCD sensor on the other, and a lens in the middle) are integrated into the support structure and track internal deformations on the order of a few μm. MDT chambers vary in size (depending on their distance from the IP and spatial conflicts with magnets and support structures) as well as shape (rectangular in the barrel, trapezoidal in the end-caps); the average resolution per chamber is about 35 μm in the bending plane (η). See Figures 2.14(a) and 2.14(b).

In the innermost end-cap layer ($2 < |\eta| < 2.7$), a higher particle flux and track density are better handled by Cathode-Strip Chambers, which have high spatial, time, and two-track resolution as well as improved radiation-hardness. CSCs are multi-wire proportional chambers: a series of radially-oriented anode wires biased at 1900 V are suspended in Ar/CO_2 gas between parallel-plate cathodes; wires are separated from both each other and each cathode plate by 2.5 mm. The cathodes are segmented into strips for individual read-out, with one plate aligned perpendicular to the wires providing a precision track coordinate in the bending plane (40 μm resolution), and the other aligned parallel to the wires providing a less precise transverse coordinate in the non-bending plane (5 mm resolution). The position of a muon track is determined by interpolation of the charge induced on several neighboring strips. The CSC system consists of two end-cap disks, each with eight small and eight large sectors of four CSC planes apiece. This configuration gives four measurements in $\eta \times \phi$ per outgoing muon. See Figures 2.14(c) and 2.14(d).

Trigger Chambers

RPCs and TGCs are used primarily to provide clear p_{T} thresholds for triggering, measure the muon track coordinate in the non-bending (ϕ) plane, and associate LHC bunch crossings to outgoing muons.

In the barrel ($|\eta| < 1.05$), muon triggering is provided by Resistive Plate Chambers. An RPC *detector layer* consists of two parallel, resistive electrode-plates separated with insulating spacers by a 2-mm gap filled with a hydrocarbon gaseous mixture; a 4.9 kV/mm electric field between the plates allows for charge avalanches to form along the ionization trail of a passing muon. Signal is read out by two sets of capacitively-coupled metallic strips, with set one aligned in ϕ and the other in η, allowing for measurements in both bending and non-bending planes. RPCs are arranged in three concentric layers, called stations; each RPC contains two, overlapping, contiguous *units*, which themselves consist of two, independent detector layers. This geometry is illustrated in Figure 2.15(a). Trigger coincidence between the inner and outer stations select for high-p_{T} (9 – 35 GeV) muons, while coincidence between the two inner stations select low-p_{T} (6 – 9 GeV) muons. The intrinsic time resolution of the RPCs is 1.5 ns, with $\sim$ 15 ns added from signal propagation and electronics — more than sufficient for tagging bunch crossings.

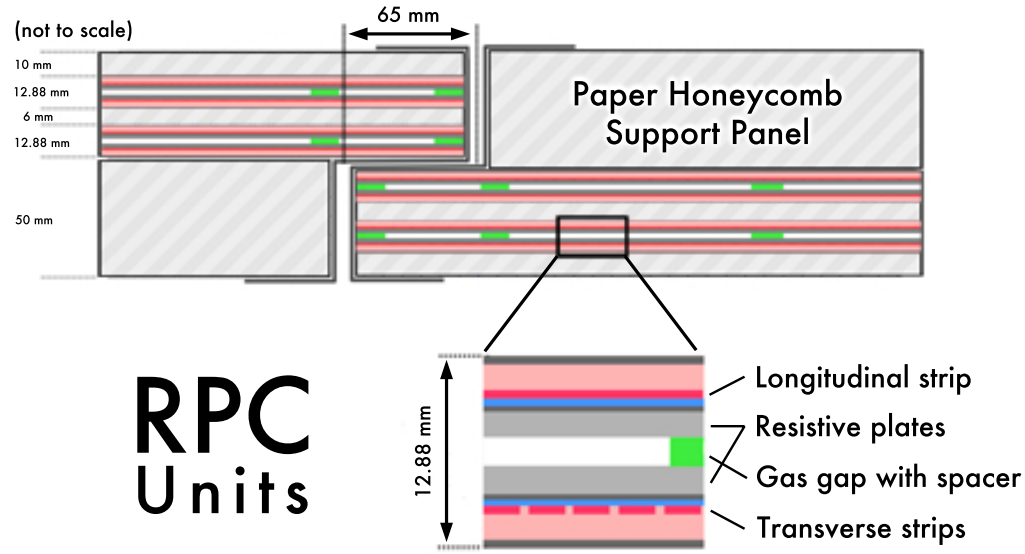

(a)

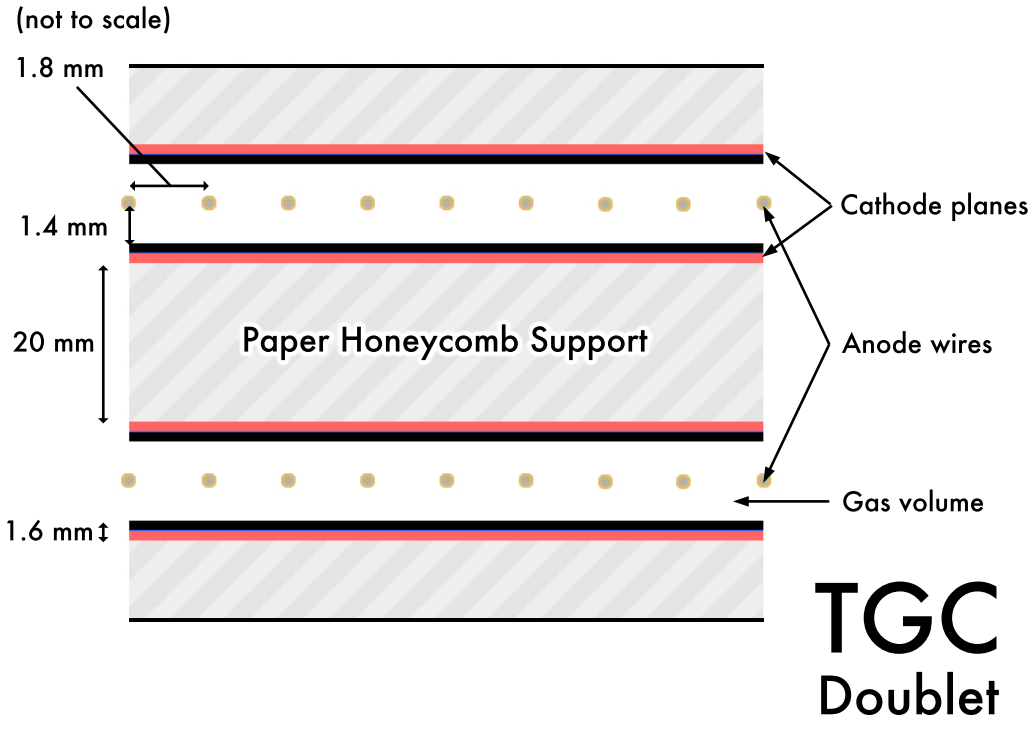

(b)

Figure 2.15: Cross sections through (a) an RPC chamber, consisting of two, two-layered units joined together supported by paper honeycomb panels; and (b) a TGC doublet module, consisting of two detector layers separated by paper honeycomb panels. Inspired by images in [72].

In the end-cap ($1.05 < |\eta| < 2.4$) region, Thin Gap Chambers are used for muon triggering as well as azimuthal coordinate measurements to complement the MDTs' bending-plane measurements. TGCs are multi-wire proportional chambers (discussed previously) with a plane of 50-μm anode wires biased at 2900 V and suspended in a quenching CO_2/n-pentane gas mixture between two cathode planes. Cathodes are 1.6-mm thick G-10 fiberglass plates with a graphite coating on the inside and copper read-out strips on the outside. TGCs have differing anode-anode and anode-cathode distances of 1.8 and 1.4 mm, respectively; the small wire pitch and high electric field around the wires lead to a good intrinsic time resolution of 4 ns and a 99% efficiency for bunch-crossing identification. TGCs are grouped into two-layered doublets or three-layered triplets arranged in circular disks with an inner (forward) ring and an outer (end-cap) ring, with varying azimuthal segmentation. An example is shown in Figure 2.15(b).

2.2.6 Forward Detectors

ATLAS has three small detectors covering the very forward region. Located $\pm$17 m from the interaction point, LUCID (LUminosity measurement using Cerenkov Integrating Detector) [85] detects inelastic proton-proton interactions in order to measure integrated luminosity as well as provide online monitoring of instantaneous luminosity. At $\pm$140 m from the IP, the Zero-Degree Calorimeter [86] detects forward ($|\eta| > 8.3$) neutrons from heavy-ion collisions in order to determine the *centrality* of such events. Located at $z = \pm 240$ m, ALFA (Absolute Luminosity For ATLAS) [87] is a scintillating-fiber detector responsible for measuring small-angle elastic scattering and, from that, determining the absolute integrated luminosity.

2.2.7 Trigger and Data Acquisition Systems

Under nominal operation, the LHC collides proton bunches every 25 ns, yielding an event rate of roughly 40 MHz. Recording *every* event is technologically impossible, both for the data acquisition system used for data storage and the computing resources used for offline analysis. Fortunately, it is also unnecessary from a physics perspective: the most common processes aren't statistically-limited, so the vast majority can be discarded, while the "interesting" (but rare) processes are typically distinguished by high-p_T leptons and jets and large missing transverse energy.

ATLAS employs a three-tiered trigger system — Level-1 (L1), Level-2 (L2), and Event Filter (EF) — that sequentially refines event selection criteria, reducing the event rate to a more manageable $\sim$ 400 Hz for those events actually recorded to disk. A Data Acquisition System (DAQ) reads out and buffers the detector information, provides the trigger system with the information it needs to make a decision,

and handles the permanent storage of raw data. A block diagram of the trigger and data acquisition systems (TDAQ, collectively) is shown in Figure 2.16.

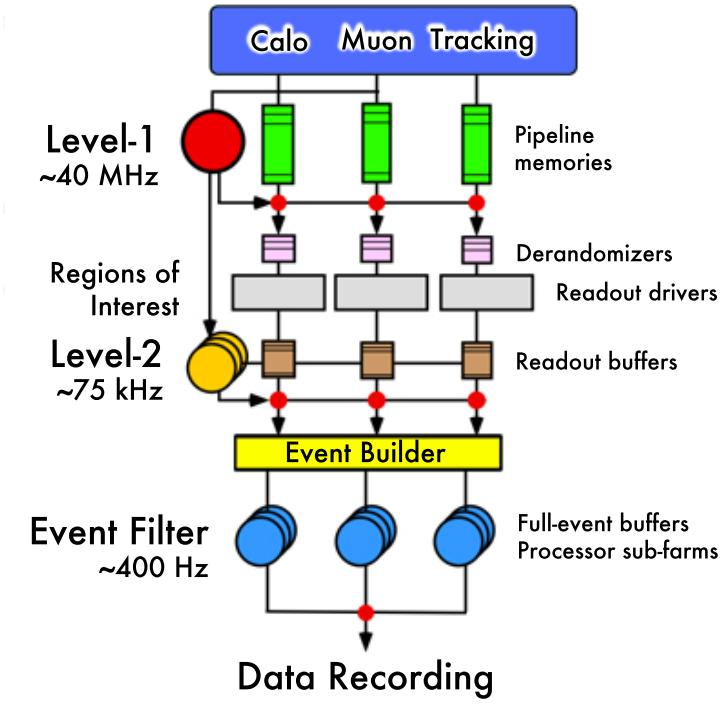

Figure 2.16: Block diagram of the TDAQ system, with approximate event rates indicated on the left side. Modified version of an image in [88].

Level-1 Trigger

The Level-1 trigger [88] is the first to decide if an event is interesting and merits further analysis; including signal propagation time, this initial decision must be made within about 2 μs. Custom-built electronics process a subset of coarse detector information coming from the muon spectrometer (L1Muon) and calorimeter (L1Calo) trigger systems, searching for high-p_{T} muons, electrons, photons, jets, and τ-leptons, as well as large missing and total transverse energy. The results from L1Muon and L1Calo (e.g. multiplicities of objects passing certain thresholds) are combined in a Central Trigger Processor, which classifies events according to a trigger "menu" of various trigger combinations useful for analyses. *Regions of Interest* (RoIs) are defined as coordinates in η and ϕ where the L1 trigger has identified interesting trigger objects in the event. While the L1 trigger is making its decision, the detector readout information is stored in pipeline memories on the detector itself; after an affirmative decision is made, this information is passed on to the DAQ.

Overall, the event rate is reduced from about 40 MHz to 75 kHz.

High-level Trigger

The Level-2 and Event Filter triggers are collectively referred to as the High-level Trigger (HLT) [89]. Rather than hardware, these triggers are implemented entirely in software running on a "farm" of off-the-shelf computers, and rather than sequentially, events are processed in parallel.

The L2 trigger refines event selection by analyzing the full-resolution detector information from both the muon spectrometer and calorimeter as well as the inner detector, for improved particle identification. To conserve bandwidth, information is confined to the RoIs defined previously by the L1 trigger (about 2% of the total event data). The average processing time for the L2 trigger is 40 ms; it reduces the event rate to less than 3.5 kHz.

The final trigger decision is made by the Event Filter, which processes the full information for an event using reconstruction algorithms similar to those used for offline analysis — see Chapter 4. The EF classifies events into *physics streams*, including the `Muon`, `Egamma`, and `JetTauEtmiss` streams. A typical event requires ~ 4 s of processing time, and the final event rate is approximately 400 Hz. Those events passing the EF are transferred to CERN's central data-recording facility for permanent storage.

CHAPTER 3

Event Simulation

> The generation of random numbers is too important to be left to chance.
>
> Robert R. Coveyou

A primary objective of present-day particle physics experiments is to search for physics beyond the Standard Model by making measurements that deviate from SM predictions. But, given the SM's success in accurately and *precisely* describing a wide range of particle phenomena, such deviations — and the "new physics" behind them — are expected to be small effects. Clearly, excellent predictions of both SM *backgrounds* and new physics *signals* are needed in order to make meaningful comparisons with data; for most analyses, those predictions are provided by Monte Carlo (MC) event generators.

From a theoretical model of a given physics process, event generators simulate the initial "hard" (large momentum transfer) interactions and evolve them through distinct phases/scales, ultimately yielding a randomized sample of events with production rates and final states as expected in Nature. These simulated events are then passed through a detailed detector simulation and processed by the same reconstruction algorithms used to interpret (non-simulated) collision data. Thus, a direct comparison between simulated samples and observed data is possible [90].

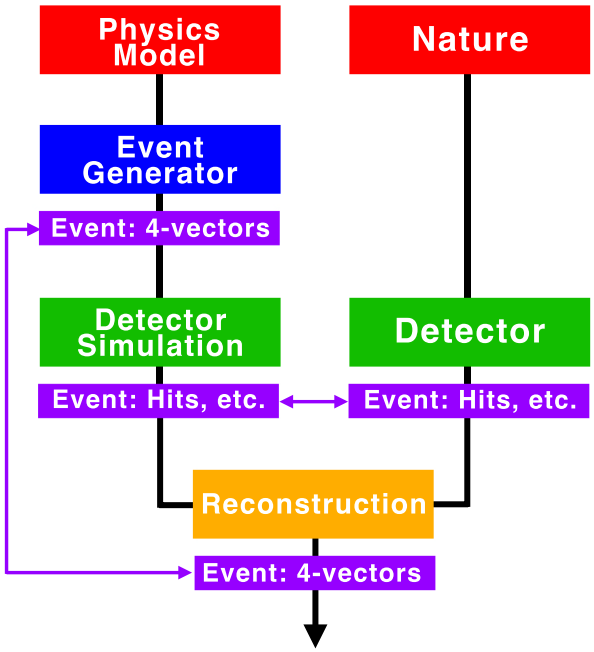

Figure 3.1: Event simulation flow chart, from an initial physics model to a sample of events reconstructed in the same manner as data. The purple lines show avenues for useful comparisons.

A flow chart of this process is shown in Figure 3.1, whose components are the subject of this and the following chapters.

3.1 Event Generation

Understanding — and simulating — the range of final states produced by the LHC is a great theoretical and technical challenge: hundreds of particles may be produced over many orders of magnitude in momentum, evolving from systems approximately described by perturbative QCD to inherently non-perturbative final states requiring phenomenological solutions, all of which require complex numerical solutions and massive computing power. Figure 3.2 shows an illustration of a typical hadron-hadron collision event, which consists of several processes and evolutionary phases: a primary hard subprocess, showers of both incoming and outgoing colored particles, hadron formation and decay, and secondary interactions between the remnants of the beam [91]. The enormity of the problem is lessened by the *factorization* of the system, as well as the software required to describe it, into separate components based on the scale of momentum transfers involved [92].

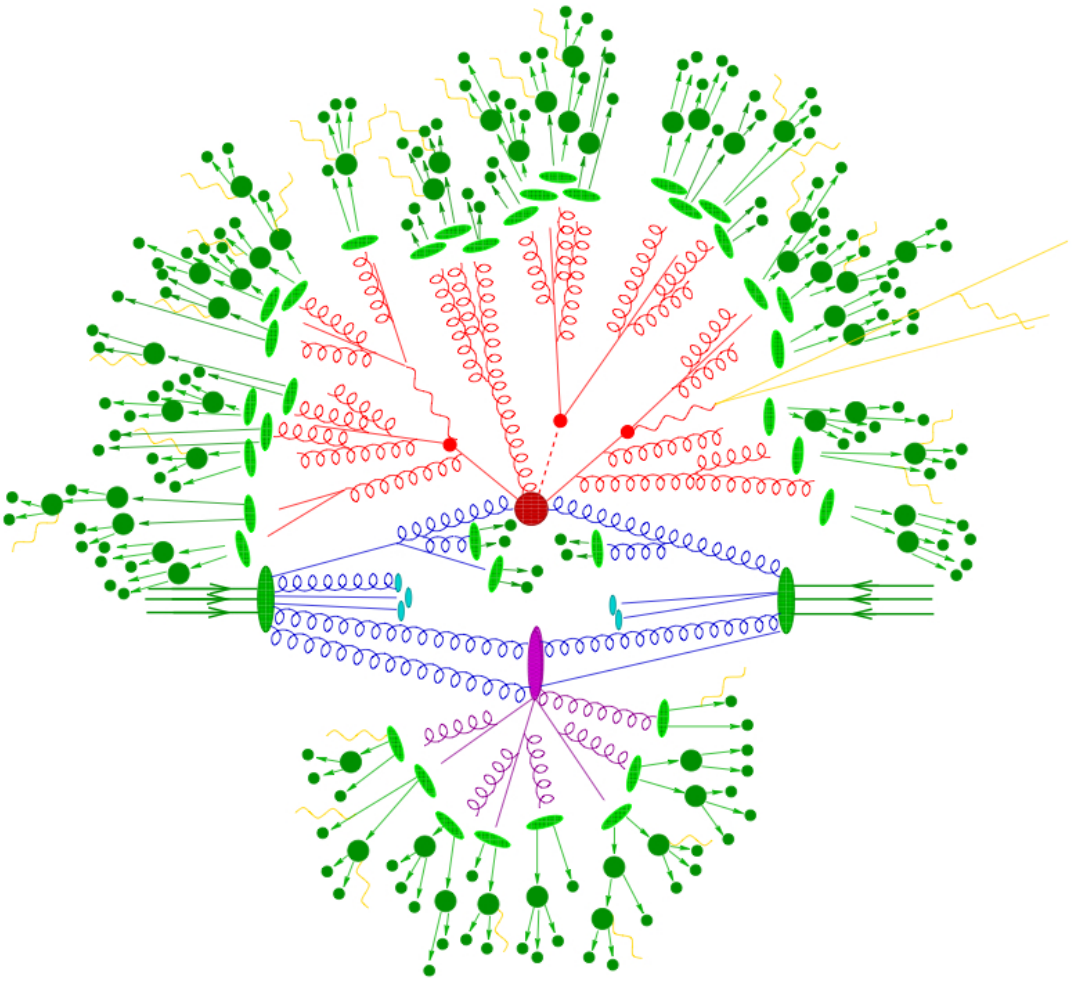

Figure 3.2: Illustration of a typical hadron-hadron collision: the red blob represents the hard subprocess; the light green blobs indicate hadronization, and the dark green blobs are their subsequent decays; the purple blob corresponds to the underlying event. [93]

3.1.1 Hard subprocess

At the LHC, interesting events typically begin with a hard interaction between two *partons* (i.e. quarks and gluons) bound inside incoming hadrons (i.e. protons). Owing to the asymptotic freedom of QCD, the interacting partons can be treated as free particles and are therefore describable by perturbative QCD [4]. The cross section for a scattering subprocess between partons a and b in hadrons h_1 and h_2 to a final state with n particles can be written as follows:

$$\sigma(ab \to n) = \sum_{a,b} \int_0^1 \mathrm{d}x_a \mathrm{d}x_b \, f_a^{h_1}(x_a, \mu_\mathrm{F}) \, f_b^{h_2}(x_b, \mu_\mathrm{F}) \, \hat{\sigma}_{ab\to n} \,, \tag{3.1}$$

where the sum is over all parton species in the incoming hadrons; $f_i^h(x_i, \mu_\mathrm{F})$ is a parton distribution function (PDF) giving the probability of finding a parton i with momentum fraction x with respect to its parent hadron h, dependent on the factorization scale μ_F; and $\hat{\sigma}_{ab\to n}$ is the partonic cross section for the production of n final-state partons from initial-state partons a and b [93]. Calculating this parton-level cross section requires the integration of the differential cross section over phase space:

$$\begin{aligned} \hat{\sigma}_{ab\to n} &= \int \mathrm{d}\hat{\sigma}_{ab\to n} \\ &= \int \left(\prod_{i=1}^{n} \frac{\mathrm{d}^3 p_i}{(2\pi)^3 2E_i} \right) (2\pi)^4 \delta^{(4)} \left(p_a + p_b - \sum_{i=1}^{n} p_i \right) \frac{1}{2\hat{s}} |\mathscr{M}_{ab\to n}|^2, \end{aligned} \tag{3.2}$$

where the sum and product are over all final-state partons, p_a and p_b (p_i) are the initial-state (final-state) momenta, and $\mathscr{M}_{ab\to n}$ is the matrix element for the process, which can be thought of as a sum over Feynman diagrams contributing to the process [91]. Note that this is to leading order only.

In determining the cross section for a given process, event generators are faced with two main challenges: computation of the matrix elements and integration over a multi-dimensional phase space.

Matrix elements are calculated in a perturbative expansion in powers of the strong coupling constant α_s, organized in terms of Feynman diagrams. This expansion is often truncated at tree-level or leading order, thereby introducing a fundamental uncertainty on the prediction, because higher-order loop calculations require the cancellation of divergences between real and virtual corrections and removal of collinear singularities — a non-trivial task. Even LO calculations are challenging, since the number of diagrams used to construct the matrix elements grows roughly factorially with the number of final-state particles. Comprehensive lists of LO matrix elements and phase-space parameterizations for $2 \to 1$, $2 \to 2$, and

some $2 \rightarrow 3$ processes are built in to most general-purpose event generators. For higher-multiplicity final states, dedicated software packages are used to automatically evaluate the growing number of Feynman diagrams [93]. In recent years, next-to leading order event generators have been developed that include terms with extra particles in loops and/or "legs" (i.e. final-state partons) and propagate them through the evolution of the process.

Integrating over the many-dimensional[1] phase space is a complicated task ideally performed with Monte Carlo methods. The first task is to sample the phase space [92]: candidate events are defined by choosing a value for each degree of freedom (component of a particle's momentum) with a random number generator. The probability of the candidate event occurring is directly related to its differential cross section $d\sigma$, or *event weight*. The average of many candidate event weights $<d\sigma>$ is approximately equal to the integral $\int d\sigma$ and converges to the actual cross section; this is the basic principle of all MC methods. At this point, however, the candidate events are distributed uniformly in phase space, so in order to derive physically meaningful predictions, they are *unweighted*, typically using the "hit-and-miss" method.[2] The end result is a sample of events with frequencies as expected in Nature.

3.1.2 Parton Showering

The initial hard scattering of partons results in the acceleration of color-charged particles, which in turn causes them to emit QCD radiation (gluons), as accelerating electrically-charged particles emit QED radiation (photons). Unlike photons, however, gluons are themselves colored, so their emission gives rise to further radiation and parton multiplication, resulting in a "shower" or partons. The effect of this higher-order radiation in hadron collisions is significant, and it is dominated by soft (low-energy) and collinear gluon emission [94].

Approximating the effect of such higher-order corrections is the role of a parton showering algorithm, in which both the initial- and final-state partons are permitted to split or "branch" into other partons, which themselves may also branch, and so on. Starting at the initial hard interaction scale, partons are recursively evolved through successive branchings until reaching a lower energy scale on the order of a few GeV, i.e. the hadronization scale. In essence, this amounts to determining the evolution scale t at which a parton a produced at scale $t' > t$ would be likely to branch into two daughter partons b and c, and the flavors and kinematics of those

[1] Namely, $3n-4$ dimensions corresponding to three momentum components for each particle produced minus four constraints for energy-momentum conservation, plus flavor and spin states [91]

[2] Also known as the acceptance-rejection method or the Von Neumann method. [92]

daughters [93]. That probability can be written as

$$\mathrm{d}P_a(x,t) = \frac{\mathrm{d}t}{t}\,\frac{\alpha_s}{2\pi}\,P_{ca}(x)\,\mathrm{d}x, \tag{3.3}$$

where x is the momentum fraction of parton c with respect to a, and $P_{ca}(x)$ is a universal, flavor-dependent "splitting" function whose azimuthal dependence has been averaged out. The inclusive LO cross section of the hard subprocess multiplied by factors of $\mathrm{d}P_a(x,t)$ for each branching gives the partial cross section of the exclusive process, and by the "unitarity of the shower process," the sum of all partial cross sections is equal to that of the initial hard subprocess [94]. Note that the probability diverges in the soft ($x = 0, 1$) and collinear ($t = 0$) regions, a problem resolved by imposing a cutoff scale t_0 below which a detector would be unable to resolve a branching on account of being too low-energy or at too small a splitting angle.

Typically, several emissions above the cutoff scale are possible; in order to generate an exclusive parton shower, they are ordered in terms of the parent parton's virtual mass-squared or *virtuality* q^2 using a *Sudakov form factor*:

$$\Delta_a(q_1^2, q_2^2) = \exp\left[-\int_{q_2^2}^{q_1^2}\frac{\mathrm{d}q^2}{q^2}\,\frac{\alpha_S}{2\pi}\int_{Q_0^2/q^2}^{1-Q_0^2/q^2} P_{ca}(x)\,\mathrm{d}x\right], \tag{3.4}$$

which represents the probability that no additional emissions occur from partons between q_1^2 and q_2^2, with q^2 as the *evolution variable* and Q_0^2 as the cutoff set by the hadronization scale [91]. It's worth noting that different showering algorithms use different evolution variables, and this *does* have an effect on their final output.

The evolution of a parton shower[3] proceeds as follows: Starting from the initial scale of the hard subprocess Q^2, for each initial parton one solves the equation $\Delta_a(Q^2, q_1^2) = \mathfrak{R}_1$ for the scale of the first branching q_1^2, where $\mathfrak{R}_1 \in [0,1]$ is a random number. If $q_1^2 < Q_0^2$, the branching is unresolvable and showering for that parton ends; otherwise, branching $a \to c + d$ is allowed, and the process is repeated for the daughter partons at scales smaller than that of the branching in which they were produced, recursively, until no more resolvable branchings occur [91]. At each split, the momentum fraction and azimuthal angle of the daughter partons are given by the splitting function $P_{ca}(x,\phi)$. The end result of these successive branchings is a shower in which each parton from the hard process is matched to a "jet" of partons moving in roughly the same direction, with relative transverse momenta on the scale set by t_0 (or Q_0^2, etc.). At this point hadronization occurs.

[3] This discussion is *scandalously* short on detail, and many important complications have been omitted entirely, for brevity. For a more thorough explanation, consult the literature, e.g. [4].

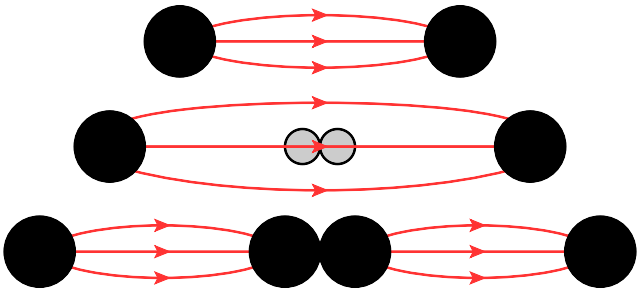

Figure 3.3: Cartoon illustration of the string model of hadronization (time flows from top to bottom).

3.1.3 Hadronization

In order to match experimental observations, the loosely-clustered collections of colored (bare) partons must transition into color-neutral primary hadrons. Unlike the previous two steps of event generation, no first-principles approach is possible for hadronization, so phenomenological models are employed instead [93]. Although QCD principles inspire the broad strokes, finer details are accounted for by fitting parameters to data. The two most common models are the following:

- **String model**: Based on the principle of "linear confinement," where the potential energy of a color-dipole field between, for example, a quark and an antiquark, increases with their linear separation [4]. The quarks are connected by a "string" or "flux tube" along color lines; at sufficient separation, when the potential is comparable to hadron masses, it becomes energetically favorable to break the string through the creation of a new pair somewhere along its length by way of quantum tunneling. The result is *two* quark-antiquark pairs, also connected by strings. This process continues until all the bare partons are bound up in what may be identifiable as hadrons [91]. A simple cartoon of this process is shown in Figure 3.3.

- **Cluster model**: Based on the principle of "pre-confinement," where post-shower partons at the hadronization scale Q_0 are clustered in color-neutral groups with invariant masses on the same order as Q_0, regardless of the hard subprocess from which they evolved [4]. Remaining gluons are forced to decay into quark-antiquark pairs, and the resulting clusters are considered to be "proto-hadrons." If sufficiently light, the proto-hadron clusters translate directly into the final-state hadrons actually observed, otherwise they decay into lighter hadrons [91].

Regardless of the model, many of the final-state hadrons generated will be unstable and undergo additional decays. Given the complexity of hadronic final-states

and the variety of their subsequent decays, full calculation of all matrix elements and integration over phase spaces isn't feasible, so once again, phenomenological models are used. Summary tables of particle decays and branching ratios (as in [4]) provide a useful starting point for setting the rates at which various decay chains occur [93]. The kinematics of the decay products must also be modeled, so some matrix elements are explicitly incorporated. The end result is a sample of events consisting of stable[4] particles readily observable by a particle detector.

3.1.4 Underlying Event

In hadron-hadron collisions, additional activity is observed beyond that expected from partons directly involved in the primary hard subprocess and subsequent showering/hadronization; this is collectively referred to as the *underlying event*. This activity sits at a higher level ("pedestal") than *minimum-bias* events in which no hard subprocess occurs. It's assumed that the dominant component comes from *multiple parton interactions* (MPIs), in which other partons belonging to the beam remnants interact [93]. Such interactions tend to be softer than the hard subprocess, resulting in a global increase in activity (larger multiplicities, summed transverse energies, etc.) and occasionally in additional reconstructed jets.

Again, phenomenological models tuned to data are used to describe the underlying event. A common method to estimate the probability for MPIs to occur is to parametrize this in terms of the *impact parameter* b of the collision: peripheral (large b) collisions are less likely to have hard interactions and have fewer MPIs overall, while central (small b) collisions are more likely to have hard interactions and have more MPIs overall [91]. The average number of parton-parton interactions per hadron-hadron collision is estimated as a function of b (and other parameters), and the additional interactions are included by the event generator in the evolution of the event state.

3.1.5 Common Event Generators

As mentioned previously, recent years have seen a marked proliferation and factorization of event generators simulating hadron collisions as produced by the Tevatron and LHC. Below, several common examples are listed and briefly described, starting with general-purpose generators and ending with more specialized software packages.

[4] "Stable" (in terms of decay length or lifetime) depends on the detector. In ATLAS, for example, muons are stable, while b quarks are not.

3.1 Event Generation

PYTHIA

PYTHIA [95] is a general-purpose event generator for the simulation of hadronic events in pp, e^+e^-, and ep colliders. It includes around 300 hard-coded $2 \to 1,2,3$ scattering processes at LO along with the most common PDF sets, with full spin correlations accounted for in subsequent decays. SM, SUSY, and several Exotics physics scenarios are handled. PYTHIA also includes initial- and final-state parton showers with evolution proceeding in terms of decreasing virtuality and angular ordering imposed by veto. MPIs are used to build up the underlying event, taking into account impact parameter and energy sharing between multiple partons in the beam remnants, among other factors. Hadronization follows the Lund string model, and unstable particles are permitted to decay. PYTHIA 6 [96] is written in `Fortran 77` and is the product of thirty years of progress in the field; PYTHIA 8 [97] is a recently-revamped successor written in `C++`.

HERWIG

HERWIG (Hadron Emission Reactions With Interfering Gluons) [98] is another general-purpose event generator for the simulation of events at lepton and hadron colliders. It contains a large number of built-in $2 \to n$ subprocesses, almost all with full spin correlations included, for both SM and some BSM frameworks, as well as an automatic $2 \to 2$ generator requiring only the relevant Feynman rules as input. The treatment of unstable resonance decays in the final state is relatively sophisticated. Initial- and final-state parton showers are angular-ordered, so emission angles get progressively smaller as evolution proceeds. Hadronization uses the cluster model. The decays of primary hadrons are performed according to phase space, with matrix elements used only in special cases. The underlying event is based on a pp minimum-bias event generator but can be interfaced specially to JIMMY. As with PYTHIA, HERWIG [99] was originally written in `Fortran` and recently replaced by a `C++` successor, called HERWIG++ [100]; this new generator features improved parton showering and hadronization modeling.

SHERPA

SHERPA (Simulation for High Energy Reactions of PArticles) [101] [102] is a relatively new general-purpose event generator, written in `C++` from the start, that is capable of simulating lepton-lepton, lepton-hadron, hadron-hadron, as well as photon-photon processes. It features automatic, tree-level matrix-element and phase-space generation of subprocesses for SM and Minimal Supersymmetric SM scenarios, as well as other exotic frameworks (given the necessary Feynman rules). Parton showers are organized in terms of parton virtuality, with angular ordering imposed by veto. Hadronization is based on the cluster model, with primary hadron decays

including full spin correlations. MPIs are treated such that parton showers resulting from the additional semi-hard collisions may evolve independently.

ALPGEN

ALPGEN [103] [104] is a partonic matrix element generator and phase space integrator for SM processes in hadronic collisions, specializing in processes with many jets in the final state. Mass effects of heavy quarks (t, b, and occasionally c) are included, as well as decays of top quarks and vector bosons with full spin correlations. A suite of standard PDF sets is built in. ALPGEN does not perform parton showering or hadronization; it outputs weighted or unweighted event samples, and the latter can be interfaced to HERWIG or PYTHIA (default options) for further simulation.

AcerMC

AcerMC [105] [106] is a specialized event generator that handles only specific SM background processes produced in proton-proton collisions at the LHC. It includes a library of dedicated matrix-element-based generators for these processes that allows for relatively fast simulation compared to the general-purpose generators. AcerMC is interfaced to PYTHIA or HERWIG to complete the event simulation, including initial- and final-state radiation, hadronization, subsequent decay chains, and the underlying event.

MC@NLO

MC@NLO [107] [108] is a NLO partonic matrix element generator for hadronic production of heavy quark pairs, diboson, and inclusive W and Z processes, among others. The NLO accuracy yields a better prediction of a subprocess' rate and a better description of the first hard parton emission. Unlike most other generators, MC@NLO produces events that may have weights of either $+1$ *or* -1. The program interfaces directly to HERWIG (or HERWIG++) for showering and hadronization, which it does not compute on its own.

POWHEG

POWHEG (POsitive Weight Hardest Emission Generator) [109] [110] is a program and methodology that interfaces NLO calculations from a matrix element generator with general parton showering generators. It performs a role similar to MC@NLO but avoids the necessity of negative event weights and interfacing to a *specific* generator for showering.

JIMMY

JIMMY [111] is a dedicated software package for the simulation of multiple parton interactions in the underlying event of hadron-hadron, photon-hadron, and photon-photon collisions. It assumes some distribution of partons inside hadrons varying with impact parameter and independent of momentum fraction, then calculates the MPI rate as a function of the hard subprocess cross section, standard PDFs, and the degree of overlap of the colliding hadrons. JIMMY is used specially by HERWIG for its underlying event simulation.

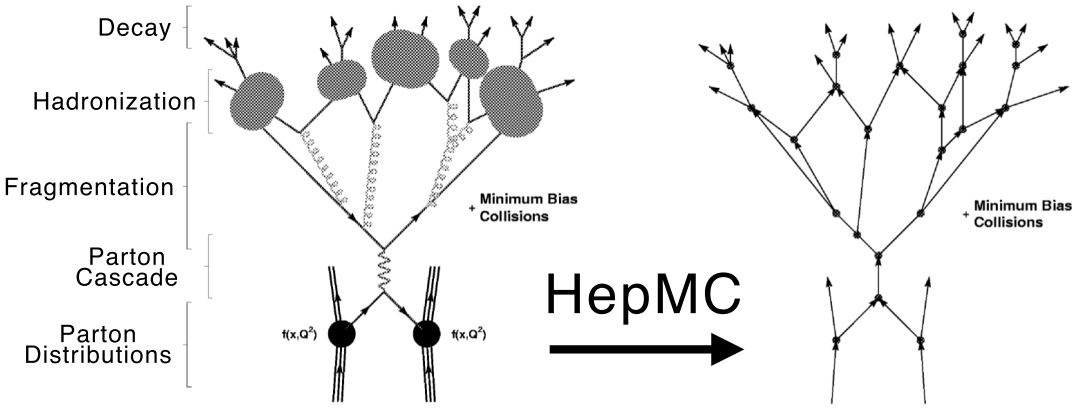

Figure 3.4: Comparison of a simple visualization of a hard scattering event (left) and the graph structure of an event in the HepMC convention (right). [112]

3.2 Detector Simulation

Ultimately, event generators output a sample of events with rates as expected in Nature, where by the HepMC convention [112] each event consists of a graph (or *graphs*, for multiple interactions) with vertices as nodes and particles as connections, and associated properties such as positions and momenta (see Figure 3.4). This output is then passed along to a sophisticated simulation of the ATLAS detector [113] built with GEANT4 (GEometry ANd Tracking), an object-oriented C++ simulation "toolkit" that describes the passage of particles through matter and their resulting interactions [114] [115]. The ATLAS simulation reproduces the full chain of event detection: the *in-situ* detector geometry, physics interactions of particles as they pass through each component, and digitization of energy depositions into voltages and currents.

Subdetector	Materials	Logical Vol.	Physical Vol.
Inner Detector	243	18,440	56,838
Calorimetry	73	35,864	182,262
Muon System	22	9,467	76,945

Table 3.1: Number of materials and volumes included in the GEANT4 simulation of the ATLAS detector. [113]

The detector geometry is represented as a hierarchy of logical and physical volumes composed of different shapes and materials: a *logical* volume represents an element of the detector with a particular shape and set of materials and properties that may be replicated many times; a *physical* volume represents the spatial placement of a given logical volume with respect to an enclosing ("mother") volume. The full complexity of the ATLAS detector is impressive: Table 3.1 shows the number of materials and volumes included in the simulation.

At the heart of GEANT4 is a set of physics models based on both data and theory — and continually validated/refined — that describes a wide range of electromagnetic, hadronic, and optical interactions (ionization, bremsstrahlung, pair-production, scattering, radiation, scintillation, showering, quark-gluon string fragmentation, etc.) over a wide range of energies ($\sim 10^2$ – 10^{10} eV). These models and their parameters are chosen and optimized specifically for the ATLAS detector. Particles are transported through the detector (a process called *tracking*) in a series of small, finite steps, either in time or space, each corresponding to an individual physics process. There are three types of steps:

- **at rest**: for discrete processes of particles at rest, e.g. decays, annihilations
- **along step**: for continuous processes that occur throughout the duration of the step, e.g. energy loss from ionization, secondary particle production, Cherenkov radiation
- **post step**: for discrete processes that take place at the end of the step, e.g. secondary particle production through in-flight decays, crossing a geometrical boundary

A "physics list" of possible processes are assigned to each particle, depending on its properties and those of the material through which it is passing; in a given step, one process is randomly invoked. The probability for a process to occur is updated after each step. Note that the many-step *trajectories* of particles through the detector need not be linear: charged particles moving in a magnetic field — as in ATLAS and its simulation — follow a helical or curved path.

3.2 Detector Simulation

Logical volumes in the detector geometry may be linked to "sensitive detectors," which generate *hits* based on the particle–matter interactions simulated in each step. A hit represents the energy deposited by a particle with an associated position and time, and is dependent on the particular sub-detector involved, whose behavior must be provided by the user. Events are output as a collection of such hits.

At this point in the simulation chain, multiple types of events are overlaid: hard scattering events, minimum bias events (those *without* a hard scatter), and other background events such as those from cosmic rays and beam halo interactions. The events appear with relative rates set by the user, as determined from *in-situ* measurements or expected beam conditions. This overlay is called *pile-up*; it is distinct from the underlying event simulation described previously. Detector noise is also added to the event. The net effect of pile-up is the presence of hits in the detector not resulting from the hard scatter but which affect its measurement and reconstruction.

Digitization is the process of converting hits into a detector signal, or "digits." Typically, this occurs when some voltage or current exceeds a threshold value over a given length of time, and the resulting digits may be either binary or also include analog information of signal shape. Adding pile-up before simulating the detector response improves the accuracy of the simulation. The individual quirks of each sub-detector's measurement (e.g. cross-talk) and conditions (e.g. dead modules) are modeled here as well. Ultimately, all the digits in an event are written to file in a format equivalent to that used for recorded data, then passed along to the next step of the process: reconstruction.

CHAPTER 4

Event Reconstruction

> Everything that can be counted
> does not necessarily count;
> everything that counts cannot
> necessarily be counted.
>
> Albert Einstein

From Nature and the Standard Model to colliders and detectors (and the simulation thereof), this tale continues into the realm of software and analysis. ATLAS is expected to produce upwards of a *Petabyte* of data per year, over the course of many years; to facilitate the distribution and analysis of this dataset with thousands of physicists working all around the world, a computing model and a software framework named `Athena` [116] were implemented, with an emphasis on modularity of function and commonality of structure/interface across sub-detectors, data formats, and steps of the software processing chain.

The raw detector readout of events — a collection of hits, times, energy depositions, etc. — is stored in `Raw Data Object` (RDO) files. Before such data can be analyzed for the underlying physics processes, however, the *physics objects* that gave rise to the measurements must first be reconstructed: charged particle tracks, vertices, muons, jets, electrons, and missing transverse energy. *Reconstruction* is the process of analyzing the raw data with pattern recognition algorithms that decide which individual signals belong to which individual objects, and from

this derive their kinematical properties.[1] Reconstructed events are saved in a series of progressively more compact file formats: from `Event Summary Data` (ESD) to `Analysis Object Data` (AOD) to `Derived Physics Data` (DPD) files, the last of which includes only an analysis-specific subset of the full event information.

The following sections describe the algorithms used to reconstruct the physics objects of interest in second-generation LQ events. It is *not* a comprehensive listing.

4.1 Tracks

With increasing instantaneous luminosity delivered by the LHC comes increasing density of tracks from charged particles in the ATLAS inner detector, imposing strict requirements on reconstruction software. Higher occupancy can lead to a degradation in the quality of tracks reconstructed as a result of spurious hit assignments, lower overall efficiency, and additional fake tracks from combinations of random hits [117]. To ensure good performance even in a high-density environment, tracks are reconstructed with a series of algorithms.

As an initial baseline, tracks in ATLAS are first reconstructed using an "inside-out" algorithm [118]. Hits in the Pixel and SCT detectors are transformed from local, two-dimensional measurements into global, three-dimensional space-points; valid combinations of three such points in the innermost four silicon layers are used as *seeds*. Then, proceeding outward from the interaction point, additional hits are added to the track candidate if they are found along its trajectory, as determined by a combinatorial Kalman filter [119]. With each additional hit, the track fit is progressively updated: the most likely hit position on the next measurement surface is extrapolated, allowing for more efficient forward filtering, and the track is smoothed in the backwards direction. Ambiguities in the resulting population of track candidates — most of which are "fake" or partial tracks — are resolved by ranking them according to their likelihood of corresponding to an actual particle's trajectory. Next, the resolved silicon-based track segments are extended into the TRT, where compatible sets of measurements are added to the track if found — *without* modifying the existing fit. Lastly, a global track is fit to all associated ID hits, resulting in three classes of tracks [120]:

- Tracks without TRT extensions (e.g. if $|\eta_{\text{trk}}| > 2$, outside TRT acceptance)
- Tracks with TRT extensions included in the global fit

[1] There are both *online* and *offline* reconstruction algorithms, where the former are used for trigger decisions and are extremely efficient, while the latter are for final event reconstruction and are more computationally-intensive. This chapter focuses on the offline implementations.

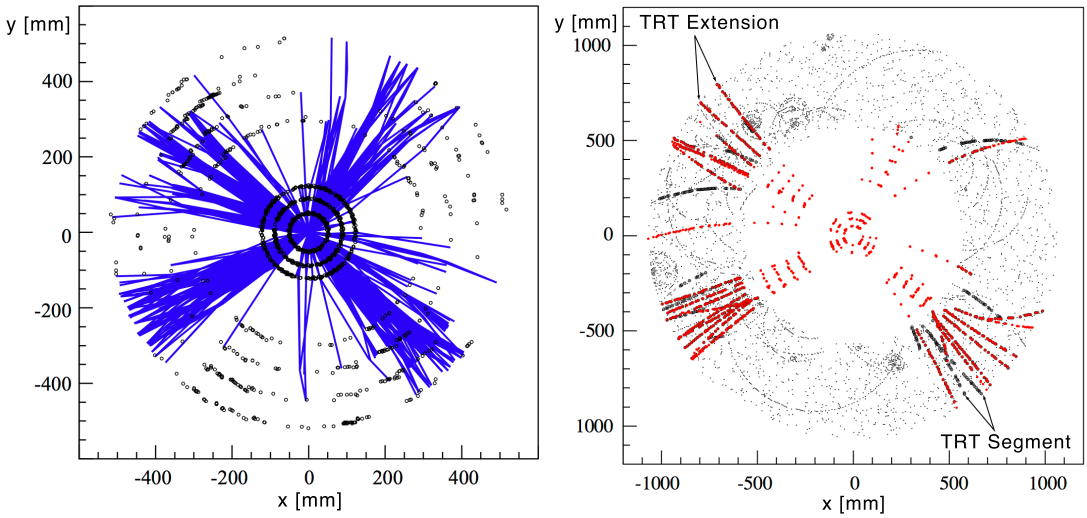

(a) (b)

Figure 4.1: Track candidates in a sample $t\bar{t}$ event at different stages of reconstruction: (a) silicon-based track segments based on three-point seeds, and (b) silicon-based track segments successfully extended into the TRT in red, with standalone TRT segments in black. [118]

- Tracks with TRT extensions excluded from the global fit (e.g. if too many TRT hits are classified as outliers)

An example of inside-out track reconstruction is shown in Figure 4.1.

The next stage of track reconstruction employs an "outside-in" algorithm in order to catch tracks potentially missed by the inside-out procedure, including those coming from secondary decays and photon conversions [118]. The algorithm begins with TRT-based track segments derived only from hits *not* already used in extensions to the inside-out silicon-based tracks [120]. In the $R-\phi$ ($R-z$) plane of a barrel (end-cap) sector, tracks originating near the IP follow straight lines and can be parameterized in terms of just two variables. These variables are used to form two-dimensional histograms in which local maxima correspond to track segments; to improve longitudinal accuracy and reduce the number of overlaying tracks, the TRT is divided into several "slices" in η. The best track segments are those that pass through the most TRT straws. Then, pairs of space-points in the outermost SCT layers are used as seeds for silicon-based extensions to the TRT track segments. A Kalman filter is used to extend them inward towards the interaction point by adding successive silicon hits; this is called *back-tracking*. As in the inside-out algorithm, ambiguities are resolved, and a final, global track fit is performed on all associated ID hits. TRT segments *without* a successful extension into the SCT and

Pixel detectors are also saved as "TRT-standalone" tracks [117].

The reconstruction of tracks and vertices are coupled: the reconstructed tracks in an event are used to find the vertices from which they originated, and the resulting fitted vertices in an event are used to further constrain their associated tracks.

4.2 Vertices

Vertices correspond to the spatial positions of the various interactions in an event, i.e. where particles are produced and/or decay. *Primary* vertices are those resulting from hadron-hadron collisions (and pile-up interactions) at the center of ATLAS; *secondary* vertices come from the decays and interactions of particles produced at primary or prior secondary vertices. Accurate reconstruction of both types of vertices are critical to many analyses by enabling the identification of b-quarks from displaced secondary vertices and contributing to a better estimation of the missing transverse energy in an event, among other reasons.

Primary vertex reconstruction is performed in two steps: vertex *finding* (associating tracks to particular vertex candidates) and vertex *fitting* (determining the vertex position and uncertainties thereon). The default algorithm used in ATLAS, "finding-through-fitting," intertwines these steps, though alternative "fitting-after-finding" algorithms have been implemented [121]. First, reconstructed tracks likely to have originated in the interaction region, or *beam spot*, are pre-selected.[2] Then, from the distribution of their longitudinal impact parameters with respect to the nominal center of the beam spot (z_0), an initial vertex seed is found from the global maximum in z_0. The position of the vertex is determined by an iterative, adaptive χ^2 fit to the positions of the seed track and those in its vicinity [123]. Each track is assigned a weight based on its compatibility with the fitted vertex position, expressed in terms of a χ^2 with two degrees of freedom, and outliers are progressively down-weighted. A track displaced from the fitted vertex position by more than 7σ is used to seed a new vertex. This algorithm is repeated until no additional vertices with at least two associated tracks located within the beam spot region are found. It's worth noting that the three-dimensional constraints provided by the beam spot are significant in both finding and fitting, particularly for vertices with few associated tracks. Determination of *the* primary vertex in an event arising from the hard hadron-hadron interaction (as opposed to minimum bias and other pile-up interactions) relies on the fact that such vertices typically have more associated tracks and higher transverse momenta. An example event with multiple reconstructed primary vertices is shown in Figure 4.2

[2]The extent of the beam spot is determined every few minutes from the distribution of primary vertices recorded in the immediate time period, where no beam-spot constraint has been applied. For more detailed information, see [122].

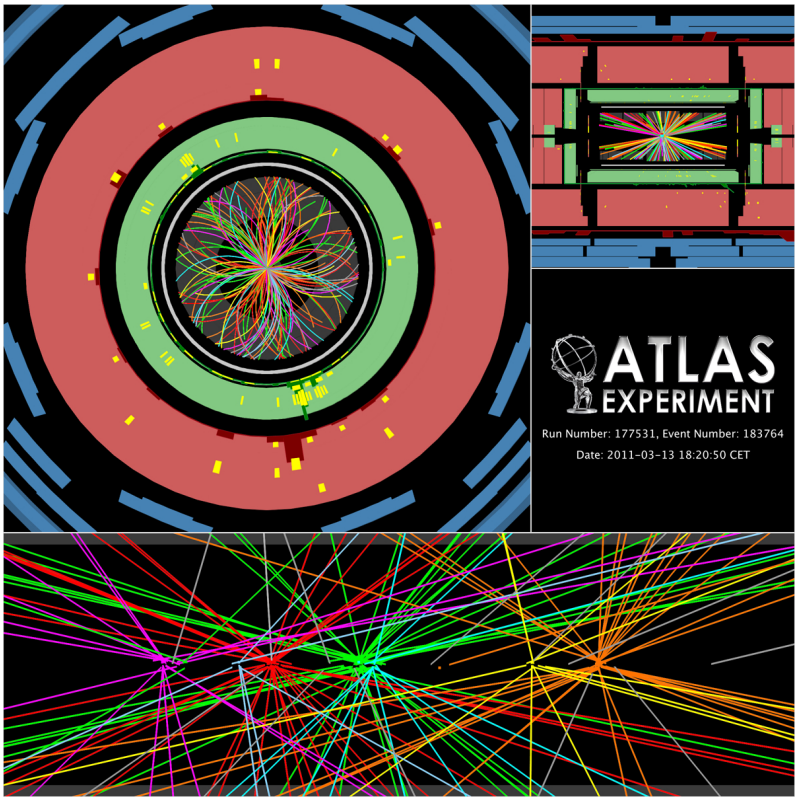

Figure 4.2: Reconstructed tracks and (seven) primary vertices in a collision event from the first stable LHC fill of 2011. Views are in the $R-z$ and $R-\phi$ planes. ATLAS Experiment © 2012 CERN

Secondary vertices are reconstructed quite differently from primary vertices by exploiting kinematic constraints on the interactions likely to produce such vertices, such as photon conversions, long-lived neutral hadron decays, and heavy-flavor decays [124]. The overall approach is to carefully select displaced tracks and perform a fit to the associated vertex given constraints on the mass of the parent particle and/or the angular distribution of its daughter particles. As an example, consider a secondary vertex resulting from a converted photon, $\gamma \rightarrow e^+e^-$: First, a pair of tracks are selected if they likely belong to electrons (using information from the TRT), have opposite charge, small initial opening angle (as expected from a massless photon parent), and a sufficiently small distance of closest approach; then, given these constraints, a conversion vertex is fit to the track pair. In long-lived particle decays, e.g. $K_s \rightarrow \pi^+\pi^-$, an un-constrained vertex fit is performed first in order to determine the proper mass constraint, which is then directly applied in the final, constrained vertex fit.

4.3 Muons

The design of the ATLAS detector allows for the efficient identification of muons and accurate determination of their momenta over a broad kinematic range. Reconstruction makes use of the *full* detector: the dedicated Muon Spectrometer[3] as well as the Inner Detector measure spatial positions, the calorimeter measures energy loss from ionization, and the magnet system enables a measurement of charge and momentum.

Currently, four kinds of muons are reconstructed, depending on which measurements are used [125]:

- **Stand-alone:** Only the MS is used to reconstruct muon trajectories and momenta, which are corrected for parametrized energy loss in the calorimeter to determine the initial momenta. The MS tracks are extrapolated back towards the beam line. Stand-alone muon reconstruction is performed using the `Muonboy` software package.

- **Combined:** Stand-alone muons reconstructed in the MS are matched to and combined with compatible neighboring tracks in the ID using a statistical algorithm. The software package used is called `STACO` (STAtistical COmbination), named after the algorithm.

- **Segment-tagged:** Tracks reconstructed in the ID are identified as muons if the extrapolated trajectories can be matched to track segments in the precision MS chambers. In this case the `MuTag` software package is used.

- **Calorimeter-tagged:** Tracks reconstructed in the ID are identified as muons if the extrapolated trajectories can be matched to energy deposits in the calorimeters consistent with that expected of a minimum-ionizing particle. Such reconstruction uses the `CaloTrkMuID` algorithm.

ATLAS employs two independent reconstruction chains, named Staco and MuID (after their respective combined reconstruction algorithms), that reconstruct stand-alone, combined, and segment-tagged muons using different algorithms. In this section, only Staco muons are discussed; for a brief description of the MuID chain, see [126].

Stand-alone muons in the MS are reconstructed by first identifying "regions of activity" using information from the RPC and TGC trigger chambers [127]. Track

[3]Recall that the MS consists of four sub-detectors, each using a different technology, split up into barrel and end-cap regions. Monitored Drift Tube chambers and Cathode Strip Chambers are used for precision measurements, while Resistive Plate Chambers and Thin Gap Chambers are used for triggering. Sub-detectors are grouped together in *stations* consisting of two *multi-layers*, such that most muons traverse three stations. Refer to Section 2.2.5 for more details.

reconstruction is initiated in all chambers intersecting these $d\eta \times d\phi \approx 0.4 \times 0.4$ regions, starting in precision chambers with trigger chambers nearby to provide associated "second-coordinate" hits. Pairs of hits in the same or adjacent stations are used to fit straight-line track segments (a good approximation at this scale), and they are kept provided they point roughly at the IP and are matched to a sufficient number of hits. Track candidates are seeded by the most robust segments and extrapolated to a neighboring MS station using full tracking in the toroidal magnetic field and multiple momentum hypotheses around an initial rough estimate derived from the seed segment. If a matching segment is found, the track is re-fit, and an improved momentum estimate is used to scan over a finer range of possible extrapolations to all other stations, re-fitting the track to any matched segments as encountered. For tracks matched to at least two segments, a final global fit is performed to the raw measurements, rather than the straight-line approximations, in order to select only "good" hits and also to include matter effects, e.g. multiple scattering, as additional parameters in the fit. Track candidates with reasonable χ^2 values are selected as reconstructed muons. Lastly, tracks are back-tracked toward the interaction point; interactions with the calorimeter and inner detector are taken into account, depending on the type and amount of material traversed. An illustration of stand-alone muon reconstruction is shown in Figure 4.3.

Combined muons are the combination of a full MS track with a compatible ID track [72]. Basically, the `STACO` algorithm is a statistical averaging of the individually-measured track parameters by means of their covariance matrices. The (5-component) vector of parameters for a combined track is given by

$$P = C \times (C_{\mathrm{MS}}^{-1} P_{\mathrm{MS}} + C_{\mathrm{ID}}^{-1} P_{\mathrm{ID}}), \tag{4.1}$$

where P_{MS} (P_{ID}) are the parameter vectors for the individual MS (ID) tracks, C_{MS}^{-1} (C_{ID}^{-1}) are their respective (5×5) covariance matrices, and C is the combined track covariance matrix:

$$C = (C_{\mathrm{MS}}^{-1} + C_{\mathrm{ID}}^{-1})^{-1}. \tag{4.2}$$

The χ^2 of an MS–ID track match, i.e. the difference between their parameter vectors weighted by C [120], can be written as

$$\chi^2_{\mathrm{match}} = (P_{\mathrm{MS}} - P_{\mathrm{ID}})^{\mathrm{T}} \, (C_{\mathrm{MS}} + C_{\mathrm{ID}})^{-1} \, (P_{\mathrm{MS}} - P_{\mathrm{ID}}). \tag{4.3}$$

This is calculated for all track combinations that roughly match in the (η, ϕ) plane at their points of closest approach to the beam line. If multiple combinations are possible, the pair giving the best χ^2_{match} is selected, and its constituent tracks are removed from consideration in subsequent combinations. This procedure continues until no valid combinations remain [72]. Combined muons have improved mo-

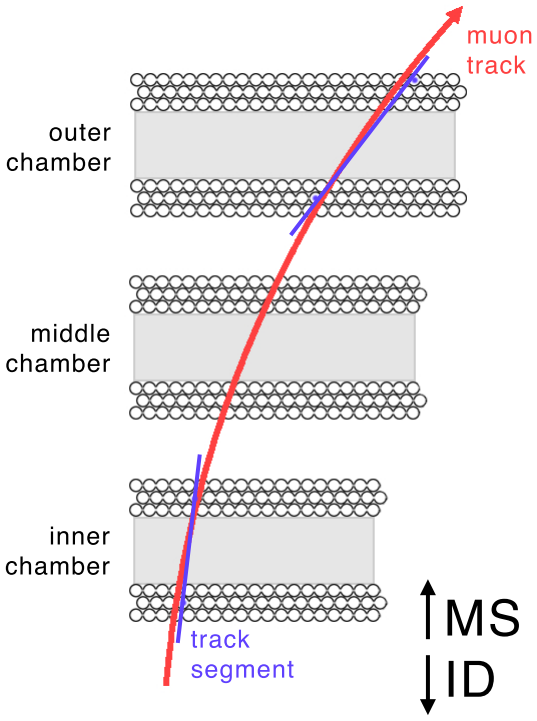

Figure 4.3: Cartoon illustration of stand-alone muon reconstruction in the muon spectrometer. Representative straight-line track segments are shown in purple, and the resulting global fit muon track is shown in red.

mentum resolution over a very wide range of values, with measurements in the ID dominating at low momenta and those in the MS dominating at high momenta.

4.4 Jets

Jets are collimated showers of energetic hadrons produced copiously in pp collisions; they characterize the hadronic final states of most physics analyses. A more precise definition, however, is ambiguous, because jets are *defined* by the algorithm used to find them and exist only in this context. In ATLAS, jets are reconstructed from topologically-related energy depositions in calorimeter cells, first merged into *clusters* and then into jets using, by default, the "anti-k_{T}" algorithm [128].

Recall that the ATLAS calorimeters are finely subdivided both laterally and longitudinally into individual cells, and particles passing through these cells deposit some fraction of their energy. Such "signal" depositions are measured on top of a random noise background arising primarily from readout electronics and pile-up

interactions.[4] The topological clustering algorithm [129] used in ATLAS groups neighboring clusters while suppressing noise in the following manner:

- All cells with a signal-to-noise ratio $S/N > 4$ are used to seed a *proto-cluster*
- In order of descending seed S/N, all cells neighboring the seed (or proto-cluster) with $S/N > 2$ are added iteratively to the proto-cluster; if a cell neighbors more than one proto-cluster, the proto-clusters are merged
- All neighboring cells with $|E| > 0$ are added to the most significant adjacent proto-cluster, and all resulting proto-clusters with $E_{\mathrm{T}} > 0$ are kept
- Proto-clusters are then split up by searching for local maxima with energy $E > 0.5$ GeV greater than any neighboring cell; they are used to seed exactly one new proto-cluster (without the possibility of further merging) composed of only those neighboring cells included in the initial round of cluster-making
- Cells bordering two proto-clusters are *shared* and assigned relative contributions to each depending on the proto-cluster energies and the distances of the cell to their centers
- The resulting new proto-clusters and any original proto-clusters lacking local maxima are sorted in order of E_{T} and re-classified as topological clusters

A topological cluster is defined as having energy equal to the sum of its constituent cells, a direction in (η, ϕ) given by the weighted averages of those cells, and zero mass [130]. An illustration of clustering is shown in Figure 4.4.

Clusters are taken as input to the anti-k_{T} algorithm, which is a particular implementation of a class of *sequential recombination* jet-finding algorithms [131]. First, two distances are defined:

$$d_{ij} = \min\left(k_{\mathrm{T}i}^{2p},\, k_{\mathrm{T}j}^{2p}\right) \frac{(\Delta R)_{ij}^2}{R_c^2} \tag{4.4}$$

$$d_{ib} = k_{\mathrm{T}i}^{2p}, \tag{4.5}$$

where $(\Delta R)_{ij}^2 = (\eta_i - \eta_j)^2 + (\phi_i - \phi_j)^2$ and k_{Ti}, η_i, and ϕ_i are the transverse momentum, pseudorapidity, and azimuthal angle of object i. R_c is the *characteristic radius* determining the final sizes of jets[5], and parameter p determines the relative power

[4] A calorimeter cell's signal is taken as the absolute value of the energy deposited in the cell, $|E|$, in the event. Energy attributed to noise in a cell is taken as the root-mean-square (RMS) of the energy deposited in randomly-triggered events.

[5] Conventional values in ATLAS are $R_c = 0.4$ or 0.6.

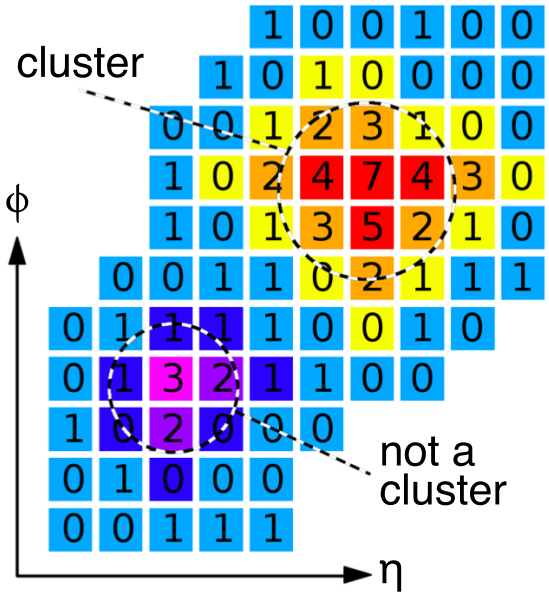

Figure 4.4: Cartoon illustration of a group of neighboring calorimeter cells that qualifies as a topological cluster and one that does not. Numbers represent the cells' S/N values. [82]

of the energy and geometrical scales. In this context, d_{ij} represents the distance between two objects, and d_{ib} represents the distance between the object and the beam. The algorithm proceeds as follows: Starting with the highest-p_{T} object ("proto-jet") i, the distances between it and all objects j as well as beam b are determined. If the smallest value is a d_{ij}, objects i and j are combined and the remaining distances are re-calculated; if the smallest value is d_{ib}, the object is considered a "complete" jet and excluded from iterations over the remaining objects i. This process repeats until no objects i remain.

The anti-k_{T} algorithm takes $p = -1$, whereas related clustering algorithms use $p = 0$ (Cambridge/Aachen) or $p = +1$ (k_{T}), which causes softer objects to merge with harder objects in order of their geometrical proximity. The jet boundaries are "resilient" to soft radiation, resulting in roughly conical jets that are *infrared safe*. For overlapping jets i and j, such that $R_c < \Delta R_{ij} < 2R_c$, the softer objects on their border are shared depending on relative transverse momenta and distances; hard objects with $\Delta R_{ij} < R_c$ are simply merged into one jet, ensuring that the algorithm is also collinear safe. An example of jets reconstructed with the anti-k_{T} algorithm is shown in Figure 4.5.

The topological clusters used to reconstruct calorimeter jets are initially measured at the electromagnetic (EM) scale, which correctly accounts for electron and

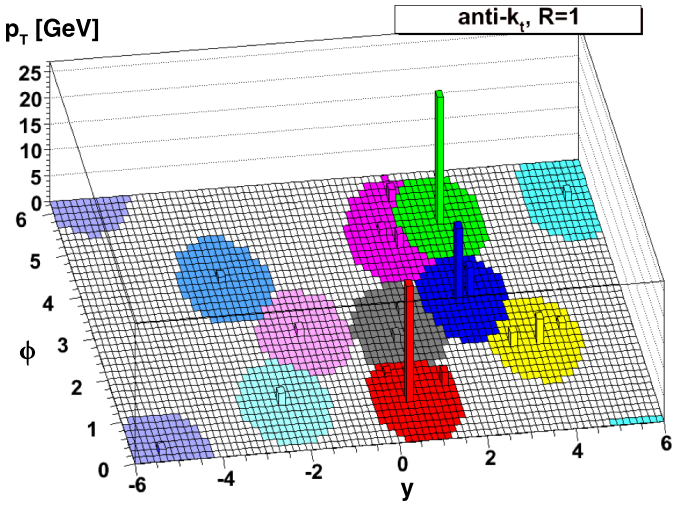

Figure 4.5: Jets reconstructed with the anti-k_{T} algorithm using $R_c = 1$ in a simulated event containing a few high-p_{T} clusters and many softer clusters distributed in rapidity y and azimuthal angle ϕ. Jet shapes are regular and nearly conical. [128]

photon showers [132] [130]; however, this scale systematically underestimates the energy of hadronic objects owing to calorimeter non-compensation, dead material, and energy "leakage." Consequently, reconstructed jets must be corrected, or *calibrated*, to the proper jet energy scale (JES). ATLAS uses a number of jet energy calibration schemes: a relatively simple one called EM+JES is used in the leptoquark analysis of Chapter 5. Calibration is accomplished in three steps:

- **Pile-up correction:** The average energy contributed by pile-up interactions is subtracted from the energy measured in the calorimeter using correction constants derived from minimum bias data; constants are given as a function of the number of reconstructed primary vertices, the bunch spacing of the beam, and the pseudo-rapidity of the jet

- **Jet origin correction:** The jet direction is corrected to point back to the primary hard-scattering vertex instead of the geometrical center of ATLAS, used as a reference in reconstruction; specifically, the topo-clusters' kinematics are re-calculated using the vector from the primary vertex to their respective centroids, and the jet's four-momentum is redefined as the vector sum of its constituent topo-clusters' four-momenta

- **Jet energy/direction correction:** The reconstructed jet energy and direction are corrected using constants obtained from comparisons of kinematic observables between specially-selected reconstructed and "truth" jets in MC

events; constants are given in terms of truth jet energy and calorimeter jet pseudo-rapidity; a further correction to the origin-corrected jet η is applied to compensate for poorly instrumented regions of the calorimeter

The result of this calibration brings the reconstructed jet energy to within about 2% of the value expected for hadronic jets. Systematic uncertainties on the JES calibration are discussed in detail in [130].

4.5 Electrons

Electron reconstruction within the acceptance of the ID ($|\eta| < 2.47$) begins by identifying energy deposits in the middle layer of the EM calorimeter and matching them to reconstructed tracks in the ID [120] [133]. First, seed clusters of longitudinal towers with total $E_{\mathrm{T}} > 2.5$ GeV are found using a *sliding window* [129] of size 3×5 in units of $\eta \times \phi = 0.025 \times 0.025$ (corresponding to the granularity of the sub-detector). Reconstructed ID tracks are then extrapolated to the middle layer of the calorimeter; if at least one track is matched in ΔR to a seed cluster, an electron candidate is defined. Next, the electron cluster is rebuilt using 3×7 (5×5) longitudinal towers of cells in the barrel (end-caps) centered on the initial seed. The electron energy is given by the cluster energy, i.e. the sum of the energy measured in the cluster, the estimated energy deposited in detector material in front of the EM calorimeter, and the estimated energy deposited outside the cluster (leakage) in both lateral and longitudinal directions. The electron direction in (η, ϕ) is given by the direction of the best-matched ID track at its vertex. A detailed description of electron identification criteria is given in [133].

4.6 Missing Transverse Energy

Owing to their exceedingly small interaction cross sections, neutrinos (as well as many hypothetical particles) easily escape the ATLAS detector *un*-detected, so their presence must be inferred from *missing transverse energy* in an event. Essentially, this is just conservation of momentum: the p_{T} in a proton-proton collision is zero both before and after the interaction, so any measured momentum imbalance is attributed to neutrinos. Note that mis-measurement of particle momenta and energy lost in inactive detector regions can also lead to apparent imbalances if not properly accounted for!

Reconstructing an event's missing transverse energy (variously written as missing transverse momentum, Missing E_{T}, MET, $E_{\mathrm{T}}^{\mathrm{miss}}$, $\not{E}_{\mathrm{T}}$, or $\not{p}_{\mathrm{T}}$) requires the reconstruction of all other physics objects in that event. The x- and y-components of

missing energy are each composed of two terms [134]:

$$E_{x(y)}^{\text{miss}} = E_{x(y)}^{\text{miss,calo}} + E_{x(y)}^{\text{miss},\mu}, \tag{4.6}$$

referred to as the calorimeter and muon terms, from which the magnitude and azimuthal angle are calculated as

$$E_{\text{T}}^{\text{miss}} = \sqrt{(E_x^{\text{miss}})^2 + (E_y^{\text{miss}})^2} \tag{4.7}$$

$$\phi^{\text{miss}} = \arctan(E_y^{\text{miss}}/E_x^{\text{miss}}). \tag{4.8}$$

The calorimeter term is defined as the negative sum of energies deposited in all calorimeter cells with $|\eta| < 4.5$, i.e.

$$E_x^{\text{miss,calo}} = -\sum_{i=1}^{N_{\text{cell}}} E_i \sin\theta_i \cos\phi_i \ , \ E_y^{\text{miss,calo}} = -\sum_{i=1}^{N_{\text{cell}}} E_i \sin\theta_i \sin\phi_i, \tag{4.9}$$

where E_i, θ_i, and ϕ_i are the energy, polar angle, and azimuthal angle of cell i. To suppress contributions from noise, only those cells associated with topological clusters (as described in Section 4.4) are included in the sum. Cells are calibrated according to the high-p_{T} reconstructed physics object to which they are exclusively associated, prioritized in the following order: electrons, photons, τ-leptons, jets, then muons. Topo-cluster cells not associated with any such physics objects are also included, with a global calibration applied.

The muon term is calculated as the negative sum of the momenta of muon tracks:

$$E_{x(y)}^{\text{miss},\mu} = -\sum_{\text{muons}} p_{x(y)}^{\mu}. \tag{4.10}$$

For $|\eta| < 2.5$, only MS tracks matched to ID tracks are used. In the case of isolated muons, the energy lost by the muon in the calorimeter to ionization is not added to the calorimeter term, so as not to double-count; in the case of non-isolated muons, the calorimeter-corrected p_{T}^{MS} is used in the muon term. For $2.5 < |\eta| < 2.7$, outside the ID acceptance, the transverse momenta of stand-alone MS tracks are used for both isolated and non-isolated muons.

Details of the object-based calibrations used in the `RefFinal` MET algorithm can be found in [134].

CHAPTER 5

A Leptoquark Search

> We are driven by the usual
> insatiable curiosity of the scientist,
> and our work is a delightful game.
>
> Murray Gell-Mann

This chapter presents a search for pair-produced, scalar, second-generation leptoquarks, where one leptoquark decays into a muon and a quark and the other decays into a muon neutrino and a quark: $pp \to LQ\overline{LQ} \to \mu\, c\, \overline{\nu}_\mu\, \bar{s}$, colloquially referred to as the $\mu\nu jj$ channel.[1] An additional but relatively small fraction of the total signal comes from events in which both LQs decay into a muon and a quark, but one of the muons fails reconstruction or selection.

The general analysis strategy is as follows. From appropriate data and simulated samples (Section 5.1), physics objects (Section 5.2) and then events (Section 5.4) are selected based on the topology expected of an LQ final state. Although this selection is highly efficient for signal events, the selected sample is overwhelmingly dominated by backgrounds, owing to their much larger production cross sections. Control regions are defined as orthogonal sub-sets of the selected event sample and are composed primarily of a single, major background (Section 5.5). They are

[1] A more consistent name would be $\mu \not{E}_{\mathrm{T}} jj$, which is the event signature one reconstructs in the detector; or $\mu\nu qq$, which represents all the particles coming directly from leptoquark decays. But the nickname stands!

used to validate the modeling of these backgrounds as well as provide a semi data-driven estimation of their yields. Finally, several strongly discriminating kinematic variables are combined into a simple joint log-likelihood ratio, used as the final discriminator between signal and background (Section 5.6).

5.1 Data and Monte Carlo Samples

5.1.1 Data

The data sample used in this analysis was collected by single muon triggers from the muon stream during periods B and D–H of the 2011 LHC run, as summarized in Table 5.1.

Period	Run Range	$\mathscr{L}_{\text{int}}$ [pb^{-1}]
B	177986 – 178109	11.4
D	179710 – 180481	154.1
E	180614 – 180776	42.4
F	182013 – 182519	122.7
G	182726 – 183462	464.2
H	183544 – 184169	240.4
TOTAL	177986 – 184169	1035.2

Table 5.1: The data sample used in this LQ_2 search, split into periods, with corresponding run numbers and integrated luminosities.

This sample amounts to a total integrated luminosity of $\mathscr{L}_{\text{int}} = 1035$ pb^{-1} recorded by the ATLAS detector for which data quality (DQ) requirements were satisfied. A good runs list[2] (GRL) is used to remove luminosity blocks or entire runs from data during which the detector or some sub-component was operating abnormally, thus rendering the data unsuitable for analysis. Specifically, the following requirements (DQ status flags green) are included in the GRL [135]:

- Data taken in 2011 LHC runs at $\sqrt{s} = 7$ TeV with the ATLAS detector included (`find run data11_7TeV.periodAllYear and partition ATLAS and db DATA`)
- ATLAS DQ working group evaluated and approved quality of the data, Level-1 Central Trigger working properly (`global_status`)

[2] `data11_7TeV.periodAllYear_DetStatus-v18-pro08-04_CoolRunQuery-00-03-98_Susy.xml`, generated by the ATLAS SUSY working group

- High-level trigger algorithms working properly, at reasonable efficiency, without timing, consistency, synchronization, or data problems (`trig_muo, trig_ele, trig_jet, trig_met_metcalo`)
- Solenoid and toroid magnet systems have stable, non-zero current (`atlsol, atltor`)
- All components of tracking system working properly (`cp_tracking, pix0, idvx`)
- All sub-detectors used in electron and jet reconstruction working properly in pseudorapidity ranges corresponding to barrel, crack[3], endcaps, and forward regions (`cp_eg_electron_barrel, cp_eg_electron_crack, cp_eg_electron_endcap, cp_eg_electron_forward, cp_jet_jetb, cp_jet_jetea, cp_jet_jetec, cp_jet_jetfa, cp_jet_jetfc`)
- All sub-detectors used in combined muon reconstruction algorithms working properly (`cp_mu_mstaco, cp_mu_mmuidcb`)
- All sub-detectors used in missing transverse energy reconstruction working properly, with all variables behaving as expected (`cp_met`)
- Good beam-spot data available, without issues (`idbs`)
- All luminosity and forward detectors working properly (`lumi`)

The (sometimes redundant) combination of these requirements ensures that the data are good and suitable for analysis.

5.1.2 Monte Carlo

Simulated event samples are used for most of the background estimates and all of the signal estimates. All samples are official ATLAS `MC10b` samples produced using the full GEANT4 simulation of the detector and reconstruction processing chain. As detailed in Section 3.1.5, a variety of software packages are available to simulate event generation, parton showering, and hadronization, with differing capabilities; the combinations giving the best results for each process were used for their simulation.

All nominal MC samples used in this analysis are shown in Table 5.2, which lists the corresponding physics process, cross section times branching ratio times filter efficiency ($\sigma \times \mathrm{BR} \times \varepsilon$), request ID number, and production tags.

[3] Poorly-instrumented region of the calorimeter, between barrel and end-caps. In terms of pseudorapidity, the crack region corresponds to $1.37 < |\eta| < 1.52$.

5.1 Data and Monte Carlo Samples

Process	$\sigma \times \mathrm{BR} \times \varepsilon$ [pb]	Request ID	Production Tags
$W \to \mu\nu$+0p	8288.1	107690	e600, s933, s946, r2302, r2300, p605
$W \to \mu\nu$+1p	1550.1	107691	e600, s933, s946, r2302, r2300, p605
$W \to \mu\nu$+2p	452.09	107692	e760, s933, s946, r2302, r2300, p605
$W \to \mu\nu$+3p	120.96	107693	e760, s933, s946, r2302, r2300, p605
$W \to \mu\nu$+4p	30.331	107694	e760, s933, s946, r2302, r2300, p605
$W \to \mu\nu$+5p	8.2722	107695	e760, s933, s946, r2302, r2300, p605
$W \to \tau\nu$+0p	8288.1	107700	e600, s933, s946, r2302, r2300, p605
$W \to \tau\nu$+1p	1550.1	107701	e600, s933, s946, r2302, r2300, p605
$W \to \tau\nu$+2p	452.09	107702	e760, s933, s946, r2302, r2300, p605
$W \to \tau\nu$+3p	120.96	107703	e760, s933, s946, r2302, r2300, p605
$W \to \tau\nu$+4p	30.331	107704	e760, s933, s946, r2302, r2300, p605
$W \to \tau\nu$+5p	8.2722	107705	e760, s933, s946, r2302, r2300, p605
$Z \to \mu\mu$+0p	830.12	107660	e737, s933, s946, r2302, r2300, p605
$Z \to \mu\mu$+1p	166.24	107661	e737, s933, s946, r2302, r2300, p605
$Z \to \mu\mu$+2p	50.282	107662	e737, s933, s946, r2302, r2300, p605
$Z \to \mu\mu$+3p	13.922	107663	e737, s933, s946, r2302, r2300, p605
$Z \to \mu\mu$+4p	3.6156	107664	e737, s933, s946, r2302, r2300, p605
$Z \to \mu\mu$+5p	0.94179	107665	e737, s933, s946, r2302, r2300, p605
$Z \to \tau\tau$+0p	830.12	107670	e737, s933, s946, r2302, r2300, p605
$Z \to \tau\tau$+1p	166.24	107671	e737, s933, s946, r2302, r2300, p605
$Z \to \tau\tau$+2p	50.282	107672	e737, s933, s946, r2302, r2300, p605
$Z \to \tau\tau$+3p	13.922	107673	e737, s933, s946, r2302, r2300, p605
$Z \to \tau\tau$+4p	3.6156	107674	e737, s933, s946, r2302, r2300, p605
$Z \to \tau\tau$+5p	0.94179	107675	e737, s933, s946, r2302, r2300, p605
WW	44.9×0.39720	105985	e598, s933, s946, r2302, r2300, p605
WZ	18.0×0.30851	105987	e598, s933, s946, r2302, r2300, p605
ZZ	5.96×0.21271	105986	e598, s933, s946, r2302, r2300, p605
$t\bar{t}$	164.5×0.54258	105200	e600, s933, s946, r2302, r2300, p605
single top (t)	$58.72 \times 0.\overline{11}$	108341	e598, s933, s946, r2302, r2300, p605
single top (s)	$3.937 \times 0.\overline{11}$	108344	e598, s933, s946, r2302, r2300, p605
single top (Wt)	13.10	108346	e598, s933, s946, r2302, r2300, p605
LQ 300 GeV $\mu\nu qq'$	1.21×0.5	119150	e760, s933, s946, r2302, r2300, p605
LQ 350 GeV	0.477×0.5	119151	e760, s933, s946, r2302, r2300, p605
LQ 400 GeV	0.206×0.5	119152	e760, s933, s946, r2302, r2300, p605
LQ 450 GeV	0.0949×0.5	119153	e760, s933, s946, r2302, r2300, p605
LQ 500 GeV	0.0462×0.5	119211	e760, s933, s946, r2302, r2300, p605
LQ 550 GeV	0.0235×0.5	119212	e760, s933, s946, r2302, r2300, p605
LQ 600 GeV	0.0124×0.5	119213	e760, s933, s946, r2302, r2300, p605
LQ 650 GeV	0.00676×0.5	119214	e760, s933, s946, r2302, r2300, p605
LQ 700 GeV	0.00377×0.5	119215	e760, s933, s946, r2302, r2300, p605
LQ 750 GeV	0.00214×0.5	119216	e760, s933, s946, r2302, r2300, p605
LQ 800 GeV	0.00124×0.5	119217	e760, s933, s946, r2302, r2300, p605
LQ 300 GeV $\mu\mu qq$	1.21	119132	e760, s933, s946, r2302, r2300, p605
LQ 350 GeV	0.477	119133	e760, s933, s946, r2302, r2300, p605
LQ 400 GeV	0.206	119134	e760, s933, s946, r2302, r2300, p605
LQ 450 GeV	0.0949	119135	e760, s933, s946, r2302, r2300, p605
LQ 500 GeV	0.0462	119178	e760, s933, s946, r2302, r2300, p605
LQ 550 GeV	0.0235	119179	e760, s933, s946, r2302, r2300, p605
LQ 600 GeV	0.0124	119180	e760, s933, s946, r2302, r2300, p605
LQ 650 GeV	0.00676	119181	e760, s933, s946, r2302, r2300, p605
LQ 700 GeV	0.00377	119182	e760, s933, s946, r2302, r2300, p605
LQ 750 GeV	0.00214	119183	e760, s933, s946, r2302, r2300, p605
LQ 800 GeV	0.00124	119184	e760, s933, s946, r2302, r2300, p605

Table 5.2: Simulated event samples used in this analysis.

All W+jets and Z+jets events (V+jets, collectively) were generated with ALPGEN using the CTEQ6L1 PDF, interfaced to HERWIG and JIMMY for showering and hadronization. Each source consists of five exclusive samples with zero to four additional partons (np, $n = 0,1,2,3,4$) and one inclusive sample with five or more additional partons (np, $n = 5$). The LO cross sections of each sample were computed by ALPGEN; their sum is scaled to the NNLO inclusive cross section while maintaining the relative LO fractions, where the inclusive NNLO cross sections times branching ratio to a single lepton species are $\sigma(W \to \ell\nu) = 10460 \pm 520$ pb and $\sigma(Z \to \ell\ell) = 1069 \pm 44$ pb [136]. Single- and pair-produced top quark samples were generated with MC@NLO using the CTEQ6.6 PDF, interfaced to JIMMY. Cross sections are scaled to their NLO values: $164.5^{+11.4}_{-15.7}$ pb for $t\bar{t}$, and 3.94 ± 0.39 pb, 58.7 ± 5.9 pb, and 13.1 ± 1.3 pb for the s-, t-, and Wt–channels, respectively [137] [138]. Diboson events were generated with HERWIG using a modified LO MRST PDF, with NLO cross sections of 44.9 ± 2.2 pb, 18.0 ± 1.3 pb, and 5.96 ± 0.28 pb for WW, WZ ($M_{\ell\ell} > 40$ GeV), and ZZ ($M_{\ell\ell} > 60$ GeV), respectively [136].

All leptoquark signal samples were generated with PYTHIA using the D6 tune and CTEQ6 PDF. LO cross sections are scaled to those listed in Table 5.2, as in [43]. The undetermined Yukawa coupling $\lambda_{\ell q}$ is set equal to $0.01 \times (4\pi\alpha_e)$, corresponding to a full width of 1 MeV and a negligible decay length (as discussed in Section 1.3); this follows the same convention used in previous results at the DØ, CDF, and CMS experiments.

5.2 Physics Object Selection

As an initial step in event selection, good *physics objects* in candidate events are first selected, according to the following criteria.

5.2.1 Muons

Muon candidates are reconstructed with the STACO algorithm, as described in Section 4.3. They must be associated with both an ID track and an MS track, statistically combined. Muon candidates must have a combined transverse momentum $p_{\mathrm{T}} > 30$ GeV and satisfy $|\eta| < 2.4$. They are also required to match to a trigger muon within $\Delta R < 0.1$. As recommended by the ATLAS Muon Combined Performance (MCP) group [139], a number of quality requirements are imposed on the inner detector track, taking into account the status of the detector at the time of collision:

- Number of pixel B-layer hits > 0, unless the extrapolated muon track passed through an un-instrumented or dead region

- Number of pixel hits + number of dead pixel sensors crossed > 1
- Number of SCT hits + number of dead SCT sensors crossed > 5
- Number of pixel holes + number of SCT holes < 2
- A successful TRT extension if the track is within the sub-detector's η acceptance, where an unsuccessful extension results when no TRT hits are associated to the track or too many associated hits are outliers. Specifically, let n_{hits} be the number of TRT hits, n_{outliers} be the number of TRT outliers, and $n \equiv n_{\text{hits}} + n_{\text{outliers}}$; then one of two conditions must be met:
  - for $|\eta| < 1.9$, $n > 5$ AND $n_{\text{outliers}} < 0.9n$
  - for $|\eta| > 1.9$, IF $n > 5$ THEN $n_{\text{outliers}} < 0.9n$

To reduce the number of muons arising from cosmic ray interactions, the transverse and longitudinal impact parameters must satisfy $|d_0| < 0.1$ mm and $|z_0| < 5$ mm, respectively. To reduce the number of (non-prompt) muons arising from secondary decays, a scaled isolation cut of $p_{\text{T}}^{\text{cone20}}/p_{\text{T}} > 0.2$ is applied, where $p_{\text{T}}^{\text{cone20}}$ is the sum of the transverse momenta of all tracks within $\Delta R < 0.2$ of the muon track, excluding the muon track itself.

5.2.2 Jets

Jet candidates are reconstructed with the `AntiKt4TopoEM` algorithm and calibrated to the EM+JES energy scale, as described in Section 4.4. They must have $p_{\text{T}} > 30$ GeV and $|\eta| < 2.8$. Jets reconstructed within $\Delta R < 0.4$ of a good muon or electron are rejected.

Mis-reconstructed, or "fake," jets arise from a number of sources, including hardware problems, beam conditions in the LHC, and cosmic ray showers [140], and should not be used for physics analysis; therefore, a set of "cleaning cuts" recommended by the Jet/EtMiss working group are imposed [141]. Jets corresponding to real energy deposits in poorly-instrumented regions of the calorimeter (so-called "ugly" jets) are selected by the following criteria:

- More than half of jet energy deposited in the gap scintillators between the Tile Calorimeter barrel and endcaps (`TileGap3` > 0.5) OR
- More than half of jet energy coming from cell-level corrections for depositions in known dead calorimeter cells (`BCH_CORR_CELL` > 0.5)

Additionally, in data only, jets reconstructed from out-of-time energy depositions (so-called "bad" jets) are identified with a series of cuts specialized for each of three main sources of such jets:

- **Noise bursts in the Hadronic End-cap**
  - more than half of jet energy deposited in the HEC (HECf > 0.5) AND more than half of jet energy deposited in HEC cells with a large difference between measured and predicted pulse shape ($|$HECQuality$| >$ 0.5) OR
  - large amount of negative energy ($|$NegativeE$| > 60$ GeV)
- **Coherent noise in the Electromagnetic Calorimeter**
  - large fraction of jet energy deposited in the EM calorimeter (EMfrac $>$ 0.95) AND majority of jet energy deposited in LAr cells with a large difference between measured and predicted pulse shape ($|$LArQuality$| >$ 0.8) AND central pseudorapidity ($|\eta| < 2.8$)
- **Cosmics and other non-collision backgrounds**
  - large jet time with respect to event time ($|$Timing$| > 25$ ns) OR
  - small fraction of jet energy deposited in the EM calorimeter (EMfrac $<$ 0.05) AND small fraction of jet energy associated to tracks from charged particles (chf < 0.05) AND central pseudorapidity ($|\eta| < 2.0$) OR
  - small fraction of jet energy deposited in the EM calorimeter (EMfrac $<$ 0.05) AND non-central pseudorapidity ($|\eta| \geq 2.0$) OR
  - almost all jet energy deposited in a single calorimeter layer (fracSamplingMax $>$ 0.99) AND central pseudorapidity $|\eta| < 2.0$

Kinematic cuts for ugly and bad jets are loosened: $p_{\mathrm{T}} > 20$ GeV and $|\eta| < 4.5$. In both MC and data, events containing any bad jets are vetoed (see Section 5.4), and in data only, ugly jets are discarded.

5.2.3 Missing Transverse Energy

The missing transverse energy in an event is reconstructed using the RefFinal algorithm, as described in Section 4.6. In events with one or more bad jets, significant mis-measurement of MET may occur; for this reason, such events are vetoed.

5.2.4 Electrons (Veto)

A relatively loose set of requirements is applied to electron candidates, as this selection is used for an event veto (see Section 5.4). Electrons must have author $= 1$ or 3 (standard reconstruction) and pass the official Medium selection defined by the

e/gamma working group [142]. Electron clusters must satisfy $E_{\mathrm{T}} \equiv E_{\mathrm{cluster}}/\cosh(\eta_{\mathrm{track}}) > 20$ GeV and $|\eta| < 2.47$, excluding the range $1.37 < |\eta| < 1.52$ corresponding to the crack between the EM calorimeter's barrel and end-caps, where energy mis-measurement is more likely.

A scaled isolation requirement of $E_{\mathrm{T}}^{\mathrm{cone20}}/E_{\mathrm{T}} < 0.1$ is imposed, where $E_{\mathrm{T}}^{\mathrm{cone20}}$ is the sum of the transverse energy of all calorimeter topological cells within a cone of $\Delta R < 0.2$ around the electron, excluding those contributing to the electron's E_{T}. This reduces the number of non-prompt electrons as well as jets mis-identified as electrons.

Electrons must also pass standard object quality requirements [143].

5.3 MC Corrections

A number of corrections are specially applied to simulated samples in order to make them consistent with the data.

5.3.1 Muon-related

Correction scale factors (SFs) are applied to simulated events in order to account for differences with the data in trigger and muon identification efficiencies. These SFs were derived by the MCP working group from a tag-and-probe study of Z boson events [144]; they are η- and ϕ-dependent for events with a muon reconstructed in the barrel ($|\eta| < 1.05$) and p_{T}-dependent otherwise, as shown in Figure 5.1. SFs are generally $\sim$1.0, with larger localized deviations.

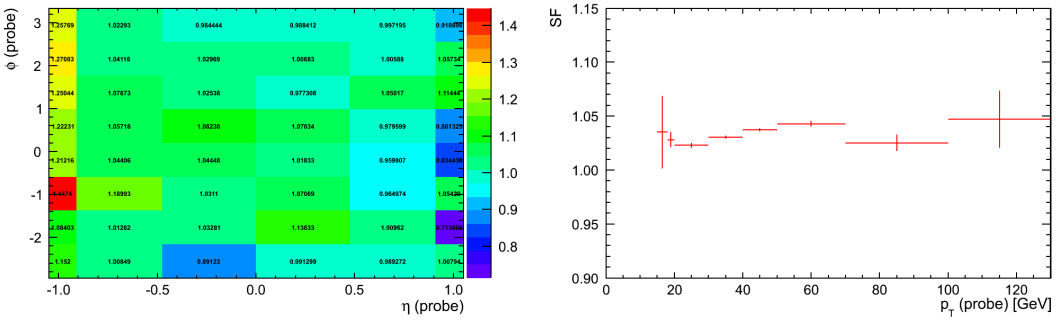

(a) (b)

Figure 5.1: Trigger efficiency scale factors applied to simulated events given (a) muons with $|\eta| < 1.05$ and (b) muons with $1.05 < |\eta| < 2.4$, as derived by MCP.

The muon momentum resolution in simulated samples is slightly better than that measured in data; therefore, a correction is applied directly to the muon p_{T} in

simulated events such that the resulting p_{T} distribution is *smeared*. Smearing parameterizations were determined by MCP by comparing the reconstructed Z boson mass distribution in selected events for data and MC. They were provided in an official software package [145].

5.3.2 Pile-up

All `MC10b` samples were generated with additional pile-up interactions overlaid, as described in Section 3.2; however, the simulation necessarily relied on a best *estimate* of future LHC beam conditions. Since the average number of pile-up interactions $<\mu>$ distribution in MC does not exactly match that seen in the analysis-specific dataset[4], simulated events must be re-weighted such that the MC and data distributions agree. The $<\mu>$ observed in data and that simulated in each background sample, both before and after re-weighting, are shown in Figure 5.2.

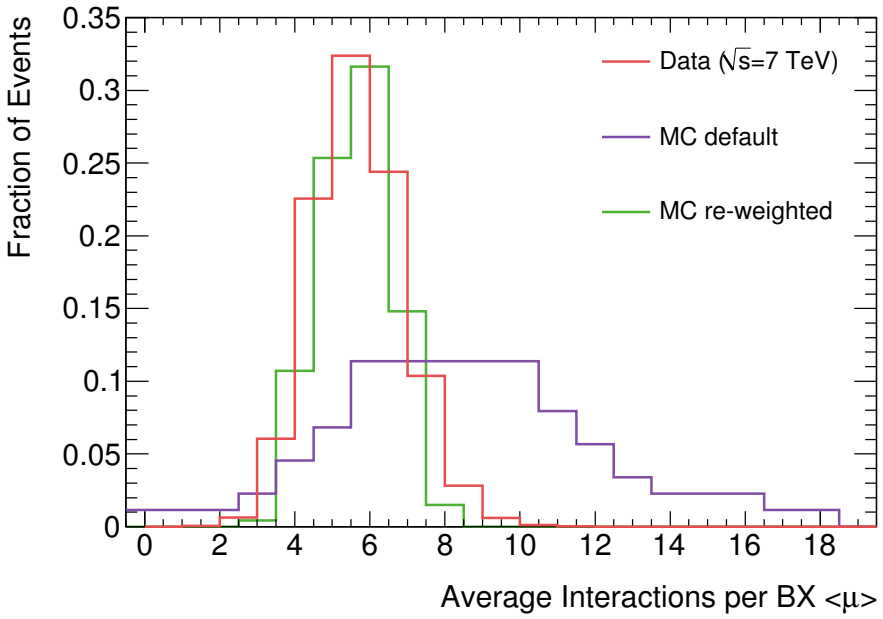

Figure 5.2: Normalized distributions of the average number of interactions per bunch crossing $<\mu>$ observed in data and simulated in `MC10b` samples, used as inputs to the official pile-up re-weighting package, as well as the resulting re-weighted MC distribution. Data has been re-binned to facilitate comparison.

[4]The data sample described in Section 5.1 with a trigger requirement applied.

5.3.3 LAr Dead Region

Early in the 2011 LHC run, an electronics failure of a crate controller for the LAr barrel calorimeter resulted in a significant dead region ($0.0 < \eta < 1.4$ and $-0.8 < \phi < -0.6$) in two longitudinal layers — the so-called "LAr hole." This failure affected periods E–H of the data, or 84% of the dataset used in this analysis. Within this region, electron reconstruction was reduced and jet energy resolution was severely degraded, with implications for MET.[5]

To effectively remove the problem from the data and simulate the effect in MC, a simple veto is applied to all affected data events and a randomly-selected 84% of MC events:

- Good electrons falling in the vicinity of the LAr hole are vetoed
- Events with a good jet falling in the vicinity of the LAr hole are vetoed, where jets in data have had their transverse momenta increased by a correction factor $(1 - \texttt{BCH\_CORR\_CELL})/(1 - \texttt{BCH\_CORR\_JET})$ to approximately account for the energy lost to the hole [140]

5.4 Selected Event Sample

The basic event signature for signal events in this analysis is a single high-p_{T} muon, large missing transverse energy, and at least two high-p_{T} jets. A sample of events is selected by criteria matching this signature.

5.4.1 Additional Variable Definitions

In the course of this leptoquark search, several kinematic variables are used in addition to the common p_{T}, E_{T}, η, and ϕ. For clarity, they are defined here.

Three variables are event quantities, larger for events with massive particles such as leptoquarks:

- $L_{\mathrm{T}} \equiv p_{\mathrm{T}}^{\mu} + \not{E}_{\mathrm{T}}$, the scalar sum of the muon transverse momentum and the missing transverse energy in an event
- $H_{\mathrm{T}} \equiv p_{\mathrm{T}}^{j1} + p_{\mathrm{T}}^{j2}$, the scalar sum of the transverse momenta of the first- and second-leading jets in an event
- $S_{\mathrm{T}} \equiv L_{\mathrm{T}} + H_{\mathrm{T}} = p_{\mathrm{T}}^{\mu} + \not{E}_{\mathrm{T}} + p_{\mathrm{T}}^{j1} + p_{\mathrm{T}}^{j2}$

[5] An additional edge of 0.1 units in η or ϕ bordering the dead region was found to be affected, so an expanded region of $-0.1 < \eta < 1.5$ and $-0.9 < \phi < -0.5$ is used in the veto.

Three other variables are related to mass reconstruction, the first of which is more general:

- $M_{\mathrm{T}}(\mu, \not{E}_{\mathrm{T}}) = \sqrt{2p_{\mathrm{T}}^{\mu}\not{E}_{\mathrm{T}}(1-\cos\Delta\phi)}$, the transverse mass of a muon–MET combination in an event

The other two variables combine the muon, leading two jets, and missing transverse energy in an event into the muon–jet and MET–jet pairs that best reconstruct the two leptoquarks expected in a signal event. To determine the best pairing, all possible combinations are considered, and the muon–jet invariant mass and MET–jet transverse mass with the smallest absolute difference in their values correspond to the best pairing, since both LQs in the event have the same mass. This algorithm determines the correct pairs in 92% of signal events, according to truth information in the signal MC samples. Thus, the final two kinematic variables are

- $M_{\mathrm{T}}(LQ)$, the transverse mass of the MET and first- or second-leading jet combination in an event closest in value to that of the invariant mass of the muon and the other leading jet
- $M(LQ)$, the invariant mass of the muon and first- or second-leading jet not assigned to $M_{\mathrm{T}}(LQ)$

These distributions are shown for selected events in Figure 5.7.

5.4.2 Selection Criteria

A series of selection requirements are used to define a selected sample of events characterized by high LQ signal efficiency but still dominated by backgrounds, particularly W+jets and $t\bar{t}$, because of their much larger cross sections. Events must fulfill the following:

- Data quality requirements in GRL described in Section 5.1 (data only)
- Fires `EF_mu18_MG` OR `EF_mu40_MSonly_barrel` trigger
- At least one primary vertex with at least three associated Inner Detector tracks; in the case of multiple primary vertices, the track requirement is applied only to the one with the highest sum p_{T}^2
- Exactly one good muon and zero good electrons, as defined in Section 5.2
- $\not{E}_{\mathrm{T}} > 30$ GeV
- At least two good jets, as defined in Section 5.2

- $M_{\mathrm{T}}(\not{E}_{\mathrm{T}}, \mu) > 40$ GeV
- Zero bad jets, and zero good jets falling within the vicinity of the LAr hole, as discussed in Section 5.3

5.4.3 Background Estimation

Multi-jet

Multi-jet (MJ) events are those in which reconstructed muons come from in-flight hadron decays, heavy flavor decays, or very energetic jets "punching through" the hadronic calorimeter into the muon spectrometer. Although such events are usually produced at much lower energies than typical signal events, the production cross section is enormous, resulting in "tails" that can extend well into a signal-rich region. The MJ background is poorly modeled by simulated samples, so data-driven methods for background estimation are employed instead. Shapes and yields are determined individually for each step of the analysis.

MJ background shape is taken from the data sample selected at a given stage of the analysis, except with a reversed muon transverse impact parameter requirement. Predicted contributions from electroweak (EWK) backgrounds (discussed later in this section) are subtracted off. An alternative MJ sample is instead derived from data events with a reversed scaled muon track isolation requirement, and is used to calculate the systematic uncertainty on the shape — see Chapter 6.

Normalization is determined with two separate methods:

- **ABCD**
  Single cuts on two variables that cleanly separate MJ events from all other backgrounds are used to divide a selected sample of events into four statistically-independent regions labeled A, B, C, and D. An illustration of this is shown in Figure 5.3. Two pairs of variables are used: $\not{E}_{\mathrm{T}}$ and muon $|d_0|$, and $\not{E}_{\mathrm{T}}$ and muon $p_{\mathrm{T}}^{\mathrm{cone20}}/p_{\mathrm{T}}$; the difference in their results is used to assign a systematic uncertainty to the MJ estimate.

  MJ shape is taken from region C. The predicted yield for MJ events in the signal region D is derived based on the assumption that the ratios of yields between paired regions are the same, which is only valid if the two variables are uncorrelated.[6] The MJ contribution in the signal region is therefore found by scaling the shape in region C to the predicted normalization in region D:

$$N_{\mathrm{D}} = \frac{N_{\mathrm{A}} N_{\mathrm{C}}}{N_{\mathrm{B}}}, \quad h_{\mathrm{D}} = h_{\mathrm{C}} \cdot \left(\frac{N_{\mathrm{D}}}{N_{\mathrm{C}}} \right), \tag{5.1}$$

[6] Correlations for both variable pairs were found to be on the order of 10%.

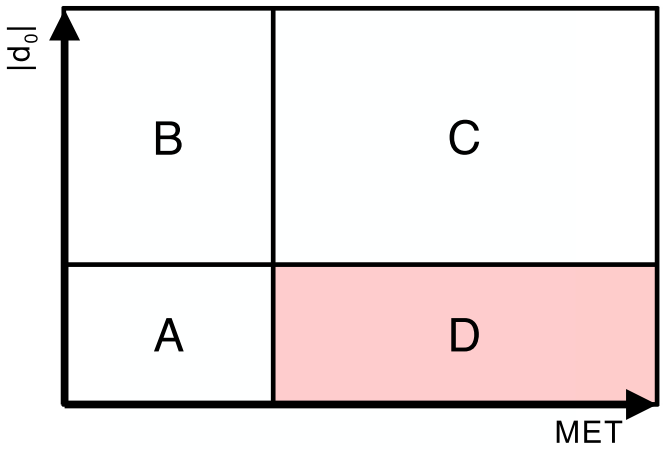

Figure 5.3: Cartoon illustration of the ABCD method regions, with signal region D filled in for emphasis

where N_A, N_B, and N_C are the data yields in regions A, B, and C minus the number of EWK background events predicted by MC, and h_C is the shape of the data distribution in region C. The selected event yields in each region (and the definitions thereof) are shown in Table 5.3.

Region	Definition	Data Yield	EWK Bkg Yield	N_i, i = A, B, C
A	$\not{E}_T < 30$ GeV and $\lvert d_0\rvert < 0.1$ mm	58275 ± 241	36139 ± 121	22136 ± 270
B	$\not{E}_T < 30$ GeV and $\lvert d_0\rvert > 0.1$ mm	5842 ± 76	41 ± 2	5801 ± 76
C	$\not{E}_T > 30$ GeV and $\lvert d_0\rvert > 0.1$ mm	2543 ± 50	167 ± 10	2376 ± 51
D	$\not{E}_T > 30$ GeV and $\lvert d_0\rvert < 0.1$ mm	97090 ± 312	—	—
A	$\not{E}_T < 30$ GeV and $p_T^{\text{cone20}}/p_T < 0.2$	58126 ± 241	36051 ± 121	22075 ± 270
B	$\not{E}_T < 30$ GeV and $p_T^{\text{cone20}}/p_T > 0.2$	75436 ± 275	144 ± 4	75292 ± 275
C	$\not{E}_T > 30$ GeV and $p_T^{\text{cone20}}/p_T > 0.2$	30983 ± 176	649 ± 8	30334 ± 176
D	$\not{E}_T > 30$ GeV and $p_T^{\text{cone20}}/p_T < 0.2$	96857 ± 311	—	—

Table 5.3: The ABCD method regions, total data yield, predicted EWK background yield, and corrected data yield using $\not{E}_T$ and $|d_0|$ (top) or $\not{E}_T$ and p_T^{cone20}/p_T (bottom) to define the regions.

- **Fitting**
  The missing transverse energy distribution[7] observed in data is fit to the sum

[7] In principle any kinematic variable distribution with a different shape for MJ and other background events *could* work, but MET offers the clearest difference between the two, and thus the best possibility for fitting.

of the MJ background and all other backgrounds. Data and total background normalizations are constrained to be equal, with MJ fraction $\varepsilon_{\mathrm{MJ}}$ (the fraction of all background events coming from MJ events) as a floating fit parameter whose nominal value is that which minimizes the log-likelihood. This is a *binned* fit: for each bin i in the MET distribution, the probability that the "MJ + other" background yield (given a set value for $\varepsilon_{\mathrm{MJ}}$) fluctuates more extremely than the data is calculated, and the negative logarithm of these probabilities are summed:

$$LL = \sum_i -\log\left(\int_{N_i^{\mathrm{data}}}^{\infty} \mathrm{Poisson}(N_i^{\mathrm{bkg}})\right), \tag{5.2}$$

assuming the observed number of data events in a bin is larger than the predicted background events. For the case $N_i^{\mathrm{data}} < N_i^{\mathrm{bkg}}$, the Poisson distribution is integrated from zero to N_i^{data}.

The fitting procedure is done for both MJ samples, i.e. reversed $|d_0|$ and reversed $p_{\mathrm{T}}^{\mathrm{cone20}}/p_{\mathrm{T}}$ requirements. The MET distributions and resulting log-likelihood fits for MJ fraction are shown in Figure 5.4, for both MJ samples.

Since no *a priori* reason was found to favor one MJ normalization method over the other, and since a given method's normalizations for both variable pairs were statistically consistent with each other, it was decided that a final normalization result at each step of the analysis would be computed from an overall average, according to the following procedure:

1. For each method (ABCD, Fitting), take the weighted mean of the two normalizations resulting from the ($\not\!\!E_{\mathrm{T}}$, $|d_0|$) and ($\not\!\!E_{\mathrm{T}}$, $p_{\mathrm{T}}^{\mathrm{cone20}}/p_{\mathrm{T}}$) samples

2. Take the simple mean of the two results from the previous step

Uncertainties on the final normalizations are both statistical and systematic: the statistical uncertainties are propagated from the initial normalization values, the systematic from the averaging of two independent methods. The results of this combination procedure are summarized in Table 5.4.

Electroweak

In this analysis, several processes contribute to the SM "electroweak" background.[8] The dominant component is the production of a W boson in association with one

[8] Technically, quantum chromodynamics plays an important role in the production of these backgrounds, e.g. in the formation of jets from quark and gluon showers; however, they are referred to as "electroweak" backgrounds because of the presence of W and Z bosons in the decay chain, and as a way to distinguish them from multi-jet backgrounds, which are dominantly QCD processes.

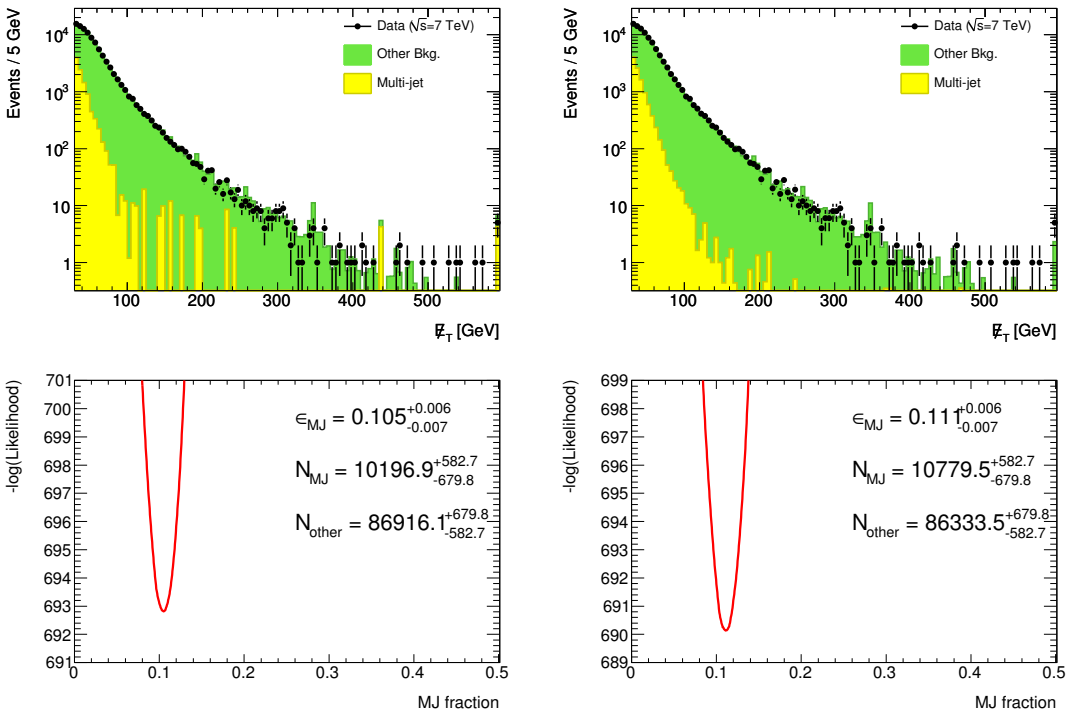

(a) (b)

Figure 5.4: MET distribution and resulting likelihood fit for MJ fraction using a (a) reversed-$|d_0|$ sample and a (b) reversed-p_T^{cone20}/p_T sample. The best fit value (ε_{MJ}) and resulting yield for MJ and all other backgrounds (N_{MJ} and N_{other}, respectively) are drawn on the corresponding lower plot.

or more jets (W+jets), where the W decays leptonically into a muon and a muon neutrino. The next largest contribution comes from pair-produced top quark events ($t\bar{t}$) with semi-leptonic decays. Both have the same $\mu\nu jj$ final state as the $LQ\overline{LQ}$ signal under study. Lesser contributors are Z+jets and diboson events.

At each step of the analysis, shape and yield estimates for all EWK backgrounds (as well as signal) are determined from simulated samples, as listed in Table 5.2, after correction scale factors are applied. The expected number of events n is given by the product of the integrated luminosity of the data sample $\mathscr{L}_{int}$, the predicted cross section σ, and the event selection efficiency ε. An additional, data-assisted normalization scale factor S is derived for each of the dominant backgrounds *only*, i.e. W+2 jets (exclusive), W+3 jets (inclusive), and $t\bar{t}$, using yields in dedicated

Method	Sample	MJ Yield
ABCD	$\lvert d_0 \rvert$	9067 ± 255
	$p_{\mathrm{T}}^{\mathrm{cone20}}/p_{\mathrm{T}}$	8894 ± 125
	Combined	8927 ± 112
Fitting	$\lvert d_0 \rvert$	10197^{+583}_{-680}
	$p_{\mathrm{T}}^{\mathrm{cone20}}/p_{\mathrm{T}}$	10780^{+583}_{-680}
	Combined	10452 ± 442
Combined	–	$\mathbf{9690 \pm 763}$

Table 5.4: MJ background yields using two methods and two samples, and their combinations. The final yield is emphasized in bold.

control regions (CRs) to be defined in Section 5.5. Thus, for a given background j,

$$n_j = \mathscr{L}_{\mathrm{int}} \times \sigma_j \times \varepsilon_j \; (\times S^j). \tag{5.3}$$

W+jets and $t\bar{t}$ normalization corrections

Constraints on the W+jets and $t\bar{t}$ backgrounds can be determined from the yields in their respective CRs. Although one background dominates in each, the regions still have significant cross-region contamination of other backgrounds, so their *correlations* must be taken into account when determining the scale factors.

The predicted background yield in a particular CR i is defined as

$$N_i^{\mathrm{bkg}} \equiv \left(S^W \times N_i^W\right) + \left(S^{t\bar{t}} \times N_i^{t\bar{t}}\right) + N_i^{\mathrm{other}}, \tag{5.4}$$

where S^W and $S^{t\bar{t}}$ are the unknown scale factors for the W+jets and $t\bar{t}$ backgrounds, respectively; N_i^W and $N_i^{t\bar{t}}$ are the predicted yields for the V+jets and $t\bar{t}$ backgrounds in CR i, respectively; and N_i^{other} is the predicted yield for all other backgrounds in CR i. These yields include all MC corrections discussed in Section 5.3.

The unknown SFs are determined by a simultaneous χ^2 fit to the observed and predicted yields in all three control regions:

$$\chi^2\left(S^W, S^{t\bar{t}}\right) = \sum_{\mathrm{CR}} \left[\frac{N_i^{\mathrm{data}} - N_i^{\mathrm{bkg}}}{\sigma_i^{\mathrm{data}}}\right]^2, \tag{5.5}$$

where N_i^{data} is the yield observed in data in CR i and $\sigma_i = \sqrt{N_i^{\text{data}}}$ is the statistical uncertainty on the data yield. The SFs giving the best fit (i.e. minimizing χ^2) are given in Table 5.5.

Background	Scale Factor	Correlation	$\chi^2/ndof$
W+jets	0.911 ± 0.005	-0.29	3.8 / 1
$t\bar{t}$	1.092 ± 0.25		

Table 5.5: Normalization scale factors for the dominant backgrounds, used to scale their yields as predicted by simulation in the selected event sample.

It's worth noting that both normalization scale factors deviate significantly from unity. The cause appears to be mis-modeling of pile-up in the MC samples: data/MC disagreement is most prominent in the low-p_{T} regime where pile-up is a larger effect; SFs get closer to unity when a jet vertex fraction[9] (JVF) requirement is added, which removes a large fraction of pile-up events; and SFs also approach unity when kinematic variable thresholds (e.g. S_{T}, jet p_{T}) are increased. For reference, Table 5.6 shows V+jets and $t\bar{t}$ scale factors derived with an additional cut of $|JVF| > 0.75$ applied and with a slightly higher jet threshold of $p_{\text{T}}^j > 40$ GeV.

Case	W+jets SF	$t\bar{t}$ SF
nominal	0.911 ± 0.005	1.092 ± 0.25
$\|JVF\| > 0.75$	1.063 ± 0.026	1.066 ± 0.025
$p_{\text{T}}^j > 40$GeV	0.942 ± 0.009	1.064 ± 0.027

Table 5.6: Normalization scale factors for the dominant backgrounds, with the nominal event selection and two alternate selections that specifically reduce pile-up.

5.4.4 Yields and Distributions

The yields for each source of background, signal, and that observed in data are shown at various steps of the selection in Table 5.7. Predicted and observed yields are in good agreement after all selection criteria have been applied.

Distributions of basic kinematic variables for muons and jets are shown in Figure 5.5; variables of and related to missing transverse energy, Figure 5.6; additional variables defined in Section 5.4.1, Figure 5.7.

[9] Defined as the fraction of a jet's transverse momentum coming from matched tracks contributed

Source	Event Yields					
	Good Event	Good Muon	Electron Veto	$\not{E}_{\mathrm{T}} > 30$ GeV	$M_{\mathrm{T}} > 40$ GeV	≥ 2 Jets & LAr
$W \to \mu\nu$+jets	4813558 ± 5191	2941147 ± 4728	2940269 ± 4728	2263506 ± 4451	2240546 ± 4448	69727 ± 284
$W \to \tau\nu$+jets	216635 ± 1523	39110 ± 622	39086 ± 621	23153 ± 468	18256 ± 437	1128 ± 29
$Z \to \mu\mu$+jets	708387 ± 19	246139 ± 17	245556 ± 17	85289 ± 11	80281 ± 11	3047.2 ± 1.8
$Z \to \tau\tau$+jets	51079.8 ± 9.0	12221.4 ± 4.5	11835.8 ± 4.4	3719.5 ± 2.3	1934.1 ± 1.6	198.46 ± 0.49
$t\bar{t}$	29492.43 ± 0.12	18361.88 ± 0.10	16846.55 ± 0.10	13697.69 ± 0.09	11291.69 ± 0.08	9789.99 ± 0.08
single top	7329.90 ± 0.37	4724.35 ± 0.37	4589.53 ± 0.37	3524.48 ± 0.35	3107.41 ± 0.34	1789.76 ± 0.26
diboson	8409.46 ± 0.13	5223.84 ± 0.11	4873.93 ± 0.11	3353.42 ± 0.09	3056.49 ± 0.09	1018.24 ± 0.05
multi-jet	—	—	—	—	—	9690 ± 255
Total Bkg.	—	—	—	—	—	96389 ± 382
Data	25081066	4449509	4445152	2768410	2675104	97113
$LQ(300)$, $\mu\nu qq'$	459.32 ± 0.06	429.14 ± 0.06	428.67 ± 0.06	426.18 ± 0.07	387.34 ± 0.07	345.11 ± 0.07
$LQ(350)$	181.4 ± 0.0	170.4 ± 0.0	170.1 ± 0.0	170.91 ± 0.01	159.13 ± 0.01	142.79 ± 0.01
$LQ(400)$	78.9 ± 0.0	73.9 ± 0.0	73.7 ± 0.0	74.5 ± 0.0	69.8 ± 0.0	62.9 ± 0.0
$LQ(450)$	36.0 ± 0.0	33.8 ± 0.0	33.7 ± 0.0	33.9 ± 0.0	31.9 ± 0.0	29.1 ± 0.0
$LQ(500)$	17.6 ± 0.0	16.4 ± 0.0	16.4 ± 0.0	16.5 ± 0.0	15.6 ± 0.0	14.0 ± 0.0
$LQ(550)$	8.9 ± 0.0	8.3 ± 0.0	8.3 ± 0.0	8.3 ± 0.0	7.9 ± 0.0	7.2 ± 0.0
$LQ(600)$	4.7 ± 0.0	4.4 ± 0.0	4.4 ± 0.0	4.5 ± 0.0	4.3 ± 0.0	3.9 ± 0.0
$LQ(650)$	2.6 ± 0.0	2.4 ± 0.0	2.4 ± 0.0	2.4 ± 0.0	2.3 ± 0.0	2.1 ± 0.0
$LQ(300)$, $\mu\mu qq$	1163.33 ± 0.14	222.86 ± 0.21	222.61 ± 0.21	157.37 ± 0.18	142.21 ± 0.18	127.87 ± 0.17
$LQ(350)$	458.34 ± 0.02	81.32 ± 0.03	81.14 ± 0.03	61.75 ± 0.03	55.85 ± 0.03	50.52 ± 0.03
$LQ(400)$	198.5 ± 0.0	35.4 ± 0.0	35.3 ± 0.0	26.1 ± 0.0	24.1 ± 0.0	22.2 ± 0.0
$LQ(450)$	91.0 ± 0.0	15.6 ± 0.0	15.6 ± 0.0	13.2 ± 0.0	11.9 ± 0.0	10.8 ± 0.0
$LQ(500)$	44.4 ± 0.0	7.7 ± 0.0	7.7 ± 0.0	6.3 ± 0.0	5.8 ± 0.0	5.3 ± 0.0
$LQ(550)$	22.6 ± 0.0	3.9 ± 0.0	3.9 ± 0.0	3.3 ± 0.0	3.1 ± 0.0	2.8 ± 0.0
$LQ(600)$	11.9 ± 0.0	2.1 ± 0.0	2.1 ± 0.0	1.8 ± 0.0	1.7 ± 0.0	1.6 ± 0.0
$LQ(650)$	6.5 ± 0.0	1.1 ± 0.0	1.1 ± 0.0	0.97 ± 0.00	0.92 ± 0.00	0.84 ± 0.00

Table 5.7: Predicted and observed event yields at each step of event selection. Note that the total background and data yields can only be compared at the end of the cut flow, since the MJ background is not estimated in previous steps. All uncertainties are statistical only (excluding the MJ background). All correction and data-assisted scale factors have been applied.

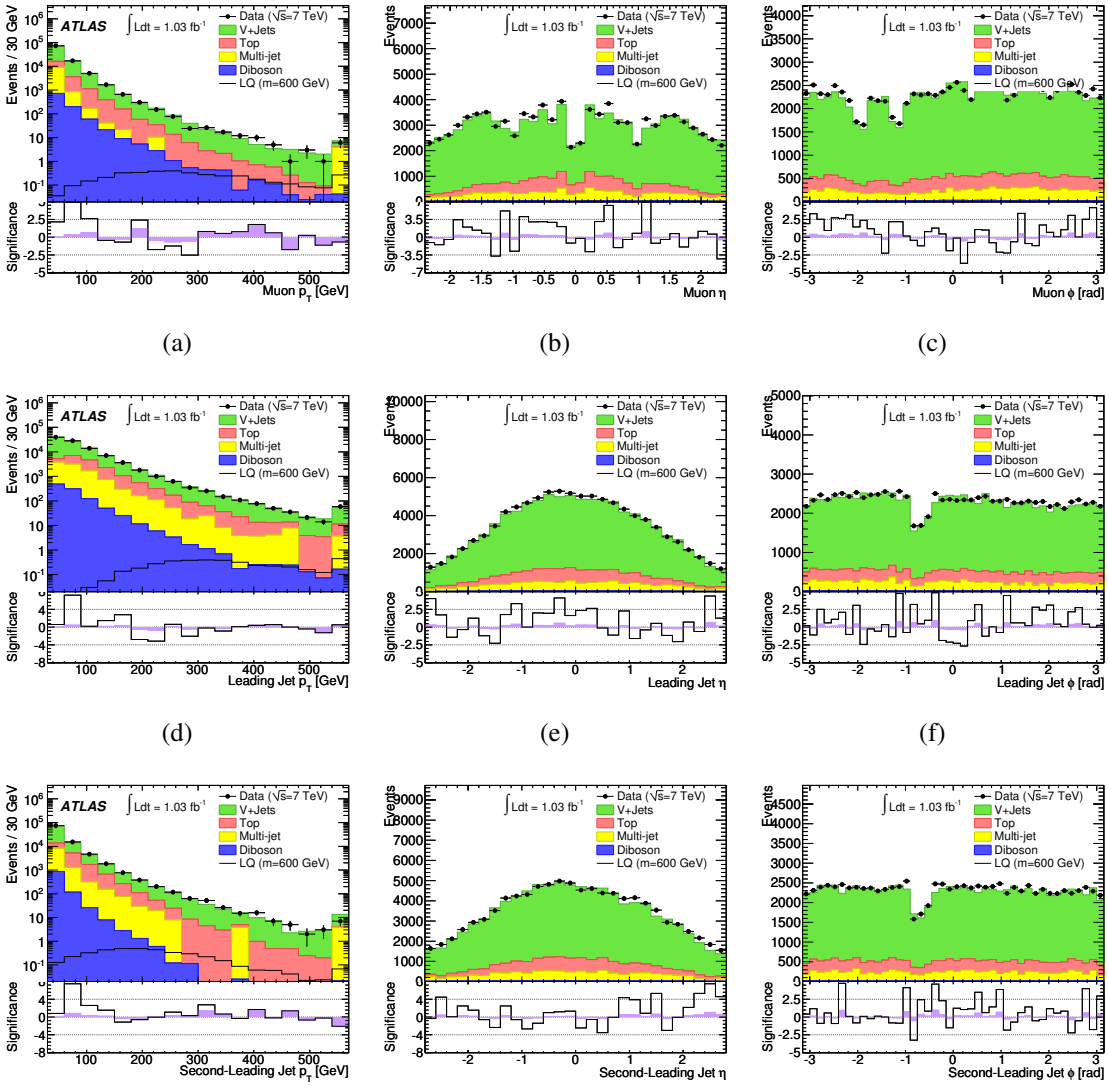

(a) (b) (c)

(d) (e) (f)

(g) (h) (i)

Figure 5.5: Distributions taken from the selected event sample: (a) muon p_{T}, (b) η, and (c) ϕ; (d) leading jet p_{T}, (e) η, and (f) ϕ; (g) second-leading jet p_{T}, (h) η, and (i) ϕ.

5.4 Selected Event Sample

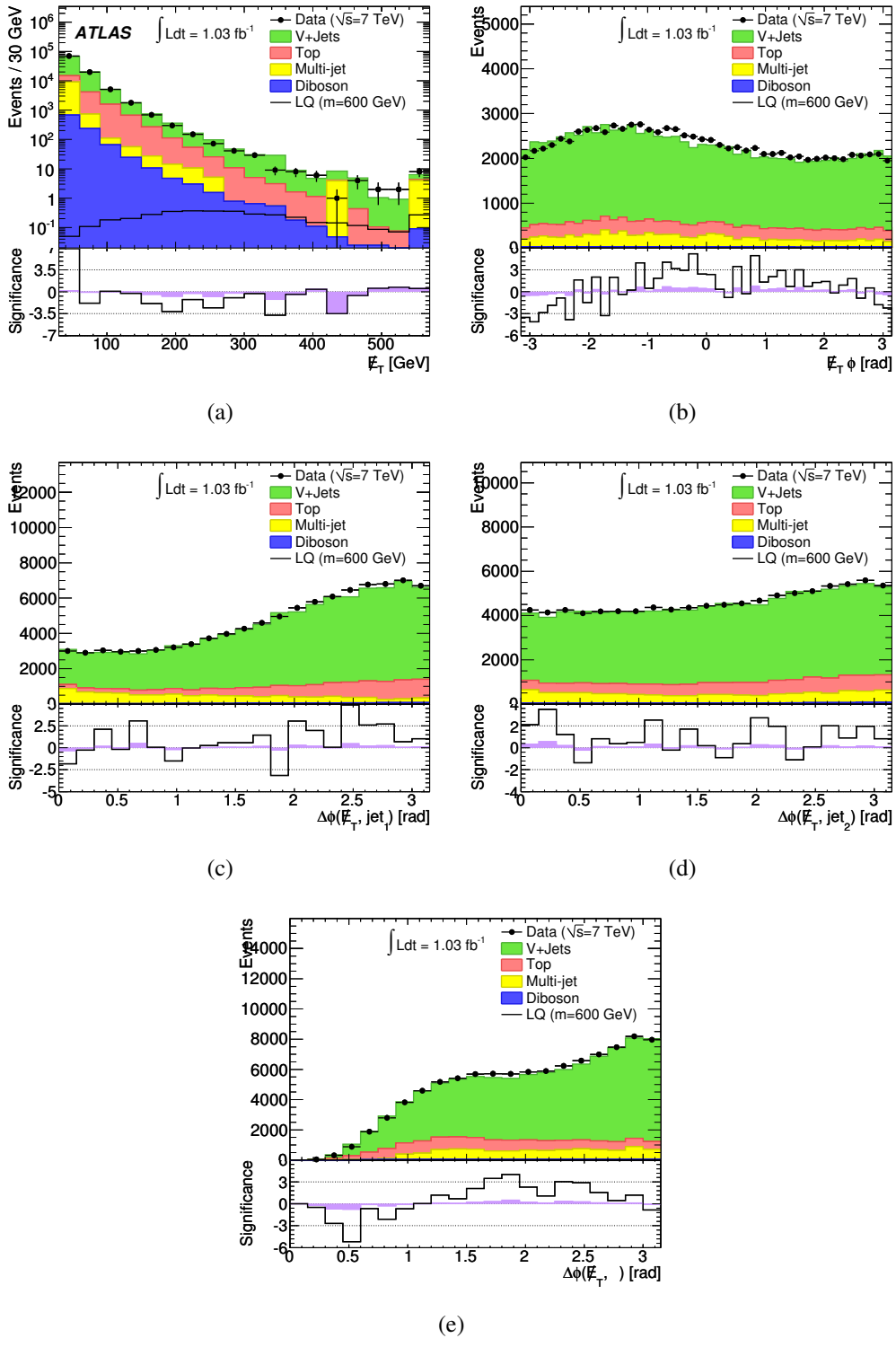

Figure 5.6: Distributions taken from the selected event sample: (a) missing transverse energy, (b) missing transverse energy ϕ, and the difference in ϕ between $\not{E}_{\mathrm{T}}$ and (c) the leading jet, (d) second-leading jet, and (e) muon.

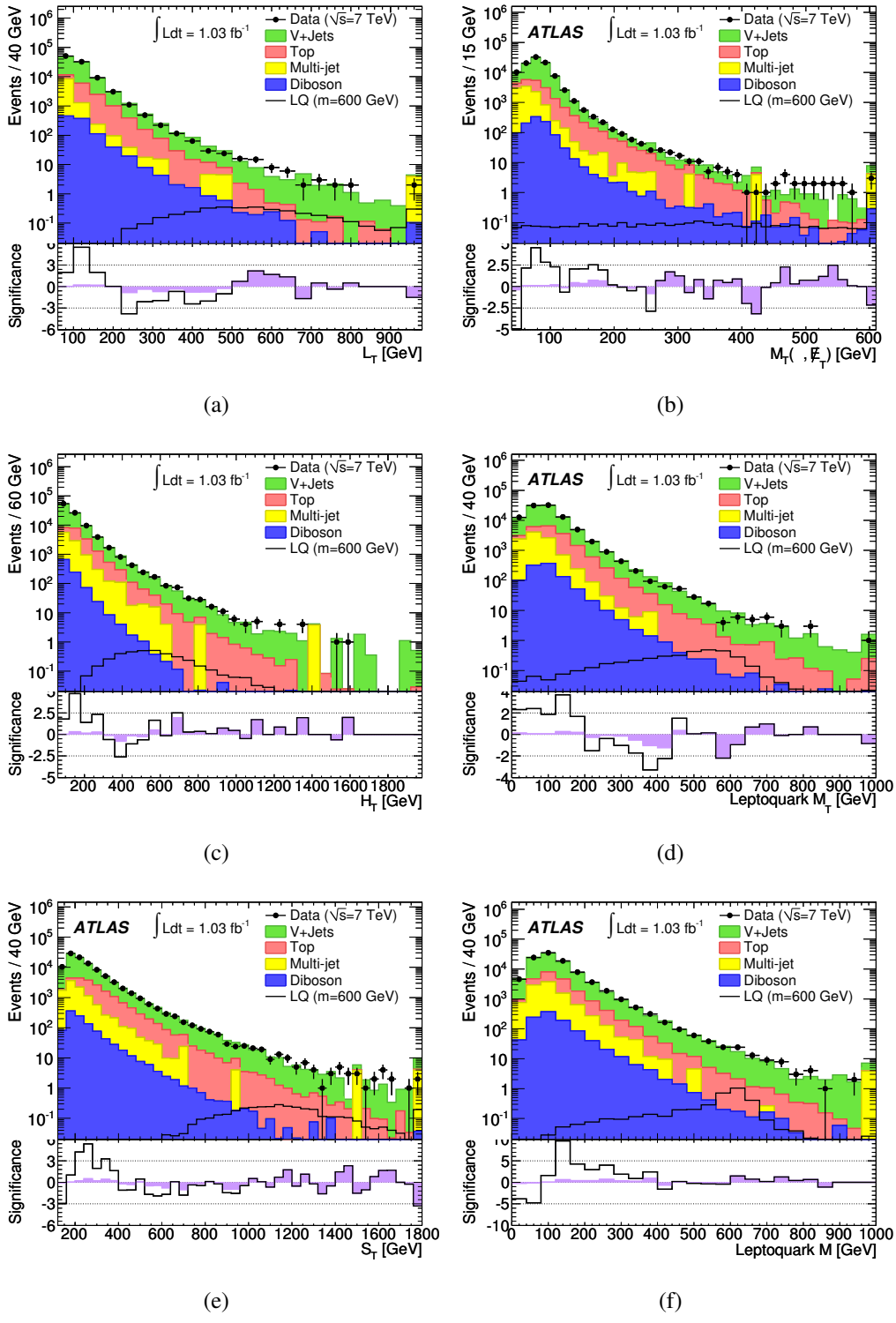

Figure 5.7: Distributions taken from the selected event sample: (a) L_{T}, (b) $M_{\mathrm{T}}(\mu, \not{E}_{\mathrm{T}})$, (c) H_{T}, (d) $M_{\mathrm{T}}(LQ)$, (e) S_{T}, and (f) $M(LQ)$, as defined in Section 5.4.1.

5.5 Control Regions

Three control regions are selected as orthogonal sub-sets of the baseline selected event sample (defined in Section 5.4.2), one for each of the dominant backgrounds: W+jets (split by jet multiplicity) and $t\bar{t}$. The CRs are used to verify the MC modeling of these backgrounds as well as derive data-assisted correction scale factors to their stated cross sections (defined in Section 5.4.3). Selection criteria are chosen in order to minimize LQ signal contamination and maximize the contribution of the primary background with respect to all others by exploiting differences in their kinematics. These differences are described qualitatively here; refer to Figures 5.11–5.12 for visual confirmation of the distinct kinematics involved in W+jets, $t\bar{t}$, and LQ events.

5.5.1 W+jets CR

In W+jets events, the muon and neutrino come from the decay of a single W boson, so their transverse mass is constrained by the W mass; in contrast, the muon and neutrino in signal events come from the decays of separate, very massive leptoquarks. Consequently, the $M_{\mathrm{T}}(\not{E}_{\mathrm{T}}, \mu)$ variable is an excellent discriminator between the two. An upper bound on an event's S_{T} is used to further reduce the number of signal events, since this value tends to be larger in events with more massive particles such as LQs and top quarks. The selection criteria are as follows:

- passes baseline event selection
- $M_{\mathrm{T}}(\mu, \not{E}_{\mathrm{T}}) < 120$ GeV
- $S_{\mathrm{T}} < 225$ GeV
- Number of jets N_{jets}
  - W+2 jets CR: $N_{\mathrm{jets}} = 2$
  - W+3 jets CR: $N_{\mathrm{jets}} \geq 3$

Note that two CRs are defined: an exclusive 2-jet sample, and an inclusive 3-or-more jet sample. The former is the largest single background in this analysis; the latter is used as a check on possible mis-modeling of jet multiplicity.

by the primary vertex out of the total transverse matched-track momentum. For jets coming from the primary vertex, $|JVF| \to 1$; for jets coming from pile-up interactions, $|JVF| \to 0$. [146]

Event Selection		
good detector status (data-only)		
fires muon trigger		
at least one primary vertex with at least three associated tracks		
exactly one good muon		
exactly zero good electrons (veto)		
$\not{E}_{\mathrm{T}} > 30$ GeV		
at least two good jets		
$M_{\mathrm{T}}(\mu, \not{E}_{\mathrm{T}}) > 40$ GeV		
zero bad jets or jets falling in the LAr hole (veto)		
W+2 jet CR	W+3 jet CR	$t\bar{t}$ CR
$M_{\mathrm{T}}(\mu, \not{E}_{\mathrm{T}}) < 120$ GeV		
$S_{\mathrm{T}} < 225$ GeV		$p_{\mathrm{T}}^{\mathrm{jet1}}$ ($p_{\mathrm{T}}^{\mathrm{jet2}}$) > 50 (40) GeV
$N_{\mathrm{jets}} = 2$	$N_{\mathrm{jets}} \geq 3$	$N_{\mathrm{jets}} \geq 4$

Table 5.8: Summary of selection criteria for the baseline selected event sample and three control regions.

5.5.2 $t\bar{t}$ CR

The other major background is $t\bar{t}$ events with semi-leptonic decays. As with W+jets events, an upper cut on the transverse mass of the muon and MET is used to select for W decays. These events tend to have many jets, and owing to the top quark's relatively large mass, the jets tend to have higher transverse momenta than those in W+jets events. The selection criteria are as follows:

- passes baseline event selection
- $M_{\mathrm{T}}(\mu, \not{E}_{\mathrm{T}}) < 120$ GeV
- leading jet $p_{\mathrm{T}} > 50$ GeV
- second-leading jet $p_{\mathrm{T}} > 40$ GeV
- $N_{\mathrm{jets}} \geq 4$

5.5.3 Yields and Distributions

For convenience, a summary of the various event selections used in this analysis are shown in Table 5.8. Yields for background and signal as well as those observed in data for each of the three control regions are summarized in Table 5.9. Predicted and observed yields are in good agreement.

Relevant kinematic distributions are shown in Figures 5.8, 5.9, and 5.10 for the $W+2$ jets, $W+3$ jets, and $t\bar{t}$ control regions, respectively.

5.6 Log-likelihood Ratio Discriminant

From the selected event sample, a set of four kinematic variables (defined in Section 5.4.1) are combined into a joint likelihood, to be used as the final discriminant in this analysis:

- $M_{\mathrm{T}}(\mu, \not{E}_{\mathrm{T}})$
- $M_{\mathrm{T}}(LQ)$
- $M(LQ)$
- S_{T}

These variables are chosen for their *individual* signal-background discriminating power.[10] Shape comparisons of these and several other variables for W+jets, $t\bar{t}$, and LQ ($m_{\mathrm{LQ}} = 600$ GeV) events are shown in Figures 5.11–5.12. The number of combined variables is kept small, for simplicity.

The distributions are normalized to unity and taken as probability distribution functions, one for the total background and one for a given signal. Then, on an event-by-event basis, a background (signal) likelihood L is calculated as the product of probabilities P for a background (signal) event to have the variable values observed in that event:

$$L_B \equiv \prod_{i=1}^{4} P_B^i(x_j) \tag{5.6}$$

$$L_S\,(m_{\mathrm{LQ}}) \equiv \prod_{i=1}^{4} P_S^i(x_j), \tag{5.7}$$

where x_j is the value of the j-th variable in a sample. The signal likelihood L_S is calculated separately for each LQ mass point, i.e. m_{LQ} between 300 and 800 GeV in 50-GeV increments, resulting in a mass-dependent optimization of the final result.

[10] This was studied in detail in [147].

Source	CR Yields		
	W+2 jet	W+3 jet	$t\bar{t}$
$W \to \mu\nu$+jets	36051 ± 249	5507 ± 84	2501 ± 25
$W \to \tau\nu$+jets	473 ± 22	74.32 ± 0.49	61.08 ± 0.36
$Z \to \mu\mu$+jets	1593.2 ± 1.4	250.25 ± 0.47	119.26 ± 0.32
$Z \to \tau\tau$+jets	90.53 ± 0.32	25.08 ± 0.18	15.30 ± 0.14
$t\bar{t}$	516.72 ± 0.02	955.16 ± 0.03	3742.17 ± 0.05
single top	477.99 ± 0.16	153.63 ± 0.07	178.92 ± 0.06
Diboson	501.38 ± 0.04	98.58 ± 0.02	33.5 ± 0.0
Multijet	5402 ± 185	1236 ± 90	620 ± 77
Total Bkg.	45105 ± 310	8301 ± 124	7271 ± 81
Data	45213	8125	7303
$LQ(300)$, $\mu\nu qq'$	0.20 ± 0.00	0.15 ± 0.00	20.21 ± 0.03
$LQ(350)$	0.04 ± 0.00	0.00 ± 0.00	5.3 ± 0.0
$LQ(400)$	—	—	2.4 ± 0.0
$LQ(450)$	—	—	0.95 ± 0.00
$LQ(500)$	—	—	0.52 ± 0.00
$LQ(550)$	—	—	0.20 ± 0.00
$LQ(600)$	—	—	0.12 ± 0.00
$LQ(650)$	—	—	0.06 ± 0.00
$LQ(700)$	—	—	0.04 ± 0.00
$LQ(300)$, $\mu\mu qq$	—	0.20 ± 0.01	7.53 ± 0.04
$LQ(350)$	0.08 ± 0.00	—	2.56 ± 0.00
$LQ(400)$	—	—	1.0 ± 0.0
$LQ(450)$	—	—	0.50 ± 0.00
$LQ(500)$	—	—	0.19 ± 0.00
$LQ(550)$	—	—	0.11 ± 0.00
$LQ(600)$	—	—	0.06 ± 0.00
$LQ(650)$	—	—	0.03 ± 0.00
$LQ(700)$	—	—	0.01 ± 0.00

Table 5.9: Predicted and observed yields in three control regions. Uncertainties are statistical only. All data-derived scale factors are applied.

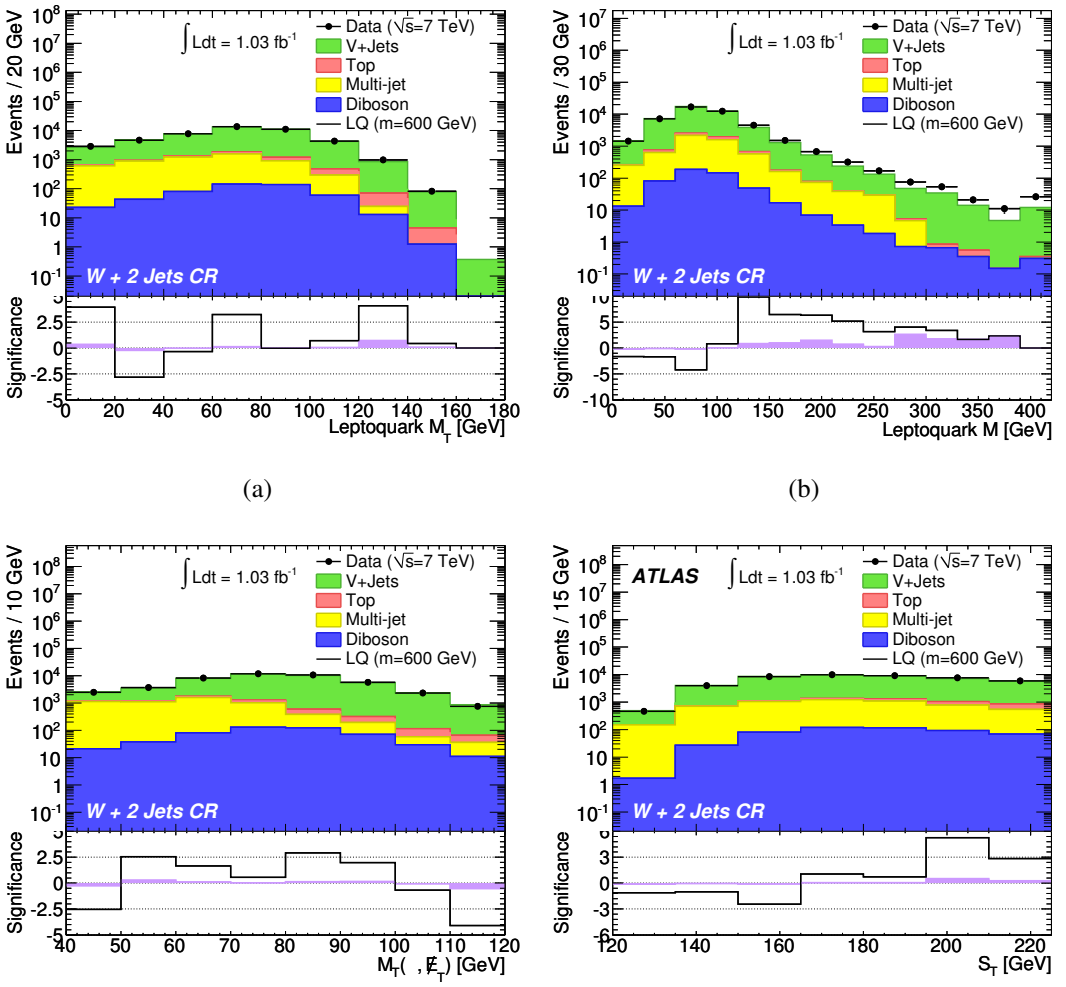

(a) (b)

(c) (d)

Figure 5.8: Distributions taken from the $W + 2$ jets control region: (a) leptoquark transverse mass, (b) leptoquark invariant mass, (c) muon-$\not{E}_{\mathrm{T}}$ transverse mass, and (d) the scalar sum of muon p_{T}, $\not{E}_{\mathrm{T}}$, and p_{T} of the first two leading jets.

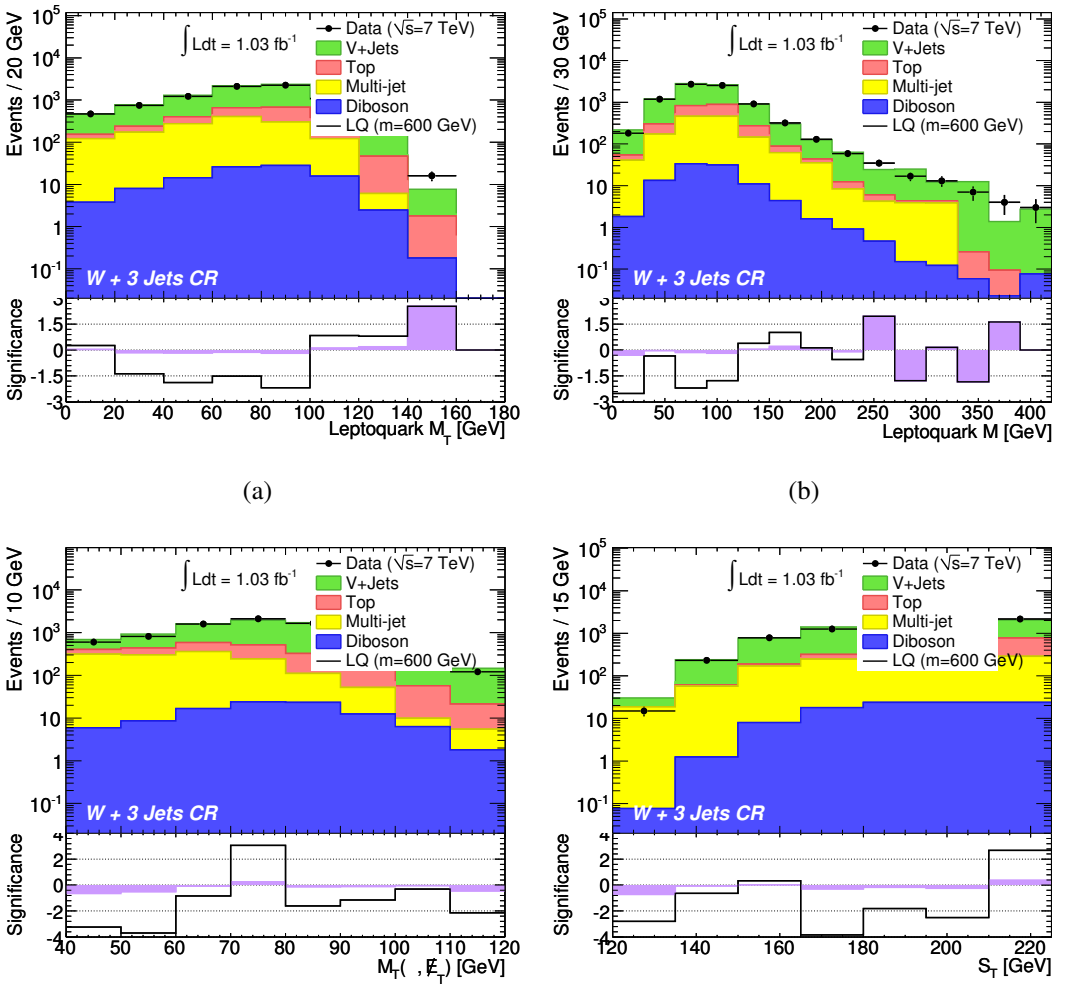

(a) (b)

(c) (d)

Figure 5.9: Distributions taken from the $W + 3$ jets control region: (a) leptoquark transverse mass, (b) leptoquark invariant mass, (c) muon-$\not{E}_{\mathrm{T}}$ transverse mass, and (d) the scalar sum of muon p_{T}, $\not{E}_{\mathrm{T}}$, and p_{T} of the first two leading jets.

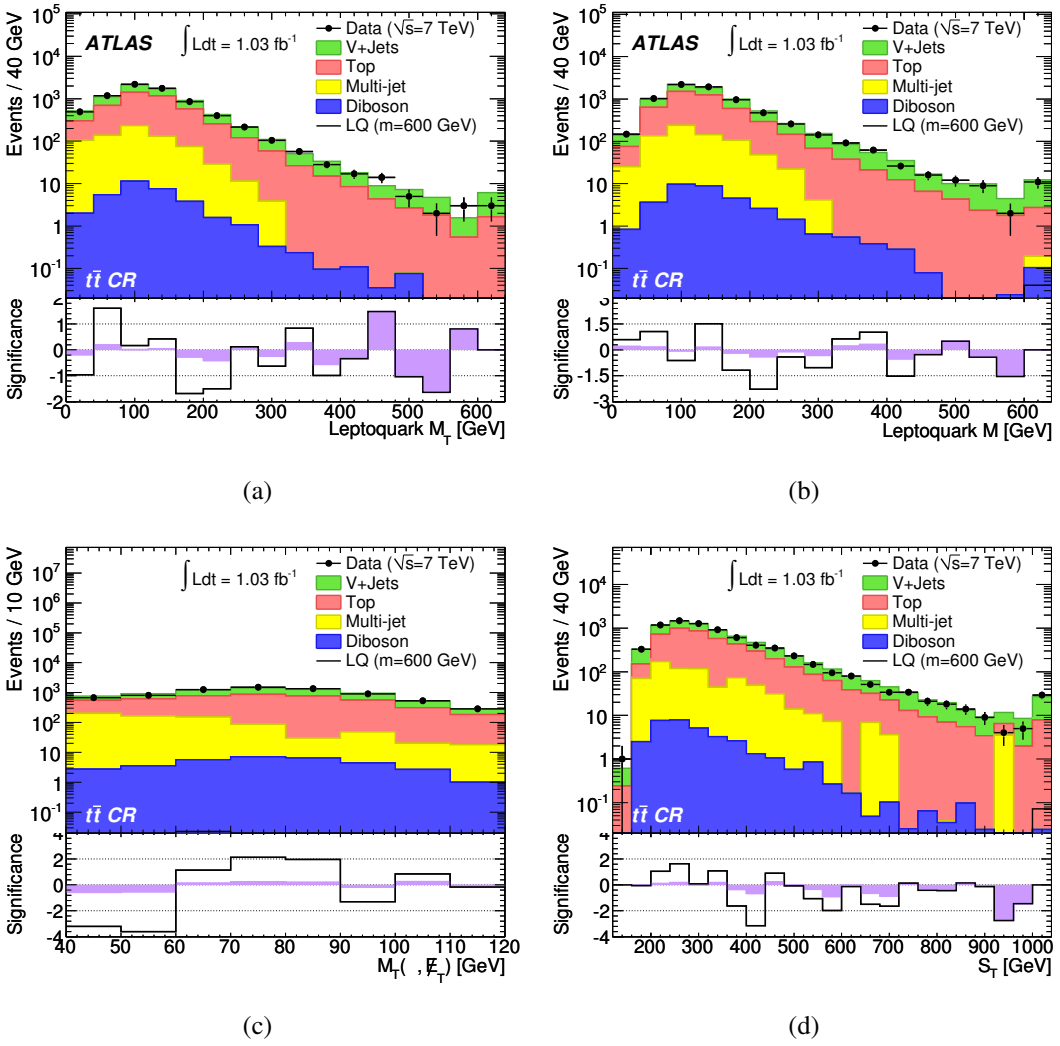

Figure 5.10: Distributions taken from the $t\bar{t}$ control region: (a) leptoquark transverse mass, (b) leptoquark invariant mass, (c) muon-$\not\!\!E_{\mathrm{T}}$ transverse mass, and (d) the scalar sum of muon p_{T}, $\not\!\!E_{\mathrm{T}}$, and p_{T} of the first two leading jets.

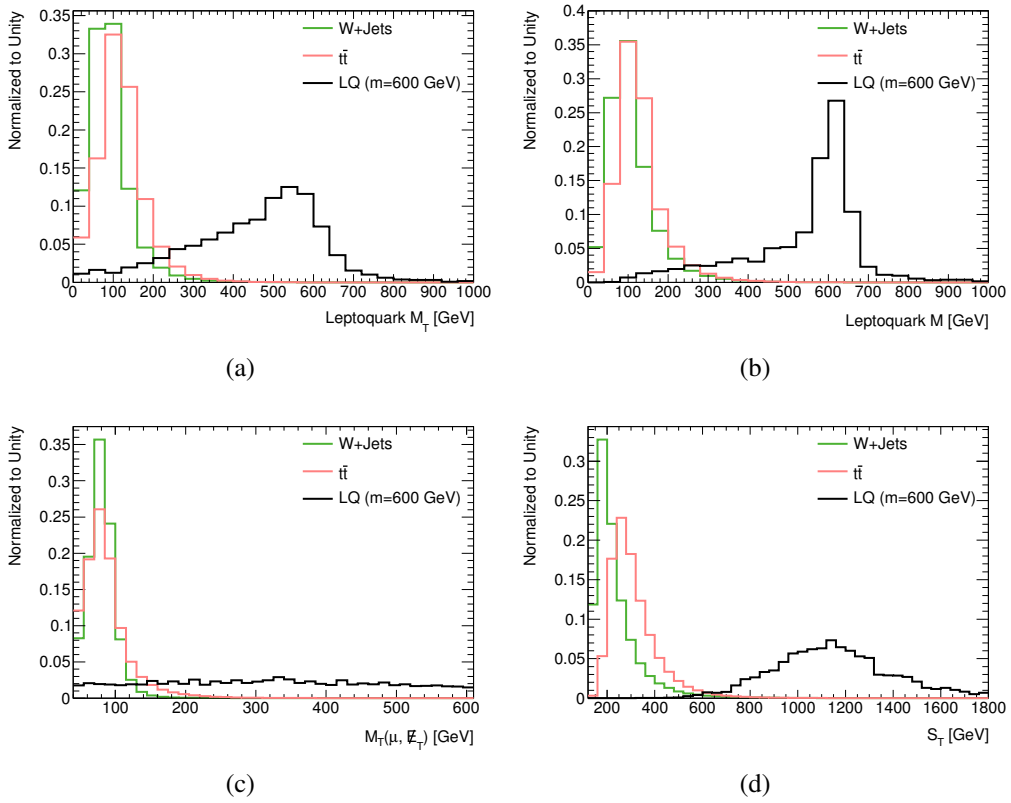

Figure 5.11: *Normalized* distributions taken from the selected event sample, for W+jets, $t\bar{t}$, and LQ signal events: (a) $M_{\mathrm{T}}(LQ)$, (b) $M(LQ)$, (c) $M_{\mathrm{T}}(\mu, \not{E}_{\mathrm{T}})$, and (d) S_{T}. These four variables are combined into a joint likelihood.

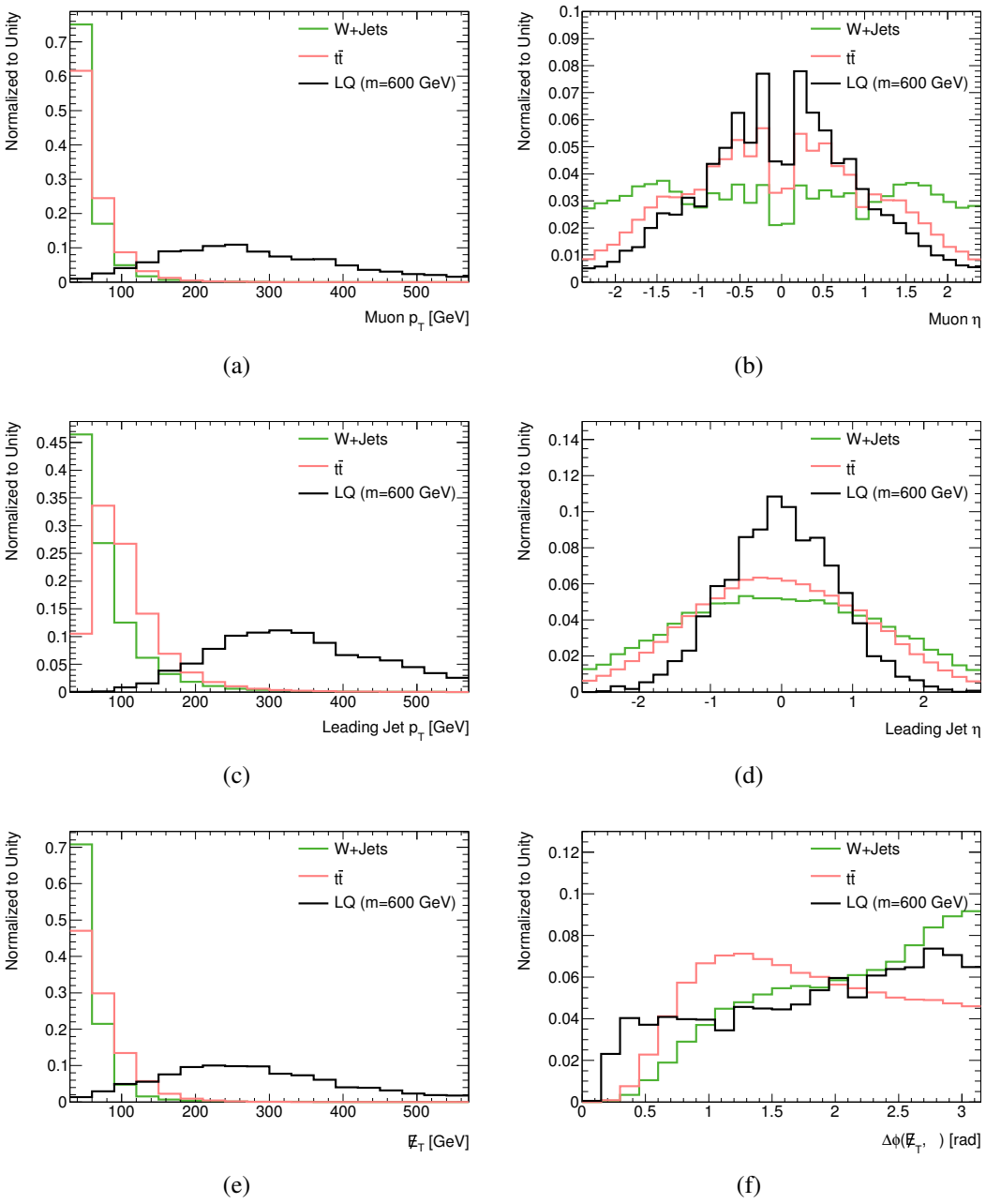

Figure 5.12: *Normalized* distributions taken from the selected event sample, for W+jets, $t\bar{t}$, and LQ signal events: (a) muon p_{T}, (b) muon η, (c) leading jet p_{T}, (d) leading jet η, (e) $\not{E}_{\mathrm{T}}$, and (f) $\Delta\phi(\not{E}_{\mathrm{T}}, \mu)$.

5.6 Log-likelihood Ratio Discriminant

The log-likelihood ratio (LLR) of the individual signal and background likelihoods is defined as

$$\mathrm{LLR}\,(m_{\mathrm{LQ}}) \equiv \log_{10}\left[\frac{L_S(m_{\mathrm{LQ}})}{L_B}\right]. \tag{5.8}$$

Signal events tend to have positive LLR values; background events, negative. For events that fall into regions of background phase space with no signal and whose LLR values therefore go to negative infinity, the LLR is set manually to a more manageable value of -15. Normalized L_B, L_S, and LLR distributions for total background and signal ($m_{\mathrm{LQ}} = 600$ GeV) are shown in Figure 5.13. The LLR distribution observed in data is compared to SM predicted background and $m_{\mathrm{LQ}} =$ 600 GeV LQ signal distributions in Figure 5.14.

It should be noted that the PDFs used as input for the LLRs are actually modified versions of the originals. Poor statistics in the tails of the background PDFs — precisely where signal is most likely to be found — proved problematic, resulting in anomalously large or small event weights driven by statistical fluctuations. Plus, any event falling in a PDF bin with zero predicted events would receive a weight of exactly zero. To avoid these problems, a function is fit to the distributions over a stable range of values then extended out into the statistics-poor region. The contents of any PDF bins with zero predicted events or a relative statistical uncertainty greater than 10% are replaced by the values given by the fit function, thereby generating a new "smoothed" PDF. As a result of poor momentum resolution for high-p_{T} muons, the PDFs required fits to *double* (not *single*) exponential functions, of the form

$$f(x) = N \cdot \frac{a \cdot e^{-x/b} + (1-a) \cdot e^{-x/c}}{ab \cdot e^{-d/b} + (1-a) \cdot c \cdot e^{-d/c}}, \tag{5.9}$$

where N is the overall normalization, a $(1-a)$ is the fraction of the first (second) exponential, b (c) is the normalization of the first (second) exponential's slope, and d is the minimum x-value included in the fit. The denominator overall serves to normalize the double exponential so that the integral under the replaced area remains the same. The original PDFs and best fits are shown in Figure 5.15.

These LLR distributions are the final background-signal discriminants. They are used as input to the statistical analysis described in Chapter 7, yielding the results presented in Chapter 8. But first — accounting for systematic uncertainties, Chapter 6

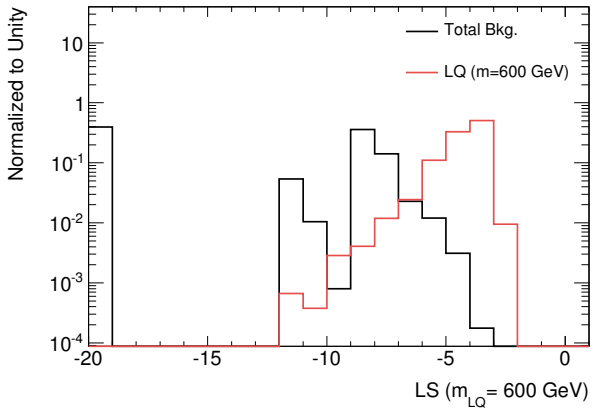

(a)

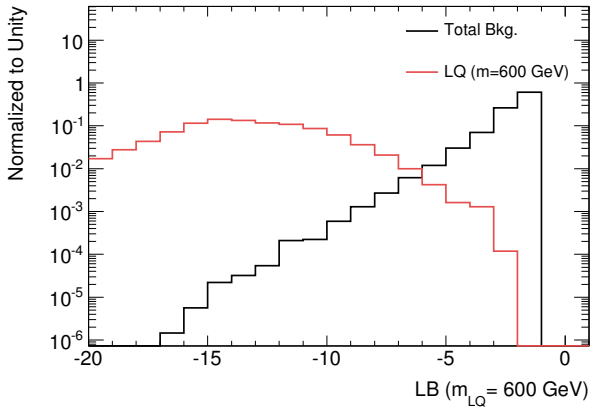

(b)

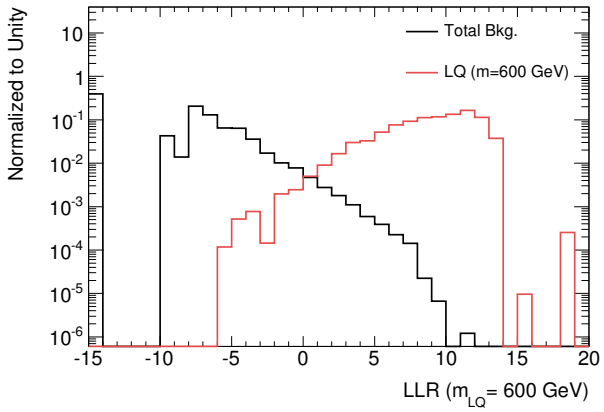

(c)

Figure 5.13: Background and signal ($m_{\mathrm{LQ}} = 600$ GeV) distributions for (a) $\log(L_S)$, (b) $\log(L_B)$, and (c) LLR, normalized to unity, emphasizing the differences in their shapes.

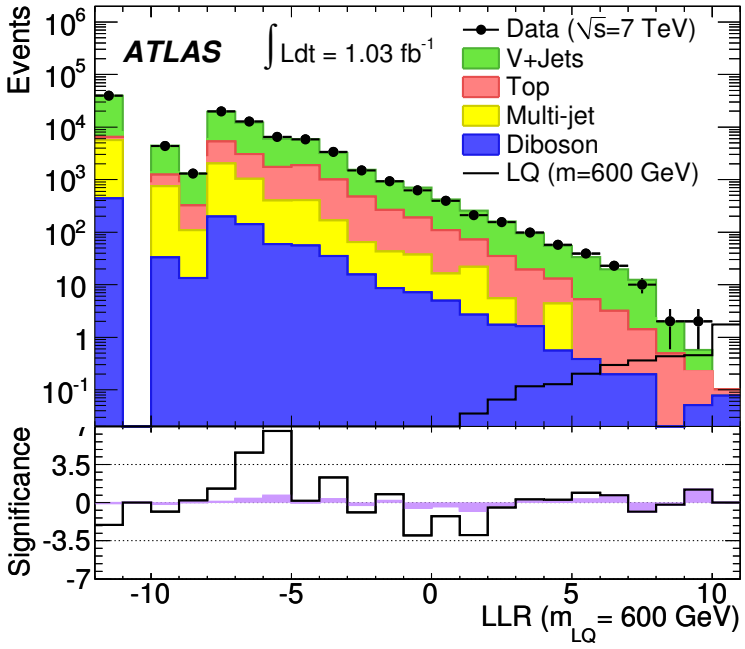

Figure 5.14: Background and signal ($m_{\mathrm{LQ}} = 600$ GeV) LLR distributions, properly scaled to their selected sample values, overlaid with the distribution observed in data.

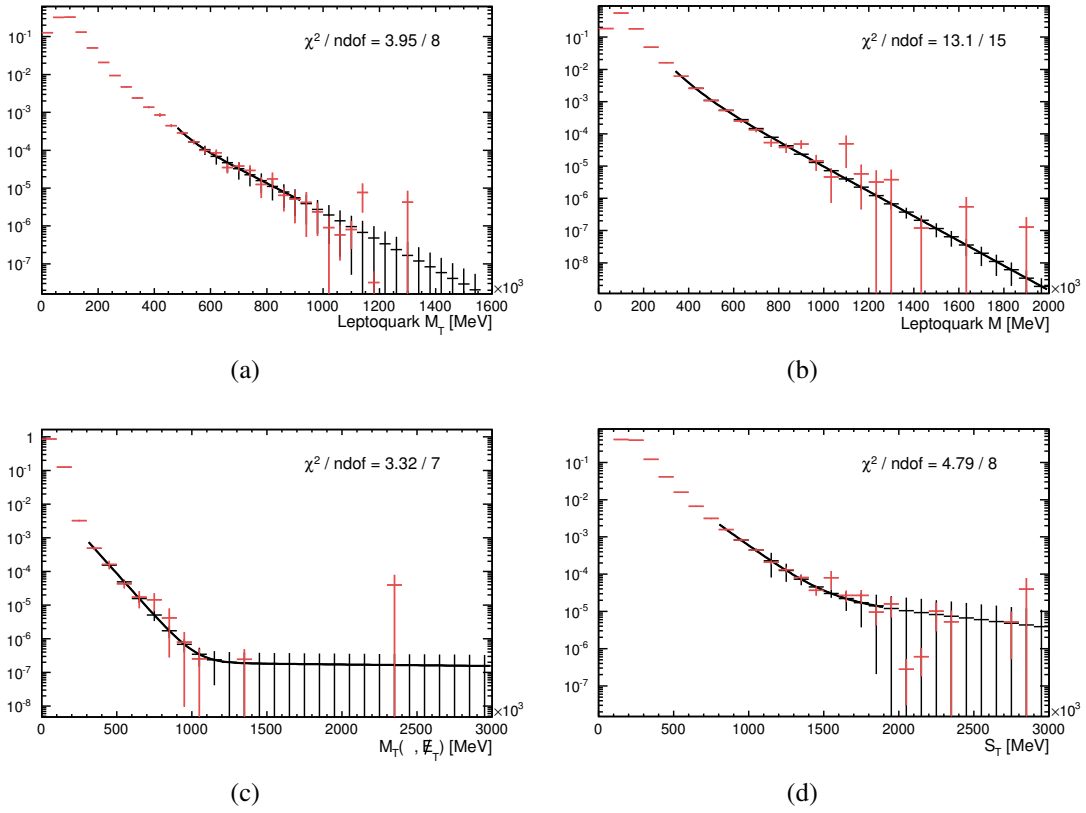

Figure 5.15: Fits to PDFs used to compute the final LLR discriminant. The original, un-smoothed distributions are drawn in red; double exponential fits are drawn as thick black curves; and the resulting smoothed PDFs are drawn in black.

CHAPTER 6

Systematic Uncertainties

> Uncertainty! fell demon of our fears! The human soul that can support despair, supports not thee.
>
> David Mallet

Systematic uncertainties are distinct from statistical uncertainties: the latter arise from random fluctuations in a measurement or experiment and can be reduced by taking more data (as $\sim 1/\sqrt{n}$, where n is the number of events); in contrast, the former arise as inherent experimental or theoretical biases that consistently shift a measurement, and thus are not reduced by taking additional data.

In this leptoquark search, both shape and normalization uncertainties are taken into account. For the final result, the full analysis is run with a single source of systematic uncertainty varied by $\pm 1\sigma$ from its nominal value, and m_{LQ}-specific LLR distributions are generated using the *nominal* PDFs shown in Figure 5.15. Each uncertainty is incorporated by integrating bin-by-bin over the LLR, sampling randomly from a Gaussian distribution whose standard deviation is set equal to the fractional change in bin yield between the systematically-varied and nominal distributions; this process is repeated for an ensemble of pseudo-experiments. For a more detailed explanation, refer to Section 5.3.

For illustration purposes only, however, the average fractional systematic uncer-

tainty for each source can be approximated by the following:

$$\overline{\text{systematic}} = \left| \frac{\int L' + \frac{1}{2}\left(\left|\delta L'_{+1\sigma}\right| + \left|\delta L'_{-1\sigma}\right|\right)\, dL'}{\int L'\, dL'} - 1 \right|, \tag{6.1}$$

where L' is the nominal LLR distribution and $\delta L'_{\pm 1\sigma}$ is the bin-by-bin difference between the $\pm 1\sigma$ systematically-varied LLR distribution and the nominal one.

Several sources of systematic uncertainty are considered in this analysis:

- integrated and instantaneous luminosity
- theoretical and data-assisted background estimation
- leptoquark signal modeling
- data/MC differences in efficiencies and resolutions
- statistics in the LLR input PDFs

A summary of the approximate uncertainty given in Equation 6.1 assigned to each source and background component is given in Table 6.1, assuming a leptoquark with $m_{\text{LQ}} = 600$ GeV.

The individual sources of systematic uncertainty and the procedures used to assess them are described in the following sections.

6.1 Luminosity

An accurate measurement of the integrated luminosity delivered to ATLAS is important in determining background expectations and signal sensitivity. The relative uncertainty on $\mathscr{L}_{\text{int}}$ was measured to be $\pm 3.7\%$ using a series of dedicated *van der Meer* luminosity scans [148], giving $\mathscr{L}_{\text{int}} = 1035.2 \pm 38.3$ pb^{-1} for the dataset used in this analysis. The uncertainty is applied to predicted signal yields as well as diboson and single top background yields; since the yields for V+jets, $t\bar{t}$, and multi-jet backgrounds are data-driven, this uncertainty does not apply. It should be noted that this is a "flat" systematic, affecting only overall normalizations and not shapes.

A separate uncertainty comes from the data's dependence on instantaneous luminosity, namely in- and out-of-time pile-up events as discussed in Section **??**. These extraneous interactions give rise to a diffuse, low-p_{T} background in the calorimeter that offsets measurements of jet energies by ~ 0.5 GeV per additional (non-primary) vertex and can significantly impact jet shapes [149]. Although such effects can be estimated, *on average*, and thus corrected for, there are uncertainties

6.1 Luminosity

Systematic	W+jets	Z+jets	$t\bar{t}$	Single top	Diboson	MJ	LQ Signal
Muon ID Reco.	<0.01	<0.01	<0.01	<0.01	<0.01	–	<0.01
Muon p Reso.	<0.01	<0.01	<0.01	<0.01	<0.01	–	0.011
Jet Energy Scale	0.169	0.167	0.053	0.068	0.125	–	0.038
Jet Energy Reso.	0.131	0.165	0.045	0.077	0.115	–	0.027
Top Mass	–	–	0.039	–	–	–	–
ISR/FSR	–	–	0.051	–	–	–	–
POWHEG/MC@NLO	–	–	0.065	–	–	–	–
PYTHIA/HERWIG	–	–	0.031	–	–	–	–
SHERPA/ALPGEN	0.043	–	–	–	–	–	–
MJ Normalization	–	–	–	–	–	0.079	–
Signal PDF	–	–	–	–	–	–	0.045
LLR Input PDF	0.125	0.108	0.193	0.178	0.171	–	0.017
Luminosity	–	–	–	0.037	0.037	–	0.037
Data Normalization	0.100	0.100	0.100	–	–	–	–
Total	0.27	0.28	0.25	0.21	0.24	0.08	0.08

Table 6.1: Approximate fractional systematic uncertainties, as defined in Equation 6.1, for each source and background, assuming a LQ with $m_{\mathrm{LQ}} = 600$ GeV. Each fraction is of the corresponding background *only*, and not of the total background.

on those corrections. This is taken into account according to recommendations by the Jet/EtMiss working group: Additional jet p_{T}- and η-dependent uncertainties are added in quadrature to the default jet energy scale uncertainties described in Section 6.5. The recommended values are given in Table 6.2.

Jet p_{T} [GeV]	Uncertainty	
	$0 \leq \lvert\eta\rvert \leq 2.1$	$2.1 \leq \lvert\eta\rvert \leq 4.5$
$20 \leq p_{\mathrm{T}} \leq 50$	5%	7%
$50 \leq p_{\mathrm{T}} \leq 100$	2%	3%
$p_{\mathrm{T}} > 100$	–	–

Table 6.2: Additional, p_{T}- and η-dependent uncertainties added to the standard jet energy scale uncertainty to account for event pile-up.

6.2 Production Cross Sections

Systematic uncertainties arising from the theoretical cross sections used to normalize single top and diboson backgrounds are given in Section 5.1. For V+jets and $t\bar{t}$, the uncertainties on the normalization scale factors in Table 5.5 are used instead.

Mass-dependent leptoquark cross sections are assigned systematic uncertainties by changing the factorization and renormalization scales up and down by factors of two, from a nominal value of $\mu = m_{\mathrm{LQ}}$ to $\mu = (1/2) \cdot m_{\mathrm{LQ}}$ and $2 \cdot m_{\mathrm{LQ}}$. The resulting uncertainties are combined in quadrature with modifications to the signal PDF, described in Section 6.3.

6.3 Background and Signal Modeling

W+jets and $t\bar{t}$ Backgrounds

Systematic uncertainties on the modeling of the W+jets background are evaluated by substituting the nominal ALPGEN MC samples with corresponding SHERPA samples. Similarly, $t\bar{t}$ modeling uncertainties are taken into account by replacing the nominal MC@NLO ($m_t = 172.5$ GeV) with MC samples generated with alternative parameters: top quark mass, initial and final state radiation (ISR/FSR), as well as production and decay models are varied separately in six samples.

Scale factors are derived for each alternative $t\bar{t}$ (W+jets) sample while keeping the nominal W+jets ($t\bar{t}$) sample(s) fixed. All samples used to assess this uncertainty are listed in Table 6.3 along with their request IDs, cross sections, and scale factors. An additional 10% uncertainty is included to account for the deviation from unity of the nominal SFs.

Distributions comparing the nominal W+jets and $t\bar{t}$ samples to their alternative samples are shown in Figures 6.1, 6.3, 6.2, and 6.4.

Multi-jet Background

As discussed in Section 5.4.3 and given in Table 5.4, the combined statistical plus systematic uncertainties assigned to the MJ background's expected yields are used to vary the normalization up and down by one standard deviation. This is propagated through the full analysis as a flat systematic.

Additionally, a separate uncertainty is assigned for the MJ background's *shape*. The nominal case takes its shape from a muon transverse impact parameter-reversed data sample with expected EWK contributions subtracted off; the alternative shape is derived from an analogous muon isolation-reversed sample. Both distributions are normalized to the final, combined value.

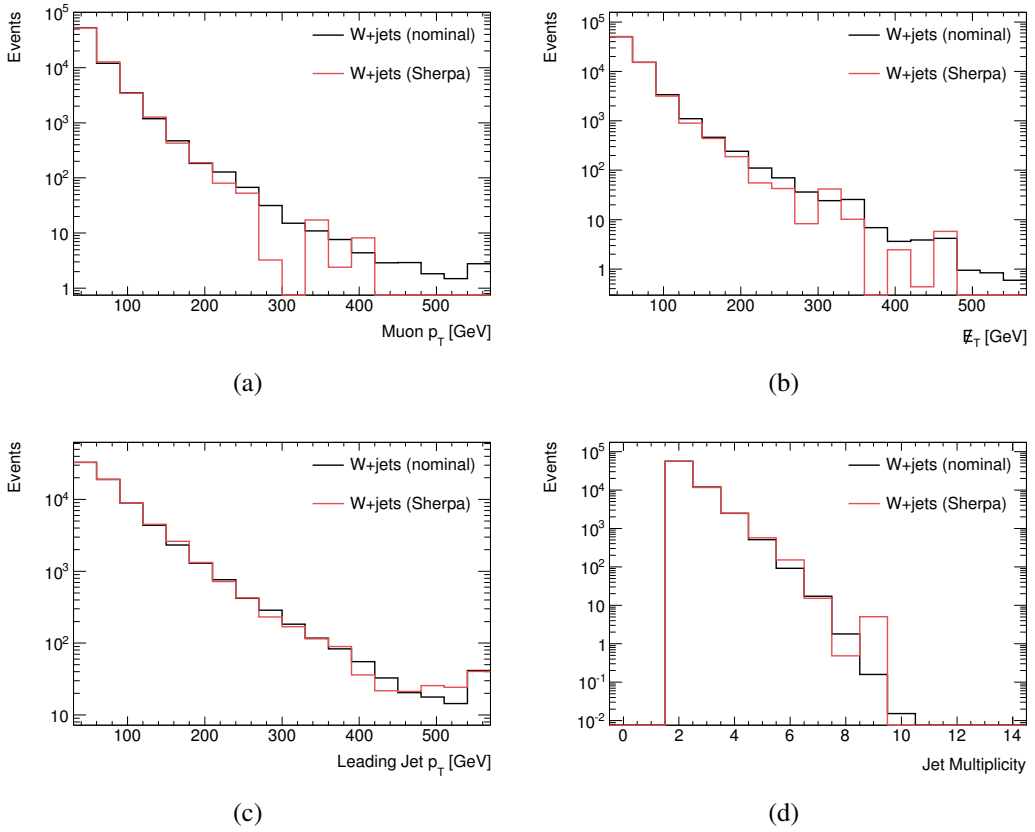

Figure 6.1: Comparison of basic kinematic distributions for the W+jets background using the nominal sample (generated by ALPGEN) and an alternative sample (generated by SHERPA).

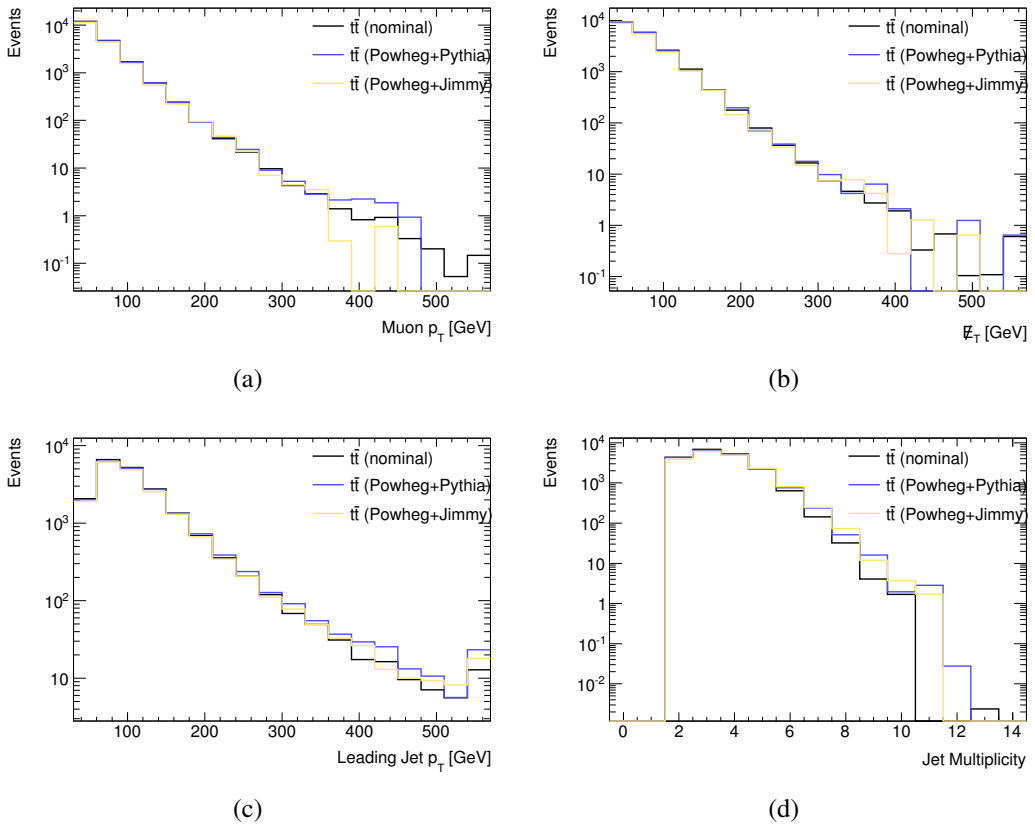

Figure 6.2: Comparison of basic kinematic distributions for the $t\bar{t}$ background using the nominal sample (generated by MC@NLO) and two alternative samples (generated by POWHEG + PYTHIA and POWHEG + JIMMY).

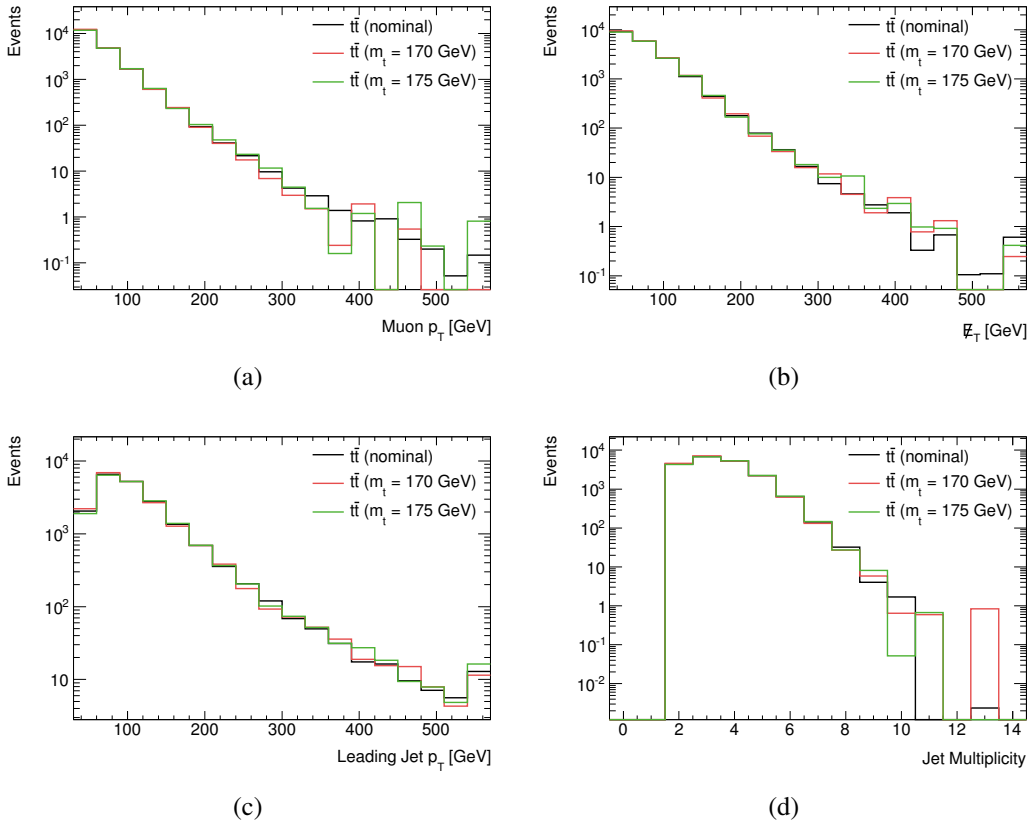

Figure 6.3: Comparison of basic kinematic distributions for the $t\bar{t}$ background using the nominal sample ($m_t = 172.5$ GeV) and two alternative samples ($m_t = 170$ GeV and $m_t = 175$ GeV).

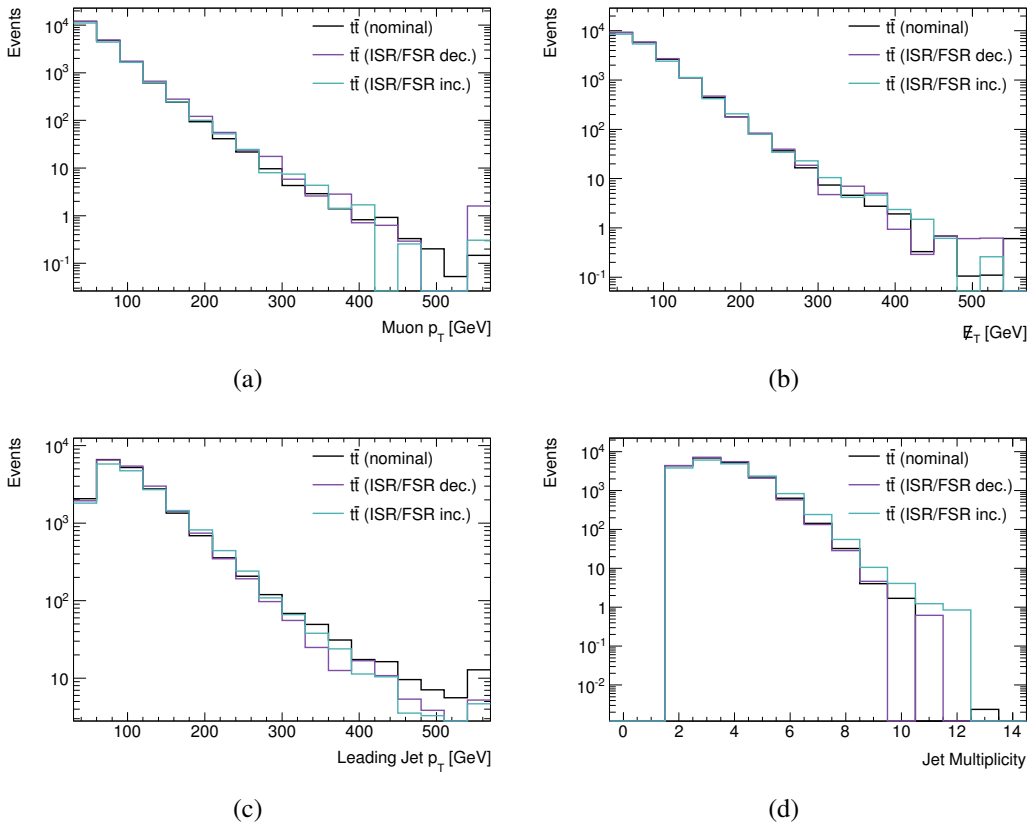

Figure 6.4: Comparison of basic kinematic distributions for the $t\bar{t}$ background using the nominal sample (generated by MC@NLO) and two alternative samples (both generated by ACER, with increased or decreased initial and final state radiation).

Process	Variation	Request ID	Cross Section [pb]	Scale Factor
$W \to \mu\nu$	ALPGEN (nominal)	107690 – 5	10460	0.911 ± 0.005
	SHERPA	119129		1.067 ± 0.011
$W \to \tau\nu$	ALPGEN (nominal)	107700 – 5		0.911 ± 0.005
	SHERPA	119130		1.067 ± 0.011
$t\bar{t}$	MC@NLO (nominal)	105200	89.3	1.09 ± 0.02
	POWHEG + JIMMY	105860	89.3	1.032 ± 0.021
	POWHEG + PYTHIA	105861	89.3	1.072 ± 0.024
	MC@NLO, $m_t = 170$ GeV	106201	96.3	1.043 ± 0.027
	MC@NLO, $m_t = 175$ GeV	106206	83.2	1.149 ± 0.021
	ACER, ISR/FSR dec.	117259	89.3	1.015 ± 0.019
	ACER, ISR/FSR inc.	117260	89.3	1.095 ± 0.023

Table 6.3: Alternative MC samples used to determine W+jets and $t\bar{t}$ modeling systematic uncertainties.

Distributions comparing the nominal, muon $|d_0|$-reversed MJ background shape to the alternative, muon $p_{\mathrm{T}}^{\mathrm{cone20}}/p_{\mathrm{T}}$-reversed shape are shown in Figure 6.5.

LQ Signal

To determine sensitivity of the leptoquark signal acceptance to MC modeling, the ISR, FSR, and multiple interaction configurations were initially turned off at the generator level; all but the ISR case had a negligible effect. To study this in more detail, various ISR/FSR flags are changed, corresponding to the following PYTHIA settings: `parp(1)=0.192`, `paru(112)=0.192`, `mstu(112)=3`, and `parp(61)=0.129`. The resulting 2% variation in acceptance is taken as the signal modeling systematic uncertainty.

The choice of parton distribution function in simulating LQ events can have a large effect on the event kinematics. Therefore, the nominal CTEQ6L1 PDF is re-weighted using standard CTEQ uncertainty sets, approximately reproducing the effect of using a modified LO MRST2007 PDF instead, testing the signal acceptance's sensitivity to this choice. The difference is incorporated as a systematic uncertainty directly in the limit-setting procedure.

6.4 Muon Reconstruction and Resolution

The MCP working group's official scale factors accounting for data/MC differences in muon reconstruction and resolution, discussed in Section 5.3, have systematic

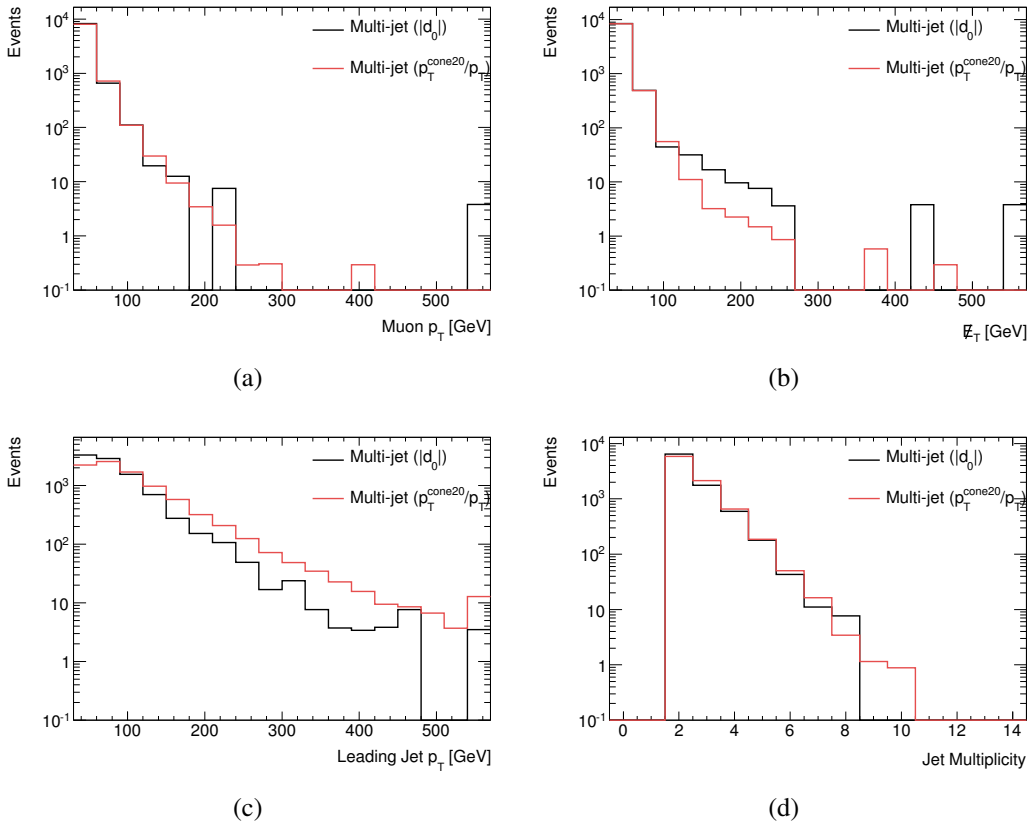

Figure 6.5: Comparison of basic kinematic distributions for the multi-jet background using the nominal sample (derived from a muon $|d_0|$-reversed data sample) and the alternative sample (derived from a muon $p_{\mathrm{T}}^{\mathrm{cone20}}/p_{\mathrm{T}}$-reversed data sample). Both are scaled to the same overall normalization.

uncertainties associated with them. Functionality is built into the official software packages to fluctuate the MC corrections up and down by one standard deviation.

Muon momentum resolution is measured in two ways: (1) from the width of the di-muon invariant mass near the Z boson mass in $Z \to \mu\mu$ decays, where the width is actually convolution of the inherent Z width and the muon momentum resolution; and (2) from the difference in independent ID and MS momentum measurements in select $W \to \mu\nu_\mu$ decays, which is sensitive to the quadratic sum of the two sub-detector's individual resolutions [150]. The overall resolution is derived from a combined fit to these two results, with systematic uncertainties arising from incomplete knowledge of the detector material, multiple scattering, and relative mis-alignments of the sub-detectors and their components. The magnitude of the Gaussian smearing applied to the muon transverse momentum is consistently increased or decreased, and the resulting variations are properly propagated through the event MET.

Muon reconstruction efficiencies are measured from data using a tag-and-probe study of $Z \to \mu\mu$ events [151]. The nominal event weights are varied by $\pm 1\sigma$ and carried through to systematically-varied LLR distributions.

The effect of the muon momentum resolution systematic uncertainty on the predicted background muon p_{T}, MET, and L_{T} shapes is shown in Figure 6.6.

6.5 Jet Energy Scale and Resolution

Jet energy scale systematic uncertainties are provided by an official Jet/EtMiss working group code package — `JESUncertaintyProvider` — and applied to all jets with $p_{\mathrm{T}} > 20$ GeV and $|\eta| < 4.5$. This uncertainty includes several components, added in quadrature [152]:

- The JES calibration method itself, by which jets reconstructed at the EM scale are corrected, on average, to the hadronic scale
- The response of the calorimeter to single particles, from which the response to jets composed of multiple particles can be inferred
- The simulation of the ATLAS detector, including electronic noise in the calorimeter and extra material in front of the calorimeter
- MC simulation of fragmentation and underlying event processes
- Relative differences in calibration between central and end-cap/forward regions of the calorimeter

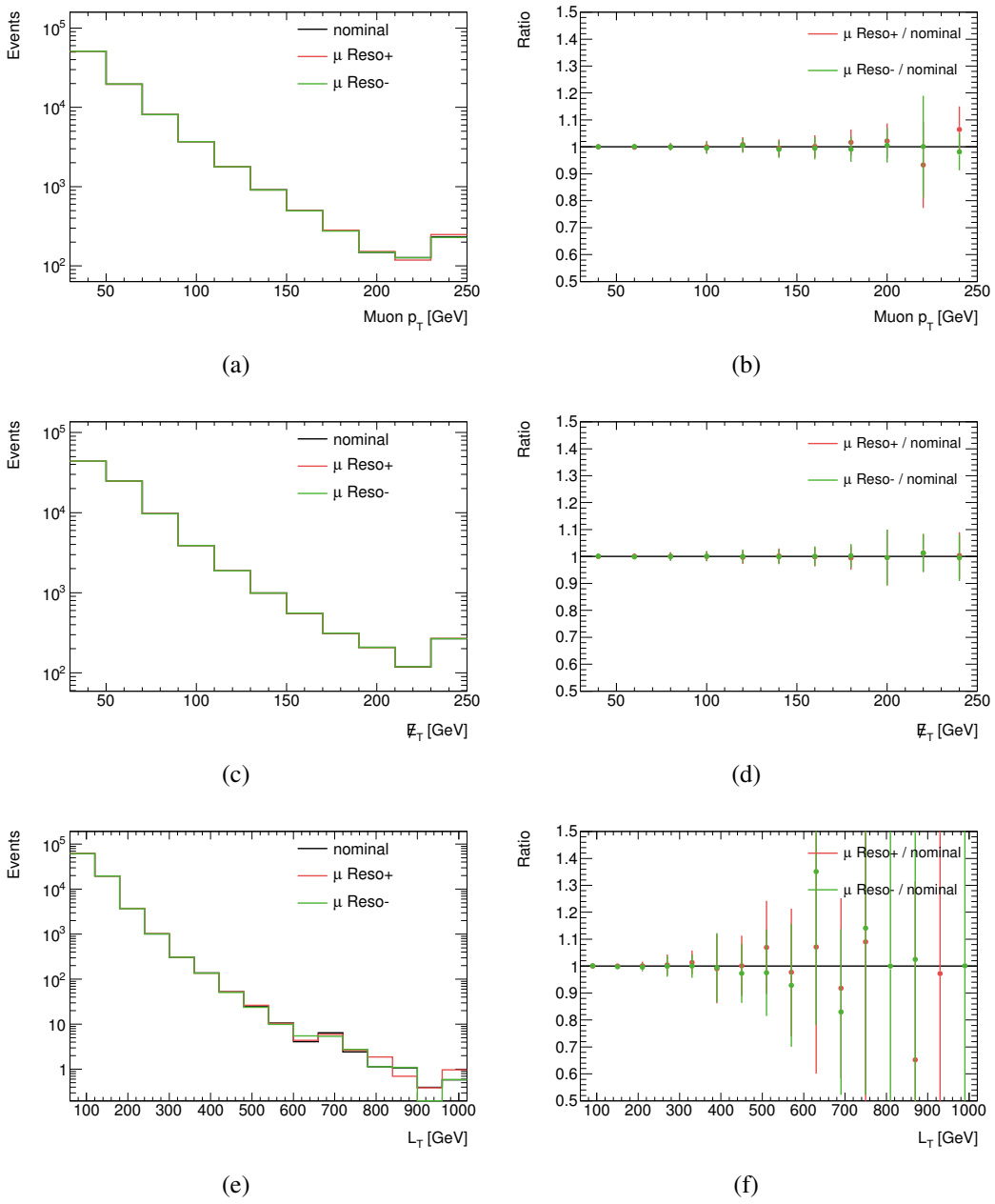

Figure 6.6: For total predicted background events, muon p_{T}, $\not{E}_{\mathrm{T}}$, and L_{T} distributions for the nominal and $\pm 1\sigma$ muon momentum resolution cases are shown in plots (a), (c), and (e), respectively. The corresponding ratios of the systematically-varied and nominal distributions are shown in plots (b), (d), and (f).

A further 5% relative uncertainty is added in quadrature to the JES uncertainty because MET is originally calculated from physics objects calibrated at the electromagnetic scale, while JES uncertainties are propagated after corrections to the EM+JES scale have been applied. An additional uncertainty to account for pile-up, as given in Table 6.2, is also added in quadrature. The overall $\pm 1\sigma$ variations are propagated through the full analysis, including their effects on the event missing transverse momentum, ultimately yielding systematically-varied LLR distributions. The magnitude of the $+1\sigma$ uncertainty's effect is slightly larger than the -1σ because there are a greater number of affected jets at lower transverse momenta.

Jet energy resolution (JER) uncertainties are also provided by an official Jet/EtMiss code package — `JERProvider` — and applied to all jets with $p_{\mathrm{T}} > 30$ GeV and $|\eta| < 2.8$. The uncertainties were determined *in-situ* using two different but complementary techniques, the *di-jet balance* and *bi-sector* methods [153]. Analysis-wise, then, the nominal jet momentum and energy are smeared by randomly sampling a Gaussian with width equal to the 1σ JER fractional uncertainty, and the sampled value (which may be negative) is added to the nominal one. The reduced range of validity of the code results in a threshold effect: jets can fluctuate *below* the standard jet selection, but no jets can fluctuate *up*, causing a noticeable deficit of jets at transverse momenta close to the 30 GeV threshold.

The effect of the JES (JER) uncertainties on the predicted background jet p_{T}, MET, and H_{T} shapes is shown in Figure 6.7 (6.8).

6.6 LLR PDF Statistics

The "smoothed" background PDFs, i.e. those fit to double exponentials (Equation 5.9), used to determine the final LLR distributions are based on histogrammed distributions with limited MC statistics, particularly at higher LLR values. The associated statistical uncertainties are propagated onward by generating ensembles for each PDF which differ from the nominal distributions in bin-by-bin fluctuations, depending on the mean and root-mean-square (RMS) values of each bin. These PDF ensembles are used to generate an ensemble of LLR distributions, which are then averaged, and the bin-by-bin RMS of the average LLR is taken as a shape uncertainty.

The nominal background LLR (assuming $m_{\mathrm{LQ}} = 600$ GeV) distribution is shown in Figure 6.9 compared to the "un-smoothed" result, for which background PDFs were not fit to double exponentials, as well as the positive and negative systematically-varied distributions accounting for PDF statistics.

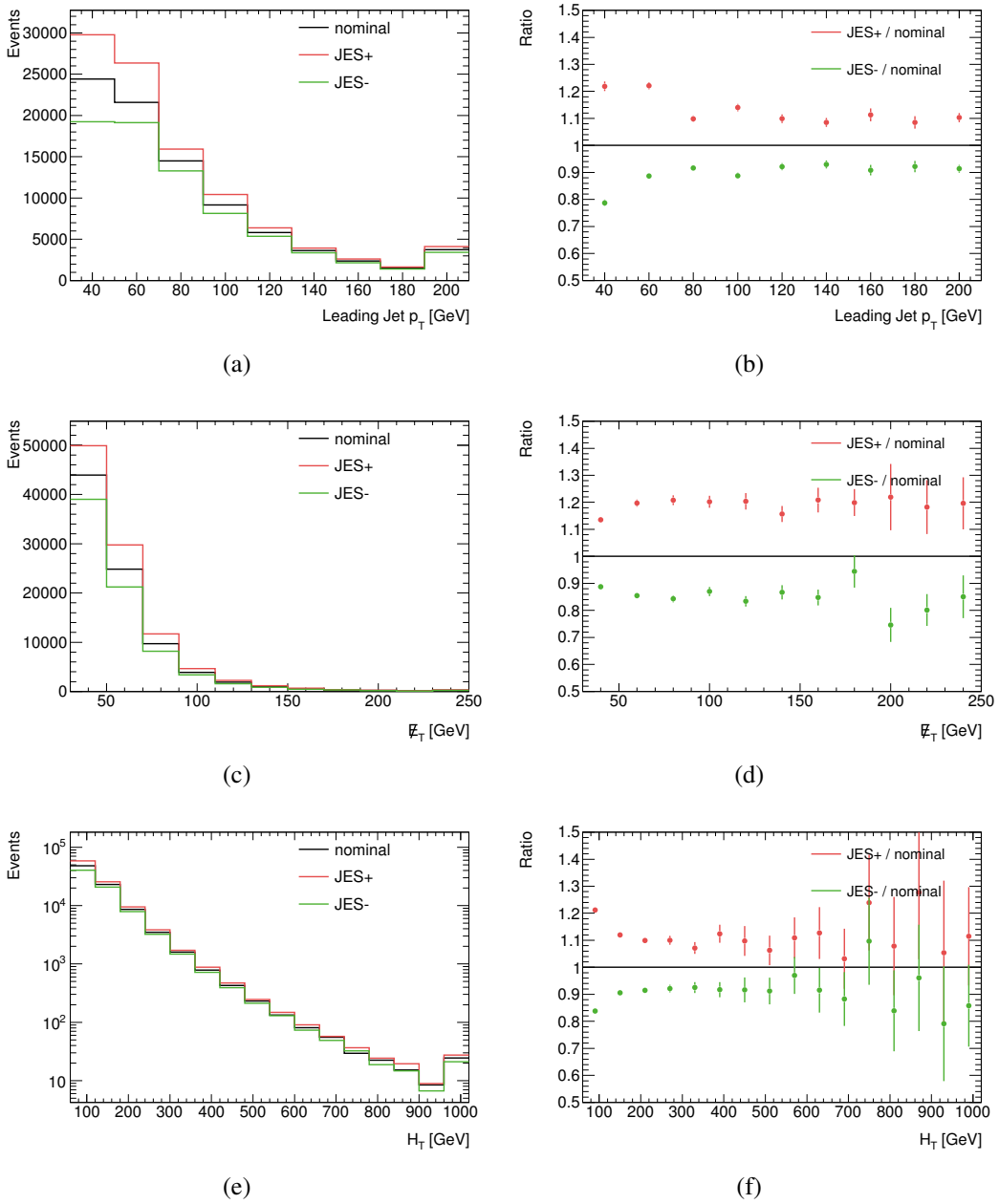

Figure 6.7: For total predicted background events, jet p_T, $\not{E}_T$, and H_T distributions for the nominal and $\pm 1\sigma$ JES cases are shown in plots (a), (c), and (e). The corresponding ratios of the systematically-varied and nominal distributions are shown in plots (b), (d), and (f).

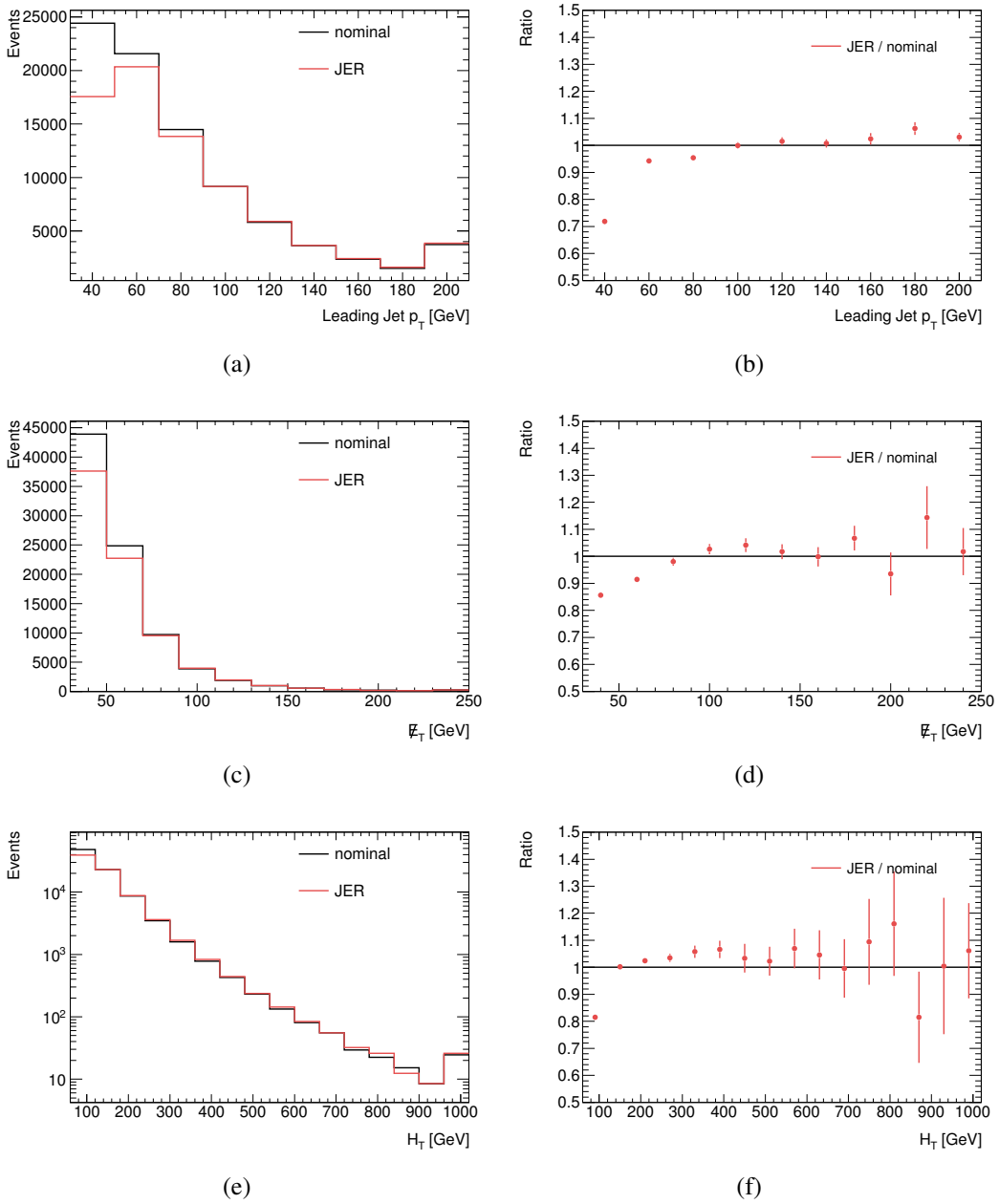

Figure 6.8: For total predicted background events, jet p_T, $\not{E}_T$, and H_T distributions for the nominal and JER-varied cases are shown in plots (a), (c), and (e). The corresponding ratios of the systematically-varied and nominal distributions are shown in plots (b), (d), and (f).

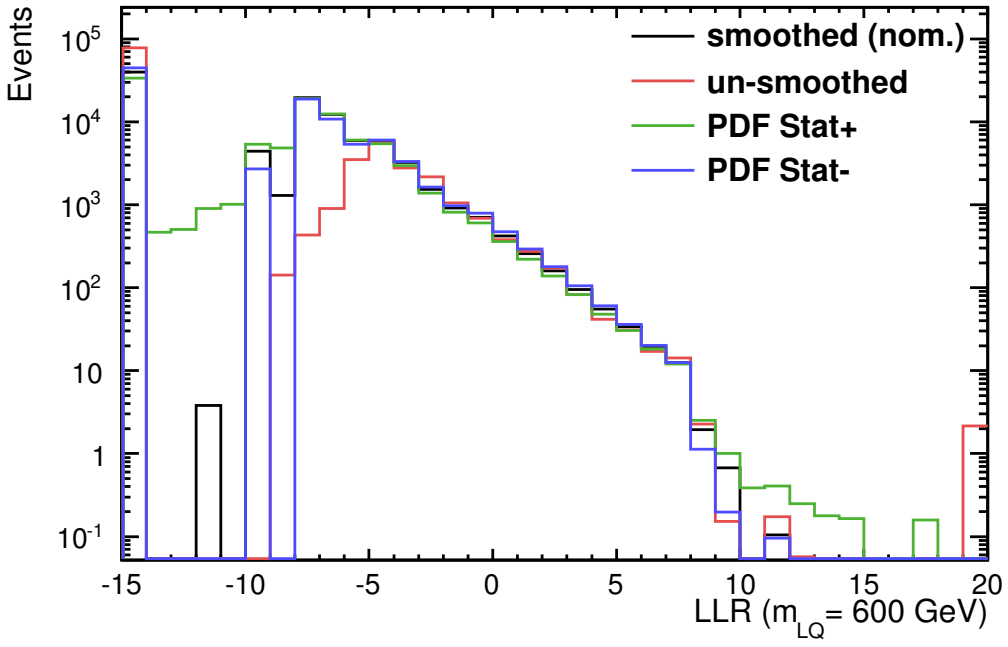

Figure 6.9: Total predicted background LLR distributions for the smoothed PDF (nominal), un-smoothed PDF, and systematically-varied for PDF statistics cases.

CHAPTER 7

Limit-Setting

Hypotheses non fingo.

Isaac Newton

The end goal of a search for new physics is to make a quantitative statement relating an experimental result to a theoretical signal model. Specifically, one wants to answer two related — but distinct — questions: 1) *Did I discover something?* and 2) *How well does my model describe the result?*

To answer these questions, two distinct approaches to statistical inference are commonly used:

- **Frequentist**: offers a statement about the probability of the data, given the hypothesis, where *probability* is interpreted as the frequency with which an outcome is likely to happen in a series of repeatable experiments; data is treated as random, while hypotheses are fixed

- **Bayesian**: offers a statement about the probability of the hypothesis, given the data, where *probability* is one's subjective "degree of belief" in a hypothesis or a parameter's true value given *a priori* knowledge and the experimental outcome; hypotheses are treated as random; data, fixed

Both interpretations are valid and, in certain cases, give identical results [4]. For the leptoquark search presented in Chapter 5, a "Bayesian-Frequentist hybrid"

method [154] is employed, with a Frequentist treatment for the primary measurement and a Bayesian technique for handling systematic uncertainties. Requisite statistical tests are computed using the COLLIE software suite [155].

7.1 Hypothesis Tests

A *hypothesis* is a statement about the experimental outcome of an analysis. Commonly, one must discriminate between two hypotheses:

- Null Hypothesis ($\mathscr{H}_0$): by convention the "background-only" hypothesis, corresponding to data consistent with the SM prediction
- Test Hypothesis ($\mathscr{H}_1$): by convention the "signal+background" hypothesis, corresponding to data described by the signal model in addition to the SM background; note that this is a function of leptoquark mass, i.e. $\mathscr{H}_1(m_{\mathrm{LQ}})$

Frequentist *hypothesis tests* are a defined set of rules for accepting or rejecting hypotheses depending on the outcome of the experiment [4].

To distinguish $\mathscr{H}_0$ from $\mathscr{H}_1$ we define a *test statistic* Q that orders outcomes from least to most signal-like. In a counting experiment, this quantity is simply the number of events satisfying some requirements ($n = L \times \sigma \times \varepsilon$), but it can also be more complicated, such as a distinguishing kinematic feature of the signal or a multivariate combination thereof. Each hypothesis determines a likelihood function $\mathscr{L}$ for Q, typically given by common forms and generated with toy MC. In the case of random counts (as in the leptoquark search), these distributions are Poisson probability distributions:

$$\mathscr{L}(x \mid \mathscr{H}_0) = \frac{(b)^x e^{-(b)}}{x!} \text{ and } \mathscr{L}(x \mid \mathscr{H}_1) = \frac{(s+b)^x e^{-(s+b)}}{x!}, \tag{7.1}$$

where s and b are the expected number of events for signal and background[1], respectively, and x is the number of events observed in data or *pseudo*-data.

According to the *Neyman-Pearson lemma*, the "uniformly most powerful" test statistic[2] is given by the likelihood ratio [4]:

$$Q(x) = \frac{\mathscr{L}(x \mid \mathscr{H}_1)}{\mathscr{L}(x \mid \mathscr{H}_0)}. \tag{7.2}$$

[1] Technically, both background and signal can (and do) arise from multiple sources. Each of these are sampled *individually* then summed together, i.e. $b = \sum_i^{\mathrm{bkgs}} b_i$. This is important when incorporating systematics, which may not apply to all background components.

[2] Test statistic defining a critical region of size α that maximizes the test's *power* $1-\beta$. Simple (not compound) hypotheses required. See end of Section 7.1 for further clarification.

A combined likelihood for all bins in a single channel's test statistic and all orthogonal (i.e. statistically independent) channels in an analysis is defined by taking the product of individual likelihoods:

$$Q(x) = \prod_{i}^{\text{channels}} \prod_{j}^{\text{bins}} \frac{(s_{ij}+b_{ij})^{x_{ij}} e^{-(s_{ij}+b_{ij})}/x_{ij}!}{(b_{ij})^{x_{ij}} e^{-(b_{ij})}/x_{ij}!} \tag{7.3}$$

$$= \prod_{i}^{\text{channels}} \prod_{j}^{\text{bins}} e^{-(s_{ij})} \left(\frac{s_{ij}+b_{ij}}{b_{ij}}\right)^{x_{ij}}. \tag{7.4}$$

For computational convenience as well as stability, the equivalent *log-likelihood ratio* is used:

$$\text{LLR}(x) = -2\ln(Q(x)) = 2 \cdot \sum_{i}^{\text{channels}} \sum_{j}^{\text{bins}} \left[s_{ij} - x_{ij} \ln\left(1+\frac{s_{ij}}{b_{ij}}\right)\right]. \tag{7.5}$$

Recall that the Frequentist approach interprets probability as the frequency of a particular outcome in an ensemble of like experiments. Given that the LHC and ATLAS experiment can only be run *once* (for practical reasons), an ensemble of *pseudo-experiments* is generated instead. In each pseudo-experiment, a Poisson distribution of mean b events is randomly sampled, yielding a pseudo-data value for x that is substituted into both $\mathscr{L}(x \mid \mathscr{H})$ likelihoods to produce a value of LLR(b). This procedure is repeated with Poisson($s+b$), yielding LLR($s+b$). With ~20,000 pseudo-experiments, one can generate smooth probability distribution functions for LLR($\mathscr{H}_0$) and LLR($\mathscr{H}_1$).

These distributions are used to define a *critical region* of *size* α: if the observed Q_{obs} falls within the critical region, $\mathscr{H}_0$ is rejected; otherwise, $\mathscr{H}_0$ is accepted. The *confidence level* (CL) for this test is equal to $1-\alpha$. A commonly accepted value in HEP is CL = 95% ($\alpha = 0.05$), which has a 5% probability of rejecting $\mathscr{H}_0$ when it's true (a "type I error"). The *power* of the test is given by $1-\beta$, where β is the probability of accepting $\mathscr{H}_0$ when it's false (a "type II error"). [156]

7.2 p-values and Confidence Intervals

Significance tests are used to quantify the level of agreement between data and a hypothesis. A hypothesis' p-value is defined as the probability, assuming $\mathscr{H}$ true, of finding a value of Q of equal or lesser compatibility with the model relative to Q_{obs} [4]:

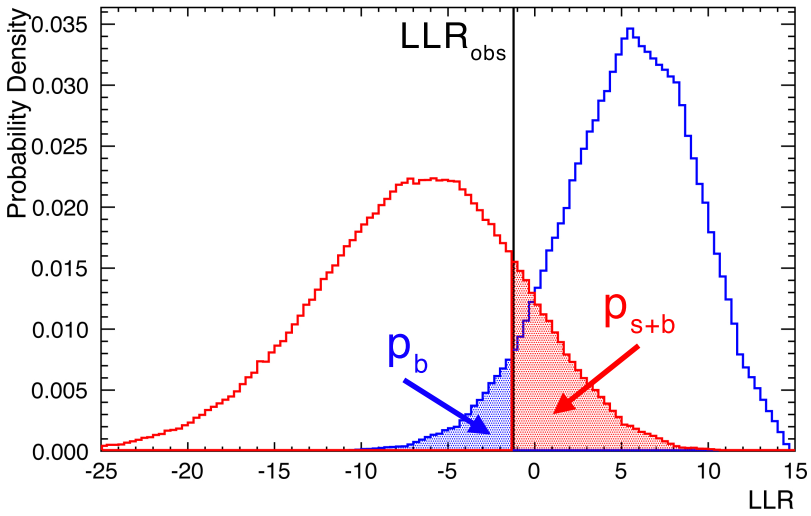

Figure 7.1: Log-likelihood ratio PDFs for the null and test hypotheses, and the observed value. Corresponding p-values are shaded in blue and red. Generated with a toy MC with $b = 6.0$, $s = 7.5$, $x_{obs} = 10$, and 100,000 pseudo-experiments.

$$p_b = \mathrm{P}(Q \leq Q_{obs} \mid \mathscr{H}_0) = \int_{-\infty}^{Q_{obs}} f(Q \mid \mathscr{H}_0)\, dQ \tag{7.6}$$

$$p_{s+b} = \mathrm{P}(Q \geq Q_{obs} \mid \mathscr{H}_1) = \int_{Q_{obs}}^{\infty} f(Q \mid \mathscr{H}_1)\, dQ, \tag{7.7}$$

where $f(Q|\mathscr{H})$ is the sampling distribution of Q under the assumption of $\mathscr{H}$. This is shown in Figure 7.1. Note that the sign of the inequality flips between null and test hypotheses.

It is more common to speak of equivalent significance z-values, related to p-values by $z = \Phi^{-1}(1-p)$, where Φ is the cumulative distribution for a standard Gaussian, and Φ^{-1} its inverse. For example, an accepted convention for "discovery" has $z = 5.0$ (a 5σ effect), corresponding to $p_b = 2.87 \times 10^{-7}$. In other words, a very small value for p_b is grounds to reject the background-only hypothesis — and consider the alternatives.

In the case that an excess of events is observed, one wants to determine a value for the LQ production cross section σ_{LQ} (and, by extension, its mass m_{LQ}), bounded by a *confidence interval* guaranteed to contain the true value of σ_{LQ} with a probability greater than or equal to some value, on average, for many repeated experiments. To this end, a test of size α is defined for a range of hypothesized values of σ_{LQ}

(each giving a new $\mathscr{H}_1$), rejecting values of σ_{LQ} for which the experimental outcome falls within the critical region. These tests are inverted to define the associated confidence interval, i.e. the set of all σ_{LQ} not rejected by the test, with CL = $1-\alpha$:

$$\mathrm{P}(x_- < x < x_+ \mid \sigma) = \int_{x_-}^{x_+} f(x \mid \sigma) dx \geq \mathrm{CL}. \tag{7.8}$$

In the case that no excess is observed in data, an *upper limit* is set on the LQ production cross section — that is, the largest value of σ_{LQ} not excluded. The cross section is bounded on the low side by zero, of course, so the confidence interval is necessarily one-sided. As explained above, the interval $[0, \sigma_{\mathrm{LQ}}^{max}]$ covers the *true* value with probability greater than or equal to the CL.

7.3 Incorporating Systematic Uncertainties

As described in Chapter 6, understanding of the signal and background models in this analysis is imperfect. In addition to statistical uncertainties, a number of systematic uncertainties affect sensitivity and, in turn, the final result. Incorporating these systematics into the limit-setting procedure, however, is difficult with Frequentist methods; a Bayesian approach proves more natural.

In Bayesian statistics, everything that is known about the parameter of interest — e.g. the signal production cross section — is given by the *posterior* probability. The relationship between the posterior and what is actually measured is given by Bayes' Theorem [156]:

$$\mathrm{P}(\mathscr{H} \mid x) = \frac{\mathrm{P}(x \mid \mathscr{H})\ \pi(H)}{\mathrm{P}(x)} \tag{7.9}$$

Systematics are introduced into the calculation as *nuisance parameters* ν and integrated over in a process called *marginalization* à la the Cousins-Highland method. Analytically, it amounts to a transformation of a *compound* hypothesis $\mathrm{P}(x \mid \mathscr{H}, \nu)$ to a superposition of *simple* hypotheses $\mathrm{P}(x \mid \mathscr{H})$, as written in Equation 7.10.

$$\mathrm{P}(x \mid \mathscr{H}) = \int \mathrm{P}(x \mid \mathscr{H}, \nu)\ \pi(\nu)\ d\nu \tag{7.10}$$

The uncertainties' *priors* $\pi(\nu)$ are modeled as symmetric Gaussian distributions with widths equal to the fractional uncertainty on the background or signal yields, except when the uncertainties are asymmetric, in which case a bifurcated Gaussian is used. COLLIE implements this procedure numerically [155]. In each pseudo-experiment, individual systematic distributions are sampled within $\pm 1\sigma$; correlated systematics (e.g. luminosity) are sampled commonly for all samples, while un-

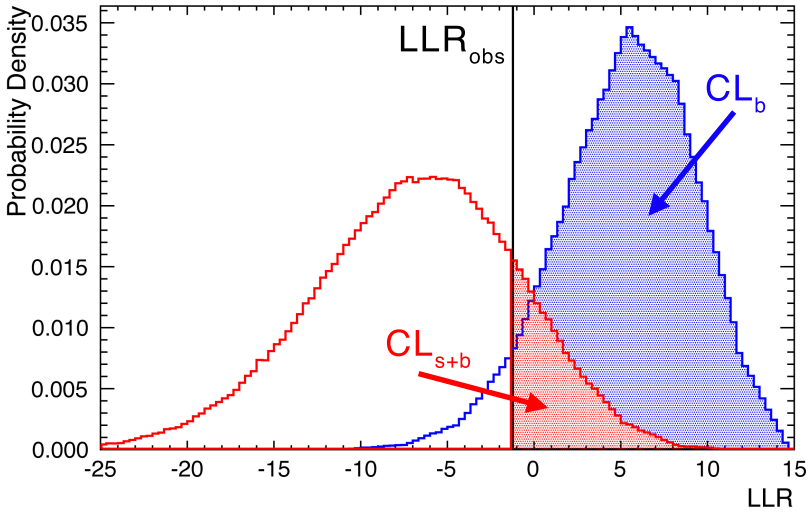

Figure 7.2: Log-likelihood ratio PDFs for the null and test hypotheses, and the observed value. Corresponding confidence levels are shaded in blue and red. Generated with a toy MC with $b = 6.0$, $s = 7.5$, $x_{obs} = 10$, and 100k pseudo-experiments.

correlated systematics (e.g. QCD normalization) are sampled independently. The mean of the nominal Poisson likelihood is shifted accordingly, and the net effect is to smear the distributions, making it more difficult to distinguish $\mathscr{H}_0$ from $\mathscr{H}_1$ and thus degrading the search sensitivity.

7.4 The Modified-Frequentist Approach

Confidence levels are defined for the background-only and signal+background hypotheses as the fraction of pseudo-experiments with LLR values less signal-like (more background-like) than that observed in the data:

$$\mathrm{CL}_b = \mathrm{P}(Q \geq Q_{obs} \mid \mathscr{H}_0) = \int_{Q_{obs}}^{\infty} f(Q \mid \mathscr{H}_0) dQ = 1 - p_b \tag{7.11}$$

$$\mathrm{CL}_{s+b} = \mathrm{P}(Q \geq Q_{obs} \mid \mathscr{H}_1) = \int_{Q_{obs}}^{\infty} f(Q \mid \mathscr{H}_1) dQ = p_{s+b} \tag{7.12}$$

where the test statistic Q is the log-likelihood ratio [157]. See Figure 7.2.

As described previously, a hypothesis is "excluded" at CL $\geq 1-\alpha$ if $p \leq \alpha$. Using the pure Frequentist CL_{s+b} to evaluate exlusion limits for the signal+background hypothesis, however, allows for exclusion of signals to which one is not experimen-

tally sensitive! In the case that the expected signal is small and the data fluctuates downward with respect to the background-only prediction, *any* signal model may be excluded with a high confidence level. Such a dependence on background modeling is problematic, and unacceptable.

To resolve this issue, a "modified-Frequentist" confidence level is defined:

$$\mathrm{CL}_s \equiv \frac{\mathrm{CL}_{s+b}}{\mathrm{CL}_b}, \tag{7.13}$$

which can be interpreted as the approximate confidence obtained if background events were removed from the selected event sample, leaving only signal. Note that CL_s gives *conservative* limits: CL_s is always larger than CL_{s+b}, resulting in a weaker upper limit. This definition ensures that signals are not excluded where there is no sensitivity. [158]

As described at the end of Section 7.2, a series of signal+background hypotheses are tested over a range of leptoquark masses, $\mathscr{H}_1(m_{\mathrm{LQ}})$. In the absence of an excess in data, one excludes the corresponding production cross section at 95% CL when 1-$\mathrm{CL}_s \geq 0.95$ and report an upper limit on σ_{LQ}. If an excess is observed, one can exclude the null hypothesis when $\mathrm{CL}_b \leq 2.8 \times 10^{-7}$ and report a confidence interval for a measurement of σ_{LQ}.

The next chapter reveals the results of this procedure for the leptoquark analysis.

CHAPTER 8

Results

> So I hope you can accept Nature as She is — absurd.
>
> Richard Feynman

The CL_s limit-setting procedure discussed in the previous chapter was applied to the second-generation leptoquark search detailed in Chapter 5. Recall that the discriminating variable used as input to COLLIE was itself a log-likelihood ratio — *not* to be confused with the LLR probability distribution functions with which p-values and confidence levels are calculated.

Separate LLR distributions were derived for test hypotheses corresponding to leptoquark masses ranging from 300 to 800 GeV, in steps of 50 GeV. Refer to Figure 5.14 for the $m_{\mathrm{LQ}} = 600$ GeV case.

No excess in data was observed. Expected and observed limits were computed as a function of m_{LQ} assuming branching fraction $\beta = 0.5$ (at which the signal expectation is maximal), and an upper limit on leptoquark production cross section and mass are reported. By varying β incrementally in the interval [0.0, 1.0], an exclusion *region* in the β vs. m_{LQ} plane was also determined. Finally, results from the $\mu\nu jj$ channel were combined with those from the complementary $\mu\mu jj$ channel to further improve search sensitivity [159].

8.1 Cross section and Mass Limits

In order to produce reliable results, COLLIE requires that all bins of the input distribution have non-zero predicted background[1]; however, the LLRs for some mass points ran afoul of this "feature." An algorithm was devised to correct the problem, and for consistency it was applied equally to all mass points.

The algorithm goes in the following manner. Starting with the highest-LLR bin in the *predicted* background distribution and progressing bin-by-bin toward lower LLR values, bins are merged together until no empty bins with LLR > 0 remain and the content of the merged bin is greater than zero yield by at least 2σ, i.e. 2.3 events. An analogous algorithm is applied on the low side for LLR < -9. The same bins for the signal and data distributions are then merged as well, regardless of their content. This procedure limits the effect of statistical fluctuations in the tails of the LLR distributions that can result in non-physical changes in search significance. Re-binned LLRs at various mass points are shown in Figure 8.1.

The resulting cross section limits are shown in Figure 8.2 for $\beta = 0.5$, with and without systematic uncertainties included. As expected, the inclusion of systematic uncertainties weakens the limit, but the effect on the final mass limit is small (≈ 10 GeV). The expected and observed upper limits on leptoquark mass, corresponding to the values of m_{LQ} at which the theoretical leptoquark cross section curve crosses the expected and observed limit curves, respectively, are given in Table 8.1. Values of CL_b for tests over a range of signal models are shown in Table 8.2, with no significant deviations between the data and SM expectations observed.

	95% CL Limit [GeV]	
Channel	Expected	Observed
$\mu\nu jj$ ($\beta = 0.5$)	555	545

Table 8.1: Expected and observed limits on leptoquark mass.

m_{LQ} [GeV]	300	350	400	450	500	550	600	650	700
CL_b ($\beta = 0.5$)	0.593	0.633	0.774	0.818	0.697	0.364	0.214	0.276	0.163

Table 8.2: Confidence levels for the background-only hypothesis for a range of signal+background hypotheses with $\beta = 0.5$.

These limits have been extended into the β vs. m_{LQ} plane by varying the value of β incrementally between 0 and 1. The resulting exclusion region is shown in Figure 8.3.

[1] In practice, a problem only arises if data events fall in these empty bins.

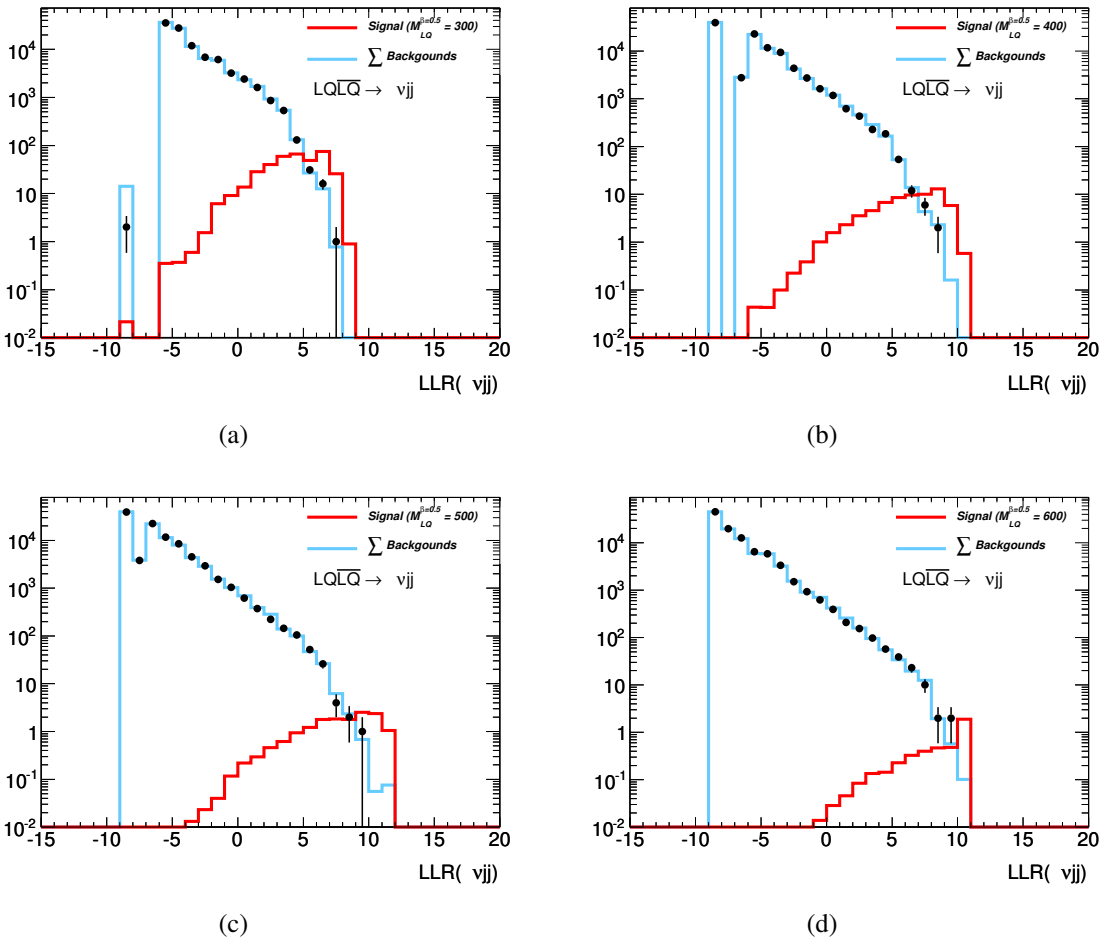

Figure 8.1: Re-binned LLR distributions used as input to the limit-setting software package, for $m_{\mathrm{LQ}} = 300$ (a), 400 (b), 500 (c), and 600 (d) GeV.

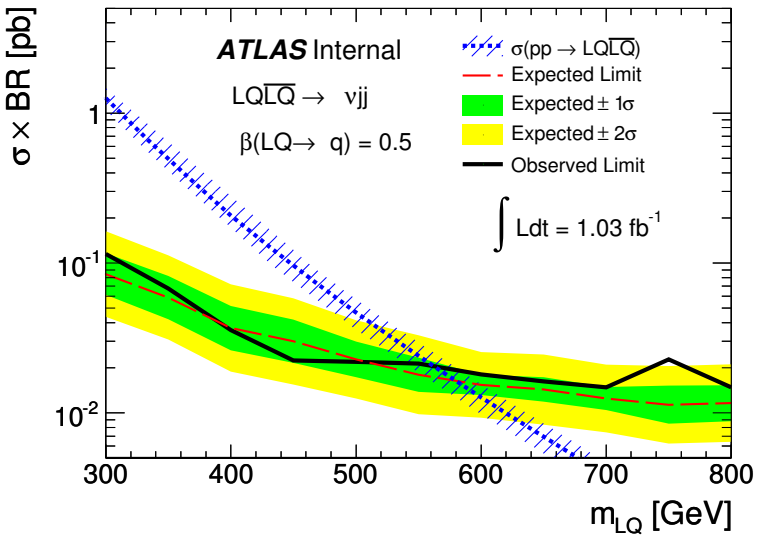

(a)

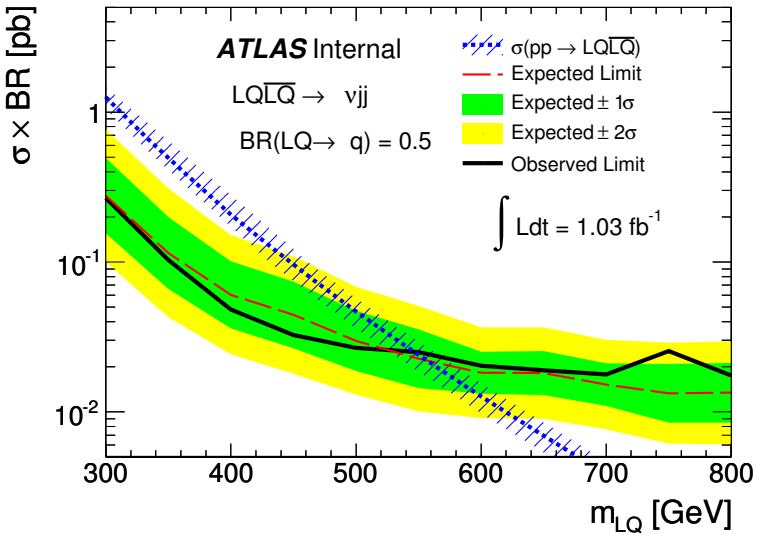

(b)

Figure 8.2: Expected and observed cross section limits as a function of leptoquark mass, with (a) and without (b) systematic uncertainties included.

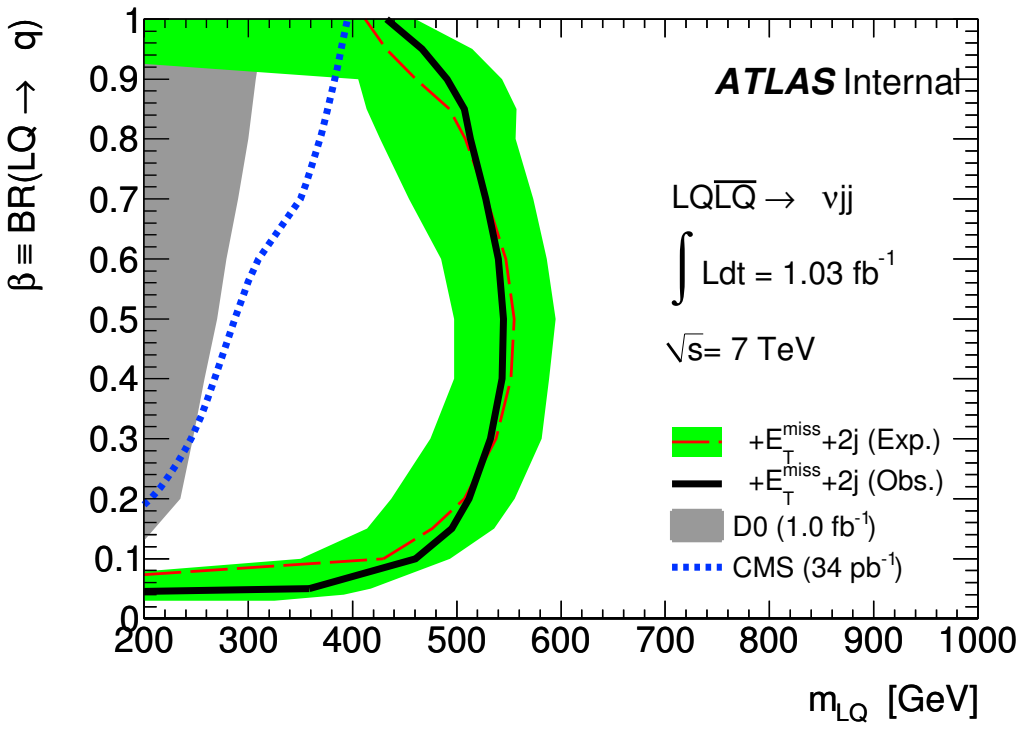

Figure 8.3: Expected and observed limits as a function of leptoquark mass and branching ratio of a leptoquark into a muon and a quark. The green band shows the 1σ systematic uncertainty. Previous results from DØ and CMS are drawn in gray and blue, respectively.

8.2 Combination with $\mu\mu jj$ Channel

As is often the case, the second-generation leptoquark search on ATLAS was split into orthogonal channels in order to maximize experimental sensitivity to the signal. As described in Chapter 1, the analysis reported here was for the $\mu\nu jj$ channel, in which one leptoquark decays into a muon and a quark and the other decays into a muon neutrino and a quark. An analysis was also performed separately for the $\mu\mu jj$ channel, in which both leptoquarks decay into a muon and a quark. The former is maximal at branching fraction $\beta = 0.5$, the latter at $\beta = 1.0$. The results for the $\mu\nu jj$ channel, reported in detail above, were readily combined with those for the $\mu\mu jj$ channel, as given in Equation 7.3.

Cross section limits from this combination are shown in Figure 8.4. Expected and observed mass limits for the $\mu\nu jj$ ($\beta = 0.5$) and $\mu\mu jj$ ($\beta = 1.0$) channels individually, as well as the combined LQ_2 limits at both branching fractions, are shown in Table 8.3. The generalization into the β-m_{LQ} plane is shown in Figure 8.5; exclusion regions for both channels individually are also drawn for comparison with the combination. Note that at all branching ratios, the combined limit is stronger than its individual components.

Channel	95% CL Limit [GeV]	
	Expected	Observed
$\mu\nu jj$ ($\beta = 0.5$)	555	545
$\mu\mu jj$ ($\beta = 1.0$)	665	675
LQ_2 ($\beta = 0.5$)	605	594

Table 8.3: Expected and observed limits on leptoquark mass for the combination of $\mu\nu jj$ and $\mu\mu jj$ channels.

m_{LQ} [GeV]	300	350	400	450	500	550	600	650	700
CL_b ($\mu\nu jj$, $\beta = 0.5$)	0.593	0.633	0.774	0.818	0.697	0.364	0.214	0.276	0.163
CL_b ($\mu\mu jj$, $\beta = 1.0$)	0.844	0.694	0.831	0.796	0.734	0.754	0.572	0.801	0.662
CL_b (LQ_2, $\beta = 0.5$)	0.689	0.677	0.897	0.900	0.808	0.611	0.327	0.480	0.359

Table 8.4: Confidence levels for the background-only hypothesis for a range of signal+background hypotheses and for the combination of $\mu\nu jj$ and $\mu\mu jj$ channels.

In all cases, observations are consistent with Standard Model expectations; however, more than one data event was *notable* in that it was particularly signal-like. An

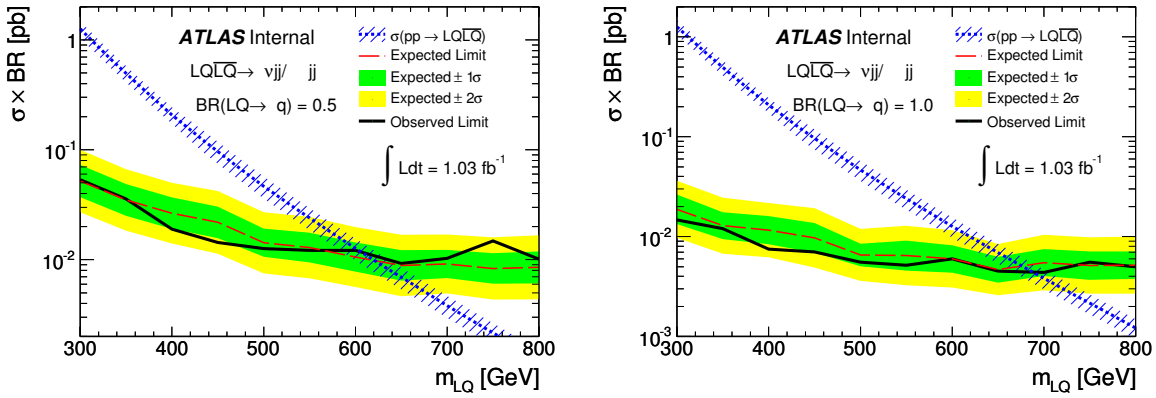

(a)

(b)

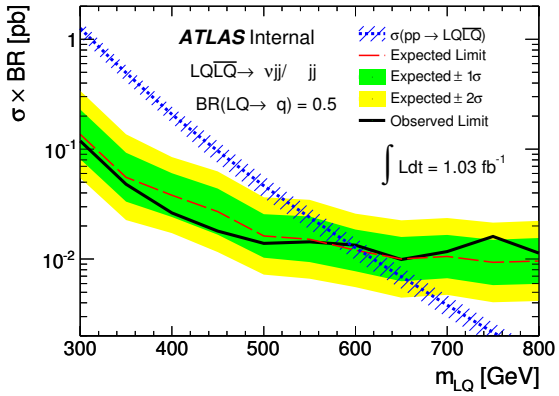

(c)

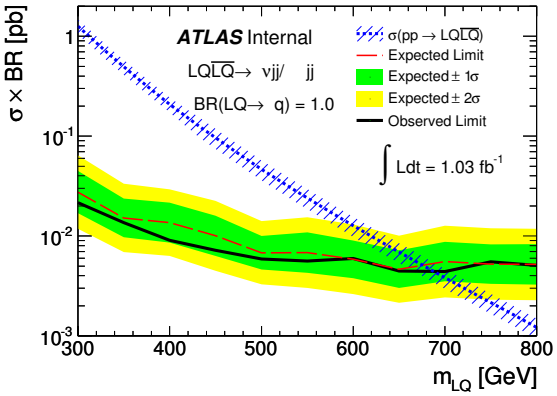

(d)

Figure 8.4: Expected and observed cross section limits as a function of leptoquark mass for the combination of $\mu\nu jj$ and $\mu\mu jj$ channels: (a) no systematics, $\beta = 0.5$; (b) no systematics, $\beta = 1$; (c) all systematics, $\beta = 0.5$; (d) all systematics, $\beta = 1$.

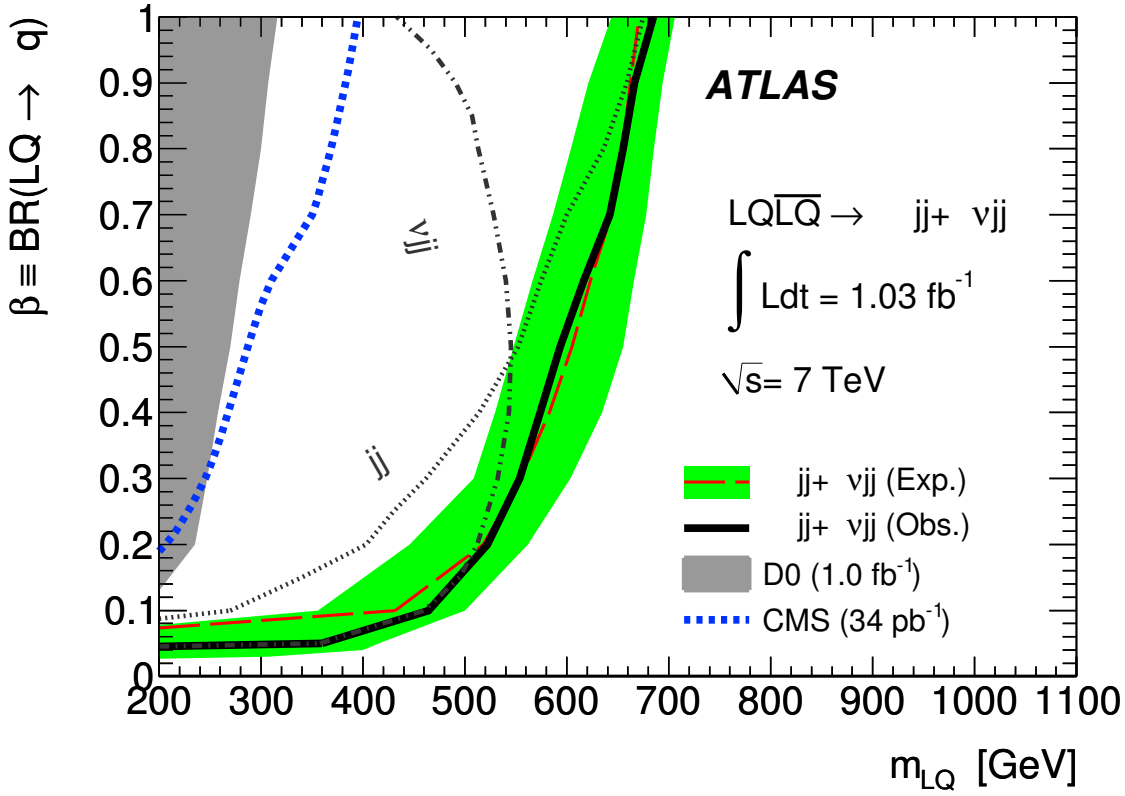

Figure 8.5: Expected and observed limits as a function of leptoquark mass and branching fraction of a leptoquark into a muon and a quark $\mu\nu jj$ and $\mu\mu jj$ channels. The green band shows the 1σ systematic uncertainty. Previous results from DØ and CMS are drawn in gray and blue, respectively, as well as limits for the individual ATLAS search channels.

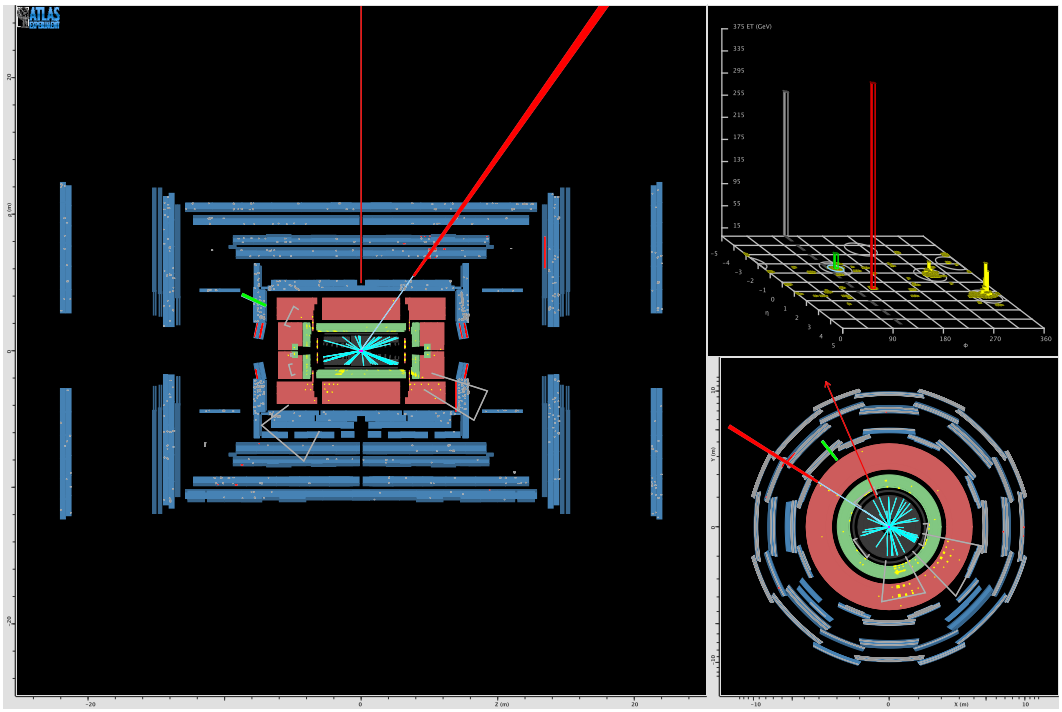

Figure 8.6: ATLANTIS event display for a signal-like data event: run number 183286, event number 121863097.

ATLANTIS [160] event display for one such event in the $\mu\nu jj$ channel is shown in Figure 8.6, and relevant kinematic properties are summarized in Table 8.5. Although no evidence for second-generation scalar leptoquark production was observed, higher mass ranges remain unexplored!

8.3 Future Outlook

An early feasibility study performed by ATLAS prior to LHC operations [161] determined that the experiment should be sensitive to all generations of pair-produced leptoquarks up to $m_{\mathrm{LQ}} \approx 1.4$ TeV — depending, of course, on decay modes and branching ratios — with 30 fb^{-1} of integrated luminosity of data at a center-of-mass energy of $\sqrt{s} = 14$ TeV. For reasons discussed in Chapter 2, the LHC operated at half-power in its 2010 and 2011 runs; *however*, in its 2012 run, the LHC is running at $\sqrt{s} = 8$ TeV, and it is expected to deliver $\mathscr{L}_{\mathrm{int}} \sim 15$ fb^{-1} before an 18-month shutdown in December for repairs and upgrades. While the increases in $\sqrt{s}$ and $\mathscr{L}_{\mathrm{int}}$ over the 2011 dataset used in this analysis are modest, they do have a significant impact on the expected sensitivity to LQ signals. Figure 8.7 shows the

Event	Run #	183286
	Event #	121863097
	Lumi Block #	558
Muon	p_{T}	379 GeV
	η	0.66
	ϕ	2.58
	match $\chi^2/ndof$	20.37/5
Jets	$p_T(\mathrm{jet}_1)$	426 GeV
	$\eta(\mathrm{jet}_1)$	1.56
	$\phi(\mathrm{jet}_1)$	-0.5
	$p_T(\mathrm{jet}_2)$	248 GeV
	$\eta(\mathrm{jet}_2)$	-0.79
	$\phi(\mathrm{jet}_2)$	-1.37
Missing E_{T}	$\not{E}_{\mathrm{T}}$	258 GeV
	$\phi(\not{E}_{\mathrm{T}})$	2.07
LLR	$m_{\mathrm{T}}(\not{E}_{\mathrm{T}},\mu)$	158 GeV
	$m_{\mathrm{T}}(LQ)$	637 GeV
	$m(LQ)$	743 GeV
	S_{T}	1311 GeV

Table 8.5: Parameters of interest and their values for a notably signal-like data event. Run number 183286, event number 121863097.

ratio of the LQ pair-production cross section at NLO for $\sqrt{s} = 8$ TeV and 7 TeV: the enhancement of $\sigma(8\text{ TeV})$ over $\sigma(7\text{ TeV})$ increases with m_{LQ}, from a factor of ~ 2 up to ~ 3.5. For comparison, the $t\bar{t}$ cross section at 8 TeV is increased by a factor ~ 1.4 over its value at 7 TeV.

Another avenue for potential improvement is in the final discriminating variable used to distinguish SM background from LQ signal. The log-likelihood ratio used in this analysis was limited to four input variables for simplicity, but the addition of one or more variables (perhaps among those shown in Figure 5.12) could, in principle, enhance its discriminating power. Furthermore, while LLRs are definite improvements over traditional "square cuts" on one or more variables, it is not the most sophisticated technique available. *Artificial Neural Networks* are systems of interconnected processing nodes whose weighted, adaptive connections depend on the inputs and the nodes themselves, allowing for powerful, non-linear statistical analysis [162] [163]. *Boosted Decision Trees* are sequences of binary splits in event samples that progressive separate signal from background, effectively combining many weakly-discriminating variables into a more powerful final classifier while avoiding some of the pitfalls of neural networks [164] [165]. Either one could

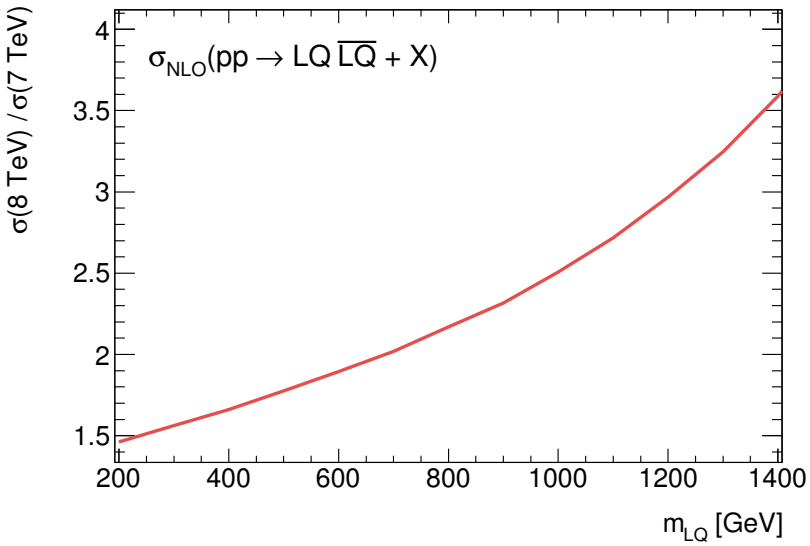

Figure 8.7: Ratio of next-to-leading cross sections for leptoquark pair-production at $\sqrt{s} = 8$ TeV and 7 TeV.

potentially enhance signal sensitivity.

Lastly, performing a search in the complementary $\nu\nu qq$ ($\not{E}_{\mathrm{T}}+$ jets) channel, which is maximal for $\beta = 0$, would greatly improve sensitivity in the low-β range. Considering that this event signature is common to many BSM searches (e.g. SUSY), it should not be unduly difficult to adapt existing studies to an additional leptoquark search.

CHAPTER 9

Conclusion

> Your theory is crazy, but it's not crazy enough to be true.
>
> Niels Bohr

The results of a search for pair-production of second-generation, scalar leptoquarks in the muon plus missing transverse energy plus jets final state have been presented. The analysis was performed on a dataset recorded in the first months of the 2011 LHC pp run, corresponding to 1.03 fb^{-1} of integrated luminosity at $\sqrt{s} = 7$ TeV. Standard Model backgrounds were estimated using Monte Carlo simulated samples as well as data-driven techniques. Comparisons between data observed and background predicted in signal-poor control regions were used to verify and improve modeling of the dominant W+jets and $t\bar{t}$ contributions. After applying event selection criteria based on the leptoquark signal topology, a multivariate log-likelihood ratio discriminant was computed to distinguish between signal and background events. Good agreement was found between the data and Standard Model prediction for the LLR distributions; therefore, 95% CL upper limits on the LQ production cross section were set. Re-interpreted in the m_{LQ} vs. $\beta \equiv \mathrm{BR}(\mathrm{LQ} \to \mu q)$ plane, the limit excludes leptoquarks with $m_{\mathrm{LQ}} < 545$ GeV for $\beta = 0.5$ at 95% CL. Combining these limits with those from the orthogonal, complementary di-muon plus jets channel extended the exclusion region: leptoquarks with $m_{\mathrm{LQ}} < 594$ (685) GeV for $\beta = 0.5$ (1.0) were excluded at 95% CL. These are currently the world's

best limits on second-generation scalar leptoquark production [166].

The sensitivity of this analysis was limited by a number of factors. Searches for new physics typically run up against insufficient statistics in the data, and the LQ_2 search was no exception. As the LHC delivers and ATLAS records more data, the analysis reach will extend to higher leptoquark masses. Furthermore, higher-energy collisions significantly increase LQ production cross sections, improving sensitivity through enhanced signal statistics. The full 2011 LHC pp run amounted to roughly 5 fb^{-1} of data; in 2012, the LHC is running at $\sqrt{s} = 8$ TeV, and the expected integrated luminosity is ~ 15 fb^{-1}. Understanding of the ATLAS detector is ever improving, so systematic uncertainties associated with the detector itself — most notably the jet energy scale and resolution — are reduced over time. Similarly, studies of top quark and vector boson production at the LHC, along with continued progress in MC event generation, may lead to improved modeling of these backgrounds and consequently reduced systematic uncertainties. Clearly, significant improvements in sensitivity to leptoquark production can be expected in subsequent iterations of the analysis.

Although the analysis presented here was (largely) model-independent, one experimentally-motivated assumption was that LQs couple only to quarks and leptons of the same generation. As such, this second-generation LQ search is complementary to searches for first- and third-generation leptoquarks. An (ATLAS) analysis has been published for pair-production of first-generation scalar leptoquarks, yielding a comparable exclusion region in the m_{LQ1} vs. β plane [167]. Work on a third-generation LQ search is ongoing.

The Standard Model has been spectacularly successful in describing the properties and interactions of the elementary constituents of matter; however, both theoretical and experimental considerations strongly suggest that new physics is to be found at higher energy scales. The LHC and its experiments have been designed to explore this new *energy frontier*. Thousands of physicists work to operate the experiments safely and productively, simulate and reconstruct hadron collision events, and analyze the data for a better understanding of Nature on its most fundamental level. What they find — be it leptoquarks, or something else — remains to be seen.

Bibliography

[1] D.J. Griffiths. *Introduction to Elementary Particles*. Wiley, New York, NY, 2008.

[2] W.N. Cottingham and D.A. Greenwood. *An Introduction to the Standard Model of Particle Physics*. Cambridge University Press, Cambridge, UK, 2007.

[3] Francis Halzen and Alan Martin. *Quarks and Leptons: An Introductory Course in Modern Particle Physics*. Wiley & Sons, New York, NY, 1984.

[4] K. Nakamura et al. Review of particle physics. *J.Phys.G*, G37:075021, 2010.

[5] A.D. Sakharov. Violation of CP Invariance, c Asymmetry, and Baryon Asymmetry of the Universe. *Pisma Zh.Eksp.Teor.Fiz.*, 5:32–35, 1967.

[6] Michael E. Peskin. The Matter with antimatter. *Nature*, 419:24–27, 2002.

[7] S. Fukuda et al. Solar B-8 and hep neutrino measurements from 1258 days of Super-Kamiokande data. *Phys.Rev.Lett.*, 86:5651–5655, 2001.

[8] Ziro Maki, Masami Nakagawa, and Shoichi Sakata. Remarks on the unified model of elementary particles. *Prog.Theor.Phys.*, 28:870–880, 1962.

[9] R P Feynman. *Quantum Electrodynamics: A Lecture Note and Reprint Volume*. W Z Benjamin, New York, NY, 1961.

[10] Michele Maggiore. *A Modern Introduction to Quantum Field Theory*. Oxford University Press, Oxford, UK, 2005.

[11] Roger Penrose. *The Road to Reality: A Complete Guide to the Laws of the Universe*. Jonathan Cape, London, UK, 2005.

[12] R Escribano and E Mass. High precision tests of QED and physics beyond the standard model. Technical Report hep-ph/9607218. UAB-FT-385, Barcelona Univ. Dept. Fs. Ter., Barcelona, Jul 1996.

[13] S.L. Glashow. Partial Symmetries of Weak Interactions. *Nucl.Phys.*, 22: 579–588, 1961.

[14] Steven Weinberg. A Model of Leptons. *Phys.Rev.Lett.*, 19:1264–1266, 1967.

[15] Abdus Salam. Weak and Electromagnetic Interactions. *Conf.Proc.*, C680519:367–377, 1968.

[16] Peter W. Higgs. Broken symmetries, massless particles and gauge fields. *Phys.Lett.*, 12:132–133, 1964.

[17] Georges *et al.* Aad. Combined search for the Standard Model Higgs boson using up to 4.9 fb^{-1} of pp collision data at $\sqrt{s}$ = 7 TeV with the ATLAS detector at the LHC. *Phys. Lett. B*, 710(arXiv:1202.1408. CERN-PH-EP-2012-019):49–66, Feb 2012.

[18] Serguei *et al.* Chatrchyan. Combined results of searches for the standard model Higgs boson in pp collisions at $\sqrt{s}$ = 7 TeV. *Phys. Lett. B*, 710:26–48, Feb 2012.

[19] Paul Langacker. Introduction to the Standard Model and Electroweak Physics. pages 3–48, 2009.

[20] Fred Jegerlehner and Andreas Nyffeler. The Muon g-2. *Phys.Rept.*, 477: 1–110, 2009. doi: 10.1016/j.physrep.2009.04.003.

[21] John D. Hobbs, Mark S. Neubauer, and Scott Willenbrock. Tests of the Standard Electroweak Model at the Energy Frontier. 2010.

[22] Katherine Garrett and Gintaras Duda. Dark Matter: A Primer. *Adv.Astron.*, 2011:968283, 2011.

[23] Lars Bergstrom. Nonbaryonic dark matter: Observational evidence and detection methods. *Rept.Prog.Phys.*, 63:793, 2000.

[24] Joseph D. Lykken. Beyond the Standard Model. 2010.

[25] A. Pomarol. Beyond the Standard Model. 2012.

[26] David E. Morrissey, Tilman Plehn, and Tim M.P. Tait. Physics searches at the LHC. *Phys.Rept.*, 515:1–113, 2012.

[27] J. Wess and B. Zumino. A Lagrangian Model Invariant Under Supergauge Transformations. *Phys.Lett.*, B49:52, 1974.

[28] Jogesh C. Pati and Abdus Salam. Lepton Number as the Fourth Color. *Phys.Rev.*, D10:275–289, 1974.

[29] H. Georgi and S.L. Glashow. Unity of All Elementary Particle Forces. *Phys.Rev.Lett.*, 32:438–441, 1974.

[30] Harald Fritzsch and Peter Minkowski. Unified Interactions of Leptons and Hadrons. *Annals Phys.*, 93:193–266, 1975.

[31] Steven Weinberg. Implications of Dynamical Symmetry Breaking. *Phys.Rev.*, D13:974–996, 1976.

[32] Steven Weinberg. Implications of Dynamical Symmetry Breaking: An Addendum. *Phys.Rev.*, D19:1277–1280, 1979.

[33] E Farhi and Leonard Susskind. Technicolour. *Phys. Rep.*, 74(CERN-TH-2975. 3):277–321. 66 p, Oct 1980.

[34] Estia Eichten and Kenneth D. Lane. Dynamical Breaking of Weak Interaction Symmetries. *Phys.Lett.*, B90:125–130, 1980.

[35] Christopher T. Hill and Elizabeth H. Simmons. Strong dynamics and electroweak symmetry breaking. *Phys.Rept.*, 381:235–402, 2003.

[36] JoAnne L. Hewett and Thomas G. Rizzo. Much ado about leptoquarks: A Comprehensive analysis. *Phys.Rev.*, D56:5709–5724, 1997.

[37] W. Buchmuller, R. Ruckl, and D. Wyler. Leptoquarks in Lepton - Quark Collisions. *Phys.Lett.*, B191:442–448, 1987.

[38] Masahiro Kuze and Yves Sirois. Search for particles and forces beyond the standard model at HERA ep and Tevatron $p\bar{p}$ colliders. *Prog.Part.Nucl.Phys.*, 50:1–62, 2003.

[39] H. Murayama and T. Yanagida. A viable SU(5) GUT with light leptoquark bosons. *Mod.Phys.Lett.*, A7:147–152, 1992.

[40] Kenneth D. Lane. Technihadron production and decay in low scale technicolor. *Phys.Rev.*, D60:075007, 1999.

[41] Alexander Belyaev, Claude Leroy, Rashid Mehdiyev, and Alexander Pukhov. Leptoquark single and pair production at LHC with CalcHEP/CompHEP in the complete model. *JHEP*, 0509:005, 2005.

[42] Sergey Kovalenko and Ivan Schmidt. Proton stability in leptoquark models. *Phys.Lett.*, B562:104–108, 2003.

[43] M. Kramer, T. Plehn, M. Spira, and P.M. Zerwas. Pair production of scalar leptoquarks at the CERN LHC. *Phys.Rev.*, D71:057503, 2005.

[44] C. Regis et al. Search for Proton Decay into Muon plus Neutral Kaon in Super-Kamiokande I, II, and III. 2012.

[45] King-man Cheung. Muon anomalous magnetic moment and leptoquark solutions. *Phys.Rev.*, D64:033001, 2001.

[46] Miriam Leurer. A Comprehensive study of leptoquark bounds. *Phys.Rev.*, D49:333–342, 1994.

[47] G.K. Leontaris and J.D. Vergados. Constraints on leptoquark masses and couplings from rare processes and unification. *Phys.Lett.*, B409:283–287, 1997.

[48] F.D. Aaron, C. Alexa, V. Andreev, S. Backovic, A. Baghdasaryan, et al. Search for First Generation Leptoquarks in ep Collisions at HERA. *Phys.Lett.*, B704:388–396, 2011.

[49] 894023. Search for Lepton Flavour Violation at HERA. 2011.

[50] V.M. Abazov et al. Search for pair production of first-generation leptoquarks in p anti-p collisions at s**(1/2) = 1.96-TeV. *Phys.Lett.*, B681:224–232, 2009.

[51] V.M. Abazov et al. Search for pair production of second generation scalar leptoquarks. *Phys.Lett.*, B671:224–232, 2009.

[52] Cecile Deterre. Search for scalar bottom quarks and third-generation leptoquarks in $p\bar{p}$ collisions at $\sqrt{s}$ = 1.96 TeV. *PoS*, ICHEP2010:418, 2010.

[53] Georges Aad et al. Search for pair production of first or second generation leptoquarks in proton-proton collisions at sqrt(s)=7 TeV using the ATLAS detector at the LHC. *Phys.Rev.*, D83:112006, 2011.

[54] Vardan Khachatryan et al. Search for Pair Production of First-Generation Scalar Leptoquarks in pp Collisions at sqrt(s) = 7 TeV. *Phys.Rev.Lett.*, 106: 201802, 2011.

[55] Vardan Khachatryan et al. Search for Pair Production of Second-Generation Scalar Leptoquarks in pp Collisions at sqrt(s) = 7 TeV. *Phys.Rev.Lett.*, 106: 201803, 2011.

[56] Lyndon R Evans and Philip Bryant. LHC Machine. *J. Instrum.*, 3:S08001. 164 p, 2008. This report is an abridged version of the LHC Design Report (CERN-2004-003).

[57] European Organization for Nuclear Research. CERN Home Page. https://public.web.cern.ch/public/, 2012.

[58] S Myers. LHC Commissioning and First Operation. (CERN-ATS-2010-123):6 p, Jun 2010.

[59] G *et al.* Aad. The ATLAS Experiment at the CERN Large Hadron Collider. *J. Instrum.*, 3:S08003. 437 p, 2008. Also published by CERN Geneva in 2010.

[60] S *et al.* Chatrchyan. The CMS experiment at the CERN LHC. *J. Instrum.*, 3: S08004. 361 p, 2008. Also published by CERN Geneva in 2010.

[61] A Augusto *et al.* Alves. The LHCb Detector at the LHC. *J. Instrum.*, 3: S08005, 2008. Also published by CERN Geneva in 2010.

[62] K *et al.* Aamodt. The ALICE experiment at the CERN LHC. A Large Ion Collider Experiment. *J. Instrum.*, 3:S08002. 259 p, 2008. Also published by CERN Geneva in 2010.

[63] G *et al.* Anelli. The TOTEM Experiment at the CERN Large Hadron Collider. *J. Instrum.*, 3:S08007, 2008.

[64] O *et al.* Adriani. The LHCf detector at the CERN Large Hadron Collider. *J. Instrum.*, 3:S08006, 2008.

[65] R Scrivens, M Kronberger, D Kchler, J Lettry, C Mastrostefano, O Midttun, M ONeil, H Pereira, and C Schmitzer. Overview of the status and developments on preliminary ion sources at CERN. Technical Report CERN-ATS-2011-172, CERN, Geneva, Sep 2011.

[66] Karlheinz Schindl. The Injector Chain for the LHC. (CERN-PS-99-018-DI): 7 p, Mar 1999.

[67] Michael Benedikt, R Cappi, M Chanel, R Garoby, Massimo Giovannozzi, S Hancock, M Martini, Elias Mtral, G Mtral, Karlheinz Schindl, and J L Vallet. Performance of the LHC Pre-Injectors. (CERN-PS-2001-011-DR):6 p, Apr 2001.

[68] R Bailey and Paul Collier. Standard Filling Schemes for Various LHC Operation Modes. Technical Report LHC-PROJECT-NOTE-323, CERN, Geneva, Sep 2003.

[69] Oliver Sim Brning, Paul Collier, P Lebrun, Stephen Myers, Ranko Ostojic, John Poole, and Paul Proudlock. *LHC Design Report*. CERN, Geneva, 2004.

[70] The International System of Units. http://www.bipm.org/en/si/si_brochure/general.html, 2006.

[71] ATLAS Fact Sheet. http://www.atlas.ch/fact-sheets-view.html. Information brochure distributed by the ATLAS Secretariat.

[72] LHC Experiments Committee. *ATLAS detector and physics performance: Technical Design Report, Volumes 1 and 2*. Technical Design Report ATLAS. CERN, Geneva, 1999.

[73] *ATLAS magnet system: Technical Design Report*. Technical Design Report ATLAS. CERN, Geneva, 1997.

[74] *ATLAS inner detector: Technical Design Report, 1*. Technical Design Report ATLAS. CERN, Geneva, 1997.

[75] Muon Momentum Resolution in First Pass Reconstruction of pp Collision Data Recorded by ATLAS in 2010. Technical Report ATLAS-CONF-2011-046, CERN, Geneva, Mar 2011.

[76] Antonio Salvucci. Measurement of muon momentum resolution of the ATLAS detector. Technical Report arXiv:1201.4704, Jan 2012. Comments: Presented at the 2011 Hadron Collider Physics symposium (HCP-2011), Paris, France, November 14-18 2011.

[77] Norbert Wermes and G Hallewel. *ATLAS pixel detector: Technical Design Report*. Technical Design Report ATLAS. CERN, Geneva, 1998.

[78] Jet energy resolution and selection efficiency relative to track jets from in-situ techniques with the ATLAS Detector Using Proton-Proton Collisions at a Center of Mass Energy *sqrts* = 7 TeV. Technical Report ATLAS-CONF-2010-054, CERN, Geneva, Jul 2010.

[79] *ATLAS liquid-argon calorimeter: Technical Design Report*. Technical Design Report ATLAS. CERN, Geneva, 1996.

[80] *ATLAS tile calorimeter: Technical Design Report*. Technical Design Report ATLAS. CERN, Geneva, 1996.

[81] *ATLAS muon spectrometer: Technical Design Report*. Technical Design Report ATLAS. CERN, Geneva, 1997.

[82] Jeremiah Jet Goodson. Private communication.

[83] J C Barriere, F Bauer, M Fontaine, A Formica, V Gautard, P F Giraud, H Graaf, C Guyot, R Hart, S Horvat, O Kortner, S Kotov, H Kroha, F Linde, I Ponsot, I Potrap, and P Schune. The alignment system of the barrel part of the ATLAS muon spectrometer. Technical Report ATL-MUON-PUB-2008-007. ATL-COM-MUON-2008-002, CERN, Geneva, Jan 2008.

[84] S Aefsky, C Amelung, J Bensinger, C Blocker, A Dushkin, M Gardner, K Hashemi, E Henry, B Kaplan, M Ketchum, P Keselman, U Landgraf, A Ostapchuk, J E Rothberg, A Schricker, N Skvorodnev, and H Wellenstein. The Optical Alignment System of the ATLAS Muon Spectrometer Endcaps. *J. Instrum.*, 3(ATL-MUON-PUB-2008-003. ATL-COM-MUON-2008-005): P11005. 49 p, Feb 2008.

[85] Peter Jenni and Marzio Nessi. ATLAS Forward Detectors for Luminosity Measurement and Monitoring. Technical Report CERN-LHCC-2004-010. LHCC-I-014, CERN, Geneva, Mar 2004.

[86] Peter Jenni, Marzio Nessi, and Markus Nordberg. Zero Degree Calorimeters for ATLAS. Technical Report LHCC-I-016. CERN-LHCC-2007-001, CERN, Geneva, Jan 2007.

[87] Peter Jenni, Markus Nordberg, Marzio Nessi, and Kerstin Jon-And. *ATLAS Forward Detectors for Measurement of Elastic Scattering and Luminosity*. Technical Design Report. CERN, Geneva, 2008.

[88] *ATLAS level-1 trigger: Technical Design Report*. Technical Design Report ATLAS. CERN, Geneva, 1998.

[89] Peter Jenni, Marzio Nessi, Markus Nordberg, and Kenway Smith. *ATLAS high-level trigger, data-acquisition and controls: Technical Design Report*. Technical Design Report ATLAS. CERN, Geneva, 2003.

[90] G. Aad et al. The ATLAS Simulation Infrastructure. *Eur.Phys.J.*, C70:823–874, 2010.

[91] Andy Buckley, Jonathan Butterworth, Stefan Gieseke, David Grellscheid, Stefan Hoche, et al. General-purpose event generators for LHC physics. *Phys.Rept.*, 504:145–233, 2011.

[92] M.A. Dobbs, S. Frixione, Eric Laenen, K. Tollefson, H. Baer, et al. Les Houches guidebook to Monte Carlo generators for hadron collider physics. pages 411–459, 2004. Compiled by the Working Group on Quantum Chromodynamics and the Standard Model.

[93] Frank Siegert. Monte-Carlo event generation for the LHC, 2010. Doctoral thesis, Durham University. Available at Durham E-Theses Online: http://etheses.dur.ac.uk/484/.

[94] M.L. Mangano and T.J. Stelzer. Tools for the simulation of hard hadronic collisions. *Ann.Rev.Nucl.Part.Sci.*, 55:555–588, 2005.

[95] Torbjorn Sjostrand *et al*. PYTHIA Home Page. http://home.thep.lu.se/~torbjorn/Pythia.html, 2012.

[96] Torbjorn Sjostrand, Stephen Mrenna, and Peter Z. Skands. PYTHIA 6.4 Physics and Manual. *JHEP*, 0605:026, 2006.

[97] Torbjorn Sjostrand, Stephen Mrenna, and Peter Z. Skands. A Brief Introduction to PYTHIA 8.1. *Comput.Phys.Commun.*, 178:852–867, 2008.

[98] Mike Seymour. Herwig Home Page. http://hepwww.rl.ac.uk/theory/seymour/herwig/.

[99] G. Corcella, I.G. Knowles, G. Marchesini, S. Moretti, K. Odagiri, et al. HERWIG 6.5 release note. 2002.

[100] M. Bahr, S. Gieseke, M.A. Gigg, D. Grellscheid, K. Hamilton, et al. Herwig++ Physics and Manual. *Eur.Phys.J.*, C58:639–707, 2008. 143 pages, program and additional information available from http://projects.hepforge.org/herwig.

[101] Sherpa home page. http://www.sherpa-mc.de/, 2011.

[102] Tanju Gleisberg, Stefan Hoche, Frank Krauss, Marek Schonherr, Steffen Schumann, Frank Siegert, and Jan Winter. SHERPA manual. Technical report, July 2008.

[103] Michelangelo L. Mangano, Mauro Moretti, Fulvio Piccinini, Roberto Pittau, and Antonio D. Polosa. ALPGEN, a generator for hard multiparton processes in hadronic collisions. *JHEP*, 0307:001, 2003.

[104] ALPGEN Home Page. http://mlm.home.cern.ch/mlm/alpgen/, May 2011.

[105] Borut Paul Kersevan and Elzbieta Richter-Was. The Monte Carlo event generator AcerMC version 2.0 with interfaces to PYTHIA 6.2 and HERWIG 6.5. 2004.

[106] AcerMC Home Page. http://borut.home.cern.ch/borut/.

[107] Stefano Frixione and Bryan R. Webber. Matching NLO QCD computations and parton shower simulations. *JHEP*, 0206:029, 2002.

[108] The MC@NLO Package. http://www.hep.phy.cam.ac.uk/theory/webber/MCatNLO/.

[109] Paolo Nason. A New method for combining NLO QCD with shower Monte Carlo algorithms. *JHEP*, 0411:040, 2004.

[110] The POWHEG Box. http://powhegbox.mib.infn.it/.

[111] JIMMY4: Multiparton Interactions in HERWIG for the LHC. Technical report, October 2004.

[112] M. Dobbs and J. Hansen. The HepMC C++ Monte Carlo event record for High Energy Physics. *Comput. Phys. Commun.*, 134:41–46, 2001.

[113] K *et al* Assamagan. The ATLAS Monte Carlo Project. Technical Report ATL-SOFT-INT-2010-002, CERN, Geneva, Feb 2010.

[114] S. Agostinelli *et al.* Geant4 – a simulation toolkit. *Nuclear Instruments and Methods A*, 506:250–303, 2003.

[115] Geant4 Collaboration. Introduction to Geant4, 2011.

[116] B Lenzi. The Physics Analysis Tools project for the ATLAS experiment. Technical Report ATL-COM-SOFT-2009-020, CERN, Geneva, Oct 2009.

[117] A Collaboration. Performance of the ATLAS Inner Detector Track and Vertex Reconstruction in the High Pile-Up LHC Environment. Technical Report ATLAS-COM-CONF-2012-014, CERN, Geneva, Feb 2012.

[118] T Cornelissen, M Elsing, S Fleischmann, W Liebig, E Moyse, and A Salzburger. Concepts, Design and Implementation of the ATLAS New Tracking (NEWT). Technical Report ATL-SOFT-PUB-2007-007. ATL-COM-SOFT-2007-002, CERN, Geneva, Mar 2007.

[119] R. Fruhwirth. Application of Kalman filtering to track and vertex fitting. *Nucl.Instrum.Meth.*, A262:444–450, 1987.

[120] Georges *et al.* Aad. *Expected performance of the ATLAS experiment: detector, trigger and physics*. CERN, Geneva, 2009.

[121] Performance of primary vertex reconstruction in proton-proton collisions at $\sqrt{s}$ =7 TeV in the ATLAS experiment. Technical Report ATLAS-CONF-2010-069, CERN, Geneva, Jul 2010.

[122] Rainer Bartoldus, Ignacio Aracena, Philippe Grenier, David Miller, Emanuel Strauss, et al. Characterization of Interaction-Point Beam Parameters Using the pp Event-Vertex Distribution Reconstructed in the ATLAS Detector at the LHC. *Conf.Proc.*, C100523:MOPEC008, 2010.

[123] R. Fruhwirth, W. Waltenberger, and P. Vanlaer. Adaptive vertex fitting. *J.Phys.G*, G34:N343, 2007.

[124] E Bouhova-Thacker, P Lichard, V Kostyukhin, W Liebig, M Limper, G Piacquadio, P Lichard, C Weiser, and P Lichard. Vertex Reconstruction in the ATLAS Experiment at the LHC. Technical Report ATL-INDET-PROC-2008-003. ATL-COM-INDET-2008-018, CERN, Geneva, Nov 2008. 14.11.2008.

[125] Muon Reconstruction Performance. Technical Report ATLAS-CONF-2010-064, CERN, Geneva, Jul 2010.

[126] B Resende. Muon identification algorithms in ATLAS. Technical Report ATL-PHYS-PROC-2009-113, CERN, Geneva, Sep 2009.

[127] R. Nicolaidou *et al.* Muon identification procedure for the ATLAS detector at the LHC using Muonboy reconstruction package and tests of its performance using cosmic rays and single beam data. *J. Phys.: Conf. Ser.*, 219, 2010.

[128] Matteo Cacciari, Gavin P. Salam, and Gregory Soyez. The Anti-k(t) jet clustering algorithm. *JHEP*, 0804:063, 2008.

[129] W Lampl, S Laplace, D Lelas, P Loch, H Ma, S Menke, S Rajagopalan, D Rousseau, S Snyder, and G Unal. Calorimeter Clustering Algorithms: Description and Performance. Technical Report ATL-LARG-PUB-2008-002. ATL-COM-LARG-2008-003, CERN, Geneva, Apr 2008.

[130] Georges Aad et al. Jet energy measurement with the ATLAS detector in proton-proton collisions at sqrt(s) = 7 TeV. 2011.

[131] L Asquith, B Brelier, J M Butterworth, M Campanelli, T Carli, G Choudalakis, P A Delsart, S De Cecco, P O Deviveiros, M D'Onofrio, S Eckweiler, E Feng, P Francavilla, S Grinstein, I La Plante, J Huston, N Ghodbane, D Lopez Mateos, B Martin, N Makovec, S Majewsky, M Martinez, D W Miller, J Monk, K Perez, C Roda, J Robinson, A Schwartzmann, F Spano, K Terashi, F Vives, P Weber, and S Zenz. Performance of Jet Algorithms in the ATLAS Detector. Technical Report ATL-PHYS-INT-2010-129, CERN, Geneva, Dec 2010.

[132] Jet energy scale and its systematic uncertainty in proton-proton collisions at sqrt(s)=7 TeV in ATLAS 2010 data. Technical Report ATLAS-CONF-2011-032, CERN, Geneva, Mar 2011.

[133] Georges Aad et al. Electron performance measurements with the ATLAS detector using the 2010 LHC proton-proton collision data. *Eur.Phys.J.*, C72: 1909, 2012.

[134] Reconstruction and Calibration of Missing Transverse Energy and Performance in Z and W events in ATLAS Proton-Proton Collisions at 7 TeV. Technical Report ATLAS-CONF-2011-080, CERN, Geneva, Jun 2011.

[135] Peter Onyisi. Twiki: Dq flag interpretation. https://twiki.cern.ch/twiki/bin/viewauth/Atlas/DQFlagInterpretation, 2009.

[136] J.M. Butterworth *et al.* Single Boson and Diboson Production Cross Sections in pp Collisions at sqrt(s) = 7 TeV. 2010.

[137] Georges Aad et al. Measurement of the top quark-pair production cross section with ATLAS in pp collisions at $\sqrt{s} = 7$ TeV. *Eur.Phys.J.*, C71:1577, 2011.

[138] Sven Moch and Peter Uwer. Theoretical status and prospects for top-quark pair production at hadron colliders. *Phys.Rev.*, D78:034003, 2008.

[139] Muon Combined Performance Group. TWiki: Guidelines for Analyses of 2011 Data for PLHC. https://twiki.cern.ch/twiki/bin/viewauth/AtlasProtected/MCPAnalysisGuidelinesPLHC2011, .

[140] Data-Quality Requirements and Event Cleaning for Jets and Missing Transverse Energy Reconstruction with the ATLAS Detector in Proton-Proton Collisions at a Center-of-Mass Energy of sqrt(s) = 7 TeV. 2010.

[141] Jet/EtMiss Working Group. TWiki: How to clean jets in 2010 data. https://twiki.cern.ch/twiki/bin/viewauth/AtlasProtected/HowToCleanJets, .

[142] e/gamma working group. TWiki: ATLAS ElectronGamma. url-https://twiki.cern.ch/twiki/bin/viewauth/AtlasProtected/ElectronGamma, .

[143] e/gamma working group. TWiki: LAr Cleaning And Object Quality. url-https://twiki.cern.ch/twiki/bin/viewauth/AtlasProtected/LArCleaningAndObjectQuality, .

[144] E Castaneda Miranda, G Gaycken, P Kluit, O Kortner, E Le Menedeu, W Liebig, K Mueller, A Ouraou, K Schmieden, M Schott, E Van Der Poel, N Van Eldik, M Vanadia, and J Zhu. Determination of the muon reconstruction efficiency in ATLAS at the Z resonance in proton-proton collisons at sqrt(s)=7 TeV. Technical Report ATLAS-COM-CONF-2011-001, CERN, Geneva, Jan 2011.

[145] F Cerutti, C Gatti, P Kluit, O Kortner, W Liebig, J Liu, G Salamanna, A Salvucci, E van der Poel, and J Zhu. Muon Momentum Resolution in First Pass Reconstruction of pp Collision Data Recorded by ATLAS in 2010. Technical Report ATLAS-COM-CONF-2011-003, CERN, Geneva, Jan 2011.

[146] D W Miller, A Schwartzman, and D Su. Jet-Vertex Association Algorithm. Technical Report ATL-COM-PHYS-2008-008, CERN, Geneva, Jan 2008.

[147] Georges Aad et al. Search for pair production of first or second generation leptoquarks in proton-proton collisions at sqrt(s)=7 TeV using the ATLAS detector at the LHC. *Phys.Rev.*, D83:112006, 2011.

[148] Luminosity Determination in pp Collisions at sqrt(s) = 7 TeV using the ATLAS Detector in 2011. Technical Report ATLAS-CONF-2011-116, CERN, Geneva, Aug 2011.

[149] In-situ jet energy scale and jet shape corrections for multiple interactions in the first ATLAS data at the LHC. Technical Report ATLAS-CONF-2011-030, CERN, Mar 2011.

[150] F Cerutti, C Gatti, P Kluit, O Kortner, W Liebig, J Liu, G Salamanna, A Salvucci, E van der Poel, and J Zhu. Muon Momentum Resolution in First Pass Reconstruction of pp Collision Data Recorded by ATLAS in 2010. Technical Report ATLAS-COM-CONF-2011-003, CERN, Geneva, Jan 2011.

[151] Muon reconstruction efficiency in reprocessed 2010 LHC proton-proton collision data recorded with the ATLAS detector. Technical Report ATLAS-CONF-2011-063, CERN, Geneva, Apr 2011.

[152] Jet energy scale and its systematic uncertainty in proton-proton collisions at sqrt(s)=7 TeV in ATLAS 2010 data. Technical Report ATLAS-CONF-2011-032, CERN, Geneva, Mar 2011.

[153] G Romeo, A Schwartzman, R Piegaia, T Carli, and R Teuscher. Jet Energy Resolution from In-situ Techniques with the ATLAS Detector Using Proton-Proton Collisions at a Center of Mass Energy $\sqrt{s} = 7$ TeV. Technical Report ATL-COM-PHYS-2011-240, CERN, Geneva, Mar 2011.

[154] ATLAS Statistics Forum. Comments and Recommendations for Statistical Techniques, 2010.

[155] W. Fisher. Collie: A Confidence Level Limit Evaluator. Technical Report DØ note 5595, Fermilab, June 2009.

[156] Roger Barlow. *Statistics: A Guide to the Use of Statistical Methods in the Physical Sciences*, chapter 7,-8, pages 118–169. Wiley & Sons, August 1989. ISBN 978-0471922940.

[157] Thomas Junk. Confidence level computation for combining searches with small statistics. *Nucl.Instrum.Meth.*, A434:435–443, 1999.

[158] Alexander L. Read. Presentation of search results: The CLs technique. *J.Phys.G*, G28:2693–2704, 2002.

[159] ATLAS Collaboration. Searches for second generation leptoquarks in dimuon plus jets and muon, Missing ET plus jets final states using the ATLAS detector. 2012.

[160] ATLAS. ATLANTIS Event Display for ATLAS. http://www.hep.ucl.ac.uk/atlas/atlantis/, 2009.

[161] Vasiliki A. Mitsou, N. Ch. Benekos, I. Panagoulias, and Th.D. Papadopoulou. Prospects for scalar leptoquark discovery at the LHC. *Czech.J.Phys.*, 55:B659–B666, 2005.

[162] Carsten Peterson and Thorsteinn Rognvaldsson. An Introduction to artificial neural networks. 1991.

[163] C.A.L. Bailer-Jones, R. Gupta, and H.P. Singh. An introduction to artificial neural networks. 2001.

[164] B.P. Roe, Hai-Jun Yang, and Ji Zhu. Boosted decision trees, a powerful event classifier. pages 139–142, 2005.

[165] Byron P. Roe, Hai-Jun Yang, Ji Zhu, Yong Liu, Ion Stancu, et al. Boosted decision trees, an alternative to artificial neural networks. *Nucl.Instrum.Meth.*, A543:577–584, 2005.

[166] Georges *et al* Aad. Search for second generation scalar leptoquarks in pp collisions at $\sqrt{s}$ = 7 TeV with the ATLAS detector. Technical Report arXiv:1203.3172. CERN-PH-EP-2012-056, CERN, Geneva, Mar 2012. Submitted to European Physical Journal C.

[167] Georges *et al* Aad. Search for first generation scalar leptoquarks in pp collisions at $\sqrt{s}$ = 7 TeV with the ATLAS detector. Technical Report arXiv:1112.4828. CERN-PH-EP-2011-202, CERN, Geneva, Dec 2011.

[168] C Gemme. The ATLAS insertable B-Layer (IBL) project. Technical Report ATL-INDET-PROC-2011-018, CERN, Geneva, Sep 2011.

[169] Krzysztof Iniewski. *Radiation Effects in Semiconductors (Devices, Circuits, and Systems)*. CRC Press, 2010. ISBN 9781439826942.

[170] Wustenfeld Gossling, Peters and Wunstorf. Influence of Surface Damage on Highly Segmented Silicon Detectors. Technical Report ROSE/TN/2000-05, CERN, Geneva, Nov 1999.

[171] E. Fretwurst, G. Lindstrom, J. Stahl, I. Pintilie, Z. Li, et al. Bulk damage effects in standard and oxygen enriched silicon detectors induced by Co-60 gamma radiation. *Nucl.Instrum.Meth.*, A514:1–8, 2003.

[172] M Capeans, G Darbo, K Einsweiller, M Elsing, T Flick, M Garcia-Sciveres, C Gemme, H Pernegger, O Rohne, and R Vuillermet. ATLAS Insertable B-Layer Technical Design Report. Technical Report CERN-LHCC-2010-013. ATLAS-TDR-019, CERN, Geneva, Sep 2010.

[173] S Grinstein. Overview of the ATLAS Insertable B-Layer (IBL) Project. Technical Report ATL-INDET-PROC-2012-004, CERN, Geneva, Jan 2012.

[174] M. Garcia-Sciveres, D. Arutinov, M. Barbero, R. Beccherle, S. Dube, et al. The FE-I4 pixel readout integrated circuit. *Nucl.Instrum.Meth.*, A636:S155–S159, 2011.

[175] Sherwood I. Parker, Christopher J. Kenney, and Julie Segal. 3-D: A New architecture for solid state radiation detectors. *Nucl. Instrum. Meth.*, A395: 328–343, 1997.

[176] A. Kok, T.E. Hansen, T.A. Hansen, N. Lietaer, A. Summanwar, et al. Fabrication of 3D silicon sensors. *PoS*, VERTEX2010:22, 2010.

[177] Thor-Erik Hansen, Angela Kok, Trond A. Hansen, Nicolas Lietaer, Michal Mielnik, et al. First fabrication of full 3D-detectors at SINTEF. *JINST*, 4: P03010, 2009.

[178] G. Pellegrini, M. Lozano, M. Ullan, R. Bates, C. Fleta, et al. First double-sided 3-D detectors fabricated at CNM-IMB. *Nucl.Instrum.Meth.*, A592: 38–43, 2008.

[179] S Grinstein. Overview of Silicon Pixel Sensor Development for the ATLAS Insertable B-Layer (IBL). Technical Report ATL-INDET-PROC-2011-042, CERN, Geneva, Dec 2011.

[180] Igor Rubinskiy. Irradiation and beam tests qualification for ATLAS IBL Pixel Modules. Technical Report ATL-INDET-PROC-2012-007, CERN, Geneva, Mar 2012.

[181] Ilias Efthymiopoulos and Adrian Fabich. The Very Low 1-9 GeV/c Tertiary Beam Extension of the H8 Beam Line of CERN SPS. 2012.

[182] C. Adorisio et al. System test of the ATLAS muon spectrometer in the H8 beam at the CERN SPS. *Nucl.Instrum.Meth.*, A593:232–254, 2008.

[183] J. Treis, P. Fischer, H. Kruger, L. Klingbeil, T. Lari, et al. A Modular PC based silicon microstrip beam telescope with high speed data acquisition. *Nucl.Instrum.Meth.*, A490:112–123, 2002.

[184] Kyrre Ness Sjbk. Full simulation of a testbeam experiment including modeling of the Bonn Atlas Telescope and Atlas 3D pixel silicon sensors.

[185] M. Morpurgo. A Large Superconducting Dipole Cooled by Forced Circulation of Two Phase Helium. *Cryogenics*, 19:411–414, 1979.

[186] Antonio Bulgheroni. Results from the EUDET telescope with high resolution planes. *Nucl.Instrum.Meth.*, A623:399–401, 2010.

[187] R. Mankel. A Concurrent track evolution algorithm for pattern recognition in the HERA-B main tracking system. *Nucl.Instrum.Meth.*, A395:169–184, 1997.

[188] P. Grenier et al. Test Beam Results of 3D Silicon Pixel Sensors for the ATLAS upgrade. *Nucl.Instrum.Meth.*, A638:33–40, 2011.

[189] A. Micelli, K. Helle, H. Sandaker, B. Stugu, M. Barbero, et al. 3D-FBK pixel sensors: Recent beam tests results with irradiated devices. *Nucl.Instrum.Meth.*, A650:150–157, 2011.

[190] Michael Kohler, Liv Wiik, Richard Bates, Gian-Franco Dalla Betta, Celeste Fleta, et al. Beam test measurements with planar and 3D silicon strip detectors irradiated to sLHC fluences. *IEEE Trans.Nucl.Sci.*, 58:1308–1314, 2011.

[191] Georges *et al* Aad. The ATLAS Inner Detector commissioning and calibration. *Eur. Phys. J. C*, 70(arXiv:1004.5293, CERN-PH-EP-2010-043):787–821. 34 p, Jun 2010.

[192] Georges Aad et al. Measurement of the ZZ production cross section and limits on anomalous neutral triple gauge couplings in proton-proton collisions at sqrt(s) = 7 TeV with the ATLAS detector. *Phys.Rev.Lett.*, 108:041804, 2012.

[193] V.M. Abazov et al. $ZZ \to \ell^+\ell^-$ v anti-v production in $p\bar{p}$ collisions at $\sqrt{s}$ = 1.96-TeV. *Phys.Rev.*, D78:072002, 2008.

[194] Victor Mukhamedovich Abazov et al. A measurement of the WZ and ZZ production cross sections using leptonic final states in 8.6 fb^{-1} of $p\bar{p}$ collisions. *Phys.Rev.*, D85:112005, 2012.

[195] Measurement of the ZZ production cross section in the llvv channel in proton-proton collisions at sqrt(s)=7 TeV with the ATLAS detector. Technical Report ATLAS-CONF-2012-027, CERN, Geneva, Mar 2012.

APPENDIX A

3D Pixel Sensors

The ATLAS Pixel detector (described in Section 2.2.3) provides three high-precision space-point measurements per track immediately outside the nominal interaction point. As such, it plays a critical role in track impact parameter resolution and, thus, vertexing and b-tagging [59]. Owing to its proximity to the IP, the Pixel detector (particularly its innermost layer, the so-called "B-layer") must operate in a high-radiation, high-occupancy environment.

The original design accounted for a total ionization dose of 0.5 MGy and a 1 MeV neutron-equivalent fluence of 1×10^{15} n_{eq}/cm^2. The annual radiation dose expected in ATLAS is shown in Figure A.1. For the B-layer, this corresponds to an integrated luminosity of around 300 fb^{-1}, which it is expected to reach before the entire Pixel detector is to be replaced during an LHC shutdown in 2020 [168]. Radiation damage degrades silicon sensor performance over time and can negatively impact physics analysis results. It can be divided in two classes, each arising from distinct mechanisms [169]:

- **Surface damage:** Ionizing radiation produces electron-hole pairs along its path; because of vastly different mobilities in the dielectric SiO_2 layer, a fraction of holes are captured at the Si–SiO_2 interface, giving rise to a build-up of fixed, positive oxide charges as well as interface traps with energy levels in the silicon band gap. Macroscopically, these phenomena reduce the width of the depletion region at the interface, lower the sensor breakdown voltage, and increase the surface leakage current and cross-talk. [170]

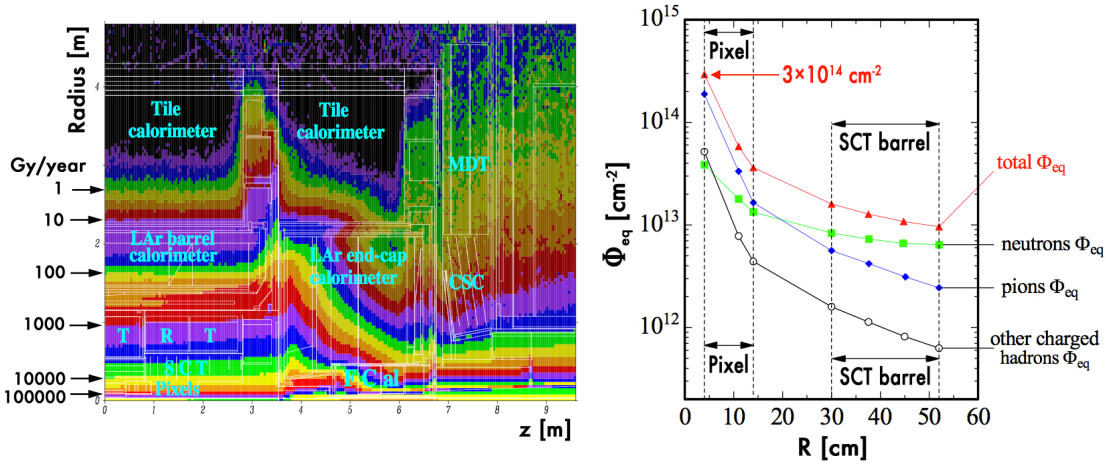

(a) (b)

Figure A.1: (a) Total ionizing radiation dose expected per year in ATLAS. The Pixel detector receives the largest dose: $\sim$ 160 kGy/year [59]; (b) Hadron fluences expected per year in the Pixel and SCT detectors [171].

- **Bulk damage:** Non-ionizing energy loss induced by through-going hadrons causes displacement of silicon atoms in the lattice, resulting in point or cluster defects with altered electrical properties.[1] Macroscopically, this decreases the charge collection efficiency and increases the full depletion voltage and leakage current of the sensor by an amount approximately proportional to the radiation fluence [171]. In practice, bulk (rather than surface) damage is the limiting factor for silicon sensor lifetimes.

Additionally, the Pixel detector was designed to handle an instantaneous luminosity of 1×10^{34} cm^{-2}s^{-1}; however, the LHC is expected to exceed (double) that value before the 2020 shutdown. The resulting increase in detector occupancy poses relatively straightforward difficulties: readout-induced inefficiencies, degraded resolution, and an increase in track fake rates. Again, the loss in Pixel performance has consequences for physics analyses. [172]

In order to mitigate radiation- and occupancy-related performance degradation of the ID, as well as improve tracking resolution and precision, it was decided to install an additional fourth layer *inside* the B-layer, mounted directly on a new beam pipe. It is called the *Insertable B-layer* (IBL) [172] [173], and it is designed to withstand radiation doses of 2.5 MGy and 5×10^{15} n_{eq}/cm^2 and an instantaneous luminosity of 3×10^{34} cm^{-2}s^{-1}. Given these challenges, new silicon pixel sensors

[1] Displacement damage depends on the type and energy of the incident hadron. A conventional reference point is 1 MeV neutrons.

(as well as readout chips [174]) had to be developed. Ultimately, two designs were selected: *n*-in-*n* planar pixels on an oxygenated float-zone bulk and 3D pixels with columnar electrodes penetrating the bulk, the latter of which is discussed below.

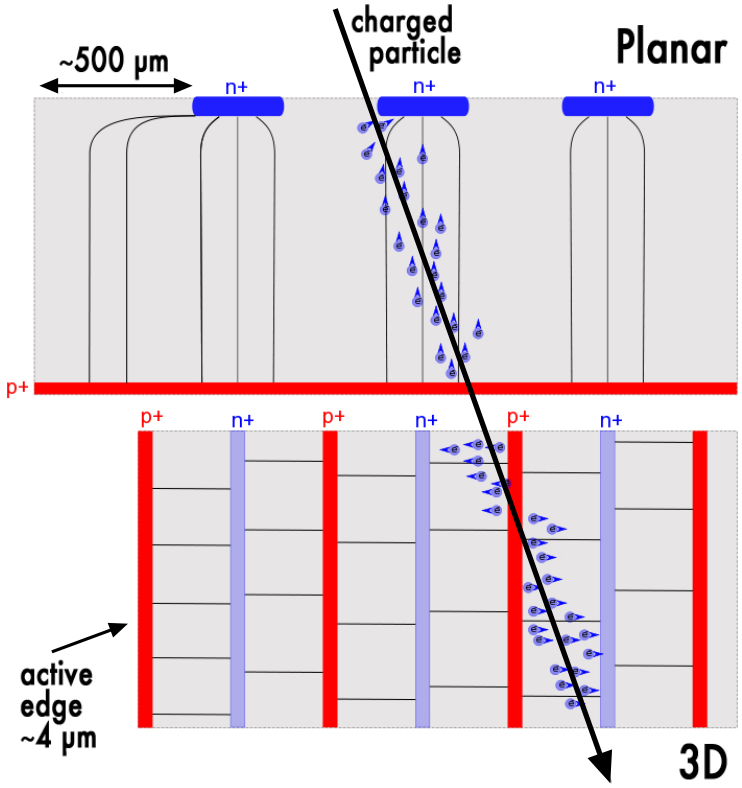

Figure A.2: Cartoon illustration contrasting planar and 3D pixel designs.

A.1 3D Pixel Design

Initially proposed in 1997 [175], 3D pixels utilize a new sensor geometry that takes advantage of recent advances in silicon sensor fabrication, including very large scale integration and deep reactive ion etching, and improved wafer-bonding techniques [176]. They are characterized by columnar electrodes ~ 15 μm in diameter that fully or partially penetrate the silicon bulk perpendicular to its surface, rather than the traditional planar structures that are implanted on the surface. This fundamental design difference is shown in Figure A.2, and it has several key features: high electric field parallel to the surface, short charge collection distance independent of wafer thickness, and an active sensor edge. This translates into performance advantages:

- fast charge collection
- high signal efficiency
- intrinsic radiation hardness
- low depletion voltage
- minimal dead zone around sensor edges

To date, two prototype configurations have been produced and tested: single-sided "Full-3D" sensors, in which both *n*-type readout and *p*-type bias electrodes fully penetrate the silicon substrate [177]; and double-sided double type column (DDTC) sensors, in which *n*- and *p*-type electrodes are etched from opposite sides and do not fully penetrate to the other side [178]. They are pictured in Figure A.3. Although the two configurations achieve comparable performance, the DDTC sensors are much simpler to fabricate.

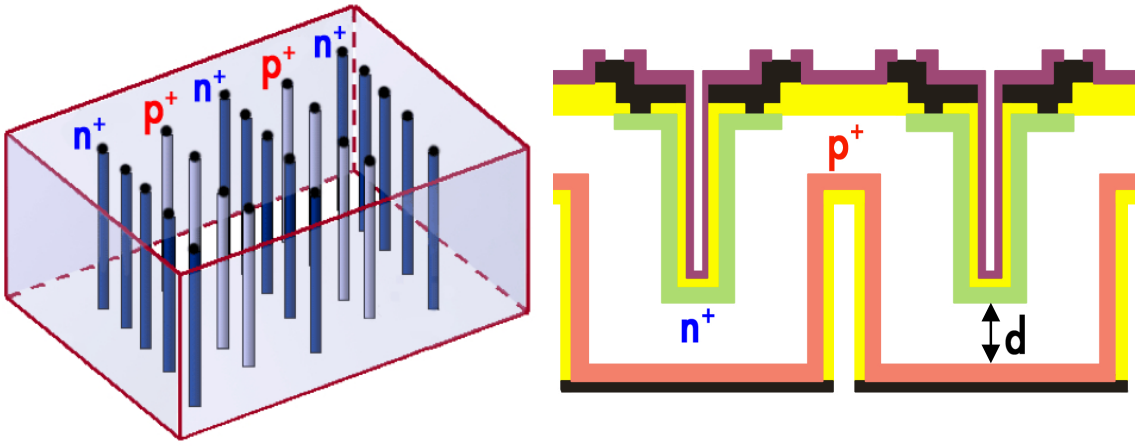

(a) (b)

Figure A.3: Full-3D (a) and DDTC (b) sensor configurations.

Silicon sensors used in the IBL will be bump-bonded to a new FE-I4 readout chip, whose larger size and active fraction than its predecessor features an array of 80×336 pixels [173]. Each pixel is 50×250 μm^2 in size and contains two *n*-type readout electrodes aligned in the longer dimension surrounded by six *p*-type bias electrodes that are shared with neighboring pixels, giving an inter-electrode distance of approximately 70 μm. (Note that earlier prototype sensors used to verify the device characteristics were connected to current-generation FE-I3 chips, and

therefore had different dimensions: 160×18 pixels of 50×400 μm^2 each, with two-, three-, and four-electrode configurations.) Signals from ionizing particles are measured digitally as a pixel's "time over threshold" (ToT) in units of 25 ns, which is (approximately) linearly related to the total amount of charge ionized. A conventional "tuning" of the FE-I3 chip gives 60 ToT for a charge of 20,000 electrons; the measurement threshold is $\sim 3,200$ e$^-$.

A.2 Test Beam Studies

Test beams are small-scale, fixed-target experiments that reproduce realistic data-taking conditions but under *controlled* circumstances — namely, the energy, type, and positioning of incident particles in the beam is known, and possibly adjustable. They are critical for performance characterization of any particle detector and complement tests that can be performed in laboratories. *Beam telescopes* are tools to precisely determine the tracks of particles passing through them. The methodology is similar to that employed in the Inner Detector[2]: a series of space-point hits are measured along the trajectory of a charged particle, then a pattern recognition algorithm proceeds along the projected path, matching hits together to reconstruct a track. The track is extrapolated to the position of a *device under test* (DUT) and compared with the DUT's independent measurement, allowing for studies of position resolution[3], hit efficiency, charge collection, and so on.

Prototype 3D pixel sensors have been studied in multiple test beams since 2008 as part of the IBL qualification program [179] [180]. Most took place at the CERN SPS North Area, which provides secondary beam lines of various leptons and hadrons with energies in the $10-400$ GeV range.[4] Specifically, charged pion beams of 120 and 180 GeV were used to characterize the 3D sensors; the high-momentum particles minimize multiple scattering effects. Two beam telescopes were used:

- **Bonn ATLAS Telescope (BAT):** The BAT [183] consists of three planes of double-sided silicon strip sensors with a 50 μm pitch, aligned along the beam line. Tracking resolution was estimated at 6 μm using a full GEANT4 simulation [184]. Event triggering was provided by two upstream scintillators in coincidence mode; a downstream scintillator with a small hole in its center vetoed events, suppressing showering and limiting the angular spread of the beam. DUTs were positioned between the first and second telescope plane.

[2]Hardware described in Section 2.2.3, software described in Section 4.1

[3]Clearly, the telescope's pointing resolution should be better than the intrinsic resolution expected of the DUTs.

[4]Dedicated documentation regarding the CERN SPS North Area is scarce. Recent upgrades to the H8 beam line are described in [181], and a representative example of the sort of physics done on such beam lines is given in [182].

The full setup was placed inside a superconducting Morpurgo dipole magnet [185] with a vertical 1.6 T magnetic field at the position of the DUTs in order to test for changes in their response.

- **European Detector (EUDET) Telescope:** This newer, high-resolution telescope consists of six planes of "Mimosa26" pixel sensors with a pitch of 18.5 μm [186]. The EUDET telescope's tracking resolution is approximately 3 μm. Pairs of scintillators both up- and downstream of the telescope planes provided event triggering. DUTs were positioned between the third and fourth telescope planes.

Diagrams of these two test beam setups are shown in Figure A.4. In both cases, Kalman filters were used to reconstruct tracks, which in turn were used to align the telescope planes; however, distinct implementations were needed to accommodate practical differences between the telescopes [119] [187].

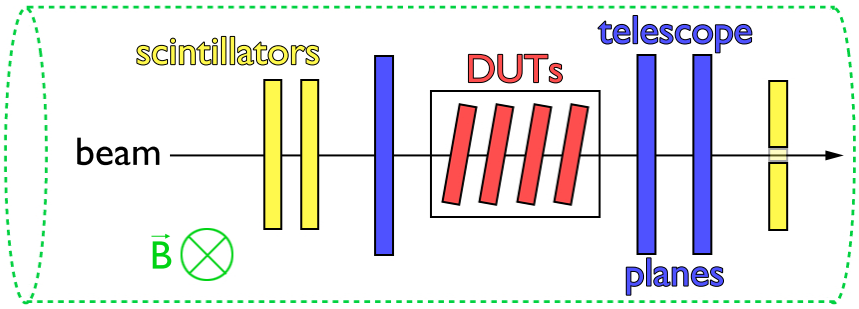

(a)

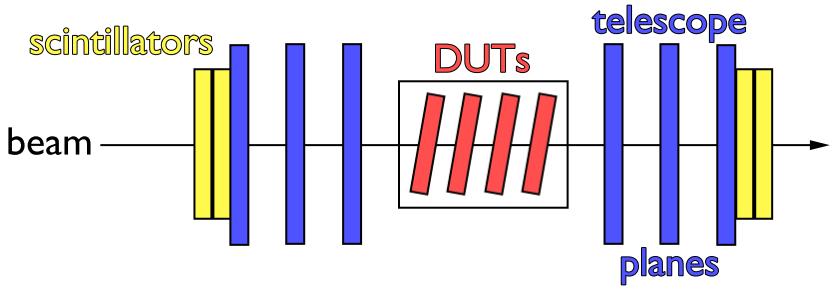

(b)

Figure A.4: Schematic top-view of a test beam setup using the (a) BAT and (b) EUDET beam telescopes. Not to scale.

A.3 Results

A few of the test beam results to which the author contributed are presented in this section [188] [189]; for more recent and other results, see [172], [180], [190]. Note: These results are for a variety of 3D pixel sensors (Full-3D and manufacturer-specific DDTCs) under different conditions (normal/tilted beam incidence angles, with/without an external magnetic field) at varying levels of irradiation.

Tracking Efficiency

The probability of finding a (DUT) hit near a (telescope) track is called *tracking efficiency*. The columnar electrodes of 3D pixels are known to be at least partially inactive, depending on their diameter, doping profile, and fabrication; consequently, a certain amount of signal loss is observed from tracks passing directly through electrodes at normal incidence. This inefficiency is recovered, however, at modest incidence angles.[5]

Figure A.5 shows two-dimensional tracking efficiency maps at normal and tilted incidence for two sensors: a Full-3D sensor fabricated at the Stanford NanoFabrication Facility (denoted STA), un-irradiated, 210 μm thick; and a DDTC sensor fabricated at IRST-FBK (denoted FBK), proton-irradiated to a fluence of 10^{15} n_{eq}/cm^2, with a wafer thickness of 200 μm and (non-optimized) bias and readout electrode penetration depths of 190 and 100 μm, respectively. At normal incidence, electrode efficiencies in the STA device are both about 50% but slightly higher in the readout electrodes, while in the FBK device bias electrodes are about 80% efficient and readout electrodes are almost fully efficient. This result is not surprising, given the difference in column depths and the higher electric field near the readout electrodes. The small difference in efficiency between bias and readout electrodes in the STA sensor may arise from their different "fillings." For both sensors, tracking efficiency is fully recovered for tracks impinging at an angle.

In the ATLAS Pixel detector, a solenoidal magnetic field is applied orthogonal to the sensors' electric field, which has the effect of either focusing or defocusing the ionized charges drifting through the silicon bulk, depending on the track's angle of incidence.[6] In contrast, the effect of a magnetic field on 3D sensors is expected to be small, given the difference in geometry and electric field orientation, and the data confirm it: Figure A.6 shows the overall tracking efficiency of 3D sensors to be basically unchanged in the presence of a magnetic field. As discussed previously, tilt angle *does* have a notable effect on efficiency, particularly in Full-3D sensors.

[5] IBL sensors will be inclined at 14°, so 3D electrode inefficiency is not a practical concern.

[6] The Lorentz angle at which maximum focusing (minimum cluster size) occurs is $\theta_L = -7.6° \pm 0.6°$ for current pixels. A measurement using cosmic ray data is described in [191].

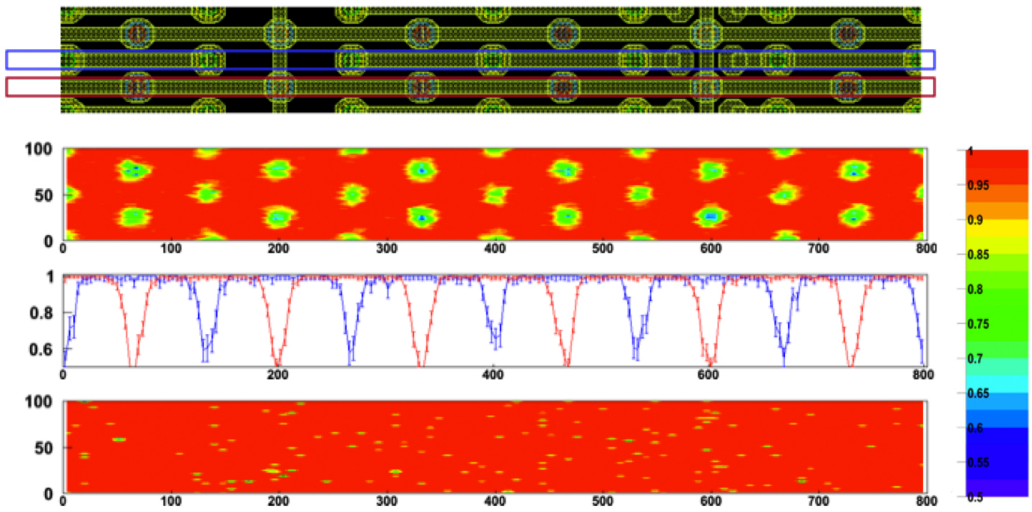

(a)

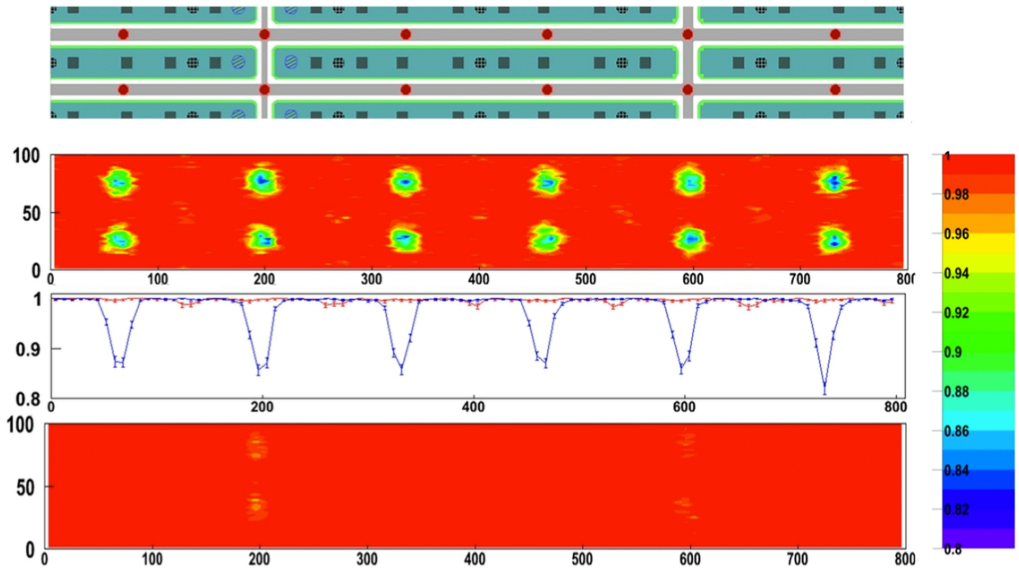

(b)

Figure A.5: Two-dimensional tracking efficiency maps for (a) an un-irradiated Full-3D STA sensor and (b) a *p*-irradiated DDTC FBK sensor. For each, the top row is a mask detail centered on one cell with an additional half-cell in all directions; the second row shows the efficiency for tracks at normal incidence, while the third row shows the one-dimensional projection in the bias and readout electrode regions; and the fourth row shows the efficiency for tracks at tilted incidence (-10° for the STA device, $+15^\circ$ for the FBK). Note the difference in vertical scale.

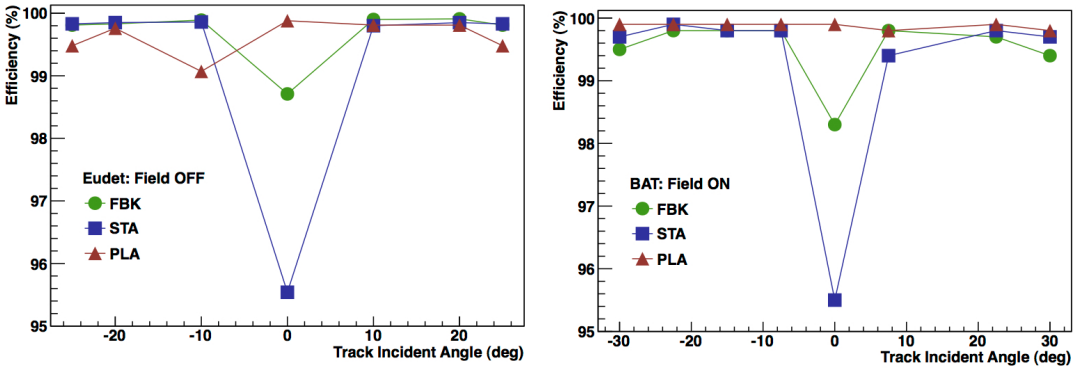

(a) (b)

Figure A.6: Overall tracking efficiency of STA and FBK 3D sensors as a function of sensor tilt angle (a) in the absence of a magnetic field, and (b) with a 1.6 T orthogonal magnetic field applied. Results for a current-generation planar pixel sensor (denoted PLA) are shown for reference.

Charge Sharing

Another fundamental feature of pixel detectors is *charge sharing* — that is, the sharing of a deposited charge between two or more neighboring cells. High charge sharing gives better tracking resolution, since the track position can be more precisely determined through, for example, charge-weighted centering of the signal. On the other hand, less charge is available per cell, so the probability of a signal being passing threshold is also lower, resulting in an increased fraction of lost hits. Considering that charge collection efficiency decreases after irradiation (see the discussion of radiation damage earlier), it is desirable to reduce charge sharing for detectors operating in a high-radiation environment, such as the IBL. 3D pixels, owing to their unusual geometry, experience a sort of "self-shielding" effect when it comes to charge sharing; relative to planar sensors, charge sharing in 3D pixel sensors is much reduced.

The charge sharing *probability* can be defined as the number of tracks associated with more than one hit divided by the total number of tracks: $N_{\text{trks}}(>1\text{ hit})/N_{\text{trks}}(\text{all})$. In Figure A.7, two-dimensional maps of charge sharing probability for normal-incident tracks are shown for three sensors: the un-irradiated STA sensor described previously, and an un-irradiated FBK sensor, 200 μm thick, with an overlap between the bias and readout electrodes of 100 μm. As expected, charge sharing occurs predominantly when tracks impinge near the edges of a cell. Furthermore, charge sharing is least probable in the Full-3D STA sensor and most probable for the reference planar (PLA) sensor, with the DDTC FBK sensor falling in between.

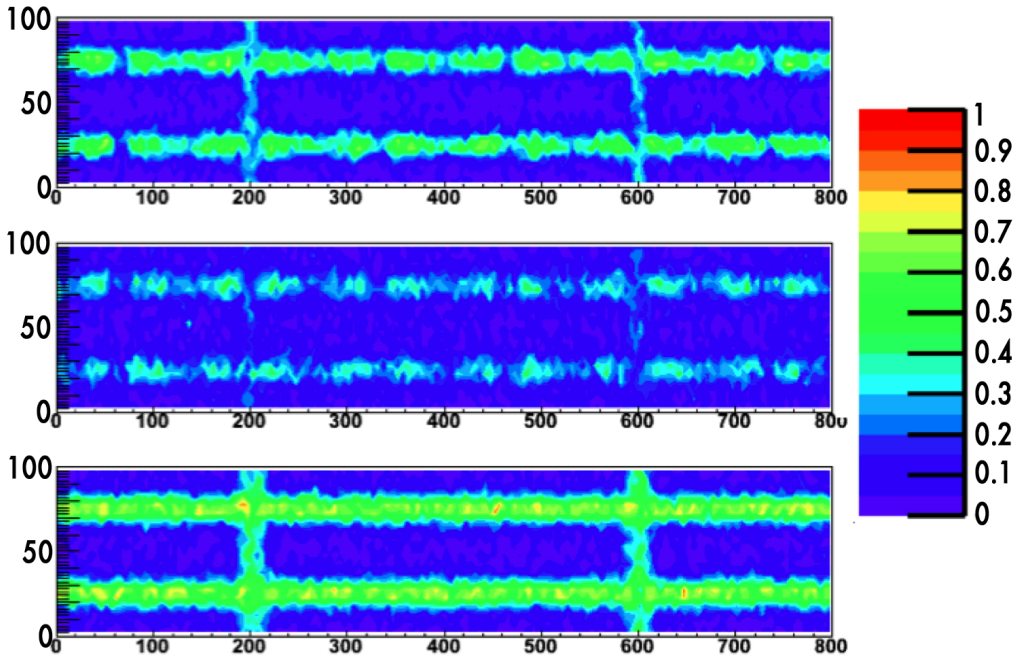

Figure A.7: Two-dimensional maps of charge sharing probability at normal incidence for three un-irradiated sensors: FBK (top), STA (middle), PLA (bottom).

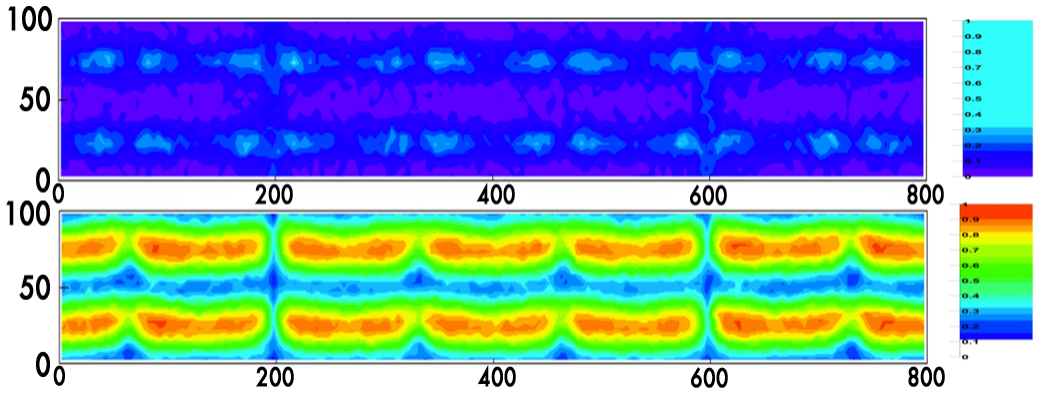

Figure A.8: Two-dimensional maps of charge sharing probability of a *p*-irradiated FBK sensor at normal incidence (top) and 15° tilted incidence (bottom).

A.3 Results

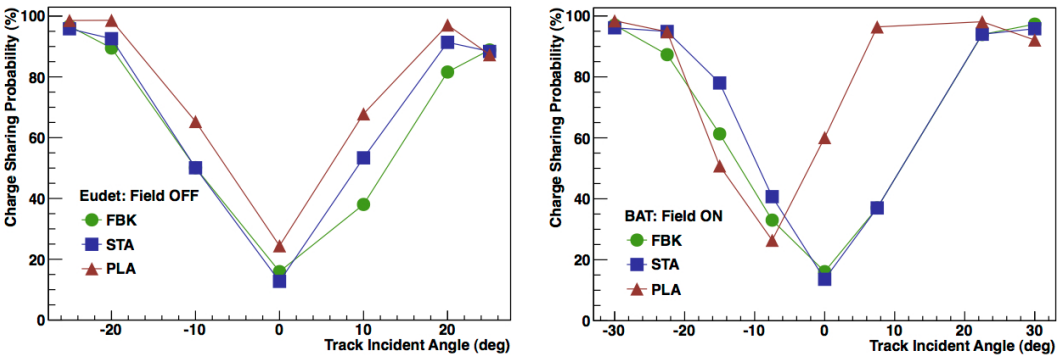

(a) (b)

Figure A.9: Overall charge sharing probability of un-irradiated STA and FBK as a function of sensor tilt angle (a) in the absence of a magnetic field, and (b) with a 1.6 T orthogonal magnetic field applied. Results for a current-generation planar pixel sensor (denoted PLA) are shown for reference.

Figure A.8 shows two-dimensional charge sharing probability maps for the proton-irradiated FBK DDTC sensor described previously. This comparison illustrates that charge sharing is much larger at non-normal track incidence, as expected. The overall charge sharing probability as a function of track incident angle shown in Figure A.9 further clarifies this point. In 3D pixel sensors, charge sharing is minimal for tracks at normal incidence, and approaches 100% for tracks at very large incident angle; this behavior is symmetric with respect to positive and negative angles, and unchanged by a magnetic field. In the planar reference sensor, charge sharing follows a similar pattern in the absence of a magnetic field, but is generally higher than that observed in 3D pixels. In the presence of a magnetic field, however, charge sharing is asymmetric, with a minimum at the Lorentz angle.

For convenience, a summary table of comparable, recent results for Full-3D, two different DDTC, and reference planar pixel sensors is given in Table A.1 [172]. For the case of interest, i.e. tracking in a high-radiation environment with an external magnetic field and tracks at non-normal incidence angles, 3D pixel sensors appear to be well suited.

Sensor	Incidence Angle (normal = 0)	Hit Efficiency [%]		Charge Sharing [%]	
		B = 0	B = 1.6 T	B = 0	B = 1.6 T
Planar	0	99.9	100.0	20.4	45.4
	13.8°	100.0	100.0	78.2	42.6
Full-3D	0	96.7	96.5	20.2	23.0
	11.4°	99.9	99.9	60.3	55.7
DDTC (a)	0	98.4	98.3	12.2	14.6
	14.1°	99.8	99.5	62.1	52.5
DDTC (b)	0	99.2	99.1	17.6	18.9
	12.0°	99.8	99.9	51.6	47.1

Table A.1: Hit efficiency and charge sharing percentages at normal and tilted incidence angles, with and without an applied magnetic field, for a planar reference, Full-3D, and two different DDTC sensors. [172]

APPENDIX B

Modified Missing Transverse Energy

In some cases, searches for physics processes suffer predominantly from instrumental backgrounds. Take, for example, Z boson pair-production in which one Z decays into two, oppositely-charged leptons (either e^+e^- or $\mu^+\mu^-$) and the other decays into two neutrinos ($\nu\bar{\nu}$), as pictured in Figure B.1(a). This process is interesting as a check on the Standard Model: Since no triple gauge boson couplings involving two Z bosons are predicted, i.e. ZZZ and $ZZ\gamma$ as in Figure B.1(b), there is no tree-level contribution from s-channel quark-antiquark annihilation. Therefore, a precise measurement of the ZZ production cross section can be used to test for anomalous (non-SM) couplings [192]. In addition, $ZZ \to \ell^+\ell^-\nu\bar{\nu}$ is a background to multiple Higgs boson decay channels, so the technique demonstrated in this analysis may also be applied to related Higgs boson searches.

$ZZ \to \ell^+\ell^-\nu\bar{\nu}$ has a branching ratio six times larger than $ZZ \to \ell\ell\ell\ell$. While the latter has no SM processes with the same final state, the former is buried in backgrounds with two, oppositely-charged leptons and significant—real or fake—missing transverse energy. Backgrounds with the same final state particles include leptonic WW and $t\bar{t}$ production. The dominant source of instrumental background is Z boson production in association with jets, where the Z decays into a di-lepton pair and $\not{E}_{\mathrm{T}}$ arises from detector mis-measurement of the lepton pair's and/or the hadronic recoil system's transverse momentum. Stringent rejection of this background is particularly important owing to its very large cross section (roughly four orders of magnitude larger than signal) and the difficulty in simulating the mis-reconstruction rates.

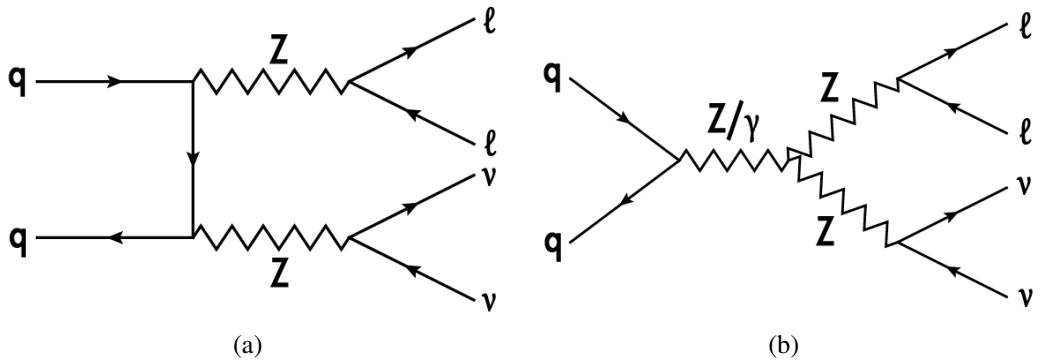

Figure B.1: Feynman diagrams for $ZZ \to \ell^+\ell^-\nu\overline{\nu}$ production (a) allowed and (b) *not* allowed in the Standard Model.

The basic event signature for the ZZ signal is a pair of high-p_{T}, oppositely-charged leptons with invariant mass close to m_Z from the decay of one Z boson in association with significant $\not\!\!E_{\mathrm{T}}$ from the neutrinos in the other Z decay. In inclusive $Z \to \ell^+\ell^- +$ jets background events, the erroneously large (mis-measured) $\not\!\!E_{\mathrm{T}}$ values result in a long tail in the distribution that effectively swamps out the signal. A simple requirement on $\not\!\!E_{\mathrm{T}}$ would reject much of this background, but at the cost of losing much of the signal as well; given the relatively small ZZ production cross section, such a cut is less than ideal. Instead, a novel approach to this challenge is presented below.

B.1 $\not\!\!E'_{\mathrm{T}}$ Algorithm

In place of the standard $\not\!\!E_{\mathrm{T}}$, a modified missing transverse energy variable, $\not\!\!E'_{\mathrm{T}}$, is constructed. It is not a more accurate estimate of the $\not\!\!E_{\mathrm{T}}$ in an event, rather the *minimum feasible* $\not\!\!E_{\mathrm{T}}$ given measurement uncertainties on the lepton pair and hadronic recoil. The di-lepton p_{T} with respect to the other final state particles is taken as a starting point; correction terms accounting for several sources of detector mis-measurement are added only if they decrease its value, otherwise they are ignored. As a result, $\not\!\!E'_{\mathrm{T}}$ is more robust than $\not\!\!E_{\mathrm{T}}$ against reconstruction mistakes. This approach has been used successfully in the past, most recently at DØ [193] [194].

The $\not\!\!E'_{\mathrm{T}}$ algorithm proceeds as in the following steps.

Axis decomposition

In order to reduce the effects of individual lepton p_{T} mis-measurement, the di-lepton transverse momentum is decomposed into two orthogonal components, one

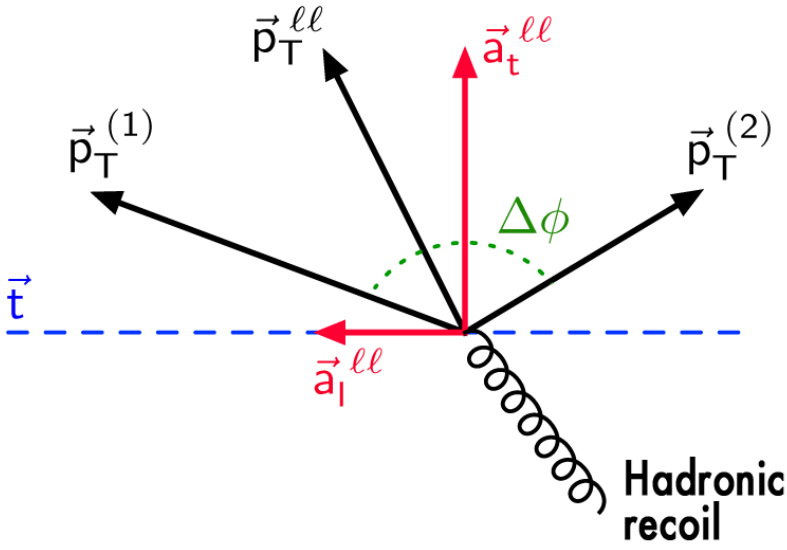

Figure B.2: Diagram of the decomposition of the lepton transverse momenta into transverse and longitudinal components.

of which is relatively insensitive to the detector's momentum resolution. To this end, the di-lepton transverse momentum and *thrust axis* in the transverse plane are defined as

$$\vec{p}_{\mathrm{T}}^{\,\ell\ell} \equiv \vec{p}_{\mathrm{T}}^{\,(1)} + \vec{p}_{\mathrm{T}}^{\,(2)} \tag{B.1}$$

$$\vec{t} \equiv \vec{p}_{\mathrm{T}}^{\,(1)} - \vec{p}_{\mathrm{T}}^{\,(2)}, \tag{B.2}$$

where $\vec{p}_{\mathrm{T}}^{\,(1)}$ and $\vec{p}_{\mathrm{T}}^{\,(2)}$ are the transverse momenta of the first- and second-leading leptons, respectively. This thrust axis maximizes the scalar sum of the individual leptons' $\vec{p}_{\mathrm{T}}$ projected onto itself, as shown in Figure B.2.

Next, a coordinate system is defined with respect to the thrust axis, consisting of unit vectors $\hat{a}_l$ and $\hat{a}_t$ parallel and perpendicular to $\vec{t}$, respectively.[1] The di-lepton system $\vec{p}_{\mathrm{T}}^{\,\ell\ell}$ is decomposed into parallel and perpendicular components:

$$a_l^{\ell\ell} = \vec{p}_{\mathrm{T}}^{\,\ell\ell} \cdot \hat{a}_l \tag{B.3}$$

$$a_t^{\ell\ell} = \vec{p}_{\mathrm{T}}^{\,\ell\ell} \cdot \hat{a}_t \tag{B.4}$$

Resolution effects are more pronounced in the $\hat{a}_l$ direction.

[1] Henceforth, subscripts l and t refer to vector components in the parallel or *longitudinal* and perpendicular or *transverse* directions.

This axis decomposition is only performed for events in which the opening angle between the two Z-decay leptons $\Delta\phi(\ell,\ell) > \pi/2$. For events with highly-boosted leptons, i.e. $\Delta\phi(\ell,\ell) \leq \pi/2$, the direction of the di-lepton $\vec{p}_{\mathrm{T}}^{\,\ell\ell}$ is used to define the perpendicular direction, while all parallel components are set to zero.

Calorimeter recoil

Two measures of the net transverse energy deposited in the calorimeter are used to determine if apparent but false $\not\!\!E_{\mathrm{T}}$ was generated in an event. For the first measure, the $\vec{p}_{\mathrm{T}}$ of those reconstructed jets pointing in the direction *opposite* to (recoiling against) the di-lepton system are summed —that is, jets for which $\vec{p}_{\mathrm{T}}^{\,\mathrm{jet}} \cdot \hat{a}_l < 0$ are added to the parallel correction, and similarly for the perpendicular correction. The second measure is the $\not\!\!E_{\mathrm{T}}$ measured by the calorimeter with the lepton pair's transverse momentum removed, leaving only the recoil of the Z boson.

The calorimeter recoil correction is thus defined as

$$\delta a_l^{\mathrm{calo}} = \min\left(\sum \vec{p}_{\mathrm{T}}^{\,\mathrm{jets}} \cdot \hat{a}_l,\ -(\vec{\not\!\!E}_{\mathrm{T}} + \vec{p}_{\mathrm{T}}^{\,\ell\ell}) \cdot \hat{a}_l,\ 0\right) \tag{B.5}$$

$$\delta a_t^{\mathrm{calo}} = \min\left(\sum \vec{p}_{\mathrm{T}}^{\,\mathrm{jets}} \cdot \hat{a}_t,\ -(\vec{\not\!\!E}_{\mathrm{T}} + \vec{p}_{\mathrm{T}}^{\,\ell\ell}) \cdot \hat{a}_t,\ 0\right). \tag{B.6}$$

By construction, this correction can only reduce the values of $\vec{a}_l^{\,\ell\ell}$ and $\vec{a}_t^{\,\ell\ell}$. Of all the correction terms, this one is typically largest.

Track Recoil

Another source of mis-measured $\not\!\!E_{\mathrm{T}}$ comes from jets that are "lost," i.e. not reconstructed in the calorimeter. Jets may fail reconstruction requirements if they may deposit some of their energy in the "crack" between the calorimeter barrel and endcap or if their composition is such that the bulk of their energy is deposited in the electromagnetic instead of hadronic calorimeter. In such cases, not all of the jet energy is recorded, resulting in apparent $\not\!\!E_{\mathrm{T}}$. However, recoil activity not observed in the calorimeter is often seen in the tracking detector as jets of tracks (*track jets*), and can thus be accounted for.

To remove poorly-measured or spurious tracks from consideration, base quality requirements are imposed: $p_{\mathrm{T}} > 1.0$ GeV, $|\eta| < 2.5$, and $\chi^2/dof < 5.0$; at least one Pixel hit, one SCT hit, and ten TRT hits; and isolation from all other jets and leptons in the event, with $\Delta R(\mathrm{track}, \ell\,\mathrm{or}\,\mathrm{jet}) > 0.4$.

A track jet is seeded by the highest-p_{T} track not yet associated with another track jet, and all un-associated tracks within a cone of $\Delta R \leq 0.5$ around the seed are then added to the track jet. This process repeats until every eligible track is associated with a track jet. Only track jets with $p_{\mathrm{T}} > 20$ GeV are kept. The track

recoil correction is defined as

$$\delta a_l^{\mathrm{trk}} = \left(\sum \vec{p}_T^{\,\mathrm{tjet}}\right) \cdot \hat{a}_l \tag{B.7}$$

$$\delta a_t^{\mathrm{trk}} = \left(\sum \vec{p}_T^{\,\mathrm{tjet}}\right) \cdot \hat{a}_t \tag{B.8}$$

As with the calorimeter correction, track jets are included only if they recoil *against* the di-lepton pair, i.e. $\vec{p}_{\mathrm{T}}^{\,\mathrm{tjet}} \cdot \hat{a}_{l,t} < 0$.

Lepton Resolution

Although uncertainties in the lepton transverse momentum are, on average, smaller than the calorimeter effects, in some cases the lepton p_{T} can still be significantly mis-measured. To account for this, the p_{T} of both leptons are individually fluctuated by one standard deviation of their fractional uncertainties (σ_1 and σ_2) such that the $\hat{a}_l$ and $\hat{a}_t$ components of the di-lepton $\vec{p}_{\mathrm{T}}^{\,\ell\ell}$ are separately minimized.

To minimize the perpendicular component $a_t^{\ell\ell}$, the p_{T} of both leptons are decreased by 1σ, giving the modified quantity

$$a_t^{\ell\ell'} = \vec{p}_{\mathrm{T}}^{\,\ell\ell'} \cdot \hat{a}_t', \tag{B.9}$$

where $\vec{p}_T^{\,\ell\ell'}$ and $\hat{a}_t'$ correspond to $\vec{p}_{\mathrm{T}}^{\,\ell\ell}$ and $\hat{a}_t$ redefined using $\vec{p}_{\mathrm{T}}^{\,(1)} \times (1-\sigma_1)$ and $\vec{p}_{\mathrm{T}}^{\,(2)} \times (1-\sigma_2)$ in place of the unscaled quantities. To minimize the parallel component $a_l^{\ell\ell}$, instead $\vec{p}_{\mathrm{T}}^{\,(1)}$ is decreased by $1\sigma_1$ and $\vec{p}_{\mathrm{T}}^{\,(2)}$ is increased by $1\sigma_2$.

The lepton resolution correction term is defined as follows:

$$\delta a_l^{\ell\ell} = \left(-\sigma_1 \vec{p}_{\mathrm{T}}^{\,(1)} + \sigma_2 \vec{p}_{\mathrm{T}}^{\,(2)}\right) \cdot \hat{a}_l \tag{B.10}$$

$$\delta a_t^{\ell\ell} = a_t^{\ell\ell'} - a_t^{\ell\ell}. \tag{B.11}$$

Combination

Finally, the four terms calculated in the previous steps are summed together separately for the parallel and perpendicular components:

$$a_l = a_l^{\ell\ell} + (c_{\mathrm{calo}} \cdot \delta a_l^{\mathrm{calo}}) + (c_{\mathrm{trk}} \cdot \delta a_l^{\mathrm{trk}}) + (c_{\ell\ell} \cdot \delta a_l^{\ell\ell}) \tag{B.12}$$

$$a_t = a_t^{\ell\ell} + (c_{\mathrm{calo}} \cdot \delta a_t^{\mathrm{calo}}) + (c_{\mathrm{trk}} \cdot \delta a_t^{\mathrm{trk}}) + (c_{\ell\ell} \cdot \delta a_t^{\ell\ell}), \tag{B.13}$$

where c_{calo}, c_{trk}, and $c_{\ell\ell}$ are constant factors chosen to optimize the performance of the $\not{E}'_{\mathrm{T}}$ variable. By construction, the $a^{\ell\ell}$ terms are always positive, and the δa terms are always negative or zero. If either a_l or a_t comes out negative, there is no

Process	$\sigma \times \mathrm{BR} \times \varepsilon$ [pb]	Request ID	Production Tags
$Z \to \mu\mu$+0p	830.12	107660	e737, s933, s946, r2302, r2300, p605
$Z \to \mu\mu$+1p	166.24	107661	e737, s933, s946, r2302, r2300, p605
$Z \to \mu\mu$+2p	50.282	107662	e737, s933, s946, r2302, r2300, p605
$Z \to \mu\mu$+3p	13.922	107663	e737, s933, s946, r2302, r2300, p605
$Z \to \mu\mu$+4p	3.6156	107664	e737, s933, s946, r2302, r2300, p605
$Z \to \mu\mu$+5p	0.94179	107665	e737, s933, s946, r2302, r2300, p605
$ZZ \to \ell\ell\nu\nu$	5.670*0.153	105932	e598, s933, s946, r2302, r2300, p638

Table B.1: Simulated event samples used to test the $\not{E}'_{\mathrm{T}}$ algorithm.

significant missing transverse momentum along that direction, so the quantity is set equal to zero to prevent artificial inflation of $\not{E}'_{\mathrm{T}}$.

The final variable, then, is a weighted quadrature sum of the two components:

$$\not{E}'_{\mathrm{T}} \equiv \sqrt{a_l^2 + (1.5\,a_t)^2}. \tag{B.14}$$

As the better-measured direction, the perpendicular component is given extra weight.[2] Recall that events with $\Delta\phi(\ell,\ell) \leq \pi/2$ take $\vec{p}_{\mathrm{T}}^{\,\ell\ell}$ as the $\hat{a}_t$ direction and set the $\hat{a}_l$ components to zero; in this case, only the perpendicular components are used in determining $\not{E}'_{\mathrm{T}}$.

B.2 Proof of Concept

As a proof of concept, the $\not{E}'_{\mathrm{T}}$ algorithm is applied to $Z+$jets and $ZZ \to \ell\ell\nu\nu$ MC samples, listed in Table B.1. Constant factors c_{calo}, c_{trk}, and $c_{\ell\ell}$ are all set equal to 2, as was done in [193]. Physics object selections are unchanged from the LQ analysis (see Section 5.2), with the exception of lowered p_{T} thresholds of 20 GeV for jets, muons, and electrons in order to increase statistics. Event selection is modified to reflect $ZZ \to \mu^+\mu^-\nu\bar{\nu}$ as signal rather than $LQ\overline{LQ} \to \mu\nu qq$. Specifically:

- Fires `EF_mu18_MG` OR `EF_mu40_MSonly_barrel` trigger
- At least one primary vertex with at least three associated Inner Detector tracks; in the case of multiple primary vertices, the track requirement is applied only to the one with the highest sum p_{T}^2
- Exactly two, oppositely-charged, good muons and zero good electrons, as defined in Section 5.2 except with $p_{\mathrm{T}} > 20$ GeV

[2] This factor 1.5 has not been explicitly optimized.

- No more than two good jets, as defined in Section 5.2 except with $p_{\mathrm{T}} > 20$ GeV
- Zero bad jets, and zero good jets falling within the vicinity of the LAr hole, as discussed in Section 5.3
- Di-muon invariant mass $70 < M_{\mu\mu} < 110$ GeV

Parallel and perpendicular components of each of the four terms contributing to the modified missing transverse energy variable are shown in Figures B.3–B.6. The final $\not{E}'_{\mathrm{T}}$ variable is shown in Figure B.7 alongside the standard $\not{E}_{\mathrm{T}}$ as well as Axial-$\not{E}_{\mathrm{T}}$ distributions, the latter of which is defined as

$$\mathrm{Axial} - \not{E}_{\mathrm{T}} = \not{E}_{\mathrm{T}} \times \cos\left(\Delta\phi(\not{E}_{\mathrm{T}}, p_{\mathrm{T}}^{\ell\ell})\right) \tag{B.15}$$

and has been used in ZZ analyses in a role similar to $\not{E}'_{\mathrm{T}}$ [195]. Also shown are signal and background efficiencies as a function of cut value on each missing transverse energy variable. Lastly, signal efficiency is plotted against background efficiency for a given cut value on each variable, plotted together in Figure B.8.

Over a wide range of signal efficiency values, $\not{E}'_{\mathrm{T}}$ rejects more Z+jets background than the other two variables. Even better performance may be achieved by explicit optimization of the constant factors for each correction term. As demonstrated here, $\not{E}'_{\mathrm{T}}$ is an effective variable for distinguishing $ZZ \to \ell\ell\nu\nu$ events with real, large missing transverse energy from the dominant instrumental background with large, mis-measured missing transverse energy.

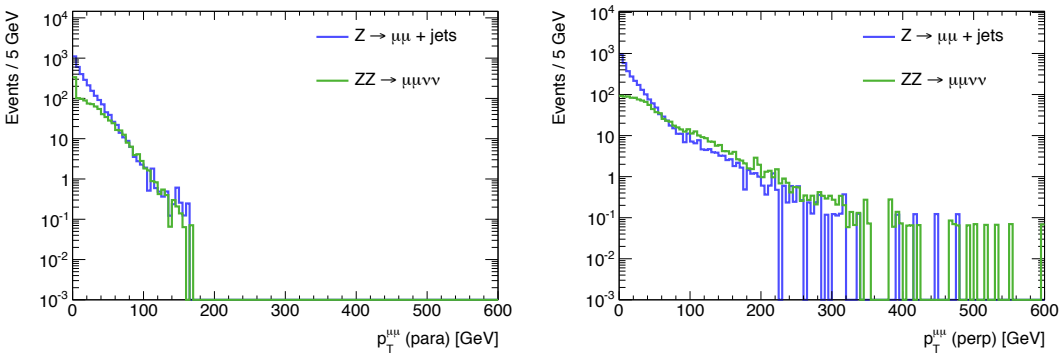

(a) (b)

Figure B.3: Di-muon transverse momentum projected onto the (a) parallel (b) perpendicular axes defined with respect to the thrust axis.

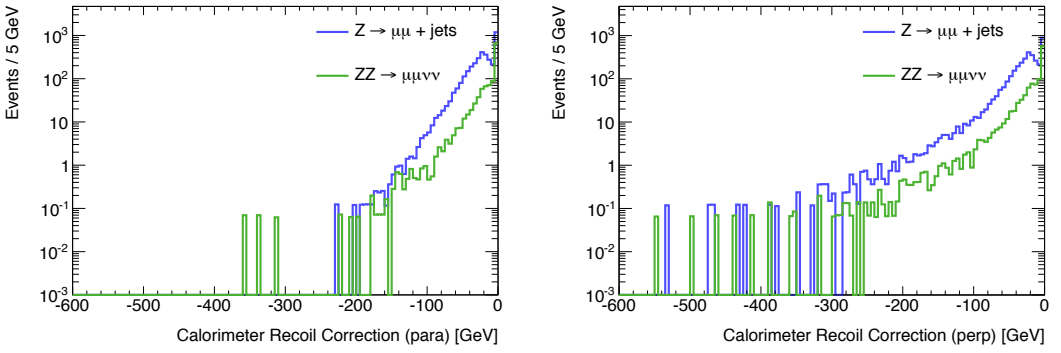

(a) (b)

Figure B.4: Calorimeter recoil correction projected onto the (a) parallel (b) perpendicular axes defined with respect to the thrust axis.

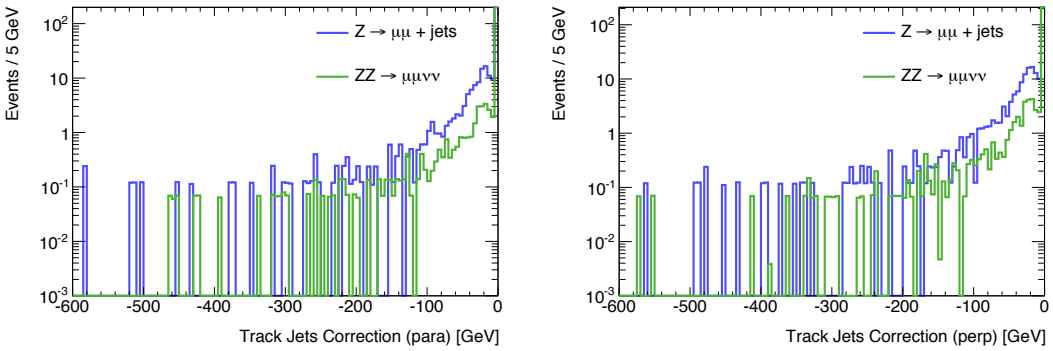

(a) (b)

Figure B.5: Track recoil correction projected onto the (a) parallel (b) perpendicular axes defined with respect to the thrust axis.

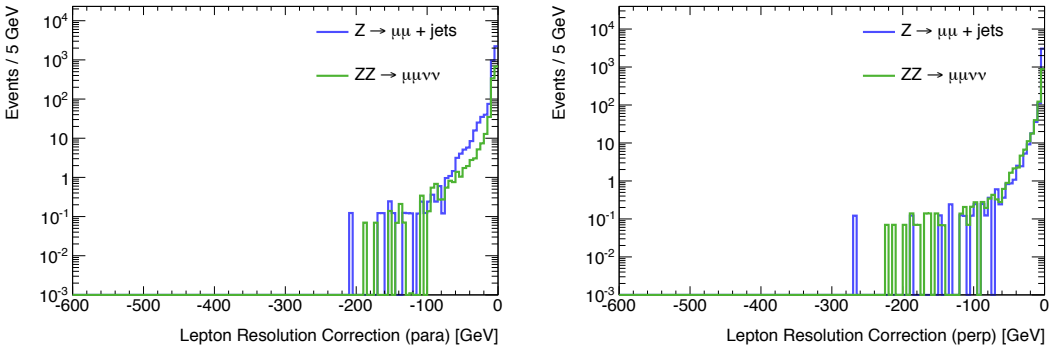

(a) (b)

Figure B.6: Lepton resolution correction projected onto the (a) parallel (b) perpendicular axes defined with respect to the thrust axis.

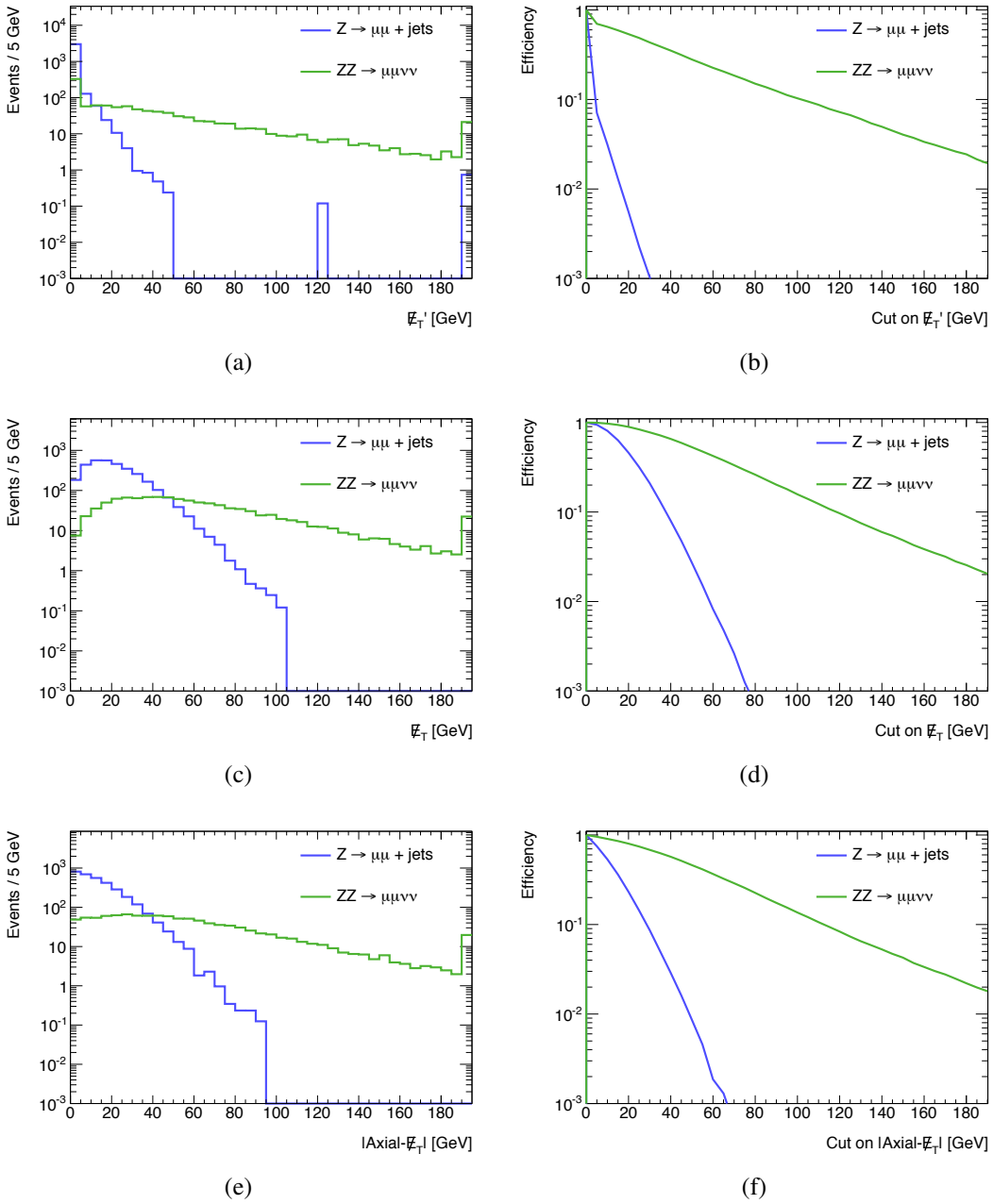

Figure B.7: ZZ signal and Z+jets background distributions for missing transverse energy variables (a) $\not\!\!E_{\mathrm{T}}'$, (c) $\not\!\!E_{\mathrm{T}}$, and (e) Axial-$\not\!\!E_{\mathrm{T}}$, as well as corresponding signal and background efficiencies as a function of cut value on those variables (b, d, and f, respectively).

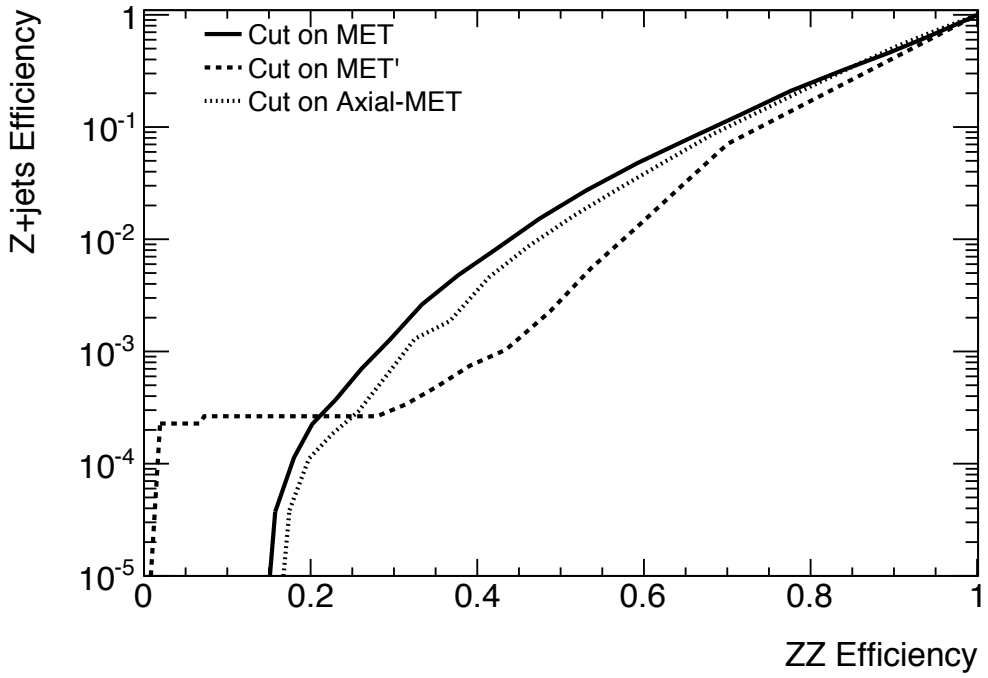

Figure B.8: ZZ signal versus Z+jets background efficiencies for a given cut value on each missing transverse energy variable ($\not\!\!E'_{\mathrm{T}}$, $\not\!\!E_{\mathrm{T}}$, and Axial-$\not\!\!E_{\mathrm{T}}$).